The Advanced Centre for Biochemical Engineering

Department of Biochemical Engineering

University College London

Elucidation of Flocculation Growth Kinetics Using a Microfluidic Approach

A dissertation submitted towards the degree of Doctor of Philosophy by,

Anand Narayanan Pallipurath Radhakrishnan

2016

Under the supervision of:

Dr Daniel G. Bracewell

Prof. Nicolas Szita

Declaration

I, *Anand Narayanan Pallipurath Radhakrishnan*, confirm that the work presented in this thesis is my own. Where information has been derived from other sources, I confirm that this has been indicated in the thesis. The thesis does not exceed the prescribed word limit, and none of the work presented in this thesis has been submitted for a qualification at any other institution.

Signature  Date 15-06-2016

Dedicated to my parents

Bright but hidden, the Self dwells in the heart.
Everything that moves, breathes, opens, and closes
Lives in the Self.

(The Upanishads)

Acknowledgements

I left India almost five years ago, in September 2011, as a graduate student, to embark upon a career-defining research degree at UCL. Pursuit of this project was made possible, thanks to the UCL ORS Scholarship and the Peter Dunnill Trust Fund for the financial support. I would like to express my immense gratitude to Dr Daniel Bracewell and Prof. Nicolas Szita for having faith in my abilities and for waking the scientific aptitude in me. As principal supervisors, they have also been a constant source of inspiration and encouragement, and I thoroughly enjoyed working at the Department of Biochemical Engineering at UCL. I would like to express my heartfelt thanks to the microfluidics group, my colleagues, friends and office-mates for their constant support, suggestions and most importantly for keeping me sane during the crunch hour. I would definitely miss the conversations, and coffee-breaks with Gregorio, Alex T., Georgina, Alice, Alex C., Alex S., and Pia. A special mention goes out to Brian O'Sullivan, Gareth Mannall, Mathew Davies, Rhys Macown and James Lawrence for their guidance during the initial struggle, training on different equipment, and for orientating me towards the kind of work that has been done. I believe I have found a genuine friend in Matt, who is not only great to work with, but imparts a lot of "microfluidic-wisdom". Marco Marques was initially appointed as my mentor, and ever since, has been a special friend and a well-wisher as well. I look forward to my time at UCL as a staff member, inspired by him. He is a unique scientist indeed. I have no words to thank him, his wife Salome and Matt for the immense moral support, especially during my struggles in the writing-up period. A special word of mention goes out to Carrie Benjamin, a former flatmate but a true friend who helped me overcome the "writer's block" by dragging me to the SOAS Library. I thoroughly enjoy spending time with her and Miquel. I also thank Miriam Beiato, and Nicola Jackson, for being the best flatmates one can find. Getting back home to them is an instant stress-relief, and they made sure that I stayed healthy and alive. I thank my colleagues from the Department of Chemical Engineering, UCL – especially Damiano Rossi for discussions about RTD and Marco Quaglio for valuable help with statistical data analysis.

Jonathan Skelton has been a friend ever since I landed in the UK. I remember our scientific conversations, which eventually led me to develop a computational script for my project. His help did not stop with just brain-storming the idea, but went much further in making sure that I successfully develop the script, including being

available at odd-hours in spite of his busy schedule. I sincerely thank him for that and do not know how to repay the favour.

Above all, I would really like to thank my family – mother Geetha, father Radhakrishnan, grandfather P.N. Nambisan and my sister Anuradha for being all ears to my never-ending whining, for their constant support, encouragement and immense faith in me. Anuradha is a person I always look up to, even though I have never admitted it to her, because she is my sister. She is the very person who encouraged me to look for a PhD, and her getting admitted into the University of Cambridge was of great motivation to me. I can't thank her and my father enough for proof-reading my thesis sent to them in eleventh hour. My parents, uncle Suresh and aunt Shylaja, have been my biggest source of strength, and they perhaps worry more than me about myself. I strongly believe that their prayers and love, is the single biggest driving factor that has made me come this far.

Abstract

The inter-disciplinary work in this thesis entails the development of a microfluidic device with bespoke imaging methodology to study flocculation growth kinetics dynamically in real-time. Flocculation is an advantageous downstream operation that increases the product-separation efficiency by selectively removing impurities. Yet, there is no unifying model defining the effect of different physico-chemical parameters on the rates of flocculation. Conventional setups for said analyses require large experimental space that are tedious to perform, and are limited by their dependence on end-point analysis, requiring sample-handling and further dispersion into typical particle-sizing instruments. In spite of the counter-intuitiveness of implementing microfluidics to study flocculation due to the anticipated channel-clogging issue, it is hypothesised that the growth kinetics can be measured by achieving a continuous, steady-state flocculation under a lower-shear environment.

Flocculation within a spiral microfluidic device (~151.8 µl volume) is evaluated against a bench-scale setup (~50 ml volume) through the comparison of floc size and zeta potential. The fluid hydrodynamics in the microchannel is assessed by an experimental mixing-time analysis (t_{mix} = 7.5 s) and a residence time distribution study (t_m = *ca.* 70 s).

In situ measurement of floc size and morphology is facilitated through high-speed imaging, with an image-processing script for robust analysis. Different flocculants are tested and growth rates calculated (~ 8 and ~12 µm s^{-1} for PEI and pDADMAC). Flocs grew linearly up to 250 µm for cationic polymers, while no growth was observed with a non-ionic PEG. Using an improved parameter-fitting step, the growth rates are compared to a simplified model for monodisperse perikinetic flocculation. The work presented should thus, enable an experimental estimation of flocculation growth kinetics and pave way for the development of accurate flocculation models for polydisperse particles. The developed system also facilitates a rapid screening of new flocculants useful for quicker process development.

Word count: 299

Table of Contents

List of Figures

List of Tables

List of Abbreviations

µTAS	Micro-Total Analysis Systems
ADH	Alcohol dehydrogenase
AR	Allura Red dye
BIF	Basic Image Feature
CAD	Computer Aided Design
CCL	Connected-component labelling
CD	Charge Density
De	Dean number
DLVO	Derjaguin-Landau-Verwey-Overbeek theory
F_D	Dean Drag Force
FEM	Finite element modelling
F_L	Inertial Lift forces
MEMS	Microelectromechanical systems
MMD	Mass Median Diameter
NRMSE	%normalised RMSE
OD	Optical density
PC	Polycarbonate
pDADMAC	Poly(diallyl dimethyl)-ammonium chloride
PDMS	Poly(dimethyl siloxane)
Pe	Péclet number
PEG	Poly(ethylene) glycol
PEI	Poly(ethylene imine)
PMMA	Poly(methyl methacrylate)
PSD	Particle size distribution
PTFE	Poly(tetrafluoro ethylene)
Re	Reynolds number
RI	Refractive Index
RMSE	Root Mean Square Error
RTD	Residence time distribution
TCB	Thermo-compression bonding

List of Symbols

θ_p	Surface site coverage	[0-1]
1/κ	Debye length	Å
$\oplus$	Morphological Dilation filter	-
$\ominus$	Morphological Erosion filter	-
U	Logical 'OR' function	-
∩	Logical 'AND' function	-
○	Morphological Opening filter	-
●	Morphological Closing filter	-
α	Collision efficiency	[0-1]
A_{Avg}	Row-vector of absorbance (OD)	AU
β_{ij}	Collision frequency between two particles '*i*' and '*j*'	s^{-1}
$\beta_{orthokinetic}$	Orthokinetic Collision frequency	s^{-1}
$\beta_{perikinetic}$	Perikinetic Collision frequency	μm s^{-1}
C_0	Concentration of tracer, tryptophan	mg ml^{-1}
d10	Particle size at 10^{th} percentile of the distribution	μm
d50	Particle size at 50^{th} percentile of the distribution	μm
d90	Particle size at 90^{th} percentile of the distribution	μm
D_h	Hydraulic diameter	μm
Ɛ	Extent of mixing	[0-1]
E(t)	Exit-age distribution	-
E(x)	Structuring element for a morphological operation	-
EM	Electrophoretic mobility	m^2 $V^{-1}s^{-1}$
f(n)	Matrix of a greyscale image	-
F(t)	Cumulative distribution function	-
fps	Frames per second	s^{-1}
g(n)	Matrix of a binary image	-
G_{avg}	Array of pixel Intensities	-
I_{Avg}	Row-vector of pixel intensities	-
k_1, k_{12}, k_{ij}	Rate of floc formation	s^{-1}
K_B	Boltzmann constant	1.381×10^{-23} J K^{-1}
k_f	Collision coefficient	-
k_{ik}	Rate of desorption	s^{-1}
L(n)	Image array with labelled particles, of size *g(n)*	-

$M_{avg,}$ $M_{A,}$ M_B	Colour Image matrix	-
n_a	Number concentration of aggregates after time 't'	mm^{-3}
N_A	Avogadro number	6.023×10^{23} mol^{-1}
P	Concentration of residual polymer after flocculation	mg ml^{-1}
P_g	8-bit pixel value	[0-255]
Q	Volumetric flow rate	µl min^{-1}
R	Protein activity	Units ml^{-1}
s^3	Skewness	$unit^3$
t'_{mix}	Theoretical Mixing time	s
t_A	Time taken for adsorption of a fraction of flocculant '*f*'	s
T_g	Glass transition temperature	°C
t_m	Mean residence time	s
t_{mix}	Mixing time	s
T_v	Binary threshold	[0-255]
V_{assay}	Volume of ADH assay mix	ml
V_{sample}	Volume of homogenate sample in ADH assay	ml
W	Width of the channel	µm
W_f	Width of the focussed stream	µm
Z'_{mix}	Theoretical Mixing length	mm
Z_{mix}	Mixing length	mm
Δabs min^{-1}	Rate of change in OD	AU min^{-1}
ζ	Zeta potential	mV
η	Dynamic viscosity	cP
η_S	Sensor efficiency	[0-1]
θ	Angle of rotation of the spiral at specific imaging locations	degrees
λ	Wavelength of sound	m
σ	Standard deviation	units
σ^2	Variance	$unit^2$
$\sigma_{experiment}$	Standard error of slope from a linear trend	µm s^{-1}
τ	Average residence time (space-time)	s
φ	Volume fraction of the flocs	[0-1]
$\chi_{0.95}^2$	Chi-Squared reference, with 95% probability	-
χ_{sample}^2	Chi-Square function	-

1. Introduction and Review of Literature

1.1 Flocculation

1.1.1 Concept

Solids can be dispersed in liquids by several means. The size of these solid particles decides the type of dispersion and in general dispersions can be broadly classified into – solutions, colloids and suspensions. The types of dispersion that are of interest in the field of pharmaceutical manufacturing are the colloidal dispersions and suspensions. These solids need to be separated from the liquid phase, so as to enable an efficient product separation and subsequent purification. An effective way to enhance the separation of these solids from the liquid phase is through flocculation followed by centrifugation or filtration. The process of flocculation is often confused with that of coagulation, and to remove the ambiguity, La Mer in 1964, framed two distinct definitions for the above mentioned processes (La Mer 1964). Flocculation, derived from the Latin word "*flocculare*", means a tuft of wool or highly fibrous structure, whereas coagulation (derived from the Latin word "*coagulare*") means to drive together. Hence, coagulation can be defined as the process where the colloidal particles and solids in suspensions destabilize and subsequently agglomerate, which is quite distinct from flocculation, which is the process by which the already destabilized particles clog to form larger aggregates and settle under the influence of gravity.

Even though flocculation as a field of research entered the scene only in the late 1960s, studies to find the mechanism of flocculation commenced as early as in 1951, when La Mer and Smellie Jr. observed the flocculation by starch. They initially focussed on the concentration of phosphate groups and found that flocculation took place by a cross-linking mechanism with the calcium ions in water. Later research by Ruehrwein and Ward in 1952, and Michaels and Morelos in 1955 provided similar findings (La Mer and Smellie Jr. 1960). Simultaneously, work was being carried out to establish the behaviour of colloids by studying the colloidal properties of manganese dioxide (Morgan and Stumm 1964), which later helped deduce the mechanism of floc-destabilization and re-dispersion.

Industrially, the applications of flocculation increased by leaps and bounds. The production of flocculating yeast strains through genetic modifications was noticed, and this was later used to produce ethanol and beer in batches (Domingues *et al.*, 2000). *Saccharomyces cerevisiae* was the most used strain in studying flocculation

due to its charge density and wide applications in industries. But considerable research has also been done on microbes like *E.coli* (Treweek and Morgan, 1977) and cyanobacterium like *Anabaena floc – aquae* (Zeleznik *et al.*, 2002).

Four different theories have since been proposed to define the process of flocculation (Treweek and Morgan 1977), as shown in Table 1.1. According to La Mer, the extent of adsorption of a particle to a polymer, and not the electrostatic interactions, dominates the process of flocculation, contradicting the Derjaguin-Landau-Verwey-Overbeek (DLVO) theory. Later, experiments on potato starch and corn starch confirmed La Mer's observation that chemical bonds were the primary factors and not electrostatic interactions (La Mer 1966). The DLVO theory was first proposed by Derjaguin and Landau in 1939-41, followed by Verwey and Overbeek independently stating that flocculation is governed by the electrostatic interaction of the double layer in hydrophobic colloids and is based on the Poisson-Boltzmann equation. The wide acceptance of this theory for a long period of time may have been because the mechanism of flocculation using long polyelectrolytes wasn't very clear then and hence was ignored.

The flocculation of clay by alum (aluminium sulphate) in water treatment can be stated as an apt example for the fourth mechanism – precipitate enmeshment. In the case of flocculation by aluminium salts, the mechanism is dependent on the pH of the solution, and hydrolysis products like aluminium hydroxides are formed. These hydroxides tend to precipitate and in doing so, adhere to negatively charged particles leading to charge neutralization. As precipitation takes place, the hydroxide-aggregates grow in size and hence, bind to more negatively charged particles, thereby 'enmeshing' them and 'sweeping' them along (Jinming and Gregory 1996). This takes place especially when supersaturation of aluminium ions takes place with respect to amorphous aluminium hydroxide. In another study conducted to remove parasitic cryptosporidiosis-causing *C.parvum* oocysts from drinking water, results showed that precipitate enmeshment is the optimal way to remove these oocysts from water, as electrophoretic mobility experiments using micro-electrophoresis showed that the isoelectric point of these oocysts were near pH 2.5 and hence were susceptible to compression of the double layer and charge neutralization, eventually followed by enmeshment at high salt concentrations as these oocysts were stable at low salt concentrations because of Lewis acid-base adduct formation and steric stabilisation (Butkus *et al.* 2003).

Table 1.1: Mechanisms of polymer flocculation

Type	Mechanism	Reference
Double – layer coagulation	The cationic polymer may screen the repulsive potential between two approaching molecules' electrical double layer by its presence. But, strong adsorption of the polymer onto the cells and the stoichiometric dependence of the system eliminate the possibility of this model.	(Treweek and Morgan 1977)
Charge Mosaic model	Polymer binds to an oppositely charged colloid surface and overcomes the total potential energy of interaction. Also known as 'adsorption coagulation'. Seen in highly charged polyelectrolytes.	(Treweek and Morgan 1977; Agerkvist 1992; Gregory and Barany 2011)
Polymer Bridging	Form bridging structures between the cells and help form a three-dimensional structure of the floc. Seen in diluted particle systems with lowly charged polyelectrolytes.	(Treweek and Morgan 1977; Agerkvist 1992; Gregory and Barany 2011)
Precipitate enmeshment	Also known as 'sweep coagulation' is greatly dependant on the adsorption of hydrolysis products that are positively charged onto the negatively charged particles; thereby leading to charge neutralisation.	(Jinming and Gregory 1996)

The concepts of polymer bridging and charge mosaic model are discussed further in the topics mentioned below with respect to 'polymer' and 'polyelectrolyte' flocculation. The key points to consider while working with flocculation systems that need to be well understood have been outlined below (Gregory and Barany, 2011; La Mer, 1966):

1. Flocculation by polyelectrolytes leads to 'subsidence' (La Mer *et al.* 1957 (b)) of the colloids whereas coagulation using salts leads to sedimentation.

2. Flocculation by polyelectrolytes leads to the formation of three dimensional flocs that are porous and fluffy thereby enhancing filtration efficiency. These flocs are distinctively different from coagula (La Mer, 1966).
3. The three-dimensional structures are formed by the protrusion of the non-adsorbed tails of the polyelectrolyte into the solvent (La Mer and Smellie Jr. 1956; La Mer *et al.* 1957 (a); Smellie Jr. and La Mer 1958; taken from La Mer 1966).
4. Incorporation of the Langmuir's adsorption isotherm, into the Smoluchowski's law (Gregory 1988) for the coagulation of primary particles has been done. This isotherm in terms of theta (θ_p) – the measure of fraction of colloid surface covered by the adsorbed polymer – modifies the Smoluchowski's law by a factor of θ_p $(1 - \theta_p)$ which constitutes the term 'sensitization' as a consequence of the bridging mechanism (La Mer, 1966). The equation for the rate of floc formation is given by Equation 1.1.

$$\frac{-dn_0}{dt} = k_1 n_0^2 . \theta_p (1 - \theta_p) \qquad (1.1)$$

Where k_1 is the rate constant and n_0 is the number of primary particles in a colloidal dispersion (Healy and La Mer 1964).

5. The Langmuir adsorption isotherm is defined as in Equation 1.2.

$$\frac{\theta_p}{(1 - \theta_p)} = bP \qquad (1.2)$$

Where b is the ratio of rate constants for adsorption-desorption of the polymer from the solid and P is the concentration of residual polymer after adsorption (Healy and La Mer 1964).

6. The optimum concentration (P_m) of a given flocculant is characteristic of a particular concentration of the flocculant on a particular substrate. An overdose of the flocculant can be identified by extrapolating values of θ_p greater than unity.
7. A very important finding is that negatively charged colloids can be flocculated by negatively charged polyelectrolytes, which disproves the DLVO theory of flocculation.
8. Zeta potential approaches zero as the isoelectric point is reached, but flocculation takes place even at non-zero zeta potential values showing the influence of pH on electrophoretic mobility values (La Mer, 1966).

9. The effect of agitation was also demonstrated by La Mer along with Healy, and they observed that in the absence of agitation, the break-up of flocs and re-dispersion was almost negligible and the value of θ_p reaching unity was extremely slow.
10. The flocculated state is metastable and as mentioned above, occurs at $\theta_p = 0.5$ wherein $P = P_m$ and the energy profile of the entire flocculation process can be understood from Figure 1.1 (Healy and La Mer 1964).
11. The effectiveness of a flocculant can be attributed to its scavenging ability – ability to gather all primary particles to form large flocs, and binding ability – ability to have a strong structure while forming cakes during filtration or centrifugation that follows (La Mer *et al.* 1957).
12. The energy states (E) can be grouped with the four possible reaction states as shown in Figure 1.2:

Dispersed state (initial state)	E1
Adsorption to $\theta_p = 0.5$	E2
Flocculated state (metastable)	E3
Redispersed	E4 ≅ E2
Adsorption reaching $\theta_p = 1.0$	E5 (Healy and La Mer 1964).

The rate of polymer dosing and the shear force in stirred vessels also affect the rate of flocculation and more importantly, the size of the flocs and its strength. It was observed that the floc size reaches a maximum during polymer dosing and then reduces in size with continued stirring. Hogg in 1989 showed that slow and intermittent addition of the polymer with continuous stirring can increase the rate of flocculation as local overdosing of particles is avoided and flocs are not allowed to grow rapidly during the early stages of the process (Elimelech *et al.* 1995). Due to the stirring, and thereby the shear, the flocs initially break up and re-disperse and with time and constant stirring, they re-form to form aged and more stable flocs with generally lesser diameters than the primary flocs. Aged flocs are macro-flocs with re-conformed polymeric flocculant, re-arranged under constant shear over a period of time. This can be pictorially depicted as shown in Figure 1.2 as observed by Gregory in 1988; wherein step ‘a’ depicts the mixing of polymers with the particles, step ‘b’ – the adsorption of polymer onto the particles, step ‘c’ – the re-arrangement of polymer chains to reach equilibrium (in case of polymer bridging), step ‘d’ – the collisions between the unit flocs to form a large floc – aggregate, and step ‘e’ – the break-up of flocs due to shear, and the dotted lines depict the formation of primary floc particles (Gregory 1988).

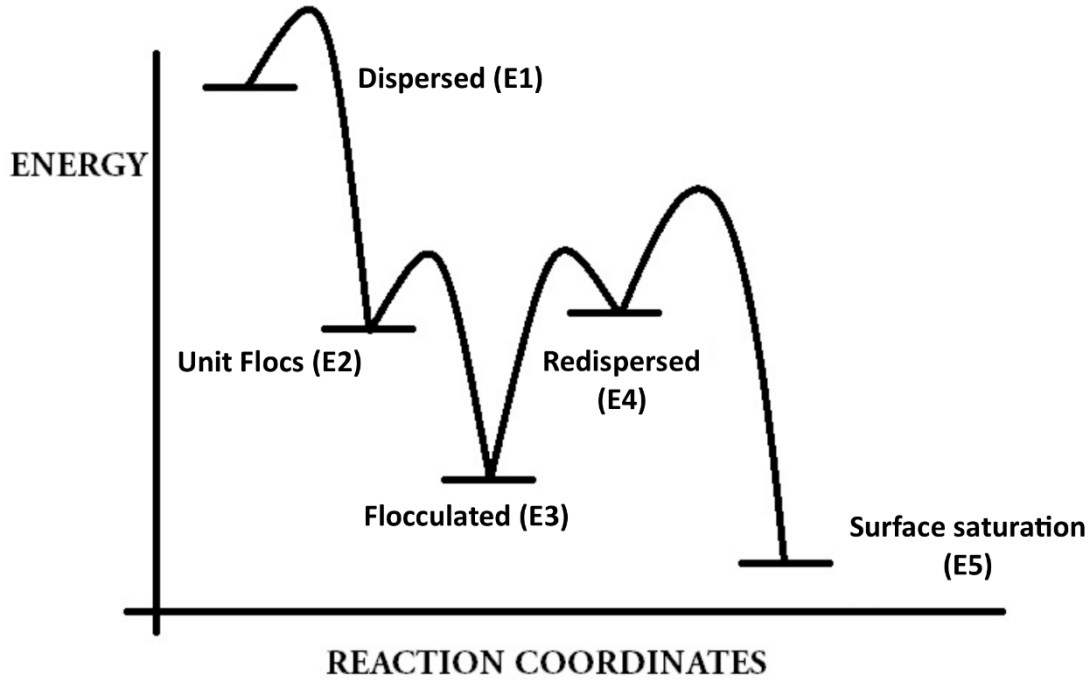

Figure 1.1: The varying energy states occurring during the process of flocculation. The reaction co-ordinates can be any variable parameter, for example the concentration of flocculant used. Image adapted from Healy and La Mer, 1964.

This can be related to the energy profile of flocculation in Figure 1.1. The step 'b' in igure 1.2 depicting the polymer adsorption onto the particles varies with the concentration of the particles and also the polymer. For dilute solutions, this step is quite long wherein the particles are not destabilized quickly for flocculation to occur. This can be overcome by increasing the shear on the particles. Concentrated solutions have rapid adsorption of polymers and flocculation takes place almost immediately after dosing.

The adsorption kinetics and re-conformation of different polymers were studied by Gregory who found that a polymer can become either 'active' or 'inactive' depending on the re-conformation step. 'Inactive' means that the polymer, after adsorption, re-conforms completely within the diffusion layer of the charged particle and hence cannot form bridges with approaching particles due to the charge repulsion by the particle. The diffuse layer is generally seen to have a thickness of the reciprocal of Debye length (1/κ) and is shown in Figure 1.3 (Gregory and Barany, 2011). The Debye length (also called Debye radius) is the measure of a charge carrier's net electrostatic effect in solution, and how far those electrostatic effects persist.

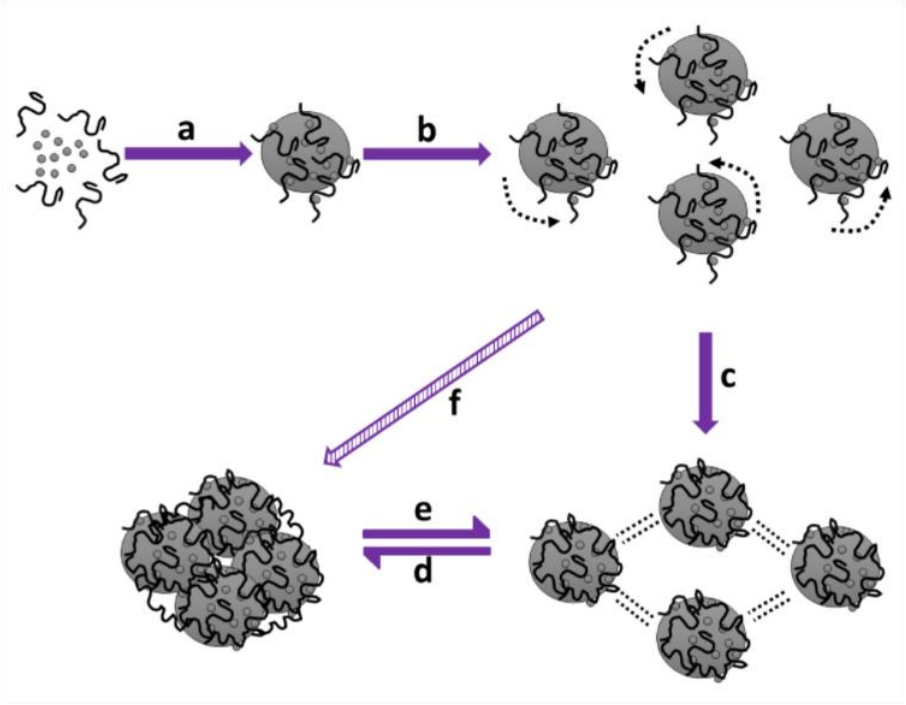

Figure 1.2: The sub-processes of flocculation as described by Gregory in 1988.

A Debye sphere is a volume whose radius is the Debye length, with each Debye length, charges are increasingly electrically screened. It is noted that the kinetics of adsorption and re-conformation are significantly different when inorganic flocculants are used, due to different flocculating mechanisms as mentioned in Table 1.1. While the compression of the Debye sphere occurs due to the screening of the charged double-layer, the importance of the active radius becomes applicable only for polymeric flocculants.

Correlating the inferences by Silberberg in 1968, and Treweek and Morgan in 1977, it can be logically deduced that as the polymer concentration increases, the interaction energy increases simultaneously. This means that more polymer segments bind to the surface, thereby increasing the θ_p value that directly affects the rate of flocculation (Equation 1.1). Therefore, when dealing with polymer flocculation, their properties must be well-understood before selecting an appropriate molecular weight and concentration.

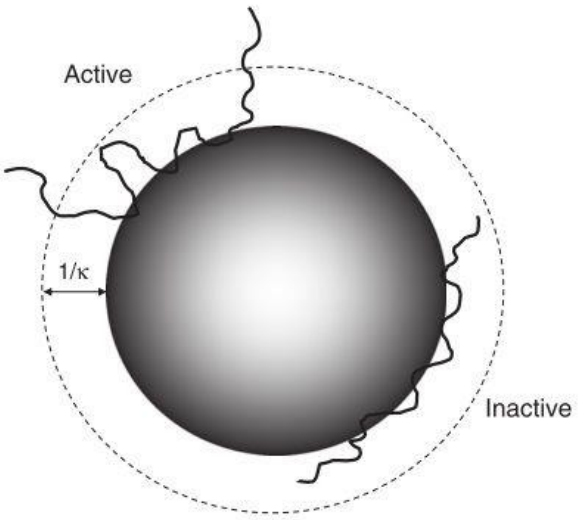

Figure 1.3: Active and inactive adsorbed polymers. Dotted lines denote the diffuse layer of thickness 1/k (Debye length); From Gregory and Barany, 2011♠. The Debye length can be estimated from the thermal energy ($K_B.T$) and potential energy (Zeta pontetial), relative dielectric constant and concentration of the charged ions.

1.1.2 Imaging and Detection Principles

For a long period of time as the mechanism of flocculation remained unclear, and hence the need to understand the mechanism for a more efficient product recovery method arose, research began in the 1970s in an effort to capture images and also detect the rate of formation of flocs. One of the widely opted methods is the light scattering technique. But this method demands a good knowledge of the variation in the number concentration of the flocs formed and also its light scattering properties. Optical methods such as the measurement of the changes in turbidity have been used extensively due to their experimental simplicity (Lips *et al.*, 1971). The result from these observations, which are generally the number concentrations are then validated with the second order differential of the kinetics of the Smoluchowski's equation (Equation 1.3); even though the optical methods that are employed assume the particles to be either spherical or cylindrical in shape. The researchers, therefore, derived the equation for colloidal stability by approximating the shapes of the colloids by assuming coalescence and hence the colloidal stability constants cannot be considered to be absolute. Equation 1.3 describes the rate of

♠ Reprinted with permission from Elsevier Limited, and also Royal Society of Chemistry for content from Journal of the Chemical Society, Faraday Transactions, 86 (9), 1990.

formation of flocs '*k*' with a number concentration of 'n_k', formed from the collision of particles '*i*' and '*j*' at a rate of k_{ij}. The breakage of particles '*k*' to particles of size '*i*' occurs at a rate k_{ik}.

$$\frac{dn_k}{dt} = \frac{1}{2}\sum_{i=1,j=k-i}^{i=k-1} k_{ij} n_i n_j - n_k \sum_{i=1}^{\infty} k_{ik} n_i \tag{1.3}$$

When the optical methods of detection are applied, the primary particles within each large floc is considered to be independent scatterers of light and scattered light from each particle interferes with the other (Lips *et al.*, 1971). But the errors caused due to approximation and the possible effects of light coincidence effects (Raasch and Umhauer, 1984), stand as drawbacks of the effectiveness of this system. There are many other particle counting techniques based on light scattering, Fraunhofer diffraction and Coulter counting (Matthews and Rhodes, 1970). These methods are fairly effective but fail in their applicability in bioprocess industries due to their need of high dilution of samples to prevent fouling of the optical systems by adherence of the flocs (Eisenlauer and Horn, 1985). All these raised the importance of inventing an on-line monitoring system that overcomes the drawbacks mentioned above. For an online optical imaging technique the measurement is not based on diffraction and hence, the problem of multiple scattering can be avoided in concentrated systems.

In 1985, Gregory devised an on-line turbidometric method to find the particle size of flocs, also taking into consideration the particle number concentration. Because the suspensions carrying the flocs are not uniform, the root mean square (RMS) value was calculated from the turbidity measurements assuming the fluctuations in particle size of the flocs to follow a Poisson distribution. The RMS value is found to be a sensitive measure of various degrees of dispersion (Eisenlauer and Horn, 1985; Gregory, 1985). The analyser has a rather simple setup with a flow cell having a light source (LED at 820 nm) and a photodetector on both sides. The output recorded by the photodetector has a large DC value that corresponds to the turbidity of the sample and a small AC reading that corresponds to the random variations in particle number and size as shown in the Figure 1.4. The RMS values helps in a very useful empirical prediction of the state of aggregation and thus enables the on-line monitoring of floc formation and thereby control the rates of polymer dosing (Gregory, 1985; Kayode and Gregory, 1988). A major drawback of this methodology is the assumption of the particles size distribution to follow a

Poisson distribution and lacks the capability in measuring the actual size of the particles and its morphology, which was crucial for the development of flocculation growth kinetics. An optical imaging methodology aimed to be developed will be applicable for a rapid-screening of different flocculation systems, while trying to unravel the growth kinetics information by *in situ* monitoring.

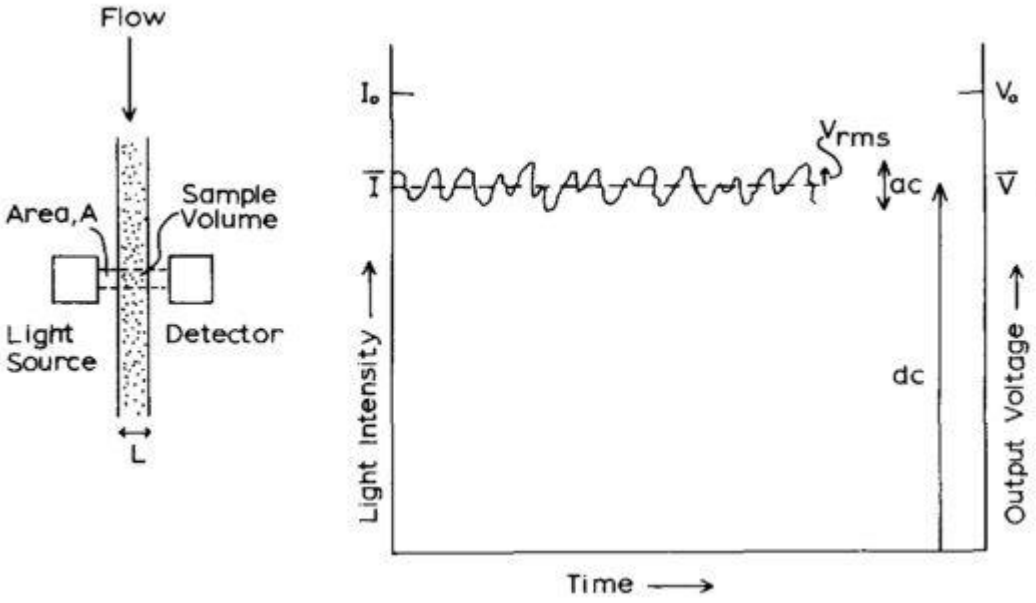

Figure 1.4: Floc analyser with turbidity measurement graph, by Gregory, 1985[♣].

Eisenlauer and Horn in the same year (1985) also came up with an *in situ* technique of monitoring floc formation rates and thereby controlling the flocculant dosing which was able to monitor even concentrated systems using a laser light based optical sensor. The concentrated suspensions were sent into the flow cell through sheath flow (hydrodynamic focussing) where an effective control of the signal to noise ratio can be done with no practical shear gradients between the sheath and the main flow (Eisenlauer and Horn 1985). Computation of frequency distributions between randomly dispersed particles is also considered to be important and pulse holography has been used to get a complete evaluation of the positions of every single molecule (Raasch and Umhauer 1989). Even though this technique has been used extensively in finding the particle size distribution, its application with respect to flocculation can be a far – fetched idea.

♣ Reprinted with permission from Elsevier Limited.

1.1.2.1 Optical Imaging of Flocs

The imaging of flocs over a period of time can also provide details of changes in floc size with varying conditions and parameters. Even though real-time imaging of flocs hasn't been published before with respect to bioprocess downstream operations, light microscopy with a high speed camera is a powerful and a sensitive tool that can record the process of floc formation and breakage over real-time. However, this technique of microscopy has been used in the field of chromatography and its ultra-scale and microscale studies (Hubbuch and Kula, 2008; Shapiro *et al.*, 2009; Siu *et al.*, 2007, 2006). Tracking of colloidal particles have been studied using image sequence analysis and its application to micro-electrophoresis and particle deposition has been studied by Wit *et al.*, in 1997, where the particle velocity was calculated using video image sequencing and a prediction method for defining the future position of the particles have also been mentioned. Similar work has been done to monitor the adsorption/desorption rates of colloidal particles on a parallel plate flow chamber, as well as the number of particles adsorbed (Meinders *et al.*, 1992). This idea may be looked into further for the development of optical image analysis for recording the flocculation process.

From a different perspective, in the 1980s research into the ways to capture *in situ* images of flocs began in search of methods for better treatment of waste water. But this area of research had a completely different aspect of finding the floc size with respect to suspended matter in oceans and seas, in the field of Marine Geology and Sea Research, as it was observed that large flocs are the vectors that carry contaminants along the path of a water body. This initiated a series of experiments to study the properties of these large flocs mainly made of clay, silt, manganese oxides, etc., so as to probe into ways of water treatment to make it potable (Droppo and Ongley, 1992). Cameras were soon developed that could take *in situ* images of suspended matter that forms flocs in oceans and coastal seas and these cameras could capture images in concentrations as low as 200-300 mg dm^{-3}. They could take a large number of photographs that helped researchers get a particle size distribution of flocs from a particular geographic region. A group of researchers came up with a submersible camera that could record a continuous size distribution, published sizes from 3.6 µm to 644 µm (Eisma and Kalf, 1996).

More recently, flocculation of *Chlorella zofingiensi* with $FeCl_3$, was studied through a visual observation technique under a Taylor-Couette flow, and subsequently a fractal analysis was performed, i.e. taking into consideration, the dimensions of the

flocs (Wyatt *et al.*, 2013). This was extended to fresh-water algae, and the critical flocculation conditions were examined (Wyatt *et al.*, 2012). Flocculation of yeast was also studied through optical imaging platforms to visualise the morphology of flocs, in an attempt to better understand the effect of physico-chemical parameters on the floc size and shape (Mondal *et al.*, 2013)

1.1.3 Floc strength – Shear sensitivity study

As flocculation is a very sensitive process that is affected by many variables, shear rates to which the particles are exposed form the primary factor in deciding the strength of the flocs or their sensitivity to shear. This is of utmost importance as all the unit operations in the process industry can possibly shear the flocs through many different ways ranging from – the mode of operation of the process itself to feed pumps, piping, valves, junctions etc. that also have to be considered. Work on testing the floc strength has not been studied extensively in the bioprocess sector. In the water treatment area, however, studies have been conducted to find the floc strength using many different techniques like – impeller mixing based shearing, ultrasonics, oscillatory mixers; and even microscopic techniques like – micromechanics and micromanipulation. Jarvis *et al.* in 2005 published a review paper detailing all these different techniques and they have discussed the importance and difficulties of finding the strength factor and correlating it with shear (Jarvis *et al.*, 2005). Many groups have also studied the strength by deriving the Kolmogorov's scale of mixing by creating microeddies. As early as in 1982, Bell and Dunnill studied the shear disruption of isoelectric soya proteins using a capillary shear device (Bell and Dunnill 1982) which seems closer to a real-time downstream operation of product separation.

As mentioned above, even microscopic techniques have been adopted to test the floc strength. Yeung and Pelton in 1996 introduced a new approach called micromechanics to this field wherein single flocs were taken and pulled apart to test their tensile strength. However, polymeric calcium carbonate flocs of size 6- 40 µm when exposed to 20-200 nN didn't show any correlation to its flocs size plotted logarithmically. In their experiment, a single floc was held by a bent-glass suction cantilever which calculated the force by its elastic deflection to axial forces, and pulled by a pipette tip from the other end; as shown in Figure 1.5. They hence defined micromechanics as follows-

"*The execution of precise mechanical experiments (e.g., measurements of tensile strengths and elastic moduli) on the micrometre scale*" (Yeung and Pelton 1996).

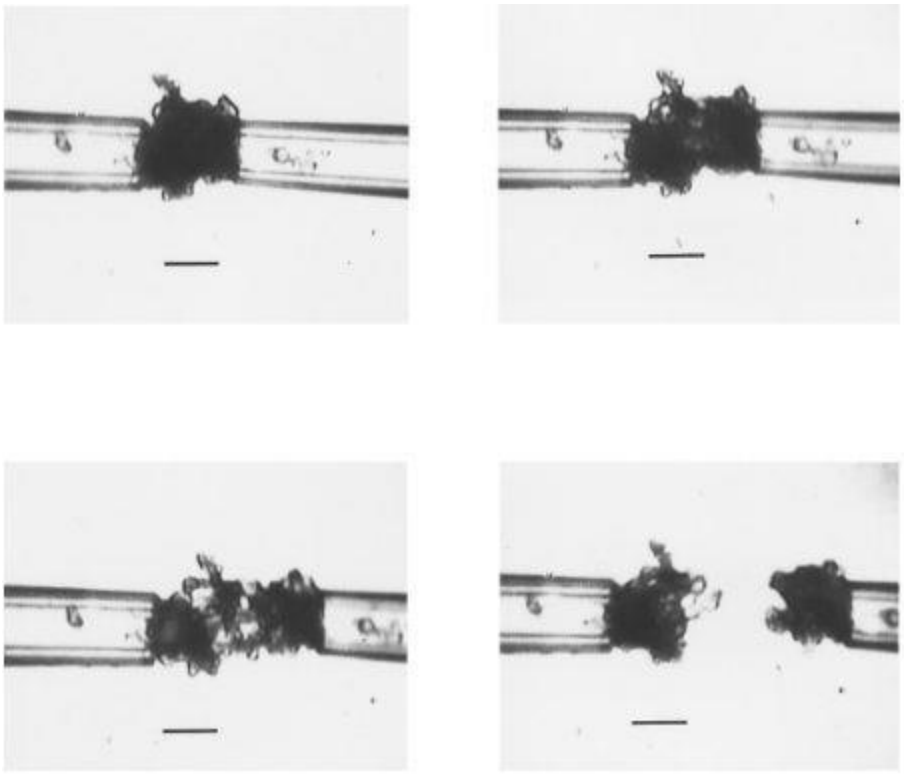

Figure 1.5: Sequence of rupture of a floc particle as the pipette is pulled back. Force transducer is on the left applying 15.7 nN μm^{-1} force (Yeung and Pelton 1996♠). Scale bars represent 10 µm.

A different technique called Micromanipulation was adopted by Zhang *et al.* in 1991, where the bursting strength of mammalian cells were measured by squeezing single cells between two parallel plates of known forces. Forces between 2.1 to 2.6 µN were used to directly find the bursting strength of mammalian cells (Zhang *et al.*, 1991). Zhang and his group have also worked on baker's yeast cells (Mashmoushy *et al.* 1998), bacterial cells (Shiu *et al.*, 1999) and latex particles (Zhang *et al.*, 1999) to find its mechanical properties. This was done by a micromanipulation rig having a microscope, a stage having the sample, a probe, force transducer to find the strength (Zhang *et al.*, 1999).

1.1.4 Challenges and Opportunities

The main challenges of conducting a flocculation setup are issues with the clarification steps, floc properties and also the scaling factor. It is a well-known fact that scaling a bioprocess from bench-scale to industrial scale is highly demanding

♠ Reprinted with permission from Elsevier Limited.

and time consuming. This puts immense pressure on the engineer to decide on a particular specification with minimum number of bench-scale runs. Hence, if we have an on-line predictive design that collects a large amounts of data, it helps us come to a proper optimised specification. Techniques for on-line control of flocculant dosing and monitoring with low response times have been developed only in the water treatment and sludge dewatering industries, as mentioned above. These detection techniques (ones involving real-time monitoring using LED / laser emitted optical methods for turbidity measurements) opens a completely new field which can help industries in their downstream operations involving controlled flocculation, by controlling the polymer dosing and the mixing rates. The ability to record and control the size of the flocs formed can be a boon to the downstream units, thereby encouraging the implementation of a flocculation step before filtration or centrifugation due to its ability to increase clarification efficiency of the latter processes. This is because, as stated previously, randomly formed larger flocs can decrease centrifugation efficiencies due to its irreversible breakage at high shear rates, whereas smaller and stronger flocs can cause fouling of membranes in a filtration process.

In order to bring about a highly effective imaging and detection system that works real-time the main challenge will be to make the flocs formed flow in a controlled manner through hydrodynamic flow focussing. Flow focussing is an area that has gained the interest of researchers in almost all fields (both analytical and process development) due to its large number of advantages despite being more complex than a regular flow setup. It has been used for various purposes ranging from microflow cytometric analysis (Huh *et al.*, 2005; Kennedy *et al.*, 2011) to particle focussing using sheath flow, sheathless flow and inertial flow (Xuan *et al.*, 2010).

The geometry of the microfluidic channel plays a major role in the production of a hydrodynamic focussed flow as the fabrication of such channels must be perfect with immaculate surfaces. Properties like type of polymer used to make the chip, aspect ratio of the channels, dimensions of the channels, type of fluid used to produce a sheath flow, etc. can vary the degree of focussed flow (Kunstmann-Olsen *et al.*, 2012; Lee *et al.*, 2006). Using microfabrication techniques on glass or silicon is another option, but due to the fabrication costs and rather tedious prototyping procedure of a certain design, these materials are usually chosen based on necessity. For example, glass or silicon is chosen for the usage of organic solvents which degrade most types of plastic polymers.

The adherence of highly viscous polymer molecules and also the cells in suspensions like yeast or *E.coli* can affect the flow of fluid or even completely clog the channel. Hence, the dimensions of the channels must be chosen appropriately in order to avoid this. This also stresses on the need for flocculation rate control right from time = 0 seconds, just when the polymer is added to avoid unwanted, randomly formed flocs of large sizes. One other challenge will be to control the external systems that inject the polymers at defined flow rates. Very low response time will be a prerequisite for such sample injectors.

Process optimization is the backbone of any successful process in an industry. The best possible way to come up with an optimized model is by incorporating a monitoring system that can rapidly improve process confidence, enable process control, etc. and thereby, accelerate process development which in turn increases reproducibility and enhances product quality (Habib *et al.*, 2000). Even though advances in various types of at-line measurement techniques have enabled direct control over products and contaminants involving feedback loops using computers, these techniques are not sensitive enough when compared to their on-line measurement counterpart techniques. The incorporation of an on-line control system enables the conversion of open-loop configurations to closed-loops circumventing the need of human intervention for sampling purposes (Habib *et al.* 2000). On-line or at-line controls seem to be really essential (refer Locher *et al.*, 1992, for a detailed information on the benefits of on-line measurements) to ensure reproducibility in a flocculation process as mentioned previously having regard to its sensitivity to the operating conditions (which have been studied in detail by Habib *et al.* 2000; Habib *et al.* 1997; Somasundaran and Yu 1994) and other parameters like ionic strength, pH, concentration of flocculant and its rate of addition, etc. (studied by Salt *et al.* 1996; Salt *et al.* 1995; Cordes *et al.* 1990). Advanced closed loop at-line sensors have been developed for fractional protein precipitation by Holwill where model parameters have been estimated by data-fitting through the method of least squares (Holwill *et al.* 1997). The need for an effective, sensitive and a fast control on-line system is hence required, where the drawbacks of at-line measurement techniques can be overcome. Using microfluidics can greatly help in developing a simple yet sensitive on-line system which can in turn help the process development unit immensely.

1.2 Miniaturized Analytical Systems

1.2.1 Historical Perspective

Microfluidics is a newly coined term even though the concept isn't new to most scientists. Thirty years ago miniaturization was first realized when a gas chromatograph of width 200 µm and depth 30 µm was devised at Stanford University (Terry *et al.*, 1979). Microelectronics has been the most significant technology of the last century that has brought forth a vast number of inventions, abiding by the Moore's law in electronics. From this, stemmed the concept of producing non-electronic miniaturized devices in the 1970s using silicon technology that later came to be known as the Microelectromechanical systems (MEMS). The early stage of microfluidics was dominated by the development of micro-flow sensors, micropumps and microvalves (Nguyen and Wereley, 2006) and soon a variety of definitions came into existence like the ones in Table 1.2.

Advances in molecular analysis, biodefense, molecular biology and microelectronics mothered the concept of miniaturization and microfluidics through processes like Gas Chromatography (GC), High Performance Liquid Chromatograhpy (HPLC) and Capillary Electrophoresis (CE) (Whitesides 2006; Manz *et al.* 1993). The second area that sparked the necessity for incorporating microfluidics is the field of Military and Defence. The Defence Advanced Research Projects Agency (DARPA) of the United States Department of Defence came up with the idea of field-deployable microfluidic chips that could detect the presence of chemical and biological threats. The field of genomics was the third area that witnessed rapid advances in the 1980s with the incorporation of microfluidics. Higher sensitivity, throughput and better resolution gave microfluidics the edge over other lab-scale analytical techniques. MEMS and silicon microelectronics stand as the fourth factor in the development of microfluidics. Advantages of elastomers over silica and glass in forming pumps and valves were soon identified and research was done extensively to come up with different varieties of polymers (Whitesides, 2006). Broadly speaking, miniaturization can also be defined as follows:

"The process of reducing the reaction-system size to micrometre scale thereby drastically increasing the throughput by altering the laws of scale for surface per volume, molecular diffusion and heat transport" (Dittrich and Manz 2006).

It is a well-known fact that an analytical process consists of five main steps, namely – sample procurement, sample pre-treatment, analyte separation from other

components in the sample, analyte quantification, and finally data interpretation (Manz *et al.*, 1993).

Table 1.2: Understanding microfluidics through different interpretations

Term	Definition	Reference
Microfluidics	*"The study of flows that are simple or complex, mono- or multiphasic, which are circulating in artificial microsystems, i.e. systems that are fabricated using new technologies."*	(Tabeling, 2005)
	"The science and engineering of systems in which fluid behaviour differs from conventional flow theory primarily due to the small length scale of the system."	(Nguyen and Wereley, 2006)
	"The science and technology of the systems that process or manipulate small (10^{-9} to 10^{-18} litres) amounts of fluids, using channels with dimensions of tens to hundreds of micrometres."	(Whitesides, 2006)
	"Microfluidics signifies any kind of experimental and theoretical research of liquid streams generated in chips comprising micro-sized channels, including fabrication, handling and practical use of these chips."	(Dittrich and Manz, 2006)
	"Theoretical microfluidics is a field that deals with the theory of flow of fluids and of suspensions in submillimetre-sized systems influenced by external forces."	(Bruus, 2008)
Micro-Total Analysis Systems (µTAS)	*"An integrated system that performs all steps in an analysis — that is, sampling, sample pre-treatment, sample transport, chemical reactions, analyte separation, product isolation and detection in a microfluidic chip."*	(Dittrich and Manz, 2006)

In order to increase the accuracy and reproducibility, researchers started turning to automated systems; which facilitate a very efficient manipulation and analysis of the properties of analytes. From this evolved the concept of 'total chemical analysis systems' (TAS) which was considered a state-of-the-art strategy in the early 1990s that included the conversion of chemical information into electronic signals. But as the trend was towards making the channel diameters smaller, tube lengths shorter-

for a short transport time, the concept of miniaturized TAS was framed - μTAS (Manz *et al.*, 1990).

Miniaturization is most often used synonymously with the term – "Microfluidics". The whole process which incorporates the techniques of miniaturization and microfluidics are generally referred to as 'Lab-on-a-chip'. Microfluidic chips can be produced by many different methods, the process of fabricating a chip being known as Microfabrication or Mircomachining; and they were initially done on silica or silica-compatible materials. Materials like glass, quartz, metals, plastics, etc., apart from silicon polymers, were also employed in making chips that acted as substrates for reactions. Previously, silica was preferred to other materials as it could be produced with high purity and in a pure crystalline form. Its low production cost, high availability, suitable mechanical and chemical properties made it the most desirable material for such applications (Manz *et al.*, 1990). By incorporating many channel geometries, mixing can be brought about in an efficient manner even though the flow inside a microfluidics chip is laminar. Thus, microfluidics has grown into a discrete field in itself, with its applications ranging from analytical systems to the ones in production. To better understand the wide applicability of microfluidics, a few examples have been dealt with in the topics that follow. With exponential growth in the applications of microfluidics, the need for studying particles in the sub-micron sizes grew and more recently, the scaled – down version of microfluidics namely, 'Nanofluidics' has been developed, which is better equipped to deal with sub-micron sized particles.

1.2.2 Capabilities brought-forward by miniaturisation

The microfluidics approach provides the user with a wide range of capabilities. Microfluidic technology has been implemented in a wide area of research, and a select few articles have been summarized in Table 1.3. The capabilities and the applicability of microfluidics is governed by three factors, namely performance, resolution time and sample volume as shown in Figure 1.6. The figure describes the different time and volume requirements of a process, taking immunoassay on different scales as an example (Lion *et al.*, 2004).

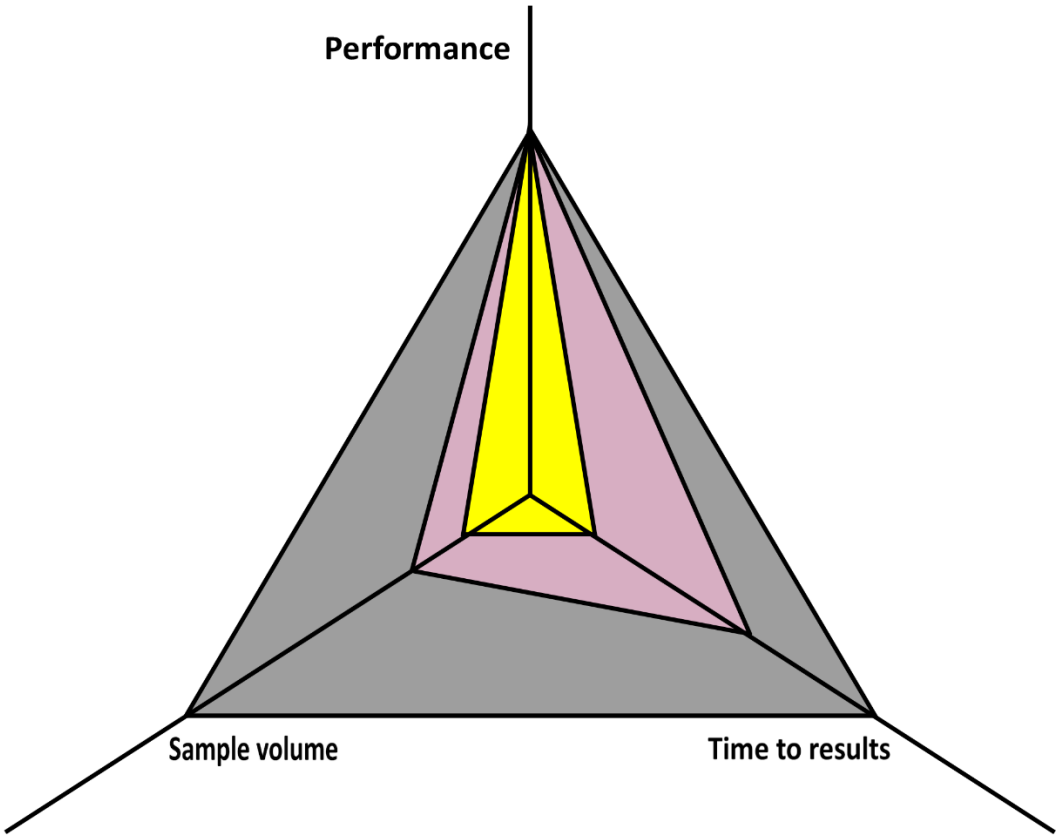

Figure 1.6: The analytical triangle. For example, an immunoassay in a microtitre plate requires large volumes and several hours for detection (grey area). Immunoassay in a microarray needs only smaller volumes, but has long incubation time (pink area), whereas in the microfluidics platform, the assay finishes in minutes, with small volumes (yellow area). Image modified from Lion et al. 2004.

The sensitivity of a sensor that is used in a microfluidics system is limited by the concentration of the analyte used and hence the sample volume required is governed by this concentration. This relation between the sample volume and analyte concentration can be expressed as follows:

$$Sample\ Volume, V = \frac{1}{\eta_S . N_A . A_i} \tag{1.3}$$

Here η_S is the sensor efficiency lying between zero and unity, N_A is the Avogadro number, and A_i is the concentration of the analyte (Nguyen and Wereley, 2006).

Table 1.3: Applications of microfluidics in various fields

Research Area		**Reference**
In-vivo sensing		Chen *et al.* 2002; taken from (Lion *et al.*, 2004)
Mass sensing		(Weng *et al.*, 2011)
Optical Detection	UV-Visible Spectophotometry	(Pena-Pereira *et al.*, 2011)
	Optofluidics	(Heng *et al.*, 2006; Psaltis *et al.*, 2006)
	Use of Optical fibres	(Zhang *et al.* 2012)
Analysis of pathogenic microorganisms		(Zhou *et al.* 2004)
Enzyme biosensing		(Srinivasan *et al.*, 2004)
Protein Separation and analysis		(He *et al.* 1999 taken from de Mello, 2002; Hertzog *et al.*, 2004; Pollack *et al.*, 1999)
Cell screening and sorting		(Crosland-Taylor, 1953; Fu *et al.*, 2004; Huh *et al.*, 2002; Hung *et al.*, 2005; Schrum *et al.*, 1999; Yamada *et al.*, 2004)
Cells and Tissue engineering		(Andersson and Berg, 2004; Takayama *et al.*, 1999)
Stem Cell Culturing		(Kim *et al.*, 2006)
Genetic Engineering	DNA Hybridisation	(Regenberg *et al.*, 2004)
	DNA deformation	(Wong *et al.*, 2003)
	Synthetic Biology	(Vinuselvi *et al.*, 2011)
	Bioreactors	(Szita *et al.*, 2005; Zanzotto *et al.*, 2004, 2002; Zhang *et al.*, 2006)
	Microreactors	(Boccazzi *et al.*, 2005)
Defence and safety		(Wang, 2004)

The capabilities of microfluidics can be understood by virtue of its design characteristics and functions; the features that are fabricated within a chip that enables users to apply them realistically for fulfilling different requirements. Based on standard operations, a microfluidic chip can be broadly used for performing the following functions – sample preparation, injection and pumping (Xu *et al.* 2010; Clicq *et al.* 2004), flow switching (Blankenstein and Larsen 1998; Lee *et al.* 2001) and control using microvalves, reactions in microreactors (Szita *et al.* 2005), mixing

and flow focussing (Gupta *et al.* 2011; Knight *et al.* 1998; Pollack *et al.* 1999; Hertzog *et al.* 2004; Regenberg *et al.* 2004), droplet and bubble generation (Garstecki *et al.* 2004; Takeuchi *et al.* 2005), particle production (Martín-Banderas *et al.*, 2005), flow control (Kim *et al.* 2006), immobilization of substrates for enzymatic reactions (He *et al.*, 2010), separation and analysis (various optical and non – optical methods; refer - West *et al.* 2008; Dittrich *et al.* 2006; Dittrich and Manz 2006).

The µTAS user receives electronic information relevant to the chemical information at regularly spaced intervals, and with a µTAS system placed on-site, the user is able to monitor even industrial processes by being able to manipulate and control the parameters without the worry of any dramatic change taking place. Therefore, one of the major advantages of miniaturization is the elimination of the dependence on external analyses, wherein the sample has to be collected at regular intervals and analysed separately (Manz *et al.* 1993).

Miniaturization has lots to offer in terms of benefits and they revolve around the practicality of processes. To start with, it is less hazardous as we deal with µl to a few ml of sample within the closed environment of the chip. This also greatly reduces the cost as the volume that is handled is very low (Lion *et al.*, 2004), not to mention the economical chip-fabrication processes.

Theoretically, as the diameter and the column lengths within the chips are very small, we should get a better resolution than a normal lab-scale analytical process (Davies *et al.*, 2014). Microfluidics and the lab-on-a-chip concept can have a revolutionizing impact on the fields of analysis, synthesis, process development and optimization, screening, and the pharmaceutical and healthcare sectors (Nguyen and Wereley, 2006). Through microfluidics a superior and precise liquid control is also possible in a Lab-on-a-chip device (Kunstmann-Olsen *et al.*, 2012). It also has a provision to conduct scalable experiments in parallel thereby exploring a large experimental space at the expense of small quantities of reagents. Being able to control the ‘soluble microenvironment’ is one of the biggest advantages especially when it comes to stem cell culturing, which cannot be done in large-scale static and perfusion cultures. Customization due to flexible designs is possible and microsystems also allow the reduction in the number of uncontrolled variables bringing the experimental results closer to theoretical ones (Kim *et al.*, 2006). Due to short distances, the mass and heat transport times are shortened (Davies *et al.*, 2014). High surface to volume ratio enhances the heat supply, thereby providing

faster heating and cooling rates. One of the biggest advantages of such systems is the ability to integrate multiple units for reaction, detection and separation within a single channel network. The most important factors like temperature and concentrations can also be regulated with absolute precision, making the miniaturized techniques suitable for a wide variety of fields (Shapiro, 2009); ability to calibrate the system also adds to the long list of possibilities (Manz *et al.*, 1993). It has been observed that microreactors yield higher conversion rates and better selectivity. But since generalization is not possible, each system must be treated individually. Automation of the system in a microfluidic chip also allows collation of the information collected in real-time (Mora *et al.*, 2011; Shapiro, 2009). Continuous flow in microfluidic chips is a boon to analysts and engineers, as on-line analysis in real-time and combination of multiple reaction steps are possible. Reaction optimisation and feedback control can be incorporated on a single device, thereby adding to the never-ending list of possibilities of a μTAS system (Dittrich and Manz, 2006). The drawbacks due to the unavailability of fully automated systems have been overcome as now chips with a fully end-to-end control and autonomous fluid flow have been devised (Lion *et al.*, 2004; Mora *et al.*, 2011).

Dispensing with the use of analytes, availability of which is limited, as well as the use of reagents that are cost prohibitive, less complex peripheral fluid handling, lower operating costs, and minimal evaporation of volatile solvents are the other benefits of using microfluidic environments for analytical purposes (Gupta *et al.*, 2011; Kricka, 1998). Different aspects of a microfluidic design add to the challenges of building an integrated system. To start with, the circulation of fluids within the channels is an issue. Microplumbing needs careful attention to details of fluid outlets, valves, pumps and tubes etc., so as to successfully attain the performance level that the chip is expected to deliver. Having fluidic interconnections between two or more microfluidic systems is very advantageous to not only analytical labs but also to industries. But the main obstacle to the integration of two or more systems is their fabrication and linkage. Pumps and valves that act as control elements in a chip are complicated to fabricate and difficult to incorporate into a microfluidic system. They are generally fabricated by milder and slower techniques to attain the necessary perfection, and the materials used in making these elements need to be chosen properly to cater for a wide range of possibilities (Tabeling, 2005). Fluid injection stands as the next major obstacle or challenge as the analyte concentration and volume play a major role in limiting the design of the microfluidic chip. The problem arises when the sample under consideration is available in very

low quantities. Dilution is one solution, but leads to many complications such as the need to implement a more sensitive instrumentation. Other challenges involve systems where the physico-chemical phenomena cannot be rationalised in a microplumbing platform, for example, a gas flowing in a micro-capillary that doesn't follow the predicted hydro-dynamic boundary conditions. Incorporating electrical fields to control the flow of fluids appears to be exciting in paving ways that seemed to be impossible earlier (Tabeling, 2005). The other challenges to consider, apart from the design considerations are the characteristics that control the reaction process – 1. Response time, 2. Analysis time and 3. Cycle time. If we include one or more sample handling and separation steps to mask the contaminants or a component that is closely related to the analyte, we will require a highly selective detector (Manz *et al.* 1993). Semi-automatic systems that require manual introduction of samples, aliquoting, etc. demand designs that are accessible to the user, making their design highly challenging. Reduction of the sample volume can lead to problems in analysis using microanalytical techniques as the concentration of the analyte can be well below the detection limit. For example if a 1 L sample of an analyte at 1 fmol L^{-1}, will have only 6020 molecules; then reducing the sample volume to 1 nl leads to the presence of only 6 molecules of the analyte that can be way below the detection limit (Kricka, 1998).

1.3 Microfluidic- Flocculation Approach

1.3.1 Flocculation has not been explored using Microfluidics

From an extensive review of literature it was observed that flocculation has not yet been explored using microfluidics. It was also understood that flocculation has been primarily studied only along with filtration and centrifugation that were scaled-down (Berrill *et al.*, 2008).

Indeed, one of the biggest challenges that still remain is the scalability between platforms to ensure a successful process development, where the efficiency of flocculation, as both a pre- and a post-centrifugation step, has been evaluated to test its impact on product recovery (Chatel *et al.*, 2014; Espuny Garcia del Real *et al.*, 2014). Furthermore, flocculation as a step to enhance microfiltration was performed, where the effect of dosing rate, and stirring speed of a flocculation system on tangential flow microfiltration was studied (Kim *et al.*, 2001). Lesser interest in studying flocculation as a separate downstream unit operation can be attributed to perhaps the trivialization of the process which has been seen only as a sub-process to the above mentioned operations.

But the main drawbacks may be due to the complexity of the mechanism of flocculation (Section 1.1) and the requirements of highly controlled parameters, like mixing and polymer dosing. The process of floc formation involves rapid energy dissipation of the particles in suspension as well as the added flocculating agent, which come together to form large aggregates in a random fashion. Because of the variations in size, e.g. from 25 µm to 1 mm or more, using poly(ethyleneimine) (PEI), a definite channel diameter cannot be fixed easily without careful considerations of factors mentioned above.

The wide variation of floc stability with shear rates poses the next problem. A defined shear rate profile within micro channels is required, especially as the flow of fluid is in the laminar region. Floc formation is initiated by the adsorption of the polymer onto the surface of the particles in suspension. The polymeric particles are brought to the particle surface by collisions that are brought about by Brownian-diffusion limited motion (perikinetic) or by external mechanical forces (orthokinetic); both of which require considerable mixing in order to bring the particles together (Thomas *et al.*, 1999). This can be of concern due to the lack of turbulence in fluids within microchannels.

One of the biggest other problems is that, the mechanism involving the formation of stable/aged flocs (Figure 1.2), has five different reaction steps which take place in a very random manner and not sequentially. This makes the control of the fluid flow difficult as the particles won't have uniform sizes or shapes. One will have to resort to hydrodynamic focussing (sheath flow) (Eisenlauer and Horn, 1985) in order to bring about uniformity in the fluid flow as it has been observed that hydrodynamic forces limits the growth of floc size by not just helping in floc formation, but also in their breakage (Muehle and Domasch, 1991).

1.3.2 Potential Test Bed Systems of Flocculation

A flocculation experiment is done on cells or homogenates with the addition of a flocculating agent, for example- PEI, a cationic polymer. There are many factors that influence the properties and decide the fate of the flocs that are formed. The properties of the flocs that are of interest to us are – electrophoretic mobility, zeta potential, size of flocs, growth rate, shear resistance etc. and the factors that influence them are primarily the pH, electrolyte concentration, molecular weight of PEI, temperature etc. and also other factors like flocculant dosage, molecular weight, charge density and mode of addition (Somasundaran and Yu 1994).

The success and efficiency of a flocculation experiment can be studied by flocculating a protein and observing its activity, percentage recovery and purity. Residual turbidity of PEI, floc size, growth of flocs, shear resistance of flocs and finally its electrophoretic mobility were studied by Salt *et al.* in 1996 (Salt *et al.*, 1996). A method for testing the activity of proteins in the flocs resulting from the flocculation step was framed by Milburn *et al.* in 1990, wherein the following assays were carried out to find the resultant activities of proteins – Bergmeyer assay for alcohol dehydrogenase and glucose-6-phosphate enzymes, and a method mentioned by Racker for testing fumarase activity. DNA was isolated by Burton's method and RNA by the Orcinol reagent method. Total lipid was measured by the Folch's method of using chloroform/methanol/water and the total protein was measured by the Ehresmann method (Milburn *et al.* 1990). A colorimetric method with a dye- red oil was used to find the residual lipids after PEI treatment of the cells (Salt *et al.*, 1995). The mechanism of flocculation using polymers was also studied by Agerkvist in 1992 where chitosan with varying degrees of deacetylation was used as the flocculating agent (Agerkvist, 1992). The effect of flocculation on soluble proteins by four cationic polymers other than PEI was observed; the effect of cationic density on the proteins (Shan *et al.* 1996) and by anionic low molecular weight copolymer and high molecular weight polyacrylamide (Yu *et al.* 1999; Yu *et al.* 2002), where the copolymer was added first to interact with the proteins and later flocculated by the addition of polyacrylamide were studied.

The effect of the rate of addition of the polymer into the suspension has been studied and it has been observed that if the droplets of added polymer aren't rapidly mixed, they form a nuclei for floc formation (Gregory, 1988); the rate of addition of polymer as well as the data of rate of settling, supernatant turbidity, zeta potential and also spectroscopic techniques like ESR, NMR, Raman etc. for probing the adsorbed polymer at the solid-liquid interface, have been put to use in tandem for elucidating the mechanism of stabilization and flocculation of different aqueous and non-aqueous suspensions using different polymers (Somasundaran and Yu, 1994).

1.3.3 Key Missing Elements and benefits of implementing microfluidics

The potential flocculation systems in the bioprocess sector as described above does not allow room for the tracking of a single floc and analysing it for the changes in their sizes. This cannot be used for real-time analysis and monitoring, as all the analytical experiments are done through off-line or at-line measurement techniques. The time frame available to the personnel in the process development and design

unit often make them undergo immense pressure in building an optimised experimental system. With such off-line/ at-line measurement techniques, accurate control of flocculation process is difficult, even though the effectiveness of the flocculation step can be analysed completely through various protein and nucleic acid assays. Various advanced at-line measurement systems for monitoring the flocculation processes have been developed that lack the sensitivity of a much superior on-line system that provides a faster response. It is a known fact that the size of the flocs formed affects the rate and efficiency of the step that follows, that is either centrifugation or filtration. Various developed control mechanisms have capabilities of only controlling the rate of formation of flocs but not their sizes. The benefits of using microfluidics and the advantages that it has to offer have been explained previously. In the case of flocculation which we are interested in, implementation of microfluidics can be of benefit in the following ways –

Microfluidics can help focus on a single floc and observe its formation, breakage and even the ageing process over a period of time. Potential tracking of single flocs can help greatly in studying the changes in the micro–environment of the particle in suspension and the flocculating agent, and how it affects the floc formation dynamics over time. Different designs can be rapidly prototyped and tested, and modifications made to suit the process of flocculation in confined spaces (Reichen *et al.*, 2014).

Flow focussing – Visualization of floc formation can be done in real-time which increases the system complexities. A uniform flow rate of the suspension and the flocculating agent is required and this sought to be achieved by using flow focussing floc particles that can be focussed into laminar paths of width which can be modified by changing the flow rates at the inlet. This helps in easier visualization of a single flocs over a period of time.

Typical lab-scale or industrial scale experiments have many variables; few of which are difficult to control because of their intrinsic nature, like rheology changes, morphology of cells etc. Through microfluidics not only can a better control of parameters be achieved, but the number of intrinsic variables that affect a reaction mechanism can also be reduced.

Shear rate profiles and diffusion rates can be defined properly within microfluidic channels, thereby enabling us to expose the flocs formed to definite shear rates. A single floc can also be exposed to different shear rates or as a gradient along the

length of a channel to study its relation to the size of flocs formed. Mixing can be brought about, even while maintaining laminar flow modes by incorporating different structural patterns within the channels that induce mixing. Flocs can be made to form and develop using a known number of cells and flocculating agent molecules by making a certain volume of known concentration flow as droplets that are evenly spaced from each other. Finally, they can be easily integrated with optical imaging platforms, facilitating an *in situ* real-time measurement (Jaccard *et al.*, 2014a, 2014b).

1.4 Aims and Objectives

The work presented in this thesis, aims at the development of a microfluidic device, hyphenated with analytical equipment, which would enable the study of flocculation in real-time, and ultimately unravel growth kinetics information. Renewed interest in flocculation as a downstream processing unit-operation, and difficulty in studying flocculation due to its sensitive nature, makes this work an important development in the field of bioprocessing.

This inter-disciplinary work stemmed from the lack of fundamental understanding of floc-formation, particularly its relationship to particle (floc) strength and size. Typically, efforts to achieve this understanding in traditional bench scales (volume > 50 mL) result in a very large experimental challenge, which may not be realistic in the timeframe available for process development. Hence, there is a need for tools to understand the fundamentals of flocculation (by decoupling floc growth from floc breakage) which will enable the design of flocculation operations in an altogether faster and economical manner.

This research thesis, therefore deals with the development of such an experimental platform, although the design and operation of a robust microfluidic-flocculation setup poses a considerable challenge. The implementation of microfluidics for flocculation is counterintuitive due to the physical scale of the microfluidic device. Clogging of the microchannels by the flocs and issues with experimental scalability are anticipated. To overcome these issues, and to have a robust flocculation setup providing high-content of data, the objectives for the research undertaken, can be summarized as follows:

- The microfluidic device must not only be able to have a comparable scalability, but also address the problem of handling flocs. The device must function under

a low-shear condition, with controlled hydrodynamics, so as to achieve a total control over the factors affecting flocculation growth.

- Mixing must be achieved in a passive manner *via* diffusive effects and without introducing energy from an external source, to avoid inflicting shear upon the flocs that would result in its breakage, making the quantification of growth kinetics all the more difficult.
- The microfluidic device should also be adaptable with an optical analytical equipment to truly exploit its advantages over conventional systems. Along with the pivotal microfluidic device, the optical analytical methodology must facilitate an *in situ* real-time observation of flocs, avoiding disruption of its natural size and morphology due to manual handling.
- The setup would further legitimize its advantages only if it provides a high content of meaningful data which is practically relevant and compares favourably over other commercial analytical equipment. Therefore, the sequence of flocculation events occurring in the microchannels will be recorded using a high-speed imaging setup and then analysed using a computational image analysis script developed for measuring the floc size and morphology.
- Finally, the whole setup should be robust, and easy-to-use, ultimately yielding reproducible and valuable information for rapid and cost-effective process development, especially in testing new flocculation systems.

2. Design and fabrication of a flocculation-suitable microfluidic device

This chapter discusses the design and fabrication of microfluidic test systems with hydrodynamic properties suitable for flocculation studies, and their comparison with a lab-scale flocculation system to examine the differences in the floc properties. Another important aspect is the assessment of the suitability of microfabricated channels to perform flocculation experiments.

2.1 Introduction

The mechanism of flocculation is a complex process due to several processes that are initiated simultaneously, upon the addition of the flocculants, as outlined in the previous chapter. The process of flocculation is essentially a dynamic equilibrium between floc growth and breakage/ageing after the initial adsorption of the flocculant with the particles (Gregory, 1988) and is highly dependent on the pH, flocculant dosage (Mondal *et al.*, 2013; Narong and James, 2006; Salt *et al.*, 1996) and shear (La Mer, 1960; Salt *et al.*, 1996; Wyatt *et al.*, 2013). However, due to the aforementioned complexities making the measurement of flocculation kinetics difficult, no unifying mechanistic model can be found as yet, especially relating the effect of physico-chemical parameters on the floc properties (Wyatt *et al.*, 2013). Microfluidics was applied as an experimental platform to tackle the lack of appropriate analytical tools, which had in one way been detrimental to the advancements of research in flocculation kinetics. In theory, different designs could be tested and fabricated with a streamlined prototyping methodology, enabling rapid improvements (Reichen *et al.*, 2014). As the physico-chemical processes occur in a more precisely controlled environment in the microfluidic scale than in a conventional larger scale system (Kang *et al.*, 2013; Leyden *et al.*, 2012; Marques and Fernandes, 2011), a higher degree of process-understanding can, therefore, be achieved.

This chapter on design and fabrication of a microfluidic flocculation device, gives an insight into the design variables and parameters that have been considered to build a microfluidic platform to suit flocculation and also to accommodate different analytical methodologies. Following this, the chapter then presents the floc size and zeta potential comparisons of flocs formed in the microfluidic device, with that of a conventional lab-scale flocculation setup, thereby introducing a highly advantageous experimental platform to study yet another bioprocessing technology.

2.2 Materials and Methods

2.2.1 Microfluidic chip design and fabrication

2.2.1.1 Device designing and rapid prototyping: Laser ablation

Two designs were created using the 3D computer aided design (CAD) software, SolidWorks® 2011 (Dassault Systèmes SolidWorks Corporation, Massachusetts, USA). The designs for initial experimentation were micro-machined on poly(methyl methacrylate) (PMMA, 824-480, RS Components Ltd., Northants, UK) using laser-ablation with a 25 W CO_2 laser-marking head (wavelength of 10.6 µm; Synrad Inc., Washington, USA) through the WinMark laser-marking software. A laser-marking speed of 200 mm s^{-1} was used on 1.5 mm thick PMMA substrates of size at most 85 × 85 mm at 50% power for machining the channels, and 10 mm s^{-1} for the through holes and the device edges. PMMA has a surface free energy of 41.1 mN m^{-1} at 20 °C.

2.2.1.2 Thermal annealing of the laser-ablated trenches:

For enhanced surface smoothness, simple 'U'-shaped trenches 2.5 cm long (0.5 cm arc length, varying channel widths between 500 – 1000 µm with a 100 µm increment, were designed and laser ablated on a 1.5 mm thick PMMA layer. This PMMA layer was wrapped in a single piece of aluminium foil (standard household foil, ~10-15 µm thick), then placed in a pre-heated oven (Memmert, Büchenbach, Germany) at 120 °C for 30 minutes, followed by 170 °C for 30 minutes. Phase contrast images of the channel beds were taken using a light microscope (Leica DMRA 2, Leica Microsystems (UK) Ltd., Milton Keynes, UK) for visual inspection.

2.2.1.3 Precision micro-milling

Following initial experimentation with the laser-machined chip, the spiral microfluidic device was fabricated using a micro milling machine (Folken IND, Glendale, USA). The SolidWorks® design was translated to the machining language (G-code) for the micro-milling machine using the MasterCam software (MasterCam X4, CNC Software, Inc., USA). A 0.2 mm solid carbide 2-flute square end-mill (1610-0079L024, KYOCERA Precision Tools, Inc., North Carolina, USA) was used to machine the 500 µm wide channels through a pocket-milling routine, and a 2.0 mm solid carbide 2-flute square end-mill (1610-0787L236, KYOCERA Precision Tools, Inc., North Carolina, USA) was used to machine the through holes and the outer edges of the device. The PMMA layer with the ablated channel was fastened on a polycarbonate sacrificial layer (*ca.* 150 × 150 mm, 1 mm thick), which was in turn

held firmly on the milling table, using strips of double-sided adhesive tape, on both occasions. A diluted soap solution was used to lubricate the tip of the end-mills during the milling process. This also helped in the easy removal of plastic debris.

A robust, leak-free fluidic connection with the macro-world is essential to facilitate fast and easy transport of fluids (Fredrickson and Fan, 2004) into the microfluidic devices. They however, do pose a challenge in terms of their easy-integration and reusability. There is a significant interest in designing interconnect blocks for one-step integration of the fluidic injection (Sabourin *et al.*, 2009) and avoiding the need for adhesives that doesn't aid reusability (Sabourin *et al.*, 2010), therefore, interconnect bars (O'Sullivan *et al.*, 2012) designed in-house, made of polycarbonate (PC) were micro-milled. In short, the design was milled on 5 mm PC with a 2.0 mm end-mill, with two M3 holes tapped 11.1 mm apart to be held against the bonded microfluidic device with 8 mm pozi screws (OneCall, Premier Farnell UK Ltd., Leeds, UK). The screws provided a flush finish to the assembled device as the total thickness of the assembly was 8 mm. An M6 threaded hole was tapped in the centre for a standard M6 fluidic connector (P207x, Acetal black nut, Upchurch Scientific, Washington, USA). The tubing was inserted through the M6 connector, and a ferrule (P250x, Upchurch Scientific, Washington, USA) was inserted at the tip of the tubing, which forms a compression-seal between the tubing and the top PMMA layer, when the M6 connector is screwed into the interconnect bar.

2.2.2 Thermo-compression bonding (TCB) of PMMA

The PMMA layer with the etched channel and another PMMA layer with the same dimensions and bore-holes (1 mm diameter) for the inlets and the outlet, were aligned using dowel pins (1.6 mm diameter), wrapped in a single piece of aluminium foil (standard household foil, ~10-15 µm thick), and carefully placed between two machined aluminium plates bolted together with uniform torques. A suitable condition for bonding was optimized by tightening the plates on all four sides with four and eight bolts, at uniform torques of 350, 400 and 450 cNm. This setup was placed in a pre-heated oven (Memmert, Büchenbach, Germany) for varying lengths of time (60, 75 and 90 minutes) at 105 °C (glass transition temperature, T_g, of PMMA). It was then removed from the oven and allowed to cool to room temperature before disassembling the aluminium plates. For the optimization of the bonding parameters, laser-ablated spiral microfluidic devices were used. The devices were then visually inspected, using a simple desktop binocular microscope,

for proper bonding, and an optimal condition was selected (discussed in Section 2.3.2) for bonding all the devices fabricated thereafter.

The burst pressure of the bonded microfluidic device was measured to quantify the strength of the PMMA-PMMA bond and the PC interconnect bars, using a calibrated pressure sensor (40PC100G, Honeywell, USA), glued into an M6 connector (P-207, Upchurch Scientific, Washington, USA). A syringe (Plastipak with luer-locks; Becton, Dickinson and Company, Oxford, UK) carrying air, driven by a KDS200 Infuse/Withdraw Programmable Syringe Pump (KD Scientific Inc., Massachusetts, USA) was connected to one of the interconnect bars on the device, via a 3-way valve (732-8103, Bio-Rad Laboratories, UK). The sensor was connected to the third port of the 3-way valve. Interconnect bars at the other inlet and the outlet, were blocked using an M6 luer-lock plug. Pressure was recorded via a data-acquisition (DAQ) board (USB-6229BNC, National Instruments, Berkshire, UK) controlled by the LabView^{TM} 2011 software (National Instruments, Berkshire, UK).

2.2.3 Channel depth calculation

The depth of the fabricated spiral microfluidic devices were measured using an optical profiler (DektakXT, Bruker UK Ltd., Coventry, UK) provided with an automated sample stage, which can profile samples up to a thickness of 35 mm. Both laser fabricated and micro-milled devices were scanned at five different locations before and after the thermo-compression bonding (TCB) step. With a vertical resolution of up to 4 Å, a step size of 83.32 nm was used to scan a length of 3 mm across the channel cross-section. To maintain the conditions similar to the thermo-compression bonding step, the procedure mentioned in Section 2.2.2 was followed, but the layers were not allowed to bond (by placing an aluminium foil between them), as the aim of this study was to record the effect of the bonding step on the channel depth.

2.2.4 Homogenisation of *Saccharomyces cerevisiae*

Baker's yeast *(S. cerevisiae)* had to be disrupted efficiently for product-release and recovery; i.e. to release the intra-cellular proteins and also other commonly found bioprocessing contaminants like nucleic acids, lipids, etc. Of the various types of cell-disruption techniques available, mechanical high-pressure homogenisation is especially advantageous, as it is known for having high product-release rates, while keeping degradation and micronisation of debris to a minimum (Middelberg, 1995; Millis, 1996).

250 mg/ml of *S. cerevisiae* (DCL CraftBake Yeast, JW Pike, London, UK) was homogenised using a pilot-scale, Manton-Gaulin Lab 60 Homogeniser (APV-SPX Ltd., Crawley, UK) at 5 × 10^7 Pa, 5 passes at 4 °C (Salt *et al.*, 1996). 1 kg yeast was dispersed in four litres of 100 mM phosphate buffer♣ at pH 6.5. Under total recycling conditions, five passes took 20 minutes (starting from the point when the pressure reaches 5 × 10^7 Pa). A part of the resulting homogenate was used for the flocculation experiments after adjusting the pH to 7.4 using 2 M HCl and 2 M NaOH, while the rest was stored at -20 °C for further testing.

To test the efficiency of the homogeniser, an alcohol dehydrogenase (ADH) assay was carried out before and after the homogenisation process, to confirm cell disruption by quantifying the amount of intra-cellular protein released (ADH), which has a direct impact on the flocculation process. The assay protocol was adopted from Richardson *et al.*, 1990 which is based on the conversion of ethanol to acetaldehyde catalysed by ADH, released from the homogenate, represented by the equation:

$$ethanol + NAD \overset{ADH}{\longleftrightarrow} acetaldehyde + NADH + H^+ \quad (2.1)$$

The assay monitors the kinetic reaction of the conversion of NAD to NADH, which is directly proportional to the amount of ADH in the sample. The optical density (OD) is measured at 340 nm for 60 s and the change in OD, Δabs min^{-1}, is expected to increase as homogenisation progresses. The recipe for the assay mix has been reported previously (Richardson *et al.*, 1990). The chemicals for this assay were purchased from Sigma Aldrich, Dorset, UK and the composition of the assay mix is – 27.64 g L^{-1} Ethanol (absolute), 1.19 g L^{-1} NAD (N6522), 0.047 g L^{-1} Semicarbazide (S2201), and 0.31 g L^{-1} Glutathione (G4251). This mixture was made up to 1 L volume by adding deionised water and pH adjusted to 8.8 with 1 M NaOH. The homogenate from the Lab 60 homogeniser was diluted 100 times with deionised water. To 10 µl of this diluted sample, 1 ml of the assay mix was added in an acrylic cuvette for monitoring Δabs min^{-1} over 60 s.

♣ 100 mM disodium hydrogen orthophosphate + potassium dihydrogen orthophosphate, filtered using 0.2 µm Thermo Scientific Nalgene MF75 bottle top filter.

The protein activity, expressed as R (Units ml^{-1}), was then calculated from the following equation[♠]:

$$R = \frac{\Delta \text{abs min}^{-1}}{6.22} \times \frac{V_{assay}}{V_{sample}} \times DF \qquad (2.2)$$

Where, 6.22 is the molar extinction coefficient of ADH[♣], V_{assay} is the volume of assay mix in the cuvette, and V_{sample} is the volume of homogenate sample added to the cuvette. DF is the dilution factor of the homogenate.

2.2.5 Flocculation of Saccharomyces cerevisiae

A well-studied flocculation system of *S. cerevisiae* homogenate with poly(ethyleneimine) (PEI) was used for the comparative experiments between the µ-flocculation device and a bench-scale system (Salt *et al.*, 1996), after adjusting the pH of both the flocculant and homogenate to the required level using 2 M HCl and 2 M NaOH. Solutions of PEI (from a stock of 30% w/v, mol. wt. 50,000 – 100,000 Da, Alfa Aesar, Massachusetts, USA), were prepared at five different concentrations - 5, 10, 15, 20 and 25 g PEI kg^{-1} yeast (corresponding to 0.125 - 0.625 %w/v, respectively), for a set of experiments at a constant pH of 7.4. To analyse the effect of pH, aliquots of 20 g PEI kg^{-1} yeast (0.5% w/v) were prepared between pH 5 to 7.5 (increments of 0.5).

Equal volumes of yeast homogenate and PEI solutions (20 ml each) were used for the bench-scale studies, carried out in 50 ml centrifuge tubes. Upon addition of the flocculant solution to the homogenate, they were mixed by tube-inversion, uniform number of times, to ensure homogeneity. The motivation behind adopting this technique was to keep the levels of shear in the system low, in order to be comparable with that in the microfluidic scale with a steady-state laminar flow. This aspect shall be discussed in the following chapters.

For flocculation experiments conducted in the microfluidics device, 10 ml sterile syringes (Plastipak with luer-locks; Becton, Dickinson and Company, Oxford, UK) were used to inject the reactants with the help of a KDS200 Infuse/Withdraw Programmable Syringe Pump (KD Scientific Inc., Massachusetts, USA) and an Aladdin Programmable Syringe Pump (WPI Ltd., Hertfordshire, UK). Approximately

♠ Equation followed as mentioned in the Sigma Aldrich Assay Protocol (www.sigmaaldrich.com/technical-documents/protocols/biology/enzymatic-assay-of-alcohol-dehydrogenase.html)

20 cm long poly(tetrafluoroethylene) (PTFE, S1810- 10, Bola, Germany) tubing (1/16 inch external, 1/32 inch internal diameter) was used to connect the syringes to the chip, through M6 interconnects and ferrules (P207X and P250X; Upchurch Scientific, Washington, USA). Different volumetric flow rates for the two inlets in the spiral microfluidic device were tested and the resulting floc-sizes were recorded. For the remainder of experiments in the microfluidic device, the most-suited volumetric flow rates were chosen.

2.2.6 Particle size analysis

A Mastersizer 2000 (Malvern Instruments Ltd., UK) was used to measure the diameter of the flocs obtained from both the bench scale and the outlet of the chip. A refractive index (RI) of 1.60 (corresponding to *S. cerevisiae* homogenate) was set, with MilliQ water (RI = 1.33) used as the dispersant. The instrument's sample dispersion unit (Hydro SM-A) was used to push the sample through the cell window using an impeller, which is suspected to influence the floc size heavily. The dispersion unit has a minimum volume of 60 ml, which can potentially lead to the changes in the floc sizes due to dispersion effects and also turbulence brought about by the impeller. The instrument pulses the laser and the blue light through the cell window, where the diffraction pattern is recorded on a set of fixed detectors. 12,000 snapshots were acquired by the Mastersizer, in triplicates, and particle diameter values were calculated per sample, and averaged. Particle size analysis was performed for flocs formed at the conditions mentioned above.

For the flocculation experiments in the microfluidic device, flocs from the outlet of the device were directly introduced into the sample dispersion unit using a 10 cm long, ID = 0.8 mm PTFE tube (schematic representation shown in Figure 2.1).

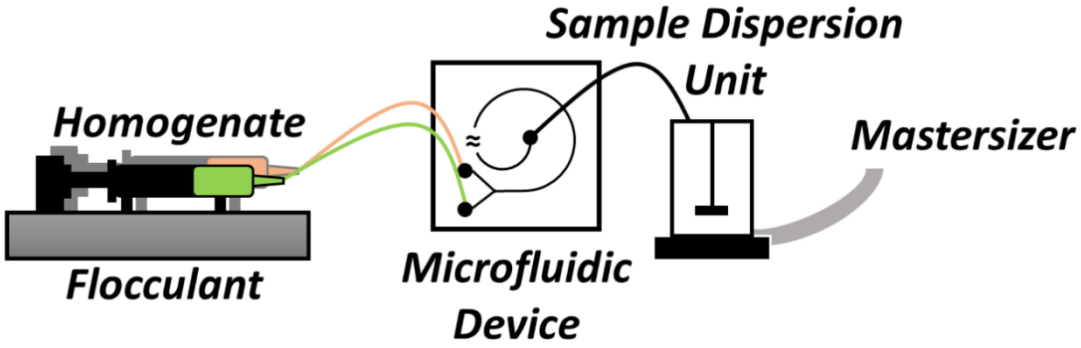

Figure 2.1: Schematic representation of the flocculation setup, for particle size analysis with a laser-diffraction instrument. The images are not to scale.

Samples from the bench-scale centrifuge tubes were introduced into the sample dispersion unit using a Pasteur pipette after *ca.* 30 s of the flocculant addition, corresponding to the average residence time (τ) of the flocs within the microchannels at flow rate used. These experiments were repeated 5 times each, unless otherwise mentioned.

2.2.7 Surface charge analysis

The zeta (ζ) potential and the electrophoretic mobility (EM) of the flocs formed in the μ-flocculation device and at the bench scale were measured using the Zetasizer Nano ZS (Malvern Instruments Ltd., UK). The instrument calculates the EM of the particles by laser Doppler electrophoresis, from which the ζ potential is calculated using known electric field and dielectric constant values. The ζ potential was measured using a disposable capillary cell (DTS 1070, Malvern Instruments Ltd., UK), requiring 1 ml sample volume. For experimentation in the microfluidic device, flocs from the outlet of the device were directly introduced into disposable cuvettes (45 μl) using 0.8 mm ID PTFE tubing (similar to the schematic shown in Figure 2.1). Flow from the syringe drives was stopped prior to the measurements. The experiments were performed in triplicates.

2.3 Results and Discussion

2.3.1 Design considerations and fabrication of flocculation-suitable devices

Two designs as shown in Figure 2.2 were created using the SolidWorks® 2011 software. To suit ease-of-use with a microscope and to address fabrication limitations (i.e., to be accommodated on the laser-ablation platform and the micro-milling bench), the footprint was limited to 85 × 85 mm for the serpentine design (Figure 2.2A) with a length of *ca.* 765 mm and 1 mm channel width. Another design, with a spiral channel, was designed with a length of *ca.* 607 mm from the point of intersection between the three inlets, within a footprint of 70 × 70 mm. A width of 500 μm was chosen, with one inlet for the sheath flow, which splits and re-enters from both sides of the focussed-flow inlet. The inlet design, hence, can also be called as a ψ-shaped inlet.

The channel lengths were chosen so as to provide an average residence time (τ) of roughly 1 minute within the microchannels for the flocs to grow, at a flow rate suitable for the adaptation of analytical methodologies (explained in Chapter 4). At a suitable flow rate, $\tau = 1$ was selected to be comparable with the residence time of

flocs in the bench scale. An aspect ratio of 1 (channel width: depth) provided a non-constrained growth of flocs in all 3 dimensions, thereby, enabling the study of its natural morphology. Any rectangular channel will constrain the floc-growth in the smaller dimension, while growth occurs naturally along the larger dimension. The dimensions of the channel cross-sections were selected based on the largest size of flocs encountered in the bench scale flocculation experiments, and as a rule of thumb, the width and depth of the spiral microfluidic device were chosen to be roughly twice the size of the largest floc (~ 250 µm), and approximately four times for that of the serpentine device.

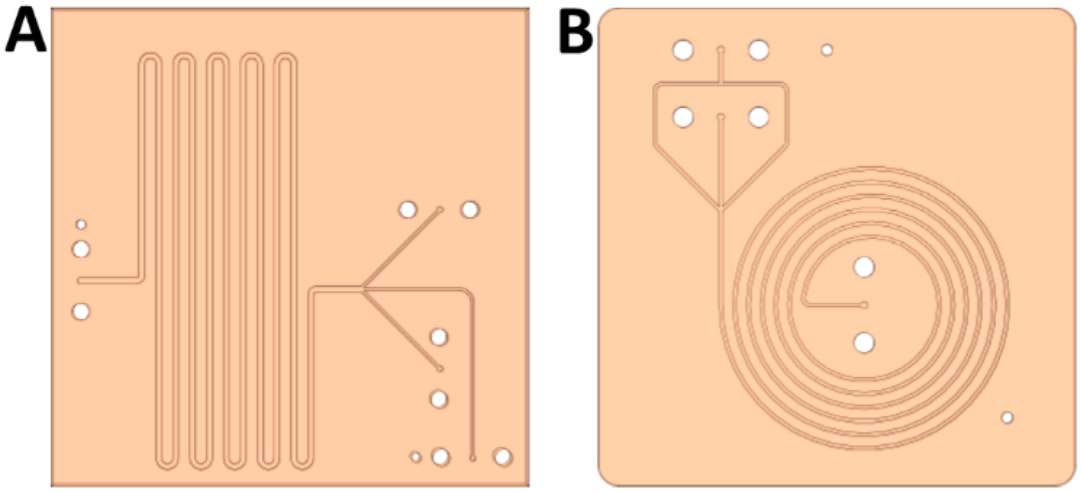

Figure 2.2: Designs of two microfluidic devices for studying flocculation in situ, designed using the Solidworks® 2011 software. ***A:*** *The serpentine design with a footprint of 85 × 85 mm, 765 mm channel length and a channel width of 1 mm. The serpentine begins 10 mm from the inlet intersection, with the side inlets intersecting 45 degrees to the middle inlet.* ***B:*** *The spiral design with a footprint of 70 × 70 mm, 607 mm channel length, and a width of 500 µm. The side inlet splits into two and re-enters to join the middle inlet from both sides, at 45 degrees, resembling a ψ-shaped inlet. This reduces the number of inlets by one and the spiral begins 14.4 mm from the intersection. The images are not to scale.*

2.3.1.1 Laser fabrication

PMMA was chosen as the substrate for performing the flocculation experiments due to its transparency to visible light enabling optical measurements (Tsao and DeVoe, 2009), its mechanical strength for robust usage, non-porosity, and ease of fabrication (Cheng *et al.*, 2004; Sun *et al.*, 2008).

The CAD designs which are SolidWorks drawings were converted to the Adobe Illustrator format (".ai") so as to enable the import of the designs into the WinMark laser-marking software. It is to be noted that, while converting the SolidWorks drawing to the ".ai" vector format, details regarding the depth of the channels and the thickness of the PMMA substrates are lost, and hence, the required depth of channels had to be achieved through 'trial and error' by varying the laser-marking speed. In spite of this operational drawback, laser micromachining carries several advantages (Cheng *et al.*, 2004; Pfleging *et al.*, 2009) like its speed of fabrication, ease-of-use, etc., thereby, enabling rapid prototyping of devices with design modifications and rapid iterations (Reichen *et al.*, 2014). The direct-type laser machining system used to fabricate the prototype devices, directs the laser from the source into the chamber using a series of mirrors. Once inside the ablation chamber, the laser is reflected by a rotatable focussing lens on to the PMMA substrate. Therefore, as the laser moves farther away from the midpoint of the focal plane, trenches are etched at increasing angles (and not normal to the PMMA plane). This was also another reason for restricting the device footprint to at most 85 × 85 mm as explained in Section 2.3.1.

2.3.1.2 Thermal annealing of laser-fabricated devices

Another drawback of using a laser-micromachined device was the creation of rough channel beds, with visible striations from the path taken by the laser. The extent of roughness of the channel bed is discussed in Section 2.3.3.

Significant consequences could potentially arise from the rough channel-beds, thereby, affecting the flocculation process in one or more of the following ways-

1. The methyl-methacrylate heads of PMMA in the surface of the channel can interact with the charge-carrying flocs, or the colloidal particles and the polymeric flocculants, resulting in their sedimentation in the craters or pockets of the channel bed.
2. The polymeric strands could potentially be de-activated, due to the confined channel dimensions resulting in the alteration of the rate of flocculation (Gregory and Barany, 2011);
3. Rough channel beds would pose a threat by shearing the flocs, where the levels of shear exposed to the flocs would not be quantifiable due to the nature of channel roughness or unevenness.

The above mentioned factors could also lead to a difference in the concentration of available flocculant strands in a given micro-environment at a given instant of time between the microfluidic scale and a larger experimental-scale. Therefore, steps to achieve smoother channels were adopted from the work reported by Cheng *et al.* in 2004, where it was observed that keeping the PMMA substrate at around 120 °C for 30 minutes (15 °C above the T_g of PMMA), followed by a second thermal annealing step at 170 °C for 30 minutes (10 °C above the melting point of PMMA) can effectively increase the surface smoothness of the laser-micromachined channels (Cheng *et al.*, 2004).

Apart from the patterns created by the laser, it was apparent that there were bubble-like formations on the channel bed (Figure 2.3, left column) and the density of such bubbles increased with increasing channel widths. This was potentially due to the entrapment of air bubbles beneath the surface during the ablation process. PMMA rapidly melts and evaporates locally as the laser passes over the substrate, and immediately re-solidifies, thereby, trapping air. Taking the temperature above the T_g of PMMA (at 120 °C) seems to release these trapped air bubbles, forming crater-like patterns on the surface of the channel (Figure 2.3, middle column). Following this step, on further increasing the temperature to 170 °C for 30 minutes, PMMA starts melting from the surface and evidently forms smoother channel beds (Figure 2.3, right column).

This two-step annealing method is, hence, a simple and effective way to create smoother microchannels from laser-ablated devices. However, it was noted that the optical transparency of PMMA greatly reduces when annealed, and consequentially affects the integration of optical analytical methodologies. While this step seemed effective, it was not implemented on the microfluidic devices as it was deemed unsuitable for the visual observation of flocculation. Therefore, micro-milling was used to create smooth channels, with precise channel depths, while retaining the optical transparency of the PMMA substrate.

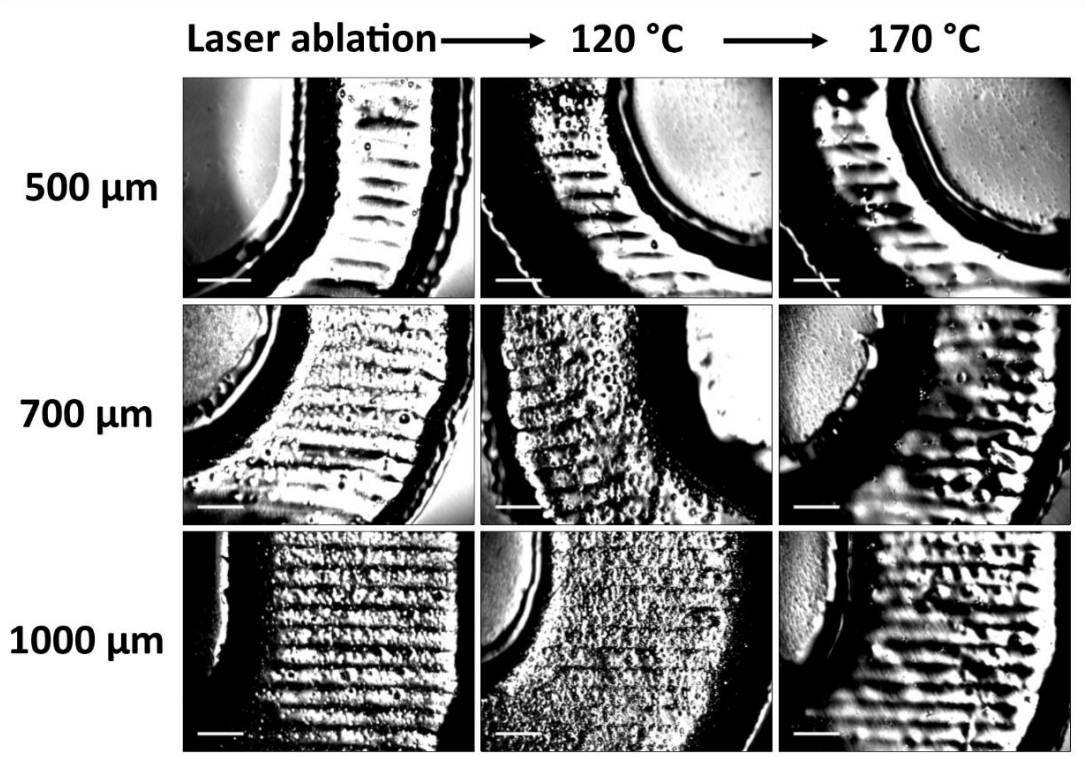

Figure 2.3: Phase contrast microscope images of 'U'-shaped trenches, 2.5 cm long, fabricated to observe the bed-roughness of laser-ablated channels and the effect of a two-step annealing process to increase the smoothness of the channels. Column-wise (left to right) - laser ablated channel; heat-treated at 120 °C for 30 minutes; and further annealed at 170 °C for 30 minutes. Row-wise (top to bottom) - increasing channel widths from 500 µm to 1000 µm. Scale bars indicate 200 µm.

2.3.1.3 Testing flocculation-suitability of the laser-ablated devices:

The fabricated serpentine and spiral microfluidic devices (after thermo-compression bonding, as mentioned in Section 2.3.2) were put to test for the first time, by introducing equal volumes of yeast homogenate and 15 g PEI kg^{-1} yeast (as mentioned in Section 2.2.5) at a combined flow rate of 200 µl min^{-1}. With a longer channel and larger cross-section, flocs in the serpentine device had an average residence time (τ) of *ca.* 229.5 s at 3.3 mm s^{-1}. Upon visual observation the flocs seemed to clog at the 'U' bends of the serpentine design, eventually leading to a complete blockage. It is believed to be the result of a combination of the low velocity and the presence of cohesive forces between the already clogged particles and subsequent particles in flow, thereby, rapidly increasing the rate of clogging. This was not the case with the spiral design, and flow of evenly-spaced large flocs

was observed at 13.3 mm s^{-1}, due to the smaller cross-section. The flocs had τ of around 46 s with 607 mm channel length. The spiral channels did clog from the walls (inwards) at the ψ-shaped inlet junction eventually, but only after around 2 hours of continuous flow of yeast homogenate and PEI solution. The spiral microfluidic device (hereinafter called as the µ-flocculation device), hence, was deemed suitable to study flocculation *in situ*, and the serpentine design was discontinued.

The laser-ablated µ-flocculation device was used to characterize the volumetric flow rates of the cell debris and the flocculant (Section 2.3.5), and has also been discussed in Section 2.3.3, regarding the channel-bed roughness. For all other experimental work performed (here and in the following chapters), micro-milled µ-flocculation devices were used.

2.3.1.4 Micro-milling the spiral µ-flocculation device:

Due to the limitations brought about by laser micromachining, the µ-flocculation device for the *in situ* observation of the flocculation process was fabricated using the micro-milling process. The channels were micro-milled using a 0.2 mm end mill under a pocket-cut setting. A cutting method of "Parallel Spiral, with clean corners" was chosen as it seemed to provide clean cuts with no debris left at the channel edges. 350 µm was fabricated in one rough step out of the 500 µm depth, followed by a smoother finishing step of 150 µm, where the feed rate (speed at which the milling head moves) was slowed to 50% of the original value.

The edges of the channel were milled in a similar fashion with a 'contour-cut' using a 2 mm end mill. This phase did not have any finishing step and the 1.5 mm PMMA layer was cut-through with 0.50 mm depth cuts. The device was then removed from the sacrificial layer, the adhesive tape removed, and cleaned with detergent and water. The channels were inspected using a table-top simple microscope to ensure no debris was present in the channels, before thermo-compression bonding.

2.3.2 Thermo-compression bonding & device assembly

Thermo-compression bonding (TCB) is a very critical step in the fabrication process, as it not only provides a permanent seal between two substrates, but also enables relatively high-pressure flow-rates while being leak-free. TCB involves taking the temperature to the glass transition temperatures (T_g) of the polymeric thermoplastic

substrates, and the combined effect of temperature and pressure enforces an exaggerated contact between polymers of two layers, at the interface, leading to the creation of strong physical linkages. Due to several advantages like possessing homogenous surface properties, and high bond-strengths, this technique is one of the most commonly applied methods to create leak-free microfluidic devices (Tsao and DeVoe, 2009).

Different types of PMMA have varying T_g values (105 °C, for the one used for this work), and while this direct-type bonding has many advantages, one major challenge is to optimise the temperature, pressure-applied, and the bonding-time (Tsao and DeVoe, 2009; Zhu *et al.*, 2007). Hence, if they are not carefully selected, the resulting devices can have global or localized deformations and also uneven layer-thickness (Sun *et al.*, 2006). This was performed by varying the bonding-time with the applied torque and number of bolts used, as reported in Table 2.1.

Table 2.1: Optimisation of different TCB parameters and the observed outcome. The devices to be bonded were placed between two aluminium plates and tightened using either four or eight bolts at 3 different torques- to have a homogenous compression. They were then placed in a pre-heated oven at 105 °C, for 60, 75 or 90 minutes.

<table>
<tr><th>Thermal bonding time (min)</th><th>350 cNm,
4 bolts</th><th>400 cNm,
4 bolts</th><th>450 cNm,
4 bolts</th><th>450 cNm,
8 bolts</th></tr>
<tr><td>60</td><td rowspan="2">Incomplete bonding</td><td rowspan="2">Air pockets between channels</td><td>Air pockets between channels</td><td>Complete bonding</td></tr>
<tr><td>75</td><td rowspan="2">Channel deformation</td><td>Visible melting of PMMA</td></tr>
<tr><td>90</td><td>Air pockets between channels</td><td>Channel deformation</td><td>--</td></tr>
</table>

Upon using 350 cNm for four bolts to hold the aluminium plates together, the bonding was incomplete when kept in the heated oven for 60 and 75 minutes, suggesting insufficient force or time to fluidize the methacrylate strands on the surface of the layers. When the bonding-time was increased to 90 minutes at 350

cNm, or 60 or 75 minutes at 400 cNm, or 60 minutes at 450 cNm, there was sufficient bonding throughout the surface, except the area between the channels, thereby, forming pockets of un-bonded areas locally in-between the channels. This is probably due to a significant curvature in these areas or the lack of enough surface area to have a strong contact with the top PMMA layer. At 400 cNm and a bonding time of 90 minutes, or at 450 cNm with 75 or 90 minutes of bonding-time, a visible deformation of the channels was observed, indicating the fluidisation of most of the bulk PMMA strands.

This even worsened when the number of bolts was doubled to eight, resulting in twice the force applied on the plates, where the entire PMMA layers became largely deformed (not only the channels). But, this was not observed when the bonding-time was reduced to 60 minutes at 450 cNm with 8 bolts. This implies that the applied force was large enough to induce good contact between the top PMMA layer and the areas in-between the channels; while at the same time, not long enough, so as to prevent the fluidization of PMMA in the bulk layer.

All devices fabricated thereafter were bonded successfully at 450 cNm, with 8 bolts at 105 °C for 60 minutes. Even though the optimization protocol was performed with laser-ablated µ-flocculation devices, the chosen parameters provided a perfect bonding for the micro-milled devices as well. The device is then assembled as shown in Figures 2.4 and 2.5 (with the technical drawings in Appendix A2.1).

Upon the fabrication of a new µ-flocculation device, the assembly was rigorously tested for leaks at the interconnect bars and at the compression-seal with the ferrules. It was observed that the planarity of both the interconnect bars and the top PMMA layer plays a crucial role in facilitating a tight, leak-free connection.

Apart from ensuring a leak-free connection, the burst pressure was measured using a calibrated pressure sensor. Pressures up to 1468 mbar (21.3 psi) were recorded successfully, displaying a strong TCB bond and a robust fluidic interconnect ports. Due to the long channels, the syringe pumps stalled beyond this pressure for syringes with different diameters used. For a combined volumetric flow rate of 200 µl min^{-1}, a theoretical back pressure (pressure drop across the length of the channel) of 10.4 mbar (~0.15 psi) was calculated, for the dimensions of the µ-flocculation device (assuming the viscosity of water at 25 °C). This value is around ~100 times lower than the pressures recorded during the experimentation. Based

on this evidence the above mentioned bonding conditions and the assembly can be considered very safe for a long-term, leak-free usage of this setup.

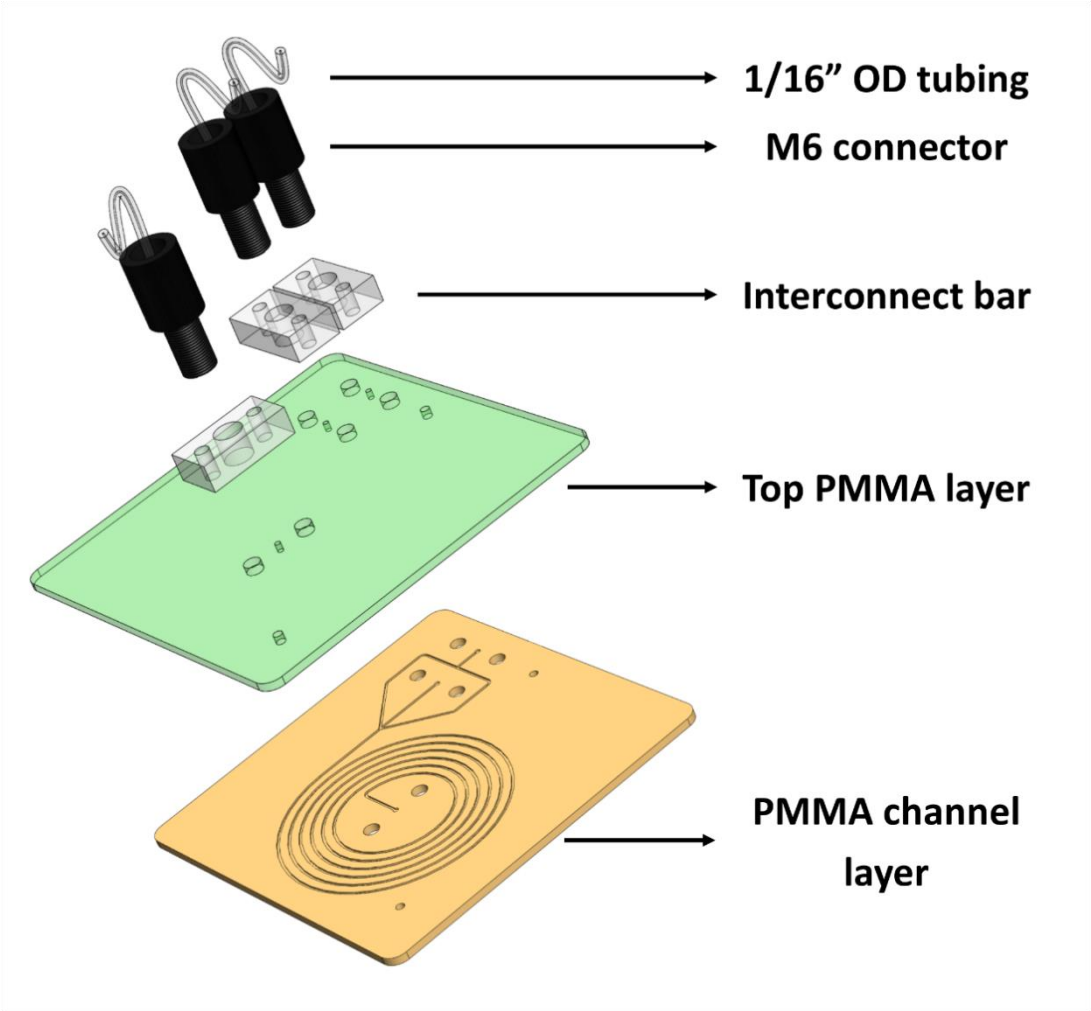

Figure 2.4: 3D CAD diagram showing the different layers of a fully-assembled µ-flocculation device. (Bottom to top)- The PMMA layer carrying the etched microchannels. This is thermally bonded with the top PMMA layer to completely seal the channels to make it leak-free. The interconnect bars are then screwed into place using 8 mm, M3 pozi screws, enabling an easily-removable connection with a threaded M6 Upchurch connector which carries the tubing with a ferrule at the tip.

2.3.3 Channel depth of the fabricated µ-flocculation devices

The depth of the channels in the fabricated microfluidic devices and the relative roughness of the channel-bed were measured using the DektakXT optical profiler. Four different devices were measured (two laser ablated devices, two micro-milled

devices – one, each, before and after TCB). Measurements were taken at five different locations of the devices (channels near the four edges and one in the centre of the device) to compare the planarity of the device and also the localized TCB-effects on the channels.

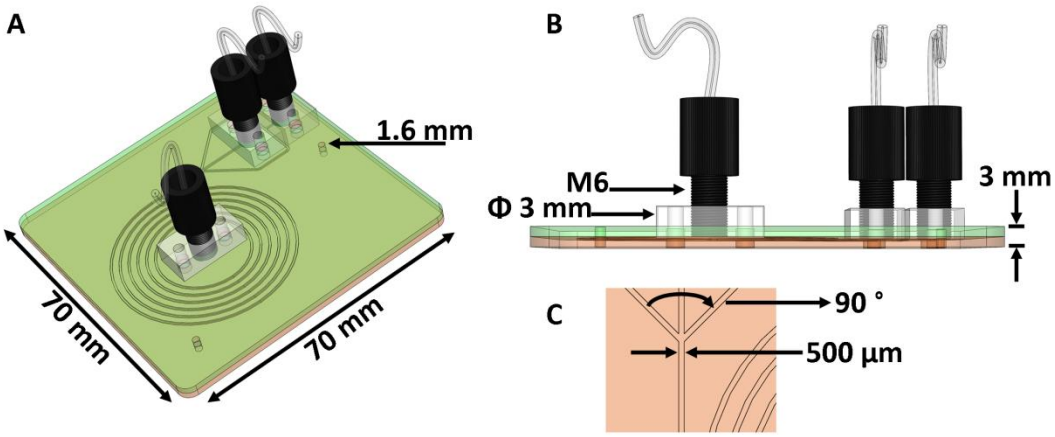

Figure 2.5: (A) – Isometric view of the device shows the footprint of the µ-flocculation device of 70 × 70 mm and holes for alignment pins of 1.6 mm diameter. (B) – side view of the device showing the height of the device, with the M6 connectors. (C) – A snapshot ψ- shaped inlet of the µ-flocculation device. Images were created using the SolidWorks® 2011 software and are not to scale.

Figure 2.6 and Figure 2.7 represent the surface profiles of the laser-ablated and micro-milled devices, respectively. It is noticeable that laser-ablation creates uneven depths, to the tune of around 83 µm (with 1 standard deviation = ± 33.8 µm, n= 5), between different points within the same device. This can be attributed to the increase in the laser's contact angle on the PMMA layer, as it moves away from the centre of the focussing lens' plane. It is also evident that the channel-beds seem to have uneven surfaces, which seem to reduce after TCB. But the biggest drawback of using laser-ablation seems to be the creation of mounds of *ca.* 50 µm along the channel walls. This was possibly a result of rapid PMMA melting during the ablation process; and these mounds could have led to the creation of air-pockets, during the TCB-optimization process (Section 2.3.2).

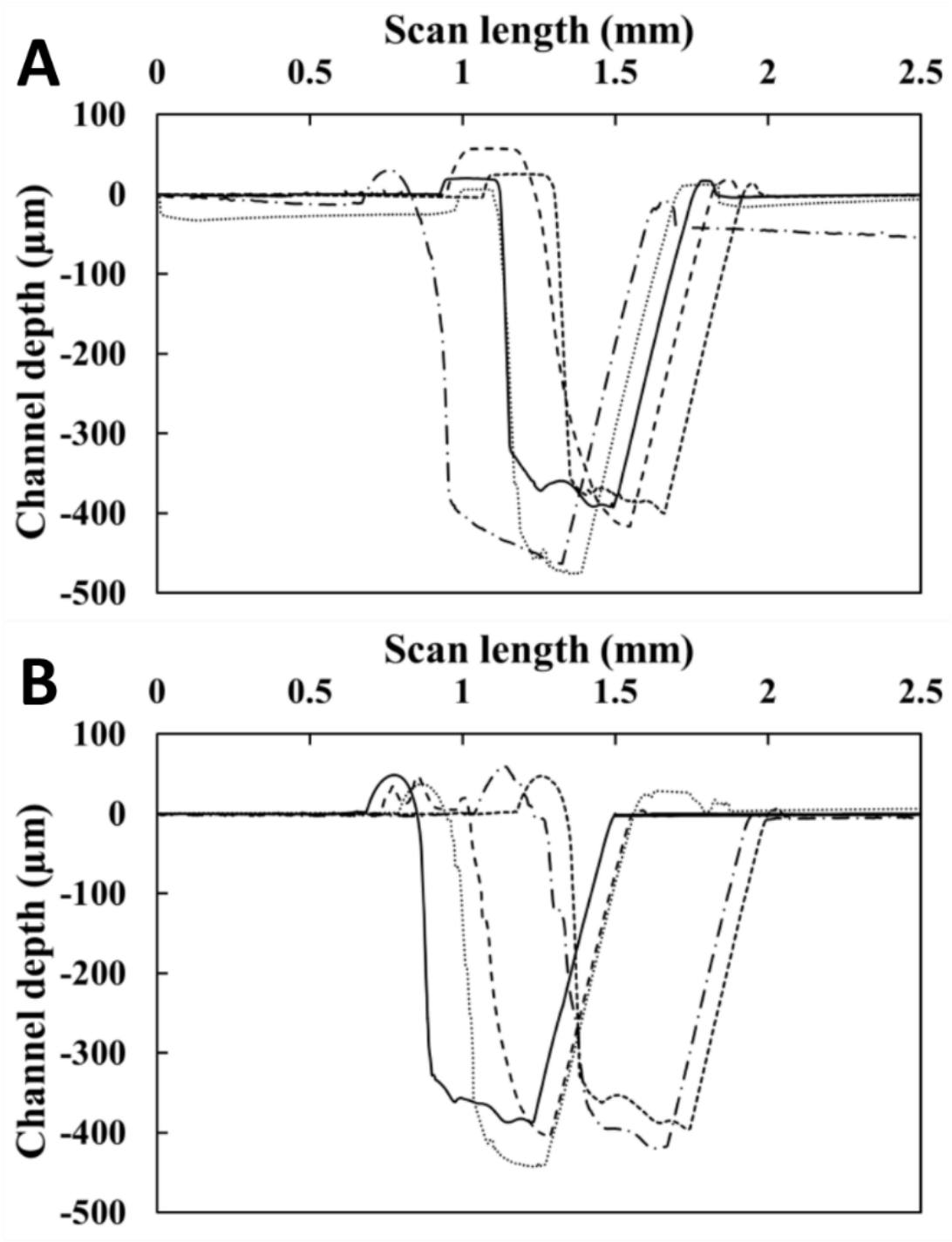

Figure 2.6: Dektak surface profiles of laser-ablated µ-flocculation devices. Measurements were taken across channels closest to the 4 edges of the device and one in the centre. (A) – Profiles of the channels before TCB, with an average depth of 429.6 ± 33.8 µm (1 σ), and (B) – after TCB, with average depth of 410 ± 19.4 µm (1 σ). The profile traced can be seen on the left-side, while the slope on the right-side corresponds to the tip-retraction of the profiler.

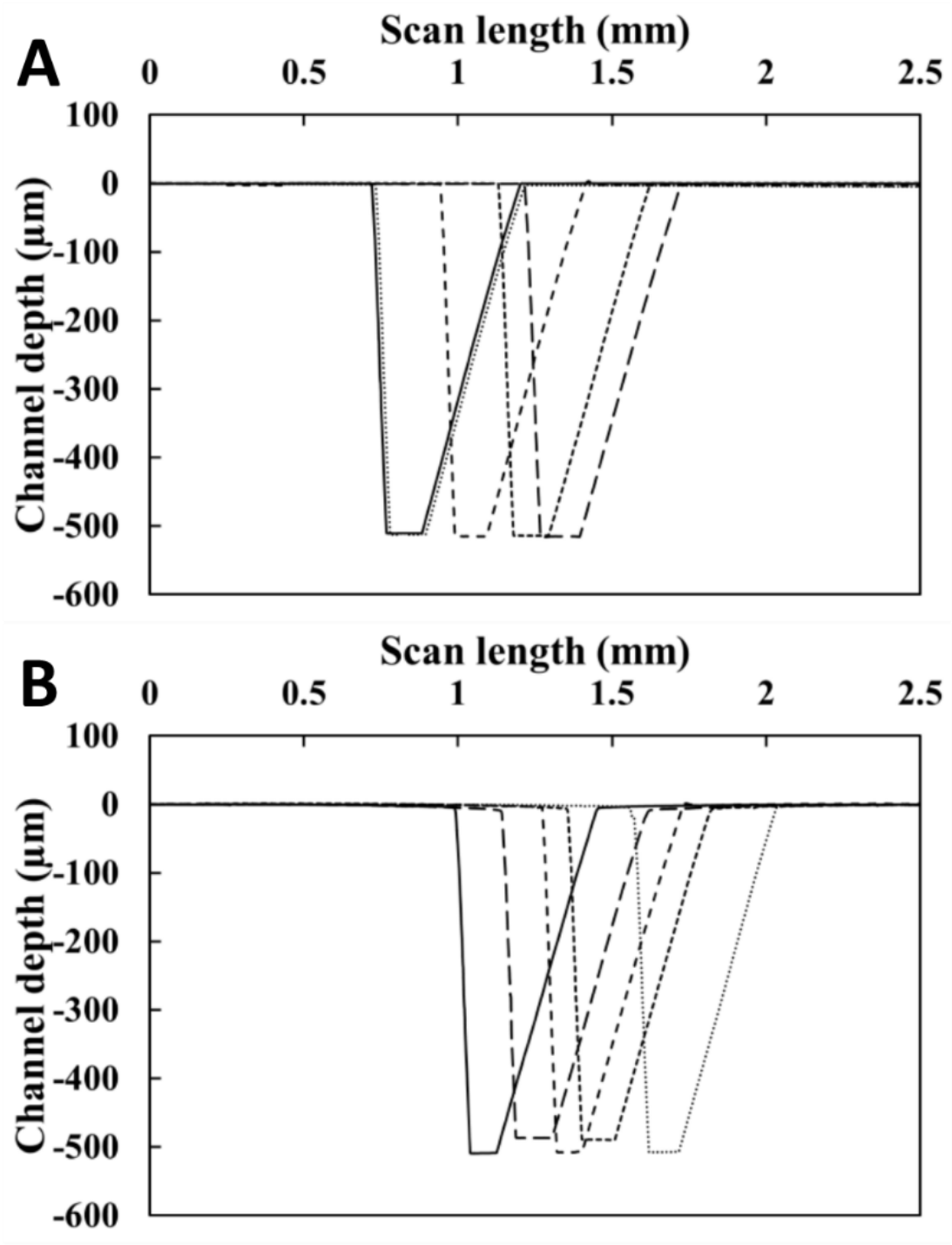

Figure 2.7: Dektak surface profiles of micro-milled µ-flocculation devices. Measurements were taken across channels closest to the 4 edges of the device and one in the centre. (A) – Profiles of the channels before TCB, with an average depth of 515.3 ± 2.4 µm (1 σ), and (B) – after TCB, with average depth of 500.4 ± 9.8 µm (1 σ). The profile traced can be seen on the left-side, while the slope on the right-side corresponds to the tip-retraction of the profiler.

Furthermore, the reduction in the channel-depth (due to fluidization of the surface-PMMA layer) before TCB (Figure 2.6A) and after TCB (Figure 2.6B) was significantly high (85.1 ± 29 µm, n = 5). Micro-milling clearly seemed to be more suitable, as the average depth before TCB (Figure 2.7A) was 515.3 µm with a small variation between different points within the same device (2.4 µm, n=5). Even though the depth was set to 500 µm during the CNC milling process, the additional 15 µm was expected due to the manual-handling. The zero-setting (in the Z-axis) on the milling machine, coinciding with the top of the PMMA layer, had to be set manually by visually observing the point where the end-mill comes into contact with the PMMA surface.

A decrease in the average channel-depth by only 14.5 µm was recorded after TCB, with a standard deviation of ± 10.9 µm, n=5 (Figure 2.7B). Additionally, the devices were observed to have a consistent depth of 500.4 ± 9.8 µm (n=5), with no noticeable mounds or unevenness (due to TCB). Based on the aforementioned observations, micro-milled µ-flocculation devices were the obvious choice, providing a smooth channel cross-section, and thereby avoiding potential problems while performing flocculation (as listed in the Section 2.3.1.2).

2.3.4 Homogenisation test of *S. cerevisiae* in a pilot scale homogeniser

The Lab 60 Homogeniser has an operational fluid volume between 1 and 4 L, and can be operated at a maximum of 6×10^7 Pa. Homogenised yeast suspension is a frequently used test-bed system to study flocculation as a downstream unit-operation and also to characterize the efficiency of product-recovery (Clarkson *et al.*, 1993; Cordes *et al.*, 1990; Habib *et al.*, 1997; Milburn *et al.*, 1990; Salt *et al.*, 1996; Tsoka *et al.*, 2000). The method of cell-disruption implemented is, therefore, critical in deciding the amount of intra-cellular proteins and nucleic acids released, which in turn affects the flocculation process, and mechanical cell disruption is often favoured because of a high product-release rate and bypassing the need for additional chemicals that may require further separation steps (Millis, 1996). As shown in Figure 2.8A, the average diameter of the yeast suspension decreases from 5.6 to 4.7 µm microns, which is not a huge shift in the sample population, and the absence of a sample population with smaller sizes is worth noting, as a significant percentage of proteins, protein aggregates, etc. is usually expected.

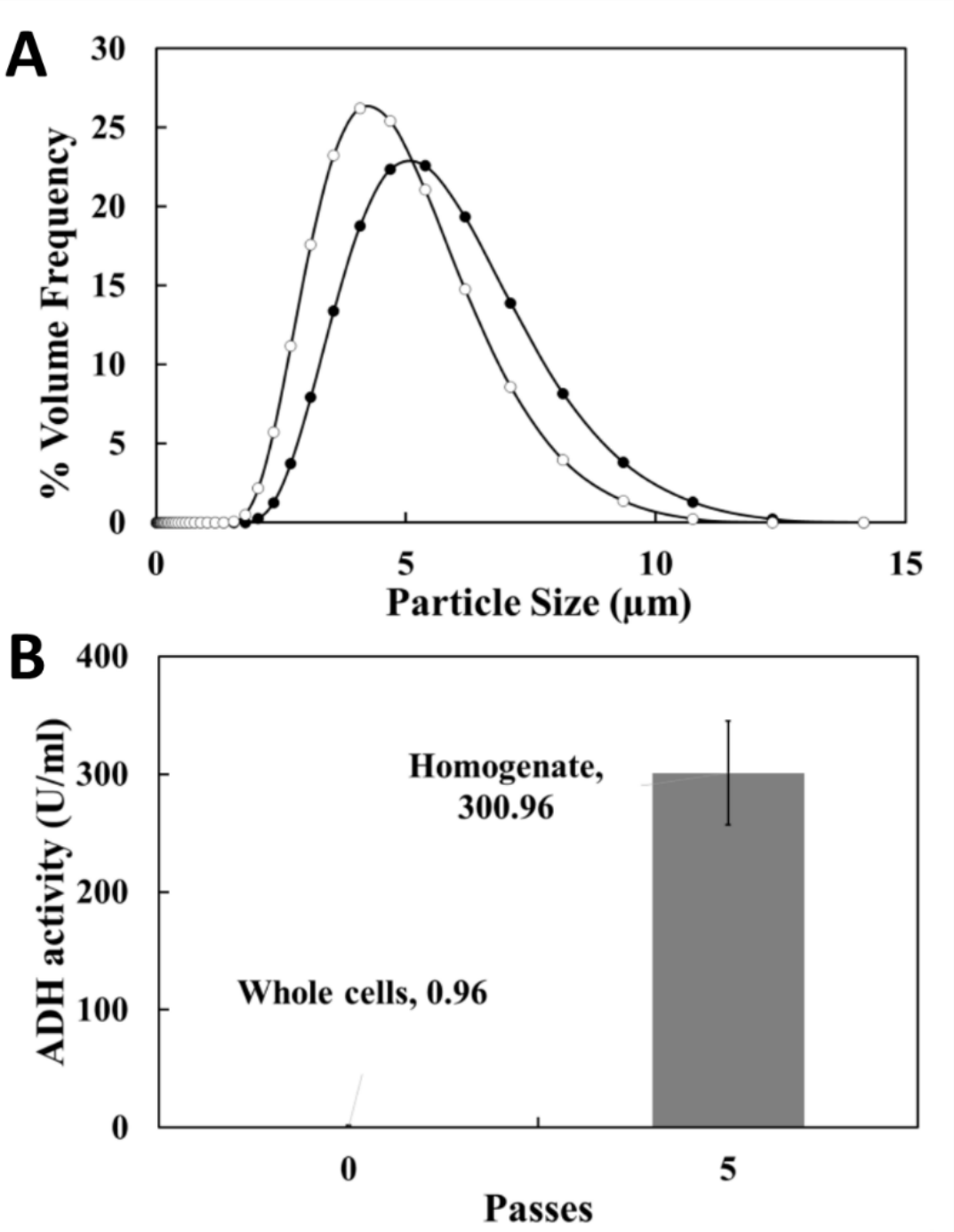

Figure 2.8: (A) - Comparison of particle size distributions (PSDs) between 25% yeast suspension before (●) and after homogenisation (○) for 5 passes at 5 × 10^7 Pa. Measurements were made using a Mastersizer 2000 instrument. The average diameters measured, decreased from 5.6 µm to 4.7 µm after homogenisation (n=3). (B) - the amount of ADH released after 5 passes of homogenisation, confirming an efficient cell-disruption. Error bars denote ± 1 σ, n = 5.

The absence of the smaller-sized population also indicates the absence of micronisation (resulting in small cell-debris) that can affect further downstream operations. Figure 2.8B confirms an efficient cell-disruption through an ADH assay (as explained in Section 2.2.4), that showed a 300-fold increase of ADH in the bulk-liquid. Homogenisation for more than 5 passes wasn't tested due to the expected micronisation of the cellular suspension (Ayazi Shamlou *et al.*, 1995; Siddiqi *et al.*, 1997). While it is important to ensure maximum product release, exposure to severe conditions can lead to product denaturation and excessive formation of cell debris. Figure 2.9 confirms sufficient disruption of yeast cells, with only a few cells retaining an intact cellular membrane.

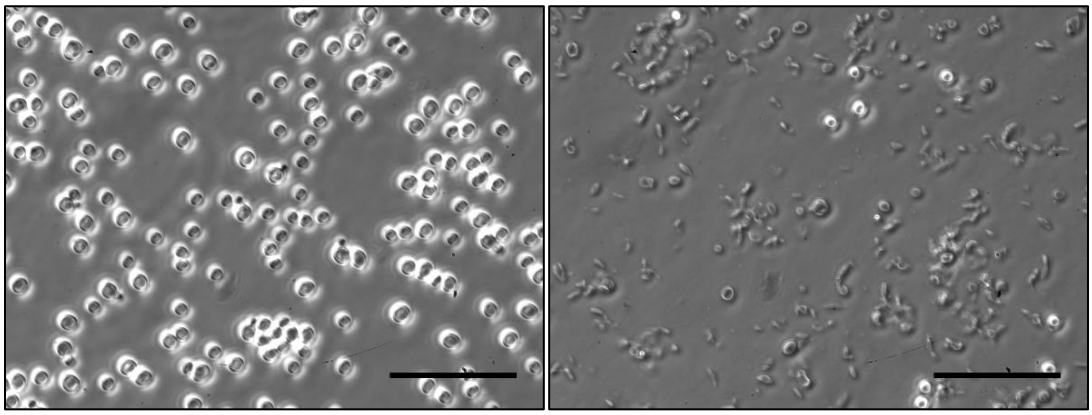

Figure 2.9: Phase-contrast microscopy images of (Left) - yeast cell suspension and (Right) - yeast homogenate after 5 passes, at 5 × 10^7 Pa in a Lab 60 homogeniser under total recycle conditions. Scale bars denote 50 µm. Images taken using a monochromatic CCD camera (Basler Scout scA1400 – 17fm, Basler AG, Germany) on an inverted microscope (Nikon TE-2000, Nikon UK Ltd., UK).

2.3.5 Particle size analysis by laser diffraction

2.3.5.1 Laser diffraction measurement system

For comparison between the flocs formed in the µ-flocculation device and the bench scale setup, a commonly used analytical instrument for size determination of various biomolecules (Chatel *et al.*, 2014; Espuny Garcia del Real *et al.*, 2014; Jarvis *et al.*, 2005; Narong and James, 2006; Tustian *et al.*, 2007; Wyatt *et al.*, 2013; Zhou and Franks, 2006), based on laser diffraction, namely Mastersizer 2000, was used. Because the scale-comparison work has been heavily dependent on this instrument, the principle behind the functioning of this device is discussed in the following paragraphs to highlight both its accuracy and its operational limitations.

Laser Diffraction functions based on the light scattering property of different colloids or aggregates and the calculation of its hydrodynamic diameter. Particles of a varied size range diffract light at different angles, causing fluctuations in the light intensity falling on a set of detectors. These fluctuations are used to find the Brownian motion velocity which is then used to find the size of the particles through the Stokes-Einstein relationship.

$$D = \frac{K_B T}{6\pi\eta} \tag{2.2}$$

The instrument uses a sample dispersion system (Hydro SM-A) to homogeneously disperse and re-circulate the sample in the cell-window placed in the optical unit of the instrument (Figure 2.1). The lowest operational dispersant-volume of the Hydro SM-A was 60 ml, which was used to meet the low sample volumes from the µ-flocculation device.

The Mastersizer is known to give accurate measurements of particle sizes as it is based on the 'Mie theory' which explains the scattering of electromagnetic radiation by a sphere. This theory is more accurate than the Fraunhofer model (Malvern Instruments website), but it does assume that some specific information about the particle, such as its refractive index (RI), and its absorption, are accurately known.

There are three distinct operational procedures involved in measuring the particle size of a sample using the Mastersizer.

a. **Sample preparation:** Firstly, the sample is prepared and dispersed into the Hydro SM-A, to a final concentration indicated by the 'Laser Obscuration' value in the software. Laser Obscuration is a measure of the amount of laser light lost due to the introduction of the sample within the analyser beam. This value is generally around 10-20 % for particles above 1 µm in size. One of the evident drawbacks is the need for collecting enough sample (floc) volume, resulting in the possible sedimentation of the aggregates in the collection vials, thereby affecting the particle sizes. Additionally, end-point measurements using this setup do not accommodate the measurement of growth kinetics data. The flocs need to be dispersed in a larger volume of dispersant and is re-circulated using an impeller. This exposes the flocs to shear, and hence, leads to an alteration of the floc size and strength.
b. **Measurement:** Secondly, the scattering pattern from the prepared sample is generated using a red laser (4 mW He-Ne, 632.8 nm) for particles above 1 µm

and a blue LED light source (0.3 mW LED, 470 nm) for sub-micron sized particles, which is captured on the detector. The detector array within the optical unit is made up of many individual detectors corresponding to fixed sizes. As the laser is pulsed through the cell-window, the detector array takes "snap-shots" of the scattering pattern. Typically over 12000 snap-shots are made for each measurement, with each snap-shot taking 1 ms. Two implications which can be observed are that only a small proportion of flocs from a large population is typically collected for measurements, and the time for a single measurement lasts for around 24 seconds (12000 ms for background imaging + 12000 ms for sample measurement). This potentially affects the size of the flocs under constant re-circulation in the dispersion unit.

c. **Data Processing:** The 'residual' is an indication of how well the calculated data was fitted to the measurement data. A good fit is indicated by a residual of less than 1%. If the residual is over 1%, this may be an indication that incorrect refractive indices and absorption values for the sample and dispersant have been used. The residual was around 0.8- 0.95% for most of the measurements performed, thereby showing that the RI chosen for the yeast homogenate – PEI system, were accurate. Because the array of detectors is arranged in a semi-circular fashion, they correspond to fixed size ranges, increasing in a logarithmic scale. This results in particle size distributions (PSDs) and also the average circular diameters, namely - the d50, which is the size in microns corresponding to the 50th percentile of the size range (i.e. 50% of the sample is smaller and 50% is larger than this size in the distribution). This value is also known as the Mass Median Diameter (MMD). d90 is the size of particle below which 90% of the sample population exists.

2.3.5.2 Reproducibility of the Mastersizer 2000

Figure 2.10 shows flocculation experiments performed between yeast homogenate and 15 g PEI kg^{-1} yeast at pH 7.4 in a centrifuge tube, performed in triplicates. A consistent increase in the floc size was recorded repeatedly, with the standard deviation being less than 0.5 µm for all data points. This demonstrates the accuracy and reproducibility of the device, but the operational drawbacks discussed above reflects the necessity for a better analytical setup to extract growth kinetics data from the µ-flocculation device in real-time and without the need for sample handling or dispersion.

2.3.5.3 *Method verification of yeast homogenate*

To ensure reproducible flocculation conditions, the effect of yeast homogenate storage was tested by performing flocculation with fresh yeast homogenate (homogenisation within 24 hours, and performing flocculation experiments, within 36 hours from delivery of yeast), and thawed homogenate (stored in -20 °C for 24 hours, and thawed back to room temperature overnight).

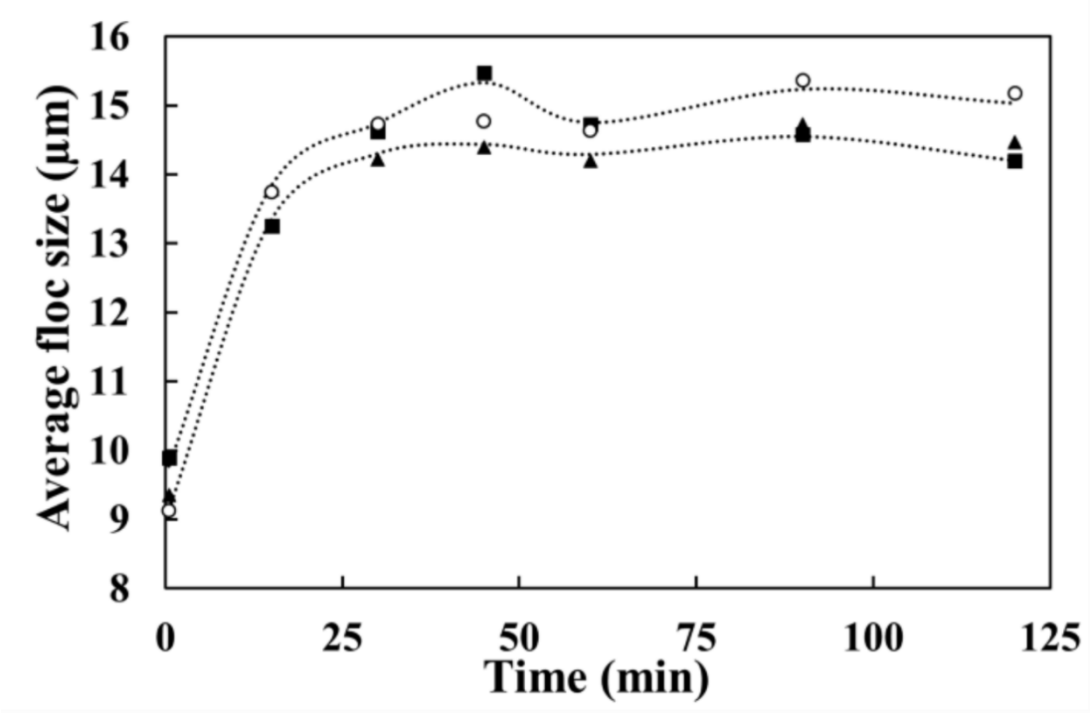

Figure 2.10: Average size (d50) variation of flocs formed from yeast homogenate with 15 g PEI kg^{-1} yeast, pH 7.4, in a centrifuge tube. Measurements were performed using a Mastersizer 2000 laser-diffraction instrument; where the dotted lines denote ± 1 σ, n=3. The largest deviation was recorded at the 45th minute data-point, which was 0.44 µm.

These were flocculated with 15 and 20 g PEI kg^{-1} yeast in a centrifuge tube and floc sizes measured using the Mastersizer. From Figure 2.11, it is apparent that freeze-thawed samples were detrimental to flocculation and therefore, fresh yeast homogenate (as described above) was used rigorously for the flocculation work reported in this thesis.

2.3.5.4 *Characterisation of volumetric flow rates in the µ-flocculation device*

The volumetric flow rates for the ψ-shaped inlets (yeast homogenate in the focussed flow and PEI in the sheath flow) were characterised for the size of flocs

emerging from the outlet of the µ-flocculation device. A schematic representation of the setup has been depicted in Figure 2.1, and the method of setting up the system has been detailed in Section 2.2.5. The PTFE tubing from the outlet was directly immersed into the sample dispersion unit of the Mastersizer, and the length of the tubing was kept as short as possible to decrease the time required for achieving adequate sample volumes. Different volumetric flow rates (relating to linear velocities suitable for high-speed imaging explained in Chapter 4) were tested.

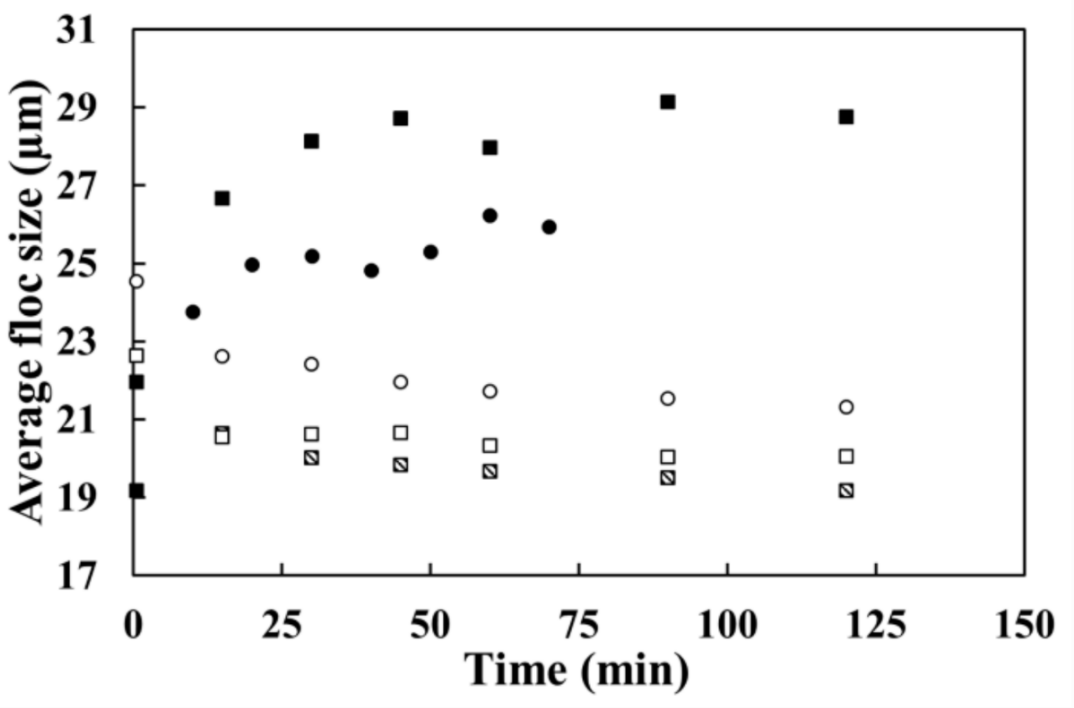

Figure 2.11: Average size (d50) variation of flocs formed from yeast homogenate with 15 g PEI kg^{-1} yeast (■ – fresh homogenate, and □ – freeze-thawed homogenate, n=2) and 20 g PEI kg^{-1} yeast (● – fresh homogenate, and ○ – freeze-thawed homogenate), pH 7.4, in a centrifuge tube. Measurements were performed using a Mastersizer 2000 laser-diffraction instrument.

These were between 75 µl min^{-1} to 213.3 µl min^{-1}, at different inlet ratios ranging from 3:1 to 1:3 as shown in Figure 2.12. Flow rates below 75 µl min^{-1} weren't tested, because channel-clogging was encountered, which started building from the inner walls of the channel towards its centre, until it blocked the channels completely. While the d50 and d90 sizes remained similar for almost all flow rates and inlet ratios, a slightly higher size was observed when the flow rate of PEI was twice that of the yeast homogenate.

Intuitively, the flow rate of PEI was reduced to a value slightly higher than that of yeast homogenate (1.13%) for three different combined flow rates, and consequently the floc sizes measured were drastically higher. In spite of performing the experiments in triplicates, this seemed to be consistent, with higher d90 values observed at all three flow rates, with the highest recorded at 106.6 µl min^{-1}. However, the 'span' of the particle distribution (d90 – d10) seemed higher at this flow rate, while d50 at 160 µl min^{-1} attained larger sizes with the lowest span. This denotes the presence of more flocs of similar sizes in the sample population. Owing to a lower span, and with faster channel-clogging observed at lower flow rates, 160 µl min^{-1} was chosen as the combined flowrate, with the individual inlets having flow rates of 75 µl min^{-1} (for yeast homogenate) and 85 µl min^{-1} (for PEI).

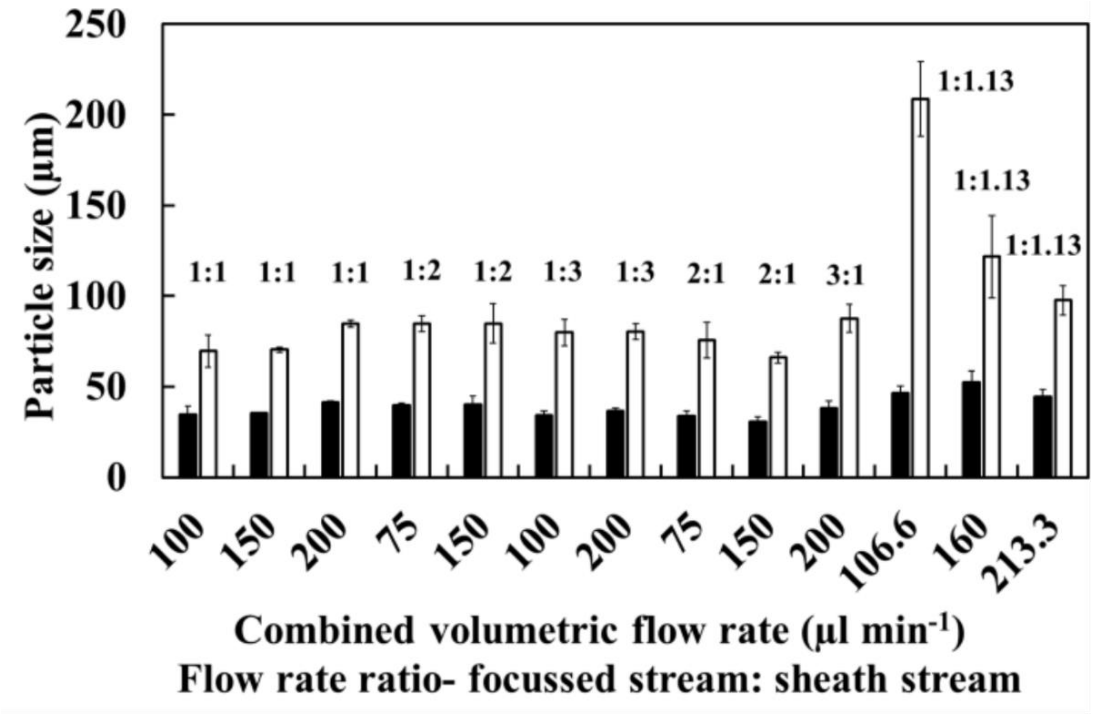

Figure 2.12: Characterization of floc sizes (d50 – filled bars, d90 – hollow bars) of a yeast homogenate – PEI system (20 g PEI kg^{-1} yeast, pH 7.4), with varying combined volumetric flow rates. Different flow rate ratios between the two inlets in the ψ-shaped focussing inlet were also tested (data labels; yeast homogenate flow rate: PEI flow rate). Error bars represent ± 1σ, n=3.

Higher d90 floc sizes at lower combined flow rates (at 1:1.13 ratio) can be attributed to a higher electrostatic interaction between the particles, and to the lower shear rates in the microfabricated channels - highlighting the sensitivity of the flocs to shear. Additionally, the slightly higher sheath flow rate would have led to the

presence of more cationic flocculants directed towards the cellular suspension, leading to an enhanced aggregation process. The calculation of shear rates from finite element modelling has been discussed in Chapter 3, where the µ-flocculation device with a continuous steady-state system, has been compared to closely-related batch flocculation rigs.

2.3.6 Floc-size comparison between µ-flocculation device and a bench scale system

After the selection of volumetric flow rates for flocculation in the microfluidic device, the device was put to test, to compare and contrast the floc size patterns with that of a bench scale system. Upon addition of the flocculant solution to the homogenate, they were mixed by tube-inversion, uniform number of times, to ensure homogeneity. Samples were then introduced into the dispersion unit of the Mastersizer within 60 seconds. This was performed to completely avoid flocs from entering the floc ageing phase, and ensure a 'time-to-analysis' proportional to τ of the flocs within the microfluidic device (~57 seconds at 160 µl min^{-1}).

Flocs formed in the bench scale, were sampled at different time points (Appendix A2.2) and a rapid formation of flocs was observed, immediately after the addition of the flocculating agent, possibly due to rapid binding of polymers to the colloidal particles. A sudden decrease in the floc size is observed for all the PEI concentrations trialled, implying the breakage of flocs due to shear. This was additional evidence for having sampled the flocs from the bench scale within 60 seconds, for the following experiments.

The floc diameters between the two scales were compared, in the first instance, at a constant PEI concentration of 20 g kg^{-1} yeast and varying pH of 5 to 7.5 as shown in Figure 2.13. An increase in floc size (both d50 and d90) was observed with increasing pH and this trend was observed in both the µ-flocculation device and the bench scale setup. While the pattern of increase appeared similar, flocs formed in the microfluidic device were significantly larger than that of the bench scale. This indicates the significance of shear rates present in a flocculation setup, and hence, needs quantification (see Chapter 3) even though the hydrodynamic conditions for floc-formation and growth were different between these experimental scales.

Variation of floc sizes with varying PEI concentrations (5 to 25 g kg^{-1} yeast) at a constant pH of 7.4 was also examined. From Figure 2.14 it is evident that the floc

sizes reached a maximum at 20 g kg^{-1} yeast, which is known to be around the isoelectric point of the flocculation system used (Section 2.3.7).

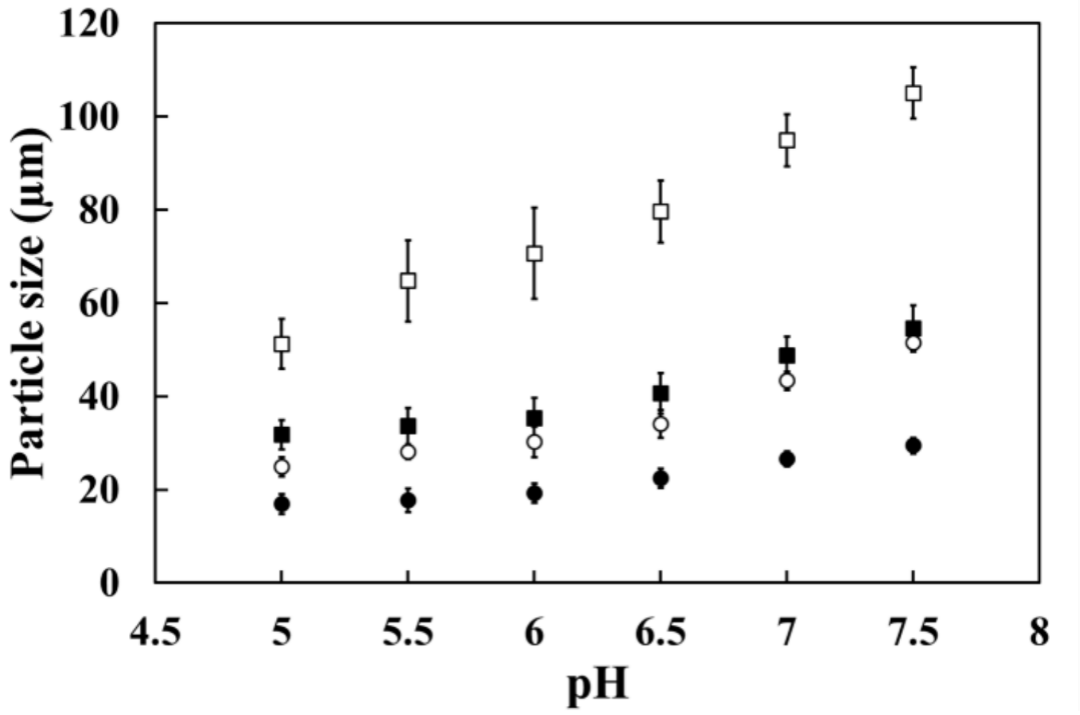

Figure 2.13: Variation of floc size with pH; at [PEI] (mol. wt. = 50-100 kDa) = 20 g kg^{-1} yeast. ● - d(50) bench scale, ○ - d(50) microfluidic chip, ■ - d(90) bench scale and □ - d(90) microfluidic chip. Volumetric flow rate in the microfluidic chip – yeast homogenate = 75 µl min^{-1}, PEI = 85 µl min^{-1}. Error bars indicate ± 1 σ, n = 5. d(50) is the size of the particle in microns which is the 50th percentile of the size range and d(90) is the size of the particle below which 90% of the sample lies.

A difference in the magnitude of floc sizes formed between the two scales was evident with different PEI concentrations, similar to that observed with varying pH. Larger d50 and d90 particle sizes in the microfluidic device can be associated with a prolonged growth condition in the microfabricated channels due to the presence of lower shear rates in the flocculation microenvironment. The pattern of variation in floc sizes recorded in both these instances was in accordance with the floc sizes obtained under similar conditions of PEI concentrations and pH, previously reported with a bench-scale flocculation system with yeast homogenate and PEI (Salt *et al.*, 1996).

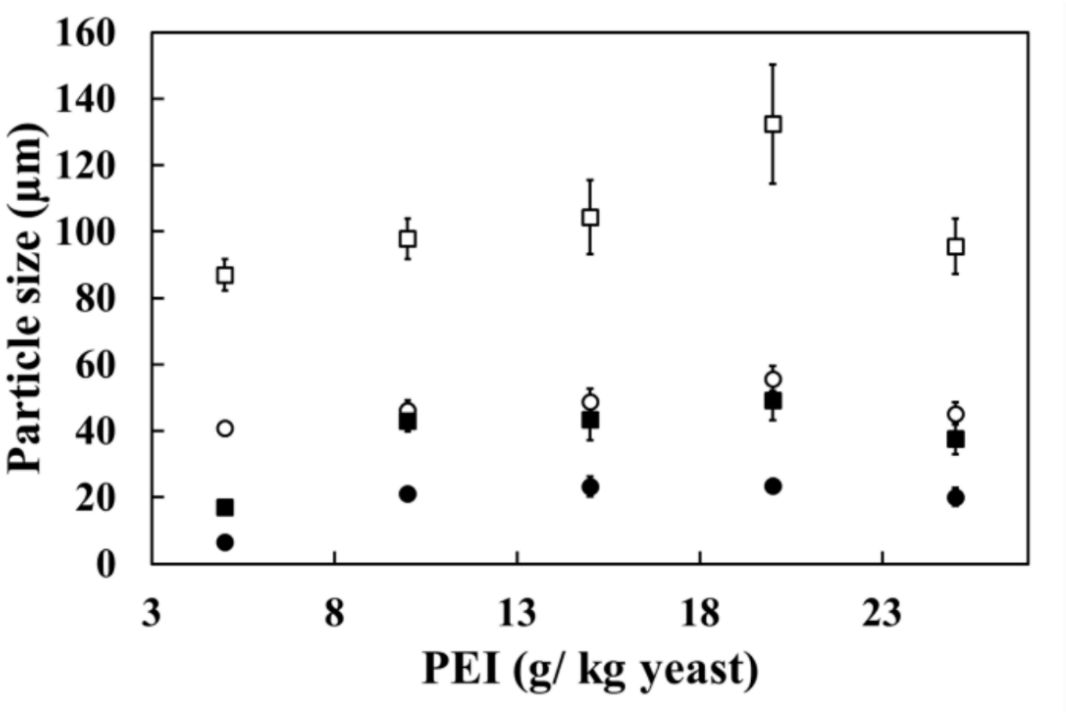

Figure 2.14: Variation of floc size with [PEI]; at pH 7.4. ● - d(50) bench scale, ○ - d(50) microfluidic chip, ■ - d(90) bench scale and □ - d(90) microfluidic chip. Volumetric flow rate in the microfluidic chip – yeast homogenate = 75 µl min^{-1}, PEI = 85 µl min^{-1}. Error bars indicate ± 1 σ, n = 5. d(50) is the size of the particle in microns which is the 50th percentile of the size range and d(90) is the size of the particle below which 90% of the sample lies.

To obtain a clearer picture of the difference in the d50 and d90 values of the two scales, particle size distributions (PSDs) were compared (as shown in Figure 2.15). The graphs represent the particle size distributions of the sample population with varying PEI concentrations.

Flocs in the bench scale belong to two distinct populations, and this can be due to the presence of higher hydrodynamic shear in the system. Based on this evidence, it can be inferred that there is an enhanced floc-formation, due to the tube-inversion method, and this can be possibly leading to the breakage of these weak flocs immediately. In the bench scale, a significant presence of particles of around 3 µm can be observed, thereby leading to lower d50 values. Flocs belonging to two size populations (with relatively narrow spans) explain the smaller difference between d50 and d90 in Figure 2.14, than that encountered in the µ-flocculation device.

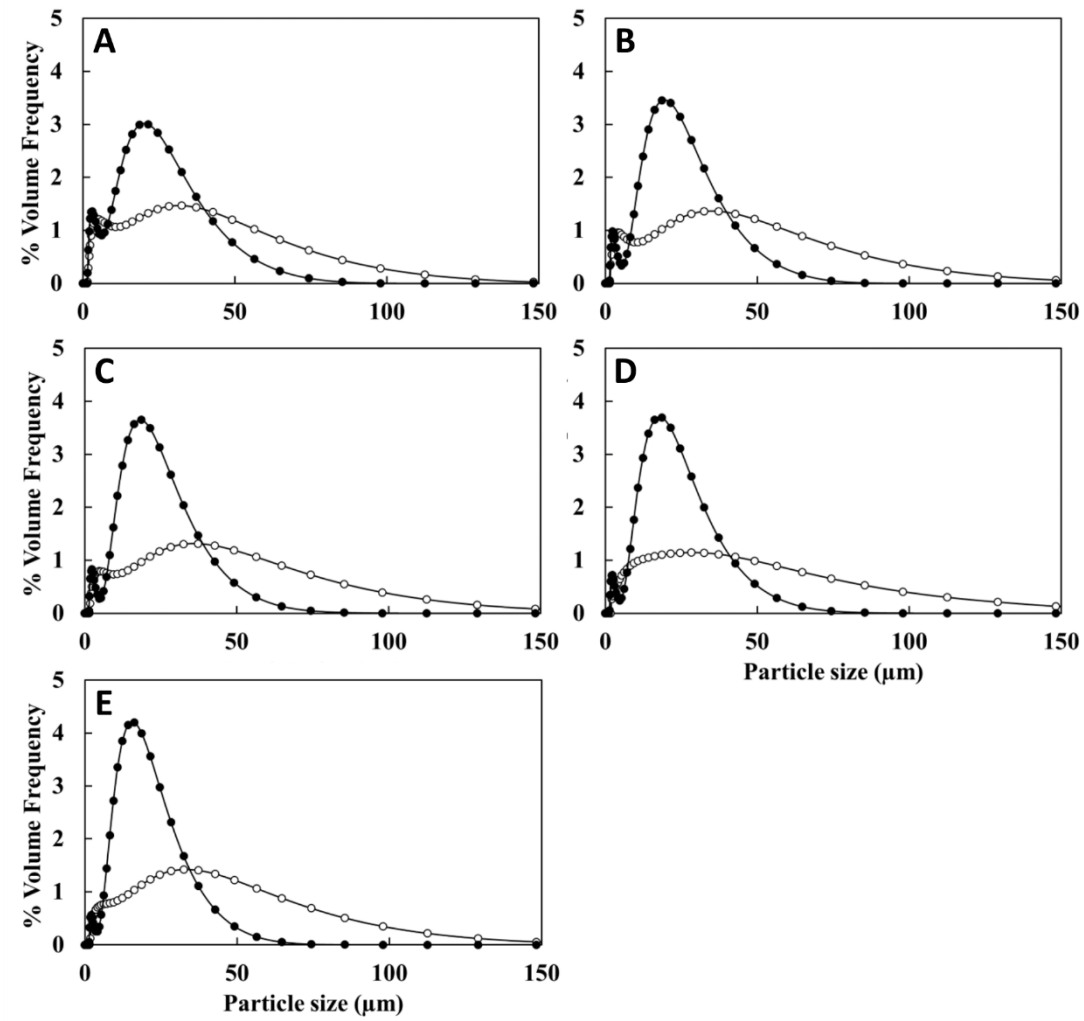

Figure 2.15: Comparison of the PSDs between floc sizes obtained in the ○ - microfluidic chip and ● - bench-scale; with varying [PEI] (mol. wt. = 50-100 kDa). (a) 5, (b) 10, (c) 15, (d) 20, (e) 25 g kg^{-1} yeast; at 25% solids yeast homogenate, pH 7.4. Volumetric flow rate in the microfluidic chip: yeast homogenate = 75 µl min^{-1}, PEI = 85 µl min^{-1}. Average PSDs have been shown, with n=5.

A gradual shift of particles from the smaller peak (cell debris, protein aggregates, etc.) towards the larger flocculated population can be observed as the concentration increases from 5 g kg^{-1} yeast to 15 g kg^{-1} yeast; but this shift stabilises thereafter. This is because of the reduction in the charge-imbalance between the cationic polymer and anionic cell homogenate as the PEI concentration reaches 15 g kg^{-1} yeast, and hence, increase in the rate of flocculation (Barany and Szepesszentgyörgyi, 2004; Gregory and Barany, 2011; Salt *et al.*, 1996). The shift in the peak also demonstrates the change in the mechanism of flocculation, where a

low surface site coverage of the colloidal particles by the flocculant (5 - 15 g kg^{-1} yeast) leads to the destabilisation of the particles, whereas at higher surface site coverage (at 20 - 25 g kg^{-1} yeast), the colloidal particles are sterically stabilised (Barany and Szepesszentgyörgyi, 2004).

In the µ-flocculation device, the flocs seem to belong to a more homogenous population with a wide span, indicating high polydispersity at low shear rates. As a result, the flocs grow continuously with considerably low levels of floc-breakage. After the point of complete fluid-homogeneity[♣] in the microfluidic device (discussed in Chapter 3), it is assumed that the yeast homogenate particles are bound to almost all the polymeric PEI strands available, thereby, leading to the formation of larger particles in the microfluidic device. PSDs of flocs formed in both the scales, under varying pH, were similar to the ones presented in Figure 2.15, with the flocs formed in the microfluidic device belonging to a wide, polydisperse population. However, the PSDs at pH 5, was an exception, with the flocs in the microfluidic device appearing in two distinct populations as observed on the bench-scale. This can be associated to the presence of acid-precipitation of colloids at pH 5. The PSDs at different pH can be found in Appendix A2.3, for the reader's perusal.

In the microfluidic device the presence of hydrodynamic focussing within confined spaces leads to the formation of nucleation zone around the centre of the channel. This invariably leads to a high-concentration region of the oppositely charged particles, increasing the proximity between the flocculant and cell suspension. Moreover, convective forces may play a role in helping the flocculants overcome the charge barrier of the colloidal suspension, in this nucleation zone. This is distinctively different from the concentration pattern found in a bench scale system, where tube inversion ensures a homogenous spread of the opposing species over a larger surface area.

2.3.7 Zeta potential analysis of flocs

The microfabricated channels must ensure that the microenvironment presented for the formation and growth of flocs are similar to that of the bench scale, and it is essential to ensure a similar flocculation environment, as the mobility and, thereby, the ζ potential, may have been modified as a result of various factors mentioned in the Section 2.3.1.2. The flocs from the outlet of the device were directly introduced

[♣] Fluid homogeneity is defined as the condition where fluids with multiple streams within the microchannels, mix completely through diffusion or convection.

into the cuvette using PTFE tubing (ID = 0.8 mm), similar to the schematic presented in the Figure 2.1.

The zeta potential values of the flocs formed in the two scales were compared, and from parity analysis, the ζ potentials, measured at bench scale and the microfluidic device over a pH range of 5 to 7.5 demonstrated a linear correlation, with an R^2 value of 0.96, as shown in Figure 2.16.

The point of zero mobility was measured to be between pH 7.0 and 7.5 and the decrease in the ζ potential values with increase in the pH indicated the increased energy-stabilisation of the PEI strands to suit flocculation in accordance to Mészáros *et al.* (Gregory and Barany, 2011; Mészáros *et al.*, 2004). This is also supported by the increasing floc size as demonstrated in Figure 2.13. This energy stabilisation of PEI leads to an increase in the electrostatic attraction in the micro-environment and higher surface site coverage, thereby enhancing the rate of flocculation.

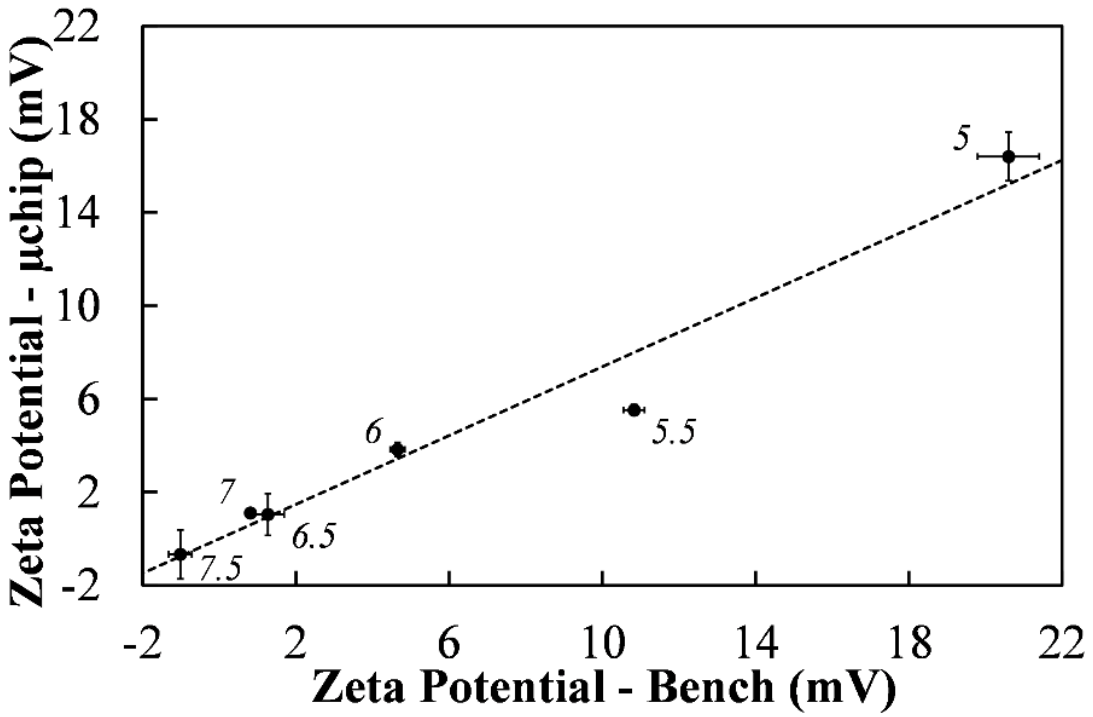

Figure 2.16: Parity analysis between the microfluidic chip and the bench scale with varying pH (5 - 7.5, data labels); at [PEI] (mol. wt. = 50-100 kDa) = 20 g kg^{-1} yeast. y = 0.74 x; R^2 = 0.96. Volumetric flow rate in the microfluidic chip – yeast homogenate = 75 µl min^{-1}, PEI = 85 µl min^{-1}. Bench - bench scale and µchip - microfluidic chip. Error bars indicate ± 1 σ, n = 3.

A strong linear correlation in the ζ potential values, between the two scales, was also observed with varying PEI concentrations (5 – 25 g kg^{-1} yeast) at a constant pH of 7.4, with R^2 = 0.99 (Figure 2.17).

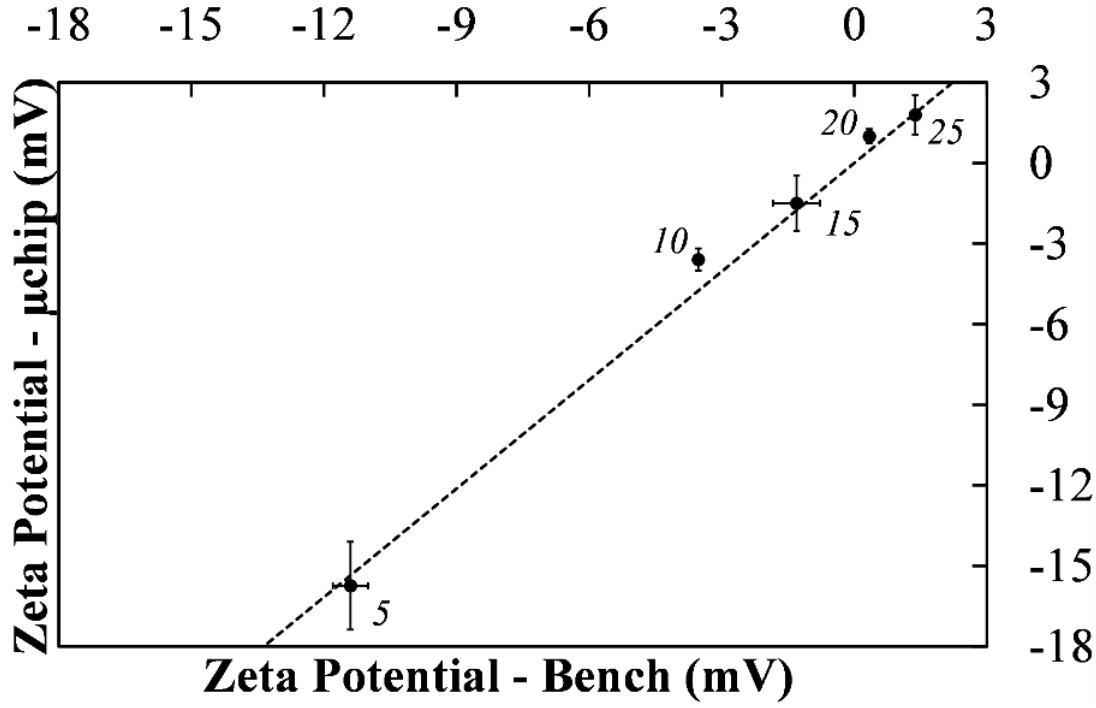

Figure 2.17: Parity analysis between the microfluidic chip and the bench scale with varying [PEI] (mol. wt. = 50-100 kDa) = 5 - 25 g kg^{-1} yeast (data labels); at pH 7.4. y = 1.35x; R^2 = 0.99. Volumetric flow rate in the microfluidic chip – yeast homogenate = 75 µl min^{-1}, PEI = 85 µl min^{-1}. Bench - bench scale and µchip - microfluidic chip. Error bars indicate ± 1 σ, n = 3.

The isoelectric point was observed to be between 15 g kg^{-1} yeast and 20 g kg^{-1} yeast. This is also in agreement with the variation of floc size shown in Figure 2.14 and PSDs shown in Figure 2.15, where the shift in the peak at 3 µm is stabilised between PEI concentrations of 15 and 20 g kg^{-1} yeast. As anticipated, this shows that flocculation takes place at both zero and non-zero mobility values, and that maximum flocculation takes place as the ζ potential values approach zero as documented in literature. However, it is noted that a complete parity wasn't observed between the two scales (observed by the more negative ζ potential values in the µ -flocculation device), due to the difference in the measurement setup and also possibly due to the difference in the flocculation systems. The outlet of the µ-flocculation device was connected directly to the cuvette in the Zetasizer, where the flow was stopped just before a measurement. Furthermore, a focussed flow within

this device leading to the formation of larger flocs could have led to the depletion of the cationic flocculants in the liquid bulk. In contrast, samples taken from a batch-mode centrifuge tube ensured a homogenous concentration of the flocculant. With smaller floc sizes recorded in the bench scale, the presence of more cationic flocculant in the liquid bulk can be attributed to the slightly more positive ζ potential values in the bench scale system.

2.4 Integration of the µ-flocculation device on to a microscope for optical image analysis

With the initial flocculation attempts proving successful, the development of an appropriate analytical tool was focussed upon, in an effort to measure the floc size in real-time, *in situ*. As previously discussed in Section 2.3.5.1, the laser diffraction instrument, like other conventional equipment, has its operational limitations in spite of being accurate, for e.g. requirement of manual sample-handling, sample dispersion, and most importantly the inability to measure growth of flocs from the µ-flocculation device, thereby, losing valuable kinetics information. Using a conventional microscopy setup facilitates the observation of flocs spatially along the spiral microchannels, thereby, providing access to record flocs as they grow. The development of a bespoke analytical methodology has been discussed in Chapter 4.

As shown in Figure 2.18, the device was placed on an inverted microscope, and a flocculation experiment was trialled with yeast homogenate and 20 g PEI kg^{-1} yeast. Flow rates of 75 and 85 µl min^{-1} for the yeast homogenate and the PEI inlets respectively, were adopted and flow was stopped before taking still images using a monochromatic CCD camera (Basler Scout scA1400 – 17fm, Basler AG, Germany).

The images were then converted to binary using the ImageJ software (Schneider *et al.*, 2012) with an automatic thresholding feature (Figure 2.19). Floc sizes were measured manually using the “freehand selection” tool and the average diameter calculated was around 123.7 ± 65 µm, from 10 flocs identified. This method of image analysis has several advantages, over the laser diffraction technique, but only if this process is automated to identify, distinguish, and measure flocs robustly.

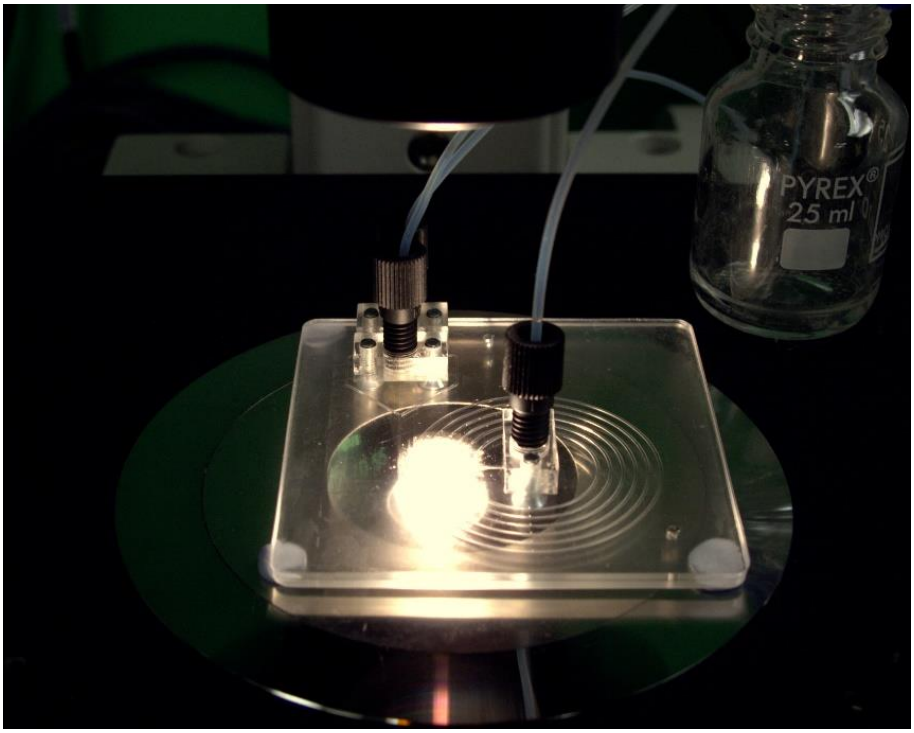

Figure 2.18: An image of the μ-flocculation device mounted on to an inverted microscope (Nikon TE-2000, Nikon UK Ltd., UK), with the ability to capture real-time images of flocs along multiple points along the microfabricated channels.

This avoids manual measurements prone to errors and drastically reduces the time taken for analysis. The development of such a computational script has been discussed in Chapter 4, and the trials performed here, proves the feasibility of a microfluidics – image analysis platform for the study of flocculation growth kinetics.

2.5 Conclusions

It has been demonstrated in this chapter that the implementation of a microfluidic device to study flocculation has shown considerable promise as an experimental platform, and has the potential to facilitate a real-time monitoring of flocs when applied with appropriate analytical methodology. It is known that the process development of flocculation in the larger scales has been difficult and time-consuming, owing to the sensitivity of the mechanism of flocculation to several physico-chemical parameters. Moreover, relying on conventional analytical equipment, leads to a loss of valuable growth kinetics information. Fabrication of a flocculation-suitable microfluidic device was observed to tackle both the

aforementioned issues, where it can potentially enable a dynamic *in situ* monitoring of flocs rapidly, with simple optical analytical tools.

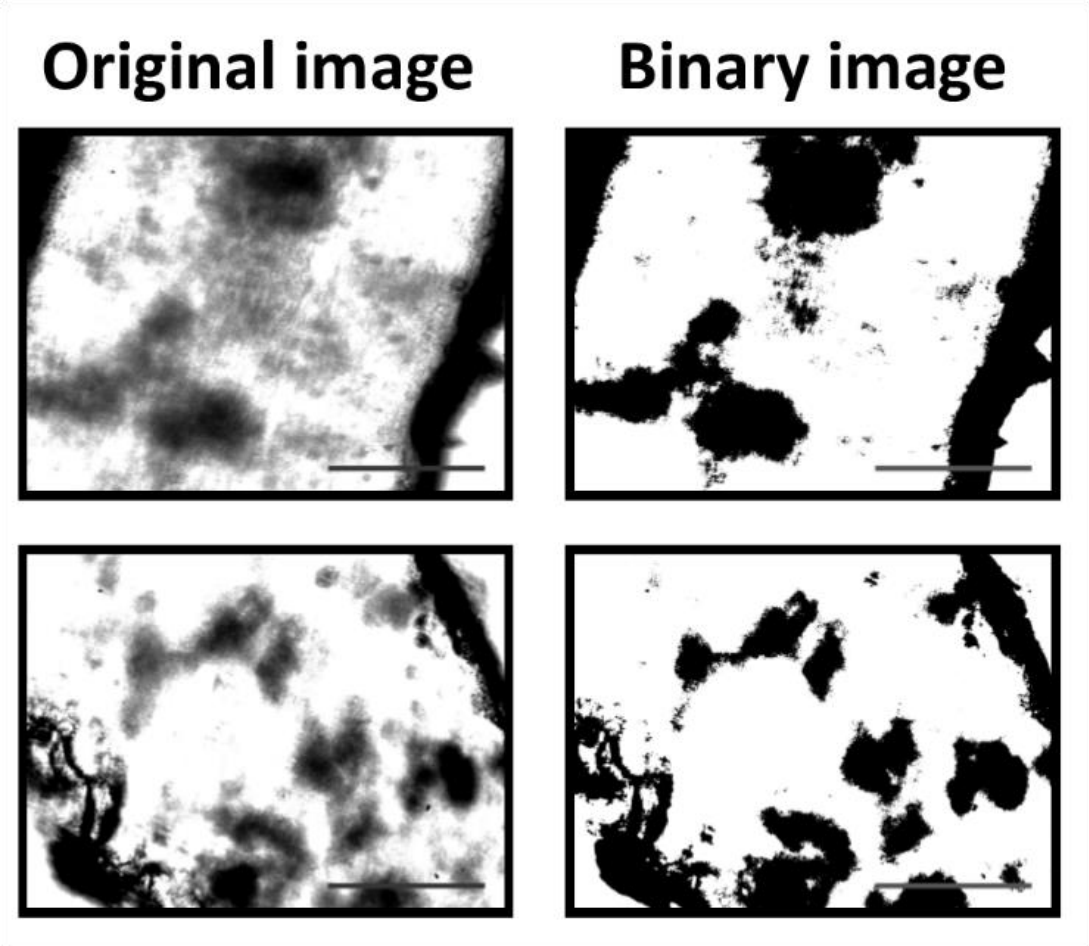

Figure 2.19: Images of flocs within the µ-flocculation device. Flocculation was performed with yeast homogenate and 20 g kg^{-1} yeast, with volumetric flow rates of yeast homogenate = 75 µl min^{-1}, PEI = 85 µl min^{-1}. The images were taken (at the outlet of the device) using an inverted microscope (Nikon TE-2000, Nikon UK Ltd., UK) with a monochromatic CCD camera (Basler Scout scA1400 – 17fm, Basler AG, Germany). Images were thresholded to a value of 130 using ImageJ software (Schneider *et al.*, 2012) *and the size of flocs were measured manually. Scale bars represent 200 µm.*

The idea of using microfabricated channels to analyse particle-aggregation seemed counterintuitive due to many anticipated challenges, like overcoming channel-clogging, and scalability issues. Of the two designed devices, the spiral microfluidic device was well-suited, as the lack of channel-bends or intersections led to a relatively slower clogging, while accommodating long channel-lengths for relatively long residence times. As evidenced in this chapter, micro-milling was the best-

suited method to fabricate the microchannels on PMMA substrate (which was chosen because it is optically transparent, easy-to-fabricate, and bonds well by thermo-compression). Thermo-compression bonding between two PMMA substrates gave a relatively strong bond strength, and together with a strong fluidic-interconnection, the device was capable of handling the volumetric flow rates chosen to study flocculation.

Comparison of the spiral µ-flocculation device to conventional bench set up, to study yeast homogenate revealed a significant difference in the size of flocs formed in the two scales, with the flocs from the µ-flocculation device being much larger. This strongly indicated the need for a more in-depth understanding of the fluid hydrodynamics within the system, which is discussed in Chapter 3. PSDs of the flocs illustrated the presence of a homogenous population of flocs with a wide span, suggesting lower shear rates. The levels of shear rates would need quantification as well, to compare the µ-flocculation device with other conventional flocculation setups. This may not be a straight-forward step, because the microfluidic device under consideration is a continuous steady-state system, unlike most bench-scale flocculation rigs.

Zeta potential measurements confirmed that the microenvironment for floc-formation in both scales were similar; indicating the applicability of microfabricated channels for flocculation studies.

As the device reported here was fabricated as a first attempt at studying flocculation, there is significant room for improvement, like choosing a different substrate like glass and adopting appropriate fabrication methodologies for glass-etching. While this substrate carries similar optical properties as that of PMMA, a glass-fabricated device would then need careful-handling. A more detailed analysis on the possible device improvements has been discussed in Chapter 7.

In conclusion, convincing evidence was obtained with regards to the use of microfluidics as a platform to study flocculation in an effort to elucidate the growth kinetics information for a faster and cheaper process development. But the platform would remain incomplete, if appropriate analytical technologies that can exploit the advantages offered by microfluidics aren't employed. Therefore, an optical microscopy methodology was tested manually and it provided assuring results, and hence, this methodology would be developed further (Chapter 4) to accommodate real-time, *in situ* monitoring of flocs with an automated floc-size analysis script.

3. Hydrodynamic characterisation of the spiral microfluidic-flocculation device

The work discussed in this chapter deals with the investigation of fluid-diffusion patterns within the spiral microfluidic (µ-flocculation) device presented in the previous chapter. This was performed to understand the hydrodynamics in the device as it was critical to understand how particles in the fluid stream diffuse and attain homogeneity. Fluid flow patterns within microfluidic channels can be characterised by estimating three interrelated factors, namely – the fluid-mixing pattern, the residence time distribution and the state of aggregation in the system. Generally, a good idea can be obtained by measuring the fluid-mixing pattern and how long particles spend inside the device (residence time distribution) (Fogler, 1999). The aim of this work was to attain a better idea of how the flocculating agents mix with the yeast homogenate stream.

The experimental work was supported by simulations using finite element modelling (FEM), which solved the Navier-Stokes for the analysis of fluid flow, within the microfabricated channels. The simulations also provided information regarding the shear rates within the microchannels, and the presence of secondary flow forces under a laminar flow regime.

The script to measure the experimental mixing time was adapted for the quantification of mixing times in a microbioreactor, and the resulting work has been published in a peer-reviewed article (Kirk *et al.*, 2016).

3.1 Introduction

3.1.1 Experimental investigation of advection through quantitative estimation of the concentration of coloured dyes

Fluid mixing is one of the important parameters, along with fluid transport and chemical reactions that needs to be well-understood to fully realize the advantages offered by a microfluidic device (Jensen, 1998). In order to estimate the point of complete homogeneity in the µ-flocculation device, fluid-advection was studied, through the flow-visualisation of dyes which is known to be one of the most used and accurate techniques (Hessel *et al.*, 2005; Nguyen and Wu, 2004). Having a simplified system devoid of any aggregating colloidal molecules (unlike a flocculating system), diffusion of a fluorescent dye that is well-documented for devices with small dimensions (up to *ca.* 100 µm depth) was initially tested. This

was followed by experimentations using a coloured dye that absorbs light in the visible wavelength.

For a system expected to have a laminar flow profile, mixing is usually brought about by advection (convection + diffusion). Since convection and diffusion are two competing parameters, it was essential to know the dominant force between the two that can eventually alter the rate of flocculation.

Measurements of light intensity profiles were made at discrete points along the channel length, in the direction of flow. Mixing length (Z_{mix}) was calculated as the point in the direction of fluid-flow at which the concentration of the dye reaches 95 % homogeneity across the cross-section of the channel (Melton *et al.*, 2002; Tan *et al.*, 2011). Mixing time (t_{mix}) can, therefore, be calculated from Z_{mix} at the corresponding fluid velocity. Mixing time is a more practically relevant parameter and is a direct indicator of fluid mixing. Although a realistic flocculation system encounters electrostatic interaction between colloidal particles and a presence of large aggregating particles, both of which affect fluid-flow, mixing time was measured in a simplified manner that was comparable with results from computational fluid dynamics and also work from literature (Lee *et al.*, 2006; Wu and Nguyen, 2005).

3.1.1.1 Fluorescein – NaOH system

Fluorescein (mol. Wt. 376.3 $g.mol^{-1}$) belongs to the xanthene dye family and attains a quantum yield of ~1.0 above pH 10 (maximum fluorescence), and remains steady thereafter (Voldman *et al.*, 2000). For this reason, attempts to observe diffusion of Fluorescein solution in NaOH were performed to understand the diffusion pattern within the µ-flocculation device. Observation of diffusion patterns in small dimension channels (between 50 – 100 µm width or depth) have been widely studied using the fluorescence imaging method (Knight *et al.*, 1998; Voldman *et al.*, 2000). Therefore, flow-visualisation of a fluorescing molecule was put to test, to check its feasibility for channels with larger channel depths (500 µm).

3.1.1.2 Allura Red – water system

A coloured dye like Allura Red has been used effectively for the determination of the rate of advection, including three-dimensional channel profiling (Broadwell *et al.*, 2001) and also for calculating diffusion coefficients (Werts *et al.*, 2012). Allura Red AC (mol. Wt. 496.4 $g.mol^{-1}$) is a red azo dye, which was chosen based on its ease

of availability, stability in water between pH 5-9 for consistent results, and its strong red hue, instead of shades of other colours.

3.1.2 Calculation of Residence Time Distribution using a step injection of a tracer

The fluid-mixing pattern provides an indication of how early or late given specie attains complete homogeneity within the microchannels; and this has been evaluated through the measurement of the mixing time (t_{mix}). Simultaneously, it is critical to know how long the molecules spend inside the channels under experimental conditions. In continuous flow processes, the temporal behaviour of particles can be characterized through the residence time distribution (RTD). Any deviations of residence times of parts of a mixture from the mean value will be reflected in the RTD, and thereby the mean residence time (t_m). Deviations can occur in reality due to the presence of stagnant zones, or even the potential adsorption of the tracer on the walls of the system (Bodla *et al.*, 2013; Fogler, 1999; Groβ and Koöhler, 2010; Levenspiel, 1999). In a laminar flow system, with convective mass transfer, the mean residence time is generally longer than the calculated residence time (volume divided by the average flow rate). Therefore, analysis of an RTD curve provides an indication of dispersion occurring in the device, making the particles spend a longer time in the microchannels.

3.1.3 Computational Fluid Dynamics using Finite Element Modelling

3.1.3.1 User-controlled meshing

Fluid flow in the μ-flocculation device was modelled using COMSOL Multiphysics 4.4.0.248 (COMSOL, Cambridge, UK). For performing finite element modelling to extract data about the laminar flow profile, the channel geometry had to be partitioned into several small units called the 'mesh elements', within which the equations are solved and carried over to the following elements (in case of a linear solver). Microchannels with a spiral design can pose a challenge in having an appropriate definition of the mesh elements, especially along the curvilinear edges that can result in the accumulation of 'solver errors', and lead to the failure of the simulation. Different mesh patterns of varying element sizes were tested, and the results were then compared with the experimental Z_{mix} results. Velocity, shear rate and pressure in the device at specified parameters were solved using the Navier-Stokes equation under laminar flow.

3.1.4 Calculation of shear rates within the microfluidic channels

Shear is one of the most important parameters affecting the process of flocculation (Gregory, 1988), that ultimately decides the strength of the flocs, and also its resultant shape and size. Efforts to study the effect of shear on flocs, or alternatively termed as the 'floc-strength', have been carried out using different techniques, as outlined in the review paper by Jarvis *et al.* 2005. However, as the aim of the work in this thesis, involved the study of the growth of flocs (by isolating it from floc-breakage), the shear rates had to be quantified as well. Results from the laminar flow solutions in the finite element model using COMSOL, provided valuable information regarding the shear rates prevalent in the microchannels at the specified flow rates.

3.2 Materials and Methods

3.2.1 Quantitative fluorescence measurements of Fluorescein

Fluorescein (F6377 Sigma Aldrich, Gillingham, UK) was dissolved in 0.1 M NaOH (~pH 13), to final concentrations of 0.002, 0.02, 0.125, 0.2, 0.25, 0.5, 1, 2, 6, and 20 µg ml^{-1}. The µ-flocculation device was mounted on to the motorised stage (MEC56110, Nikon UK Ltd., UK) of a Nikon Eclipse Ti-E inverted microscope (Nikon UK Ltd., UK). A motorised microscope stage was used to accurately control the x and y coordinates, for briskly moving to specific x-y coordinates in a repeatable manner. Flow of fluorescein was imaged using an LED fluorescent excitation system (CoolLED pE-2, CoolLED, UK), at 470 nm excitation wavelength (*ca.* 97 W, for single LED wavelength) and a GFP filter. Images were recorded using a colour CCD camera (DS Fi-1, Nikon UK Ltd., UK) at three different exposures of 10, 15 and 30 ms, and manual white balance with a pixel gain of 1.0.

Two KDS200 Infuse/Withdraw Programmable Syringe Pumps (KD Scientific Inc., Massachusetts, USA) were used to drive two Hamilton 1010 TLL glass syringes (Hamilton Company, Nevada, USA) carrying Fluorescein and 0.1 M NaOH. Images were captured at fixed cross-sections along the length of the channels. Extraction of pixel data was performed using the ImageJ software (Schneider *et al.*, 2012), and the results were analysed manually.

3.2.2 Quantitative absorbance measurements of Allura Red

Allura Red AC dye (Sigma Aldrich, Gillingham, UK) was prepared in type 1 ultrapure water (MilliQ, Merck Millipore, Massachusetts, USA) to final concentrations of 0.25,

0.5, 1, 2 and 4 mM. Experiments were performed as mentioned in the previous section (Section 3.2.1), substituting the light source by using a halogen illumination at 30 W, in the place of the fluorescent excitation system. Experiments (after calibration of the concentration with optical density) were performed in triplicates and image analysis was performed using a computational script in Python (Oliphant, 2007; van der Walt *et al.*, 2011; van Rossum, 1995), to calculate mixing times based on absorbance values.

3.2.3 Estimation of mean residence time through step-injection of a tracer

RTD within the μ-flocculation device was measured using a UV absorbance instrument (ActiPix D100, Paraytec, York, UK). A 200 mg l^{-1} solution of L-tryptophan (Sigma Aldrich, UK) as a tracer, was prepared in type 1 ultrapure water and the outlet concentration profile was measured using the ActiPix instrument in real-time with a 254 nm UV filter with 12 nm bandwidth (254BP12, Omega Optical Inc., USA). Fluid was injected into the device *via* neMESYS syringe pump (Cetoni GmbH, Germany) at 75 μl min^{-1} for the focussed flow and 85 μl min^{-1} for the sheath flow. A step-injection involves the injection of a fixed concentration of the tracer (C_0) initiated at time = 0 s. The device was purged completely with water to ensure the complete absence of the tracer in the microchannels. Therefore, symbolically, the concentration of tryptophan can be depicted as (Fogler, 1999):

$$C_0(t) = \begin{cases} 0; & t < 0 \\ C_{0,constant}; & t \geq 0 \end{cases} \quad (3.1)$$

To aid the accurate injection of the tracer, 4mM Allura Red dye was also mixed with the solution. Measurements were continued until the UV absorbance reading reached a steady state.

3.2.4 Computational Fluid Dynamics using COMSOL

Flow of Allura Red dye within the μ-flocculation device was modelled through a finite element method using COMSOL Multiphysics 4.4 (COMSOL, Cambridge, UK). A 3D model of the microchannel was designed using the SolidWorks® 2011 software, and then imported into COMSOL as a ".stl" file. As mixing was expected to be complete within 140 mm from the ψ-shaped channel inlet, based on experimental information, and to have very fine mesh elements with a feasible memory usage, only one complete spiral (outermost, radius = 21 mm) was created. The method adopted, to achieve a successful creation of a mesh network, was to break down parts of the channel into smaller units. Firstly, four different work planes were

added at z-axis depths of 0, 0.25, 0.375 and 0.5 mm as shown in Appendix A3.1. The T junction at the sheath-flow inlet was split by adding a parametric surface. A cuboidal block was then added at the ψ-shaped inlet, to reduce the complexities that arise from a multi-inlet junction where improper meshing can be encountered. Further, line segments (called 'extract edges') were created to enable the extraction of data at specific cross-sections and specific lengths, post completion of the fluid dynamics study. The faces at z = 0 mm were selected and extruded onto the other three work planes previously created. Finally, all the added structures and work planes were integrated onto the original *".stl"* file by forming a union.

Physics of laminar flow was solved to obtain information regarding the velocity, pressure and shear rates, and the module was discretised linearly. Flow rates used for the experimental mixing time estimation were adopted (focussed flow = 75 µl min^{-1} and sheath flow = 85 µl min^{-1}).

3.3 Results and Discussion

3.3.1 Evaluation of fluid-mixing using a Fluorescein-NaOH system

Different concentrations of Fluorescein (as mentioned in Section 3.2.1) were tested in the µ-flocculation device with a channel depth of 500 µm. This was not straight-forward, as the width of the focussed flow (which is an indicator of mixing time for hydrodynamic focussing inlets; Appendix A3.2) seemed to vary, as shown in Figure 3.1a.

As expected, the fluorescence values (pixel intensity) increased with increasing concentration of the dye, and provided a sharper gradient at the fluorescein - NaOH interface. However, as shown in Figure 3.1b, increasing concentrations led to narrower troughs (depicting the non-fluorescing NaOH stream) with non-zero pixel values. This can be attributed to the effect of fluorescence leaching laterally, which was picked up by the camera sensor. As seen in Figure 3.2a, there is a strong gradient of fluorescence (6 µg ml^{-1}) at the fluid interface, making it difficult to accurately estimate the width of the focussed flow. Concentrations below 0.5 µg ml^{-1} weren't quantifiable even at an exposure of 30 ms. Exposures above 30 ms weren't tested, so as to avoid streaking effects (accumulation of a large amount of photons), which can lead to inaccurate measurements. Experiments to record the diffusion of fluorescein across the channel cross-section were performed by taking images along the length of the channel. Figure 3.2a shows the fluorescein – NaOH interface at the device inlet, at two different fluorescein concentrations.

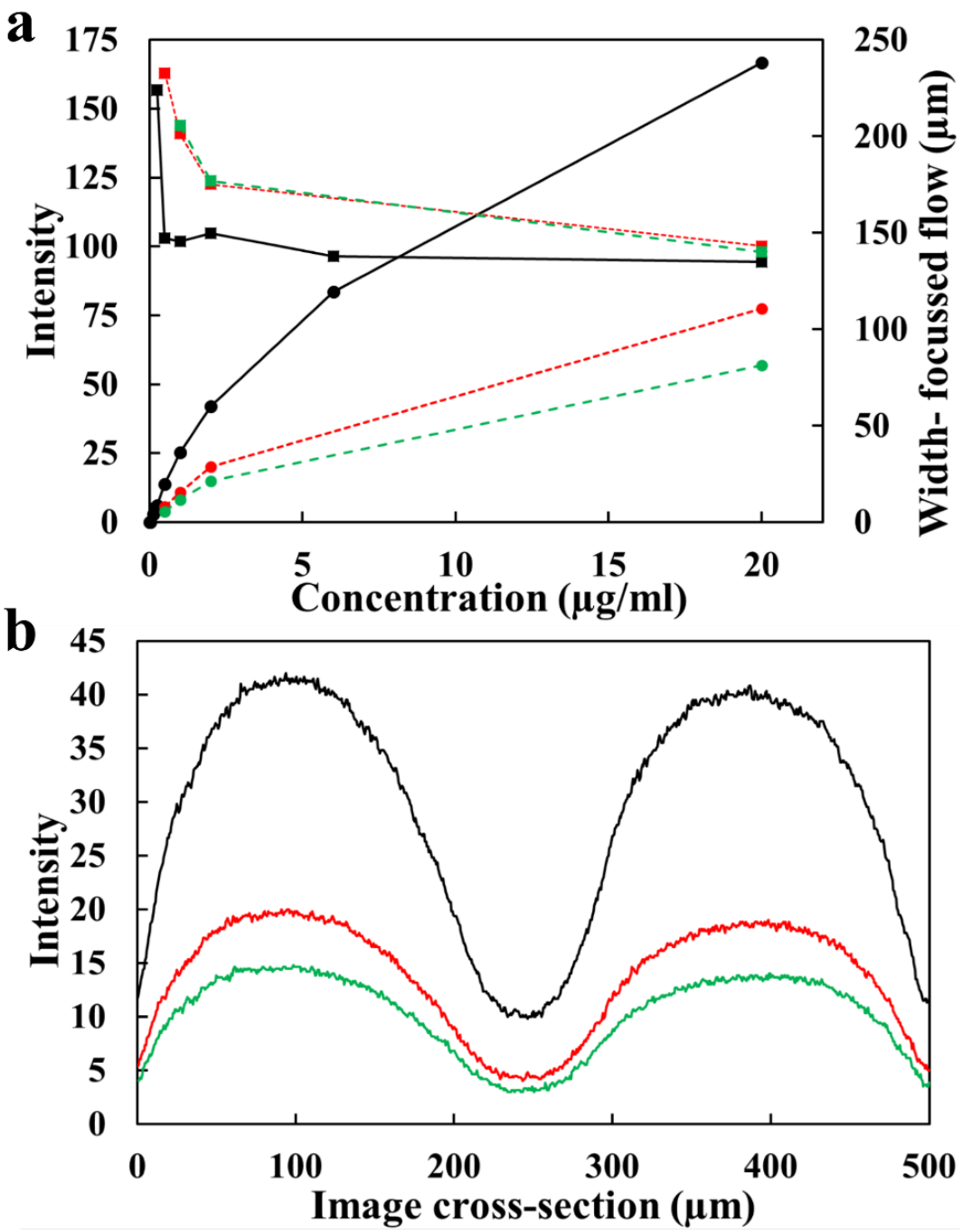

Figure 3.1: (a) Quantification of pixel intensities and corresponding theoretical-widths of focussed stream, at varying concentrations of fluorescein. Square markers depict width of the focussed stream (right y-axis) and circle markers represent intensity (left y-axis). Black – 30 ms exposure, Red – 15 ms and Green – 10 ms exposure (b) Graph represents the cross-section of the channel at the inlet, at 2 µg ml^{-1} fluorescein and different camera exposures. The images were captured at an excitation wavelength of 470 nm and a GFP filter.

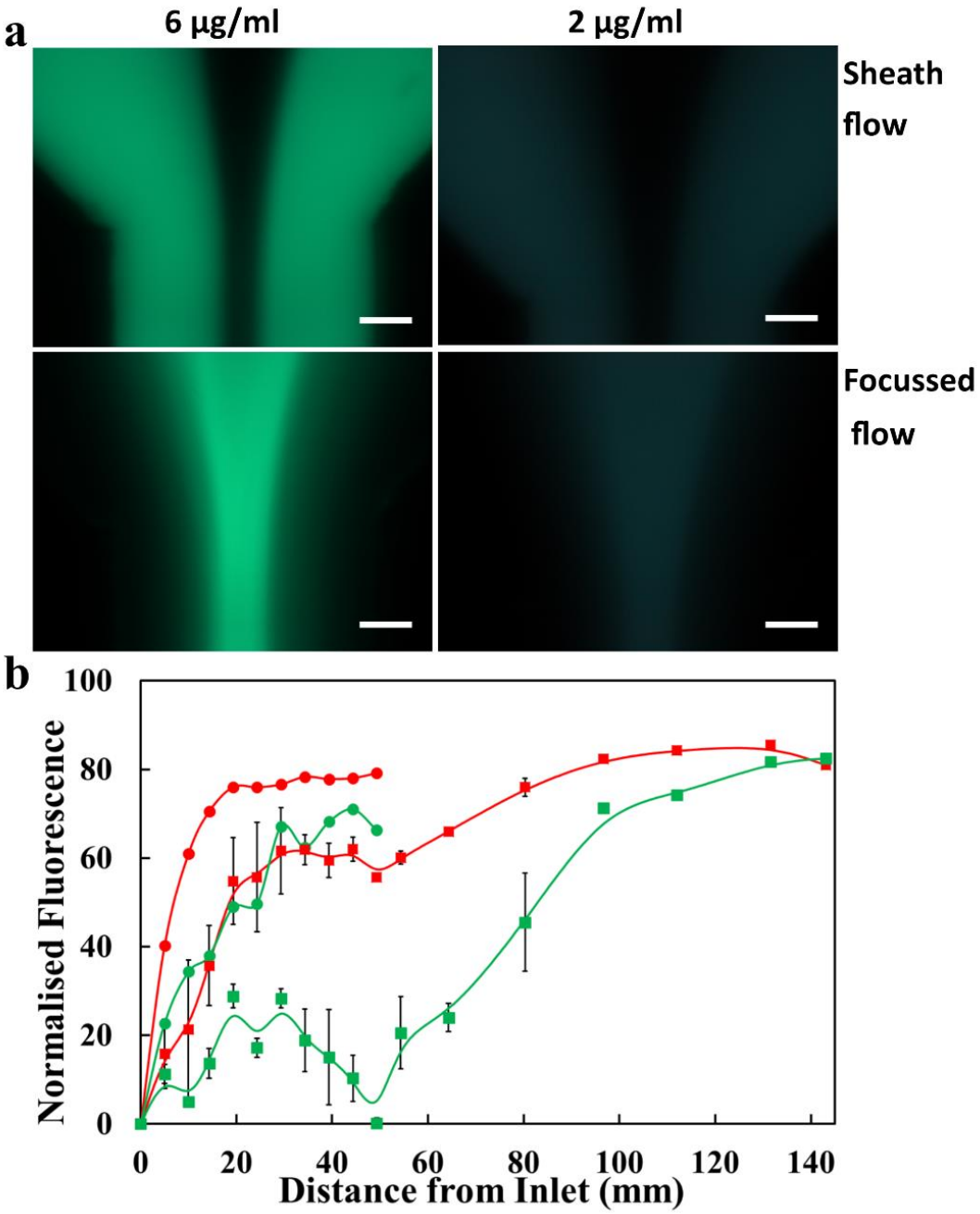

Figure 3.2: (a) Fluorescent images of fluorescein (at 6 and 2 µg ml^{-1}) in the focussed stream and the sheath stream, flowing with NaOH. Images were captured at 15 ms exposure, using a colour CCD camera (DS Fi-1, Nikon UK Ltd., UK) attached to a Nikon Ti-E microscope. Scale bars represent 50 µm. (b) Graph showing the variation of normalised fluorescence intensity along the length of the microchannel, across the entire cross-section. Circular markers depict 6 µg/ml, and square – 2 µg/ml Fluorescein. Dye in sheath flow is shown in ***red*** *and dye in focussed flow is presented in* ***green****. Error bars depict ± 1 σ, n = 2. Images were taken at specific locations, using a motorised stage, providing an accurate spatial control over the x-y coordinates.*

These provided different values for the width of the focussed flow, thereby leading to different mixing times calculated theoretically from equations reported in literature (see Equations 3.6 and 3.7 in Section 3.3.2). Measuring the mixing time accurately and reliably was difficult, particularly due to the large variation in the pixel intensity values as shown in Figure 3.2b. Pixel intensities were extracted from the images using the ImageJ software. The local maxima (the fluorescing dye section) and minima (non-fluorescing NaOH stream) were manually selected and were then normalised by calculating the ratio between the difference of the maxima and minima, and the average pixel values between the 2 local maxima (where fluorescein was in the sheath flow) or 2 local minima (where NaOH was in the sheath flow). Fluorescein at 6 μg ml^{-1}, showed a completion of passive mixing, at around 20 mm from the channel inlet. Because of the suspected fluorescence-leaching effect, trials at 2 μg ml^{-1} were performed, and the results revealed the presence of a slower mixing, in spite of the mixing being affected only by the flow rates of different streams of a ψ-shaped focussing inlet (Knight *et al.*, 1998; Walker *et al.*, 2004). An interesting observation was the fluctuation of the normalised intensity values starting from the point where the spiral begins in the microchannel. This was possibly due to the presence of secondary flow-forces that led to the lateral movement of the fluorescein molecules. The presence of secondary flow is discussed in further detail in Section 3.3.4. While the attainment of 95% homogeneity was observed at around 80 mm (at 2 μg ml^{-1}, dye in sheath flow) supporting the experiments using Allura Red, different values recorded for the dye in the focussed flow, and the trials at 6 μg ml^{-1} concentration, necessitated a more reproducible experimental setup.

Fluorescence imaging is known to provide accurate measurements in a reliable manner, but the results obtained with large channel dimensions (500 μm depth) seemed irreproducible using a conventional microscopic fluorescence imaging method. Therefore, better imaging techniques, like confocal fluorescence imaging that can be more adequate, may be implemented to obtain better results accurately. Such techniques were not attempted because it was beyond the scope of the current work.

3.3.2 Quantification of Allura Red concentration through image analysis

Following experiments with fluorescence imaging, which appeared unsuitable for devices with large channel dimensions, a simpler bright-field imaging technique with a food dye was implemented (Werts *et al.*, 2012). The following section deals with

the estimation of Z_{mix} and t_{mix} in two different ways. Firstly, Z_{mix} is calculated from the quantitative measurements of Allura Red (AR) in water. This is followed by comparison of these values with theoretical results (Z'_{mix} and t'_{mix}) from equations found in literature.

Before performing the experiment, the optical density (OD) of the dye was calibrated with increasing concentrations of AR, as shown in Figure 3.3. Because the final fully-diffused concentration of the dye in water is halved, an initial inlet concentration of 4 mM was chosen. At every imaging location (accessed reproducibly by a motorised stage), two images were taken for each trial (experiments performed in triplicates). To ensure an accurate analysis of mixing lengths, these images were processed using a bespoke script developed using the Python programming language (Hunter, 2007; Oliphant, 2007; van der Walt *et al.*, 2011; van Rossum, 1995). The sequence of analysis was adapted from the work reported by Werts *et al.* 2012 and has been explained below.

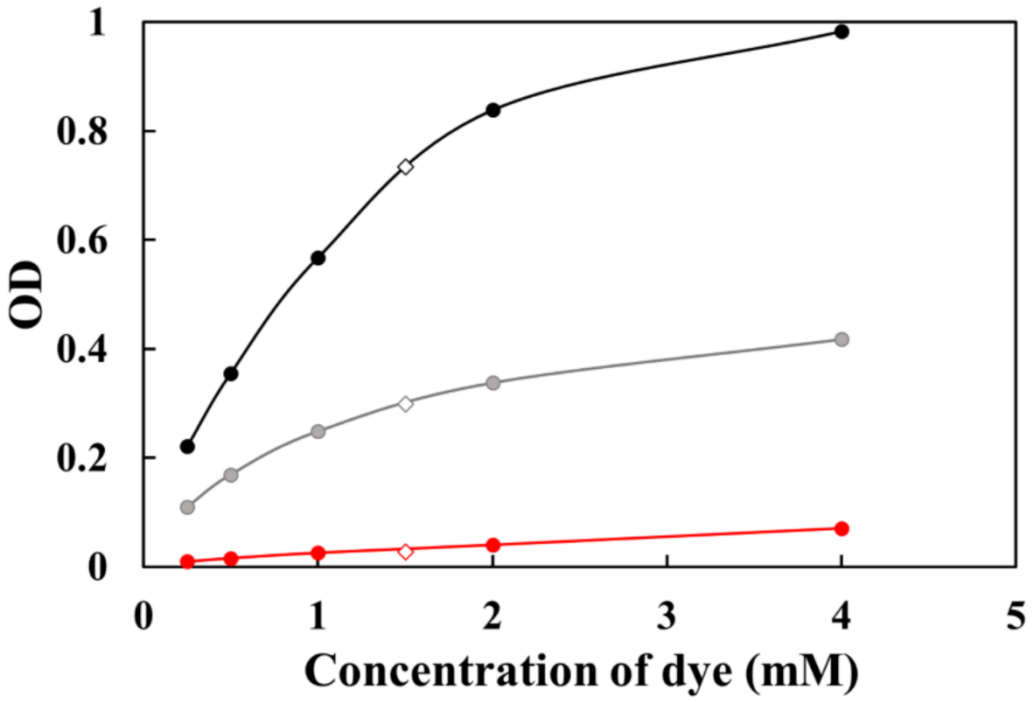

Figure 3.3: Calibration curves of Allura Red dye vs. optical density. Images were taken using the Nikon Ti-E microscope with a colour CCD camera (DS Fi-1, Nikon UK Ltd., UK). Black line represents an average OD of the blue and green channels (R^2 = 0.87), grey line depicts the OD after Luma Transform (R^2 = 0.90) and the red line shows the OD of the red channel (R^2 = 1). The open markers represent the confirmation of calibration using a 1.5 mM dye solution.

Consider the raw images taken at each location as a matrix, M, of 2560 × 1920 pixels (as shown in Figure 3.4) corresponding to sensor dimensions and pixel size of the camera used. The two images were averaged (Equation 3.2) to account for any peristaltic effects from the displacement syringe pumps, leading to variations in the width of the focussed flow.

$$\frac{M_A + M_B}{2} = M_{Avg} \tag{3.2}$$

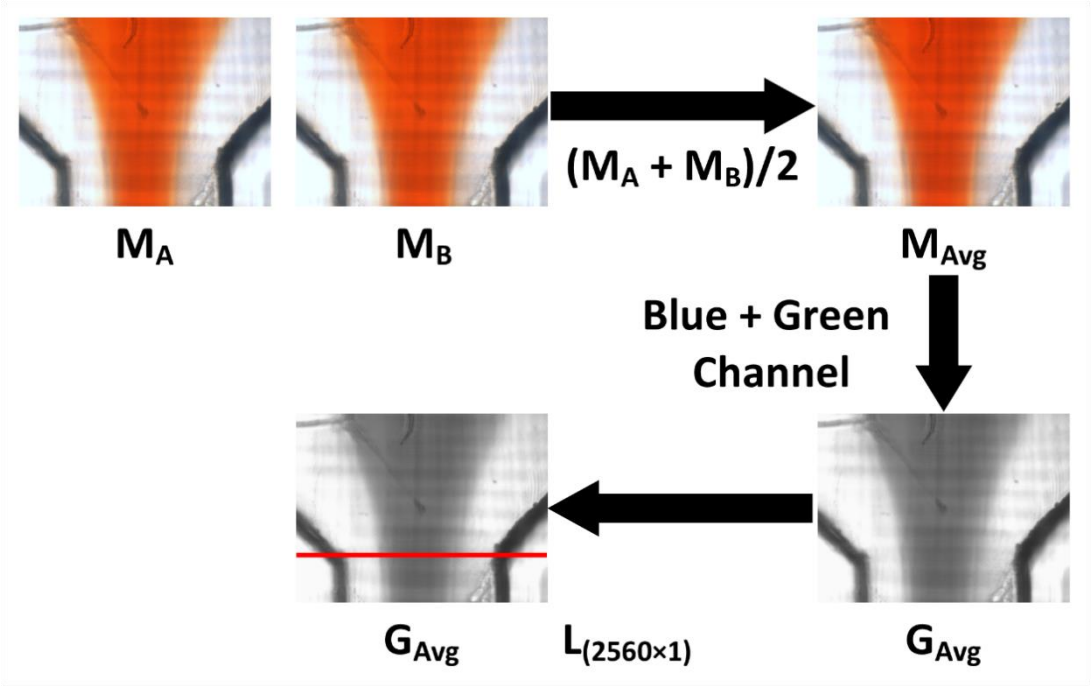

Figure 3.4: Two RGB images (M_A and M_B) of Allura Red dye flowing in the focussed stream with deionised MilliQ water were taken at each location and averaged (M_{Avg}). The red channel of the averaged pixel array is then omitted and only the average of the blue and green channels were considered (G_{Avg}) for further analysis of pixel intensities. Pixel data using a line vector was then extracted from G_{Avg} yielding a profile of the pixel value across the channel cross-section. Images were captured using a colour CCD camera (DS Fi-1, Nikon UK Ltd., UK) attached to a Nikon Ti-E microscope.

When the channel enters the spiral, the images at those locations were rotated by a certain angle (θ) to ensure that the cross-section of the channels were perpendicular to the width of the image.

The term θ is the angle of the spiral (with respect to the normal) at the corresponding point of imaging obtained from the 3D CAD SolidWorks file (Figure 3.5). As anticipated, the optical density in the red channel was near zero, because

the red dye almost completely transmitted wavelengths of light in the red spectrum. For this reason, the average of the blue and green channels were taken for further analysis, by omitting the red channel (Equation 3.3), resulting in G_{Avg} with pixel intensity values between 0 and 255.

$$G_{Avg} = \frac{(M_{Avg}^{green}) + (M_{Avg}^{blue})}{2} \tag{3.3}$$

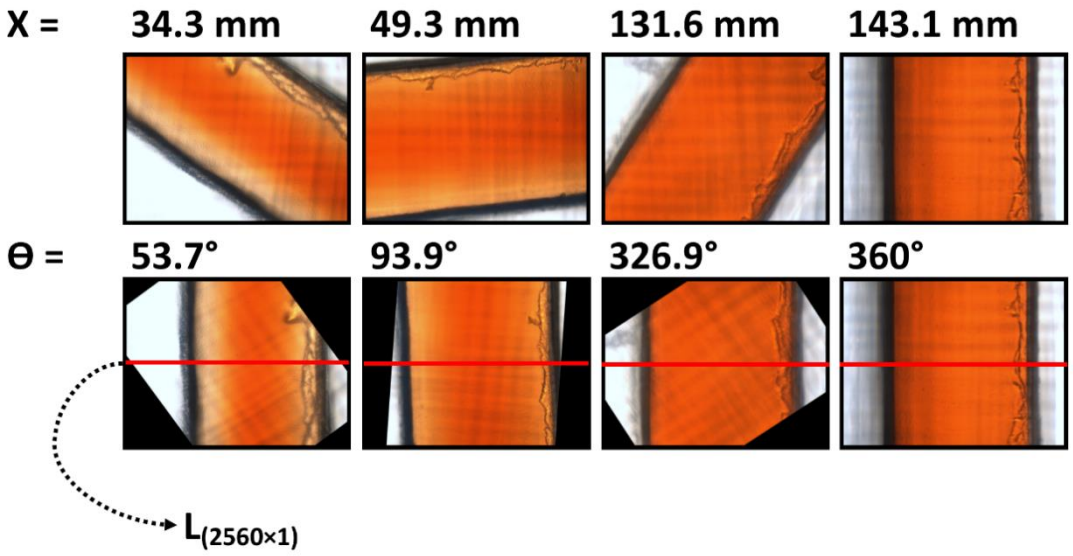

Figure 3.5: As the fluid enters the spiral, the images taken at different locations ('X' mm from the channel inlet) were later rotated to ensure that the flow direction was normal to the width of the image. The degrees of rotation (Θ) for the locations were extracted from the 3D CAD SolidWorks file. This enabled the extraction of a uniform intensity profile (using line L) that is perpendicular to the fluid flow.

Intensity values (I_{Avg}) were then extracted along the cross-sections of these images by overlaying a row vector L (2560 × 1) that is one pixel in width and 2560 pixels in length (Equation 3.4).

$$I_{Avg} = L_{(2560 \times 1)}\, G_{Avg} \tag{3.4}$$

The resulting row vectors with intensity values were then converted to absorbance A_{Avg}, providing optical density profiles (Figure 3.6), using Equation 3.5.

$$OD,\ A_{Avg} = -\log_{10}\left(\frac{I_{Avg}}{I_0}\right) \tag{3.5}$$

Where, I_0 is the maximum intensity within an image, i.e. the intensity of the image over the channel-free area. This value (I_0) was consistently around 246 ± 1 for dye in sheath flow and 250 ± 1 for dye in the focussed stream. The mixing time of the dye were then calculated from Equations 3.6 and 3.7, using these absorbance values.

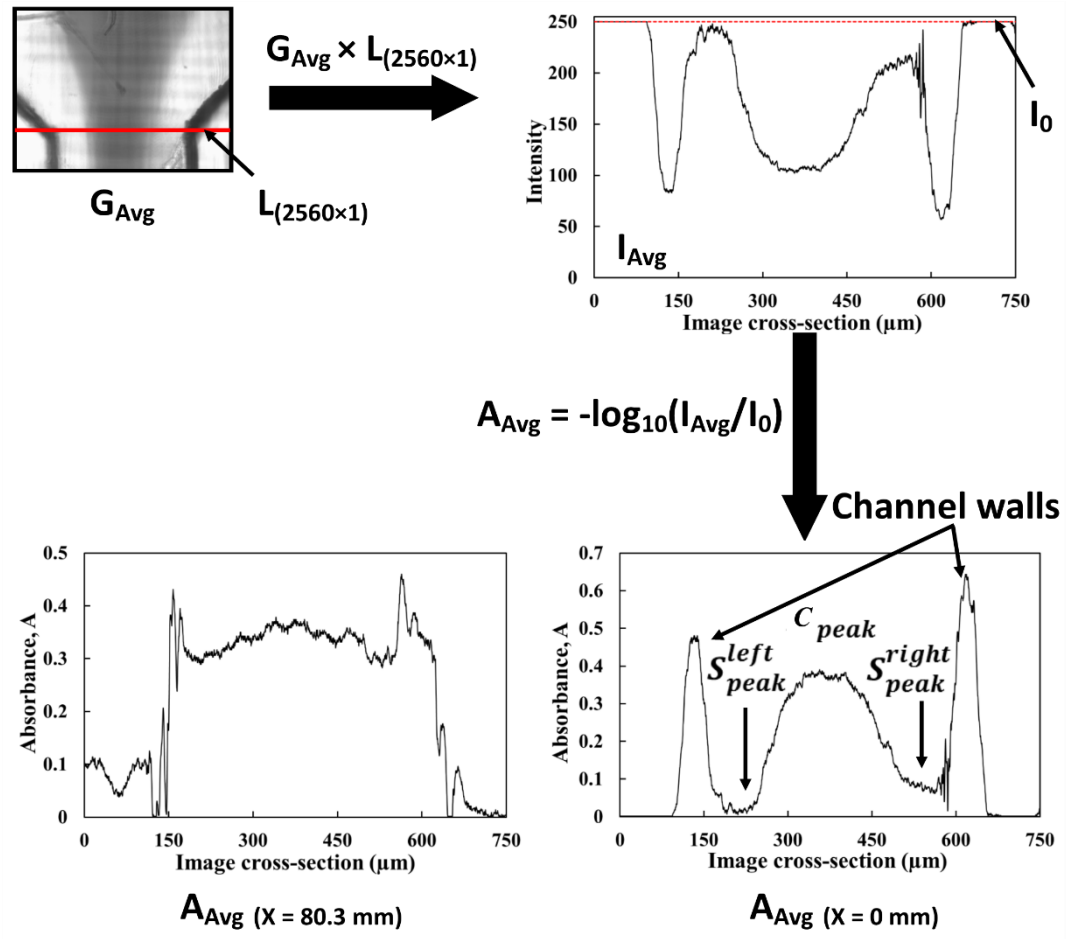

Figure 3.6: Intensity profile obtained by extracting a row vector from the G_{Avg}, which is the average of the blue and green channel. The intensity profile is then converted to absorbance values (OD), by applying a negative logarithm of pixel intensity. The S^{left}_{peak} and S^{right}_{peak} were manually chosen by selecting the local minima from the absorbance profile; and C_{peak} is the maxima between S^{left}_{peak} and S^{right}_{peak}. These values were used to calculate the extent of mixing. The peak-flattening can be observed as the fluid flows from the inlet (X = 0) down the channel (X = 80.3 mm) representing the effect of diffusion.

$$S_{peak}^{Avg} = \frac{S_{peak}^{left} + S_{peak}^{right}}{2} \tag{3.6}$$

$$\text{Extent of mixing, } \varepsilon = 1 - \left(\frac{C_{peak} - S_{peak}^{Avg}}{C_{peak} + S_{peak}^{Avg}}\right) \tag{3.7}$$

Where S_{peak}^{left} and S_{peak}^{right} were manually chosen by selecting the local minima from the absorbance profiles (Figure 3.6, X = 0 mm); and C_{peak} is the maxima between S_{peak}^{left} and S_{peak}^{right}. Therefore, as mixing progressed, it was expected that C_{peak} and S_{peak}^{Avg} attained similar values, due to an increasing homogeneity of the dye (Figure 3.6, X = 80.3 mm). This leads to the 'extent of mixing' reaching a value of 1 after attaining complete homogeneity. In this context, therefore, mixing length (Z_{mix}) is defined as the distance from the inlet, where the extent of mixing, Ɛ (Equation 3.7) reaches 95% homogeneity across the entire cross-section of the channel. This definition was adopted from previous work reported in literature, dealing with the quantitative analysis of mixing times in different systems, through the change in pixel intensities (Melton *et al.*, 2002; Rodriguez *et al.*, 2013; Tan *et al.*, 2011). From Figure 3.7, 95% homogeneity (Z_{mix}) for both dye in the focussed stream and in the sheath flow, was observed to be reached at 80.3 mm.

Similar results were observed when the G_{Avg} pixel array was created, by the grayscale conversion of the RGB M_{Avg} images, using an ITU-R 601-2 standard Luma Transform, which is the global standard used to telecast greyscale images.

The mixing time (t_{mix}) was calculated from the Z_{mix} value using the average fluid velocity at the outlet (10.7 mm s^{-1}). Therefore, the experimental t_{mix} calculated was *ca.* 7.5 seconds. This t_{mix} value of 7.5 seconds was verified by calculating the theoretical mixing time (t'_{mix}) and theoretical mixing length (Z'_{mix}). It is well established that for a hydrodynamic focussing inlet, the mixing time is dependent on the width of the focussed stream (W_f) as reported by Knight *et al.* 1998.

Channel widths were estimated from two different equations found in literature, as follows,

$$W_f = rW; \text{ where } r = \frac{1}{1+2\beta\frac{Q_s}{Q_i}} \text{ and } \beta = \frac{\eta_s}{\eta_i} \text{ (Wu and Nguyen, 2005)} \tag{3.8}$$

Where, Q is the volumetric flow rate (µl min^{-1}), η is the dynamic viscosity of the liquids with β is assumed to be 1, and 's' and 'i' represent the sheath flow and focussed flow respectively. W is the width of the channel.

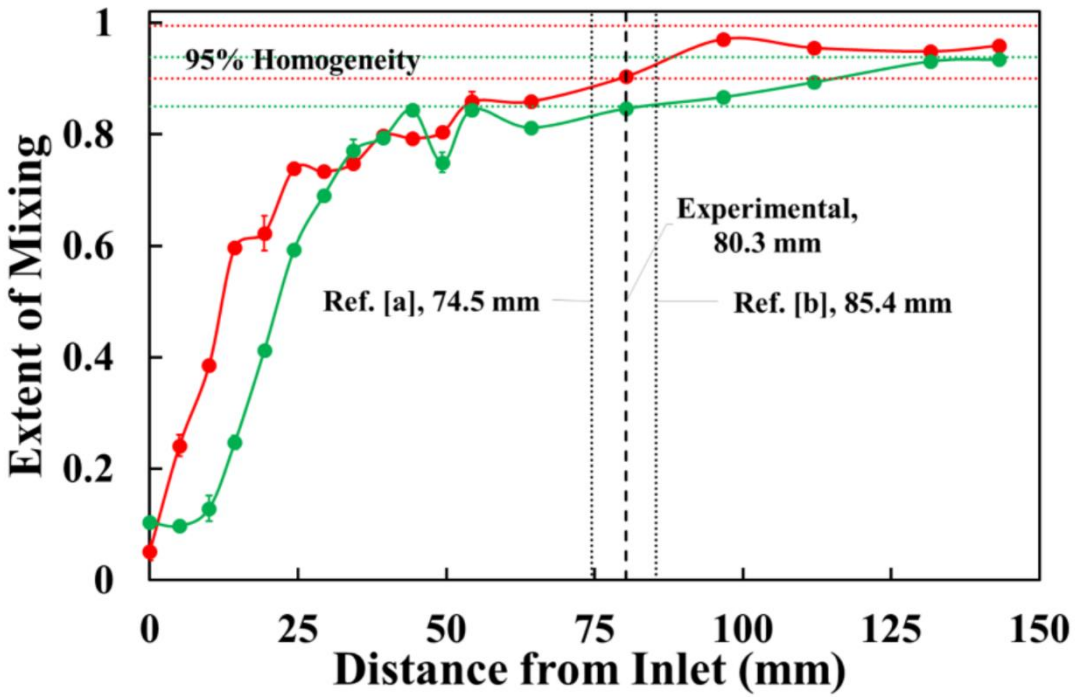

Figure 3.7: The mixing length (Z_{mix}) of 80.3 mm, obtained from the C_{peak}, S^{left}_{peak} and S^{right}_{peak} values. (●) depicts the dye in the sheath flow and (●) represents the dye in the focussed flow. The horizontal dotted lines denote the ± 5% range of the stabilised extent of mixing (Ɛ) values. Vertical dotted lines depict the theoretical mixing lengths (Z'_{mix}) of 74.5 mm and 85.4 mm obtained from references [a] – Nguyen & Wu 2005 and [b] – Lee et al. 2006 respectively. Error bars represent ± 1 σ, n = 3.

Theoretical mixing times were also estimated from the equation proposed by Lee *et al.* 2006:

$$W_f = \frac{Q_i W_o}{\frac{V_f}{V_o}(Q_i + Q_{s1} + Q_{s2})} \text{ (Lee } et\ al.\text{, 2006)} \qquad (3.9)$$

Here, W_o = W = 500 µm; Q_{s1} = Q_{s2} = volumetric flow rate of each sheath flow = 0.5(Q_s); and V_f is the linear velocity of the focussed flow and V_o - the average velocity of the outlet, estimated to be roughly around 18 mm s^{-1} and 12 mm s^{-1} respectively. The theoretical W_f obtained from Equations 3.8 and 3.9 were 153 µm and 164 µm, with corresponding mixing times (t'_{mix}) of 7 and 8 s, respectively. The t'_{mix} were calculated from the mixing time equation reported by Knight *et al.*, 1998 (Equation 3.10), and the values were in the range of the experimental mixing time of 7.5 s.

$$t'_{mix} = \frac{W_f^2}{\pi^2 D}$$ (Knight *et al.*, 1998) (3.10)

For the hydrodynamic focussing device used, Péclet numbers (P_e) of *ca*. 2401 and 2571 were obtained from Equation 3.10, for W_f of 153 µm (Equation 3.8) and 164 µm (Equation 3.9) respectively, considering 0.34×10^{-9} m^2 s^{-1} as the diffusion coefficient of AR dye (Werts *et al.*, 2012).

$$P_e = \frac{W_f V}{2D}$$ (3.11)

(Abonnenc *et al.*, 2009; Atencia and Beebe, 2005; Nasir *et al.*, 2010; Tabeling, 2009)

A Reynolds number (R_e) of 5 (assuming kinematic viscosity of water, $v = 1 \times 10^{-6}$ m^2 s^{-1}, at 20 °C) was obtained for the microchannels, confirming the presence of a fully laminar profile at the flow rates used for this study. Theoretically, as a P_e value of *ca.* 1000 times R_e is commonly seen (Nguyen and Wu, 2004), the deviation from this relation in this system can be attributed to the presence of three streams, leading to two interfaces that alters the P_e by a factor of ½ (in Equation 3.11), and also an aspect ratio of 1 for the square microchannels in the fabricated chip, thereby, having a higher hydraulic diameter unlike conventional rectangular and circular channels found commonly in literature. A value of P_e of 2493 was calculated from the experimental t_{mix} value (80.3 mm), and this showed that the mixing in the system is substantially dominated by convection (P_e above 1000, Nguyen & Wu 2005) which enhances the rate of aggregation according to Jamali *et al.* 2013.

3.3.3 Residence Time Distribution Analysis

The residence time was calculated from the RTD of tryptophan injected into the device both in the focussed flow and in the sheath flow, with volumetric flow rates of 75 and 85 µl min^{-1} for the focussed flow inlet and the sheath flow inlet respectively. For a step-injection of the tracer, the UV absorbance data (of the outlet tracer concentration, C_{out}) can be used to calculate the cumulative distribution function, *F(t)* as shown in Figure 3.8a and 3.8c. Because the concentration of the tracer is a constant, *F(t)* can be calculated by:

$$F(t) = \frac{C_{out}}{C_0}$$ (3.12)

F(t) reflects the fraction of tracer particles in the outlet stream that has spent a time less than t, in the microchannels. A differentiation of the F curve, leads to the RTD

function, which is also called the exit-age distribution, *E(t)*. This can be represented as:

$$E(t) = \frac{d}{dt}\left(\frac{C_t}{C_0}\right) = \frac{d}{dt}F(t) \tag{3.13}$$

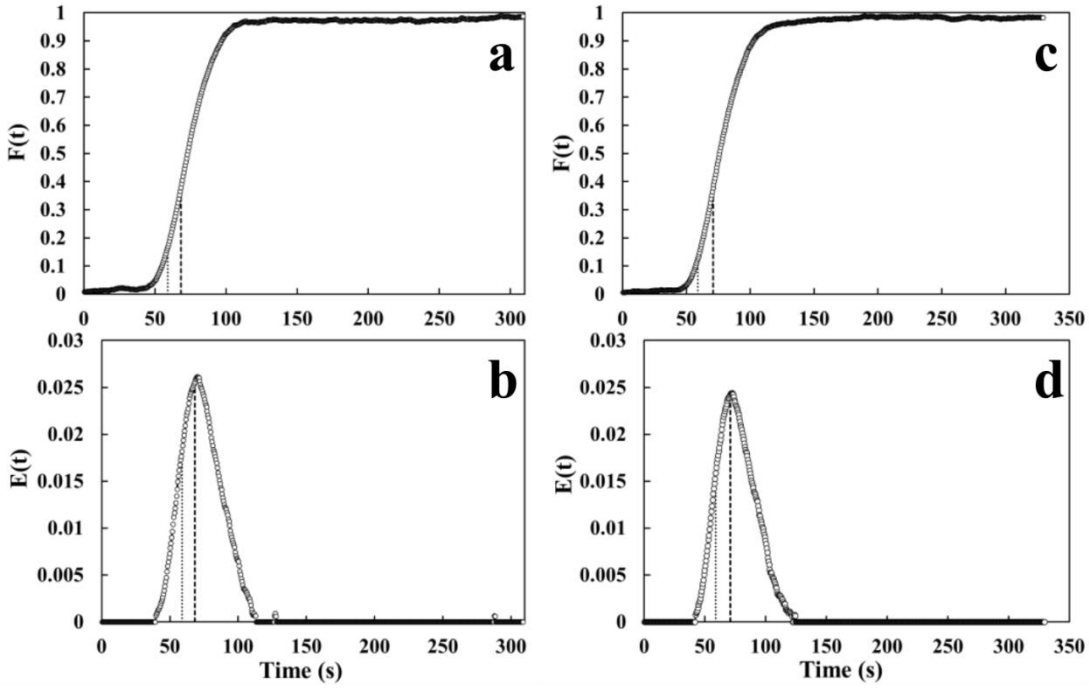

Figure 3.8*: (a) and (c) represent the cumulative distribution function of the tracer tryptophan in the focussed flow and in the sheath flow respectively. (b) and (d) are the corresponding exit-age distributions of tryptophan. The area under the peak multiplied by the time-step yielded the mean residence time (t_m). Dashed lines denote the measured t_m, while the dotted lines represent the space-time (~ 57 s). A slight asymmetry can be observed indicating the presence of secondary flow vortices.*

The *E(t)* is an indicator of the age distribution of all the tracer particles introduced into the device. The differentiation was performed numerically using a script written in Python. Figures 3.8b and 3.8d show the corresponding E curves for the tracer in the focussed stream and the sheath flow respectively. The mean residence time (t_m) can be calculated from the first moment of the E curve (Equation 3.14), which an estimation of the average time spent by the tracer molecules in the device. The denominator in the Equation 3.14 is unity since the area under the peak derived from a normalised cumulative curve is unity.

$$t_m = \frac{\int_0^\infty t.E(t).dt}{\int_0^\infty E(t).dt} = \int_0^\infty t.E(t).dt \quad (3.14)$$

For any flow system, whether ideal or non-ideal, the average residence time (τ), also known as the space-time, is equal to the mean residence time at a constant volumetric flow rate in the absence of dispersion. From the volume of the microchannels (151.7 mm^3) and the constant volumetric flow rate (160 $\mu l\ min^{-1}$), τ = 57 s. While, t_m = 70.7 ± 1.9 s and 67.4 ± 2.2 s (n = 5) were obtained from the experimental RTD experiments, for the tracer in the sheath flow and focussed flow respectively. The difference between τ and t_m suggests the significant presence of convective mass transport and secondary flow vortices in the spiral μ-flocculation device (Groβ and Koöhler, 2010). It is understood that a parabolic flow profile, following the Hagen-Poiseuille equation, causes a large distribution of the RTDs, which is supported by a variance (σ^2) of ~ 350. The variance is the second moment of the E curve and is defined as:

$$\sigma^2 = \int_0^\infty (t - t_m)^2 E(t) dt \quad (3.15)$$

Additionally, the presence of a stunted tailing effect in both the E curves also suggests that particles take longer to exit the device, possibly due to entrailment along with secondary flow forces. This stunted tail (as opposed to the ones seen in a typical laminar flow reactor) is an indication of radial dispersion. Tailing effect can be visualised by the apparent asymmetry of the E curve (Figures 3.8b and 3.8d). This is confirmed by a term called the Skewness factor (s^3), which is the third moment of the E curve:

$$s^3 = \frac{1}{\sigma^{3/2}} \int_0^\infty (t - t_m)^3 E(t) dt \quad (3.16)$$

An average s^3 of around 170 indicated the presence of tailing. But the Skewness value is not large enough to indicate the presence of dead volume elements inside the microchannels, which enhances the weight of the tail. All integration was performed via a numerical trapezoidal function through a script written on Python programming language. The width of the trapezoid was taken to be time interval of the measurement (0.5 s).

3.3.4 Understanding the Dean Flow phenomena

Results from the RTD measurements ($\tau < t_m$) with a step-injection shed light on the presence of secondary flow forces in the curvilinear channels of the μ-flocculation device, arising due to a combination of inertial lift (F_L) and drag forces acting on the particles perpendicular to the direction of flow of the liquid (Figure 3.9). The presence of secondary flow forces was also observed also *via* a preliminary solution of the Fick's law of diffusion using finite element modelling in COMSOL (data not shown). An uneven velocity profile, due to the curvature of the spiral microchannel) leads to a bigger inertia in the fluid elements in the centre of the channel than those near the channel walls. This forces the fluid to move towards the channel walls, creating a pressure gradient, and in turn makes the relatively stagnant fluid at the edges to recirculate inwards, thereby giving rise to the presence of 2 symmetrical vortices perpendicular to the fluid-flow (Di Carlo, 2009; Squires and Quake, 2005).

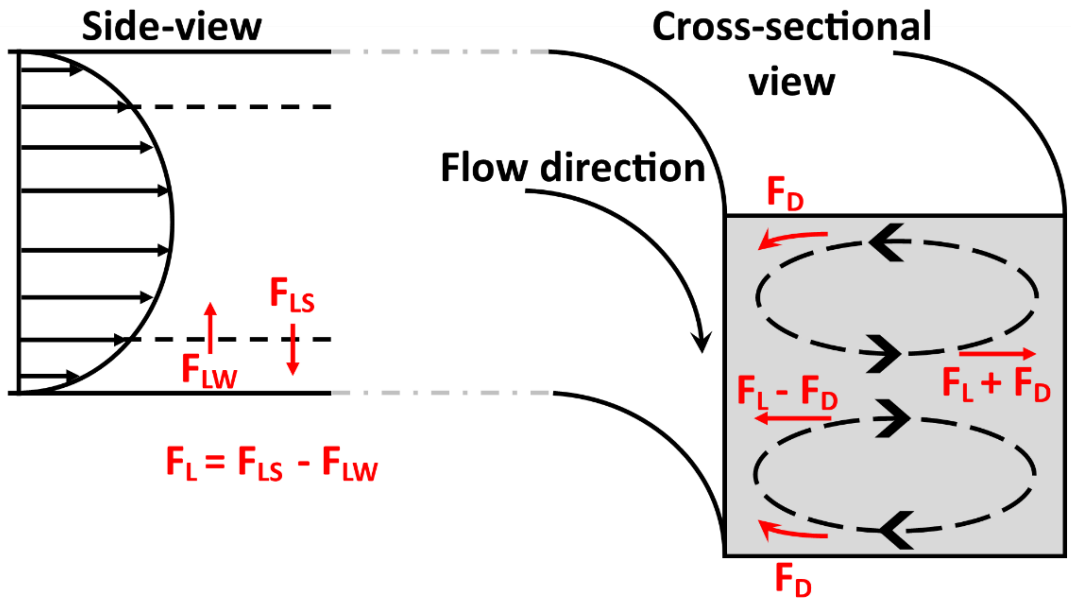

Figure 3.9: A schematic visualisation of the presence of inertial and Dean Flow forces in the square shaped microchannels. F_L which is the inertial lift force is a combination of F_{LW} (the wall-effect lift experienced by particles moving close to the channel walls) and F_{LS} (the shear gradient lift that pushes the particles along the shear gradient, which is minimal at the centre of the channel). In a spiral channel, an additional force- Dean Drag (F_D) creates a differential particle migration, acting along with F_L. The image has been adapted from the work reported by Di Carlo 2009, and Bhagat, Sathyakumar S Kuntaegowdanahalli, et al. 2008.

The drag force is commonly known as the 'Dean Drag Force' (F_D) at low Reynolds number, which transforms into 'Dean Vortices' at higher Reynold's numbers (R_e > 100). Randomly dispersed particles in the microchannels experiencing a combination of inertial lift and Dean Drag force (for 5 ≤ R_e < 20), align themselves around the perimeter of a square microchannel (Bhagat *et al.*, 2008a), as in the µ-flocculation device with R_e = 5. For the net forces ($F_D \pm F_L$) to affect particle trajectory, the particle size (a_p) to hydraulic diameter (D_h) ratio must be > 0.07, for them to be focussed near the inner wall of the channel (Bhagat *et al.*, 2008a, 2008b; Di Carlo, 2009; Di Carlo *et al.*, 2007). For a D_h of 500 µm, the a_p/ D_h has to be << 0.07 for AR dye particles to undergo a complete recirculation (due to a weak F_L, and a dominant F_D) in the Dean vortex and pushes them to the outer walls (Hou *et al.*, 2015).

While this was relatively a straight-forward analysis, studying the effect of secondary flow forces on flocculating particles inside the µ-flocculation device is a complicated procedure. Firstly, a floc's size and its rate of increase are largely affected by electrostatic interactions and Van der Waal's forces between the oppositely charged particles. Secondly, the flocs seem to be in a state of continuous growth, which makes the estimation of the size to hydraulic diameter ratio difficult.

A dimensionless number, called the Dean Number (D_e), can be calculated to characterize the extent of secondary flow in a flocculating system. The Dean number can be defined as follows (Di Carlo *et al.*, 2007; Vincent *et al.*, 2011):

$$D_e = R_e \sqrt{\frac{D_h}{2R}} \tag{3.11}$$

Where, R is the radius of curvature of the spiral microfluidic channel. A device with a straight channel will have a D_e = 0, gradually increasing to 1 at larger R or faster flow rates.

Because the design had a curvilinear shape with a decreasing R, a range of D_e values were calculated, with D_e = 0.011 at the beginning of the spiral (R = 21 mm), to D_e = 0.008 towards the outlet (R = 10 mm). Furthermore, for achieving a_p/ D_h > 0.07, flocs must reach *ca.* 35 µm in the µ-flocculation device, increasing to a_p/ D_h = 0.5 for flocs of size 250 µm (up to which a linear growth was observed, Chapter 5). Di Carlo *et al.* had reported an a_p/ D_h vs. D_e plot, displaying the dominance of Dean Drag, Dean Vortices and Inertial lift, at different regions. For a_p/ D_h values between

0.07 and 0.5, with D_e between 0.011 and 0.008, flocs are expected to experience either no focussing effect or a mild Dean Drag force (Di Carlo *et al.*, 2007). Due to the lack of experimental evidence (for $D_e < 0.011$), and based on a visual observation of flocs flowing in the centre of the microfabricated channels during optical microscopy measurements (explained in Chapter 5), it is assumed that there is no focussing effect on the flocs affecting its trajectory.

But from the mean RTD, it is apparent that the flocs flowing near the walls (away from the centre of the channel) spend longer time in the channels which can affect the growth kinetics due to uneven residence times between the ones flowing in the centre with that flowing in the low-velocity streamlines. Further, the particles flowing in the outer edge of the spiral would spend an additional amount of time due to the longer curvature radius the particles travel. It is evidenced from the high-speed videos that (Appendix A4.2) the particles flowing at near-wall streamlines are almost always small (< 50 µm) and doesn't appear to grow along the length of the channel. While a rotating ('tumbling') effect was observed due to a shear gradient and an increasing drag force towards the centre, having the cell suspension in the focussed flow to initiate nucleation towards the centre of the channel is one possible explanation for the lack of growth of these particles near the walls. A few micro-flocs could have travelled to either side of the wall during the initial straight channel in the fluid-mixing phase and stopped growing further due to the lack of anionic cell suspension to continue the floc-growth process. Meanwhile, as majority of the other micro-flocs were focussed at the centre of the channel, flowing at a higher velocity, the nucleation zone maybe considered to be around the centre of the channel. This is supported by the fact that there was growth up to 250 µm in and around the central streamlines.

3.3.5 Fluid dynamics of solid-liquid laminar flows in confined geometries

The previous section discussed the combined effect of inertial forces and Dean Force on particles travelling in a curved microchannel. While the effect of Dean Force on large aggregating flocs aren't expected, this section will briefly discuss the cross-streamline migration of spherical particles due to inertial lift forces, based on findings from literature. Inertial forces play a more dominant role over Dean Force, since it is expected to induce migration of particles of any size with respect to channel width, under a parabolic flow regime. This effect is also seen in straight microchannels. It has to be noted that fluid dynamics theory regarding irregular shaped particles under constant growth is highly complex and hasn't been

researched yet, according to the author's knowledge. A realistic flocculation system under a continuous laminar flow can be considered to be a solid-liquid two phase flow, leading to a complex fluid dynamic pattern, arguably challenging to predict. This is because the particles are in constant growth and of irregular shape, leading to a possible variation of equilibrium positions as a function of rate of floc-growth. To add complexity a curvilinear geometry of the microchannel induces additional flow forces that act along with the inertial forces, as discussed in the previous section (Di Carlo *et al.*, 2008).

Fluidic inertia of spherical particles in straight channels with laminar flow has been well studied using the Hagen-Poiseuille equation (Asmolov, 1999; Matas *et al.*, 2004a, 2004b; Schonberg and Hinch, 1989; Segré and Silberberg, 1961). It has been observed that spherical particles flowing in such pipes or between parallel plates experience a lateral migration – leading to equilibrium positions (Segré–Silberberg annulus) and different linearized equations have been developed, and solved theoretically and numerically in a low-Reynold's number regime. However, it has been noted that such models do not include cross-streamline migration effects representing the inertial factor, which can be a significant factor contributing to the Navier-Stokes equation (Di Carlo *et al.*, 2009; Yang *et al.*, 2005). It was also observed that the models and experimental systems involved a diluted particle concentration to avoid particle-particle interactions, which occurs in a realistic flocculation system. Results from Di Carlo *et al.* 2009, demonstrated the presence of equilibrium positions of spherical particles in square microchannels as a combinatory effect of inertial lift and Dean Force. The particle diameters were incrementally increased to that of the width of the channels, and they were observed to attain a position away from the midpoint (Figure 3.10). It was also reported that for particle size to channel width ratios between 0.4 and 0.9, the experimentally measured velocities varied only by 1.6% (between the maximum liquid velocity and the particle velocity). As the size of the particles was increased, rotations of such spherical particles decreased significantly, but particle migration was observed for all size ranges (Figure 3.10).

A similar approach was implemented in curved channels with a square cross-section. Gaining a better knowledge and thereby, having better control over the equilibrium positions have led to advances in particle focussing, separation and filtration of particles (Di Carlo *et al.*, 2008, 2007), among others. A semi-empirical model was proposed to describe the effect of lateral particle migration velocity as a

function of the two competing forces acting on a particle. This model assumes that the Dean number is high and further discusses a trade-off between fluid velocity (creating higher inertial lift force) and particle size (increasing Dean Force with reducing sizes) that decides the dominant force acting on a particle.

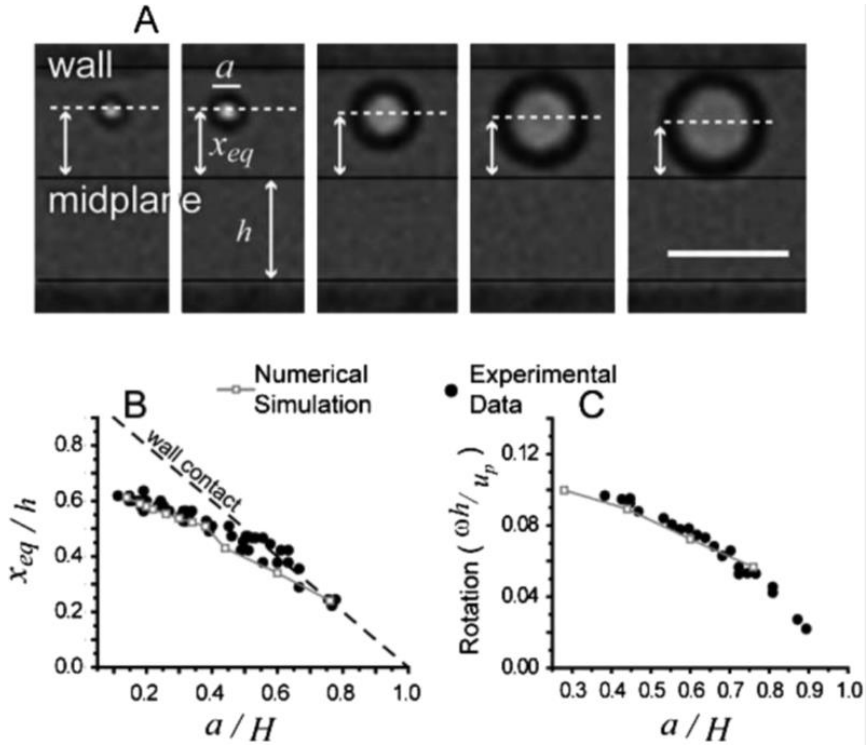

Figure 3.10: Image taken from Di Carlo et al., 2009[♣]. Numerical and experimental equilibrium positions and rotations. (a) The equilibrium positions are shown for different particle size to channel diameter ratios (a/H). The scale bar is 10 μm. (b) Normalized equilibrium positions as a function of a/H are plotted at Re = 20. The dashed line denotes positions where particles would be in contact with the wall. (c) The nondimensional rotation rate is plotted for particles focussed to equilibrium positions at Re = 20.

From the experimental and numerical findings found in literature, migration due to inertial lift has been observed for all particles sizes (particle size to channel width ratio = 0.1 to 0.9), in agreement with the initial finding of Segré and Silberberg for particle flow within circular pipes in 1961. But as discussed in the previous section, because the Dean number is very low for particle sizes similar to flocs observed within the μ-flocculation device, cross-flow migration due to Dean Flow was not anticipated. As a result, complete re-circulation of large aggregating particles do not

[♣] Reprinted with permission from American Physical Society.

occur, while migration to equilibrium positions due to inertial lift cannot be ruled out even while taking into consideration particle-particle interactions of the flocs in the growth phase. On the other hand, in a simplified tryptophan in water system having a larger Dean Number, re-circulation of the small tracer particles maybe the reason for $t_m > \tau$ and a shortened tail in the E curve.

3.3.6 Finite element modelling of laminar flow of Allura Red dye in water

Due to the spiral geometry an appropriate mesh pattern had to be applied so as to enable a proper solution of the fluid equations, and hence achieve accurate results. Therefore, along with a structured mesh, a triangular mesh was implemented and the results were analysed. Mesh elements between 30 to 80 µm were tested for a structured mesh and that between 20 to 80 µm for a triangular mesh. A structured mesh with a 20 µm element size wasn't feasible due to the very high memory build-up by the software. A 30 µm structured mesh created 3,343,088 domain elements, 992,513 boundary elements, and 65,470 edge elements, whereas a 20 µm triangular mesh consisted of 9,811,020 domain elements, 2,955,017 boundary elements, and 94,822 edge elements. A GMRES Linear Iterative pre-conditioning solver was implemented for all the cases, with a minimum of 50 iterations, within which it tries to reduce the error of the solution below a set tolerance level (1×10^{-6} RMS).

Velocity profiles from the solution of the Navier-Stokes equation were used to calculate the widths of the focussed flow from Equation 3.8, and thereby, the theoretical mixing time from Equation 3.9. In the case of structured meshes, the densest 30 µm and 40 µm meshes provided a mixing time of 84 mm (W_f = 144 µm) and 76 mm (W_f = 139 µm) respectively, which was within 5% of the experimental Z_{mix}, as well as, of the theoretical mixing times based on the equation reported by Lee *et al.* 2006 (Z'_{mix} = 85.4 mm) and Wu & Nguyen 2005 (Z'_{mix} = 74.5 mm). Interestingly, this wasn't the case with a triangular mesh, as a 30 µm element provided similar W_f, and Z'_{mix} as that of a similar sized structured mesh. Furthermore, 40, 50 and 60 µm triangular meshes appeared to have similar W_f, and Z'_{mix} results as that of a 40 µm structured mesh.

The FEM studies could further be extended to solve the convection-diffusion equation for the dispersion of Allura Red in water. However, this will require a rigorous selection of an appropriate mesh element size, much finer than 20 µm. Preliminary simulations performed on the system described in Section 3.1.3,

revealed a significant variation in the concentration profiles for the two types of meshes implemented at varying sizes. A difference in mixing times (from concentration profiles of Allura Red) of around 35% was recorded between the structured mesh and that of experimental t_{mix}. The 30 and 40 µm structured meshes provided evidence to the presence of secondary flow forces as discussed in the previous section. Furthermore, while triangular meshes yielded mixing times closer to that of the experimental t_{mix}, it failed to show the presence of secondary forces acting on the Allura Red particles, thereby questioning the validity of the meshing methodology implemented.

3.3.7 Estimation of shear rates in the µ-flocculation device under a continuous steady-state flow

Shear rate values were extracted from the laminar flow module in COMSOL, to provide an insight on the extent of shear rates exposed to the flocs, and also to compare the µ-flocculation device with other flocculation setups that were closely related. While the presence of a laminar flow profile was confirmed, with a R_e of 5, it can be safely assumed that the shear rates in the microchannels are minimal under the specified volumetric flow rates, in comparison with other larger flocculation setups. Simulation of laminar flow under a 30 µm structured mesh resulted in a shear gradient with a maximum of 207 s^{-1} at the channel's outer-wall. Due to the curvilinear symmetry of the channel, the inner wall appeared to have a lower shear rate of around 152 s^{-1}. Shear is known to be the least at the centre of the channel, which was confirmed by the presence of 12 s^{-1} at the channel centre. This value increased to roughly 80 s^{-1}, 125 µm from either side of the walls. Based on this evidence, it is understood that flocs can potentially grow up to 250 µm (half of the channel width and depth), within 80 s^{-1}, which is significantly lower than a typical batch flocculation setup.

Figure 3.11 also indicates a plateau of shear rate in the inner curve of the spiral channel. This can be attributed to boundary meshing using a structured mesh element of 30 µm size to trace a curved edge. While a triangular mesh seemed better fit to overcome this issue, the asymmetry in the mesh geometry failed to pick up important fluid dynamics phenomena – dean flow – in the convection-diffusion solution. One possible way to tackle this is by implementing a finer structured mesh along with an additional edge meshing step to solve the equations more accurately around the curved walls.

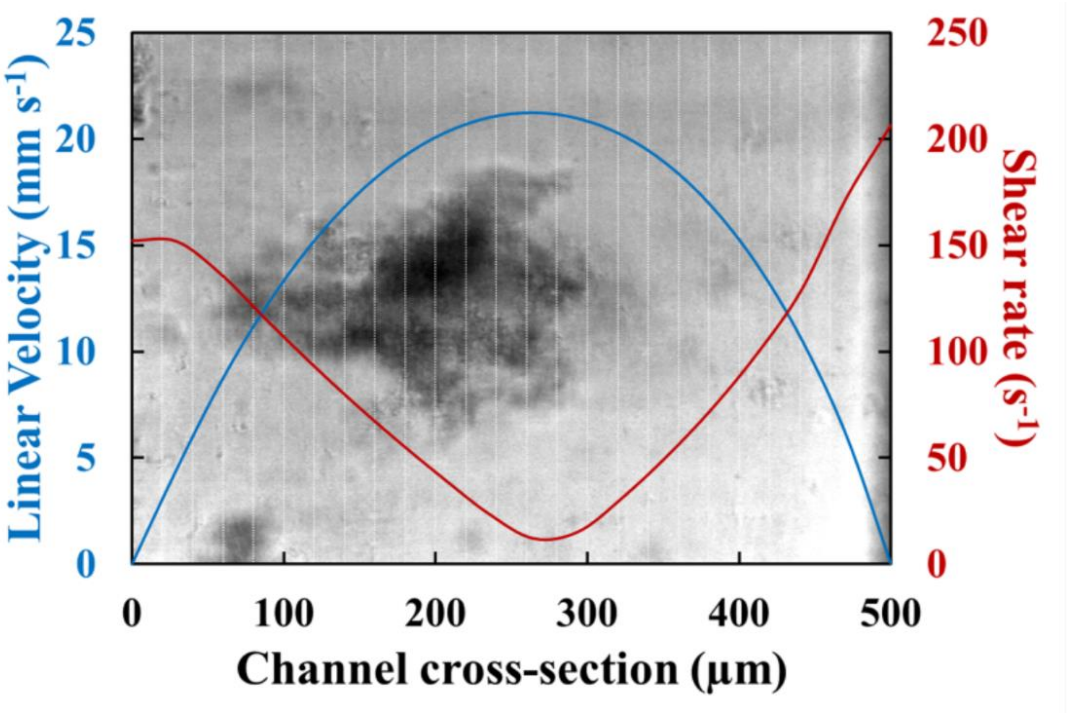

Figure 3.11: Velocity and shear rate profiles extracted from the COMSOL model solution, obtained from a 30 µm structured mesh. The profile was extracted across the channel at 131 mm from the channel inlet, and 250 µm depth. The floc in the background image (diameter = 209.1 µm) was obtained from yeast homogenate and 25 g PEI kg^{-1} yeast at pH 7, and taken at around 140 mm from the channel inlet (see Chapter 5). The length of the x-axis corresponds to the width of the channel.

Figure 3.12, shows the different d50 and d90 values reported in literature (Table 3.1) that were closely comparable with that of the µ-flocculation device. The use of a 6-blade disk-turbine, at around 300 rpm, creates a shear rate of around 102 s^{-1}, while 6-blade Rushton turbines produce much larger shear rates (> 200 s^{-1}).

It is to be noted that these shear rates are only for the purpose of comparison with the µ-flocculation device. This is because the process of flocculation in the µ-flocculation device is a continuous steady-state process, and the presence of a low R_e laminar flow profile facilitates an exaggerated floc-growth condition, as opposed to a turbulent, batch flocculation setup, where floc-ageing becomes equally dominant. The impact of shear on the flocculation process is high (Gregory, 1988), and there have been works previously reported that deal with measuring the strength of a floc using innovative approaches like micromechanics (Yeung and Pelton, 1996) and micromanipulation (Zhang *et al.*, 1999), among others.

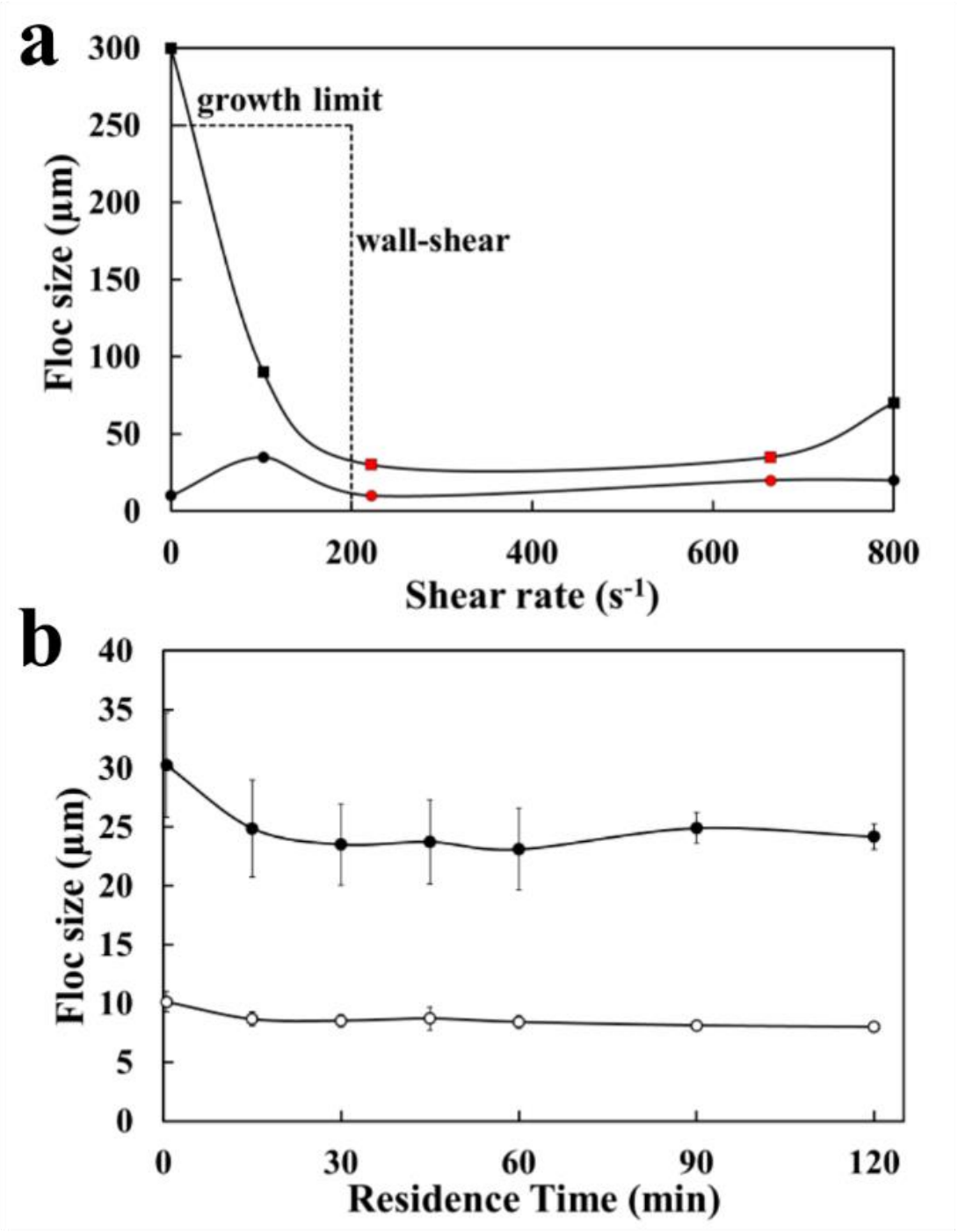

Figure 3.12: (a) Comparison of shear rates with floc sizes obtained from larger scale batch setups, previously reported (Table 3.1). The markers in red, are the floc sizes obtained from the experiments performed by the author. (b) The d50 and d90 sizes of the flocs obtained from a bench scale flocculation setup with a 6-blade Rushton turbine, at 500 rpm (221.5 s^{-1}). Error bars represent ± 1 standard deviation, n = 4.

Table 3.1: Table comparing different larger-scale flocculation setups, closely related to the one in the µ-flocculation device. All PEI reported are of 50-100 kDa molecular weights. Sampling point refers to the time-to-measurements of the floc size from the point of addition of the flocculant. Data (left – right) correspond to the data points presented in Figure 3.14a. References- [A]- Chatel et al. 2014, [B]- Espuny Garcia del Real et al. 2014, and [C] – work performed by the author shown in Figure 3.14b.

Cells	**E.coli Hom.**	**Clarified Baker's yeast Hom.**	**Baker's yeast Hom.**	**Baker's yeast Hom.**	**E.coli Hom.**
Flocculant	0.5% wt PEI	0.2% vol PEI	0.5% wt PEI	0.5% wt PEI	0.2% vol PEI
Working Volume	50 ml	1500 ml	50 ml	50 ml	50 ml
Impeller	6-Blade Rushton Turbine	6-Blade Disk Turbine	6-Blade Rushton Turbine	6-Blade Rushton Turbine	6-Blade Rushton Turbine
Sampling point	Non-sheared flocs	Flocs aged for 10 min	30 seconds	30 seconds	Flocs aged for 1 hour
Reference	[A]	[B]	[C]	[C]	[A]

Hom. refers to homogenate.

However, as the scope of this research mainly focussed on providing a low-shear environment for the growth of flocs, strategies to study floc-breakage within the µ-flocculation device have been discussed in more detail in Chapter 7.

3.4 Conclusions

A spiral microfluidic device which was fabricated for the purpose of studying flocculation was discussed in the previous chapter (Chapter 2). However, due to the necessity of achieving a full control over the parameters affecting flocculation, the hydrodynamics within the microchannels needed to be well-understood and even better – well quantified. In a passive micromixer, mixing is brought about by

advection, and from a large P_e (~2500), it was observed that convection was more dominant than diffusion, under a fully-defined laminar flow regime (R_e = 5).

To evaluate the point of complete homogeneity, a flow-visualisation experiment, in conjunction with image analysis, was implemented in the first instance with a fluorescence dye. Conventional microscopic fluorescence imaging seemed to be inadequate in providing reliable mixing data, for channels with large dimensions (~ 500 µm). This was followed by a simpler, but more effective bright-field imaging methodology using a coloured dye, where absorbance of the dye was measured directly from the pixel data of the images. Mixing of this dye (Allura Red) completed in around 7.5 s, which was in agreement with theoretical mixing values calculated from equations reported in literature. To provide a clearer understanding of the hydrodynamics, laminar flow profile was characterised using FEM *via* COMSOL. Preliminary results from the solution of the convection-diffusion equation provided similar mixing times, calculated theoretically from dense mesh elements (20 – 60 µm triangular, and 30 – 40 µm structured elements), but a variation was observed with increasing element sizes.

RTD experiments were performed to measure the mean residence time of a tracer within the microchannels. A mean residence time of around 70 s was obtained which was higher than the average residence time (57 s). This indicated the presence of secondary flow forces along with a parabolic laminar profile, making the particles trace a longer path due to convective-diffusion. An apparent asymmetry in the E curve was observed illustrating the possibility of particle entrailment and inertial forces. The presence of secondary flow was observed from 30 and 40 µm structured meshes, through preliminary solutions from convection-diffusion equation using FEM. However the mesh quality needed to be improved for accurately predicting the advection pattern, since discrepancies in results between different mesh sizes and shapes were observed.

Upon further investigation on Dean Flow phenomena, the reason for a longer t_m than τ, maybe because of the ratio between the particle size and hydraulic diameter being lesser than 0.07 ($a_p/ D_h << 0.07$), thereby making the tracer particles undergo a complete recirculation. Furthermore, the D_e number for flocs was calculated to characterize the extent of secondary flow, and a highest value of 0.011 (for the outermost spiral) was observed. Under this D_e number, knowledge from literature suggested that particles of sizes above 35 µm ($a_p/ D_h > 0.07$), experience either no focussing effect or a mild Dean Drag force. It is to be noted that a realistic

flocculation system is much more complex, involving additional electrostatic interaction forces and Van der Waal's attraction. Moreover, the irregularly shaped particles are in constant growth. This, hence, necessitates a more in-depth study in the future, but based on evidence through visual observation (explained in Chapter 5) the flocs appeared to flow in the centre of the microchannels for almost all sizes, thereby, supporting the possibility of there being no focussing effect at this specific D_e vs a_p/D_h condition. While this may hold true, the effect of inertial forces on the flocs cannot be ruled out, as they are size-independent. But estimating the inertial force on growing, non-spherical aggregates remain a challenge.

Solution of the laminar flow module from COMSOL also furnished complementary information about the shear rates present within the microchannels. It is now understood that flocs can grow up to 250 µm within a range of 12 to 80 s^{-1}. From literature, this was close to the effect of a 6-blade disk turbine at around 300 rpm. It is, however, stressed that the absolute values can only be used to compare the µ-flocculation device having a continuous, steady-state flow, with a batch flocculation setup. In the latter, there is a dynamic equilibrium between floc-growth and floc-breakage, affecting the overall size and strength of the flocs, rather than just a drag force as in the microchannels.

Results from mixing time and residence time distribution experiments, has shed light into the hydrodynamic properties of the microchannels, which facilitated the possibility of achieving a better understanding of the growth kinetics information.

4. An integrated solution for *in situ* monitoring of flocculation in microfluidic channels using high-speed imaging

The following chapter details the development of a high-speed imaging setup which enables the characterisation of individual flocs *in situ* in a µ-flocculation device in real time. This is a novel approach to the investigation of flocculation events occurring within the microfluidic device detailed in Chapter 2.

The first part of this chapter outlines a simple hardware setup for monitoring a µ-flocculation device using a microscope and high-speed camera. The second part details the development and implementation of an automated image-analysis routine to enable high-throughput characterisation of flocs from streams of images recorded by the camera. This forms a crucial component of the development of a bespoke analytical system to be used in conjunction with a microfluidic device, with the overall goal of not only enabling a robust and accurate characterisation of floc morphology, but also of widening the general applicability of these techniques as a discrete analytical toolbox.

Finally, the complete imaging setup with the image-processing algorithm was tested and cross-validated with a light-scattering instrument, with follow-up experiments conducted to measure the size of flocs formed within the µ-flocculation device.

4.1 Introduction

4.1.1 *In situ* high-speed imaging of flocs

The sensitivity of the flocculation process to various physico-chemical parameters in a macroscopic system is well documented, and has been detailed in Chapter 1. There has been significant interest in studying the size and shape of the flocs through online, *in situ* measurements, which mostly make use of optical analytical methodologies such as light scattering, high-speed imaging and electron microscopy, among others (Eisenlauer and Horn, 1987, 1985; Kayode and Gregory, 1988; Mondal *et al.*, 2013; Wickramasinghe *et al.*, 2010; Wyatt *et al.*, 2013; Zbik *et al.*, 2008). The effectiveness of microscopy as an analytical tool has been well established, and is attributed to its accuracy and its facilitating a direct analysis. Direct imaging avoids the need for the application of the approximate models upon which most conventional analytical methods such as light scattering depend. Used in conjunction with microfluidic devices, optical imaging provides a powerful

analytical platform that can provide valuable information on a process under investigation (Jaccard *et al.*, 2014a, 2014b; Tomer *et al.*, 2012). This information is generally not accessible from endpoint analysis or other offline measurements.

The application of high-speed imaging through a typical bright-field microscope setup offers simplicity in terms of its design and usage. This can be considered an integration of an analytical toolbox with experimental microfluidic platforms, whose applications are widespread, especially in the field of biological sciences.

4.1.2 Automated image-processing for rapid size and morphology analysis of flocs

Computational image analysis has, for a long time, been applied extensively for the rapid and highly-accurate analysis of different experimental systems to yield a variety of information which is otherwise not possible to extract. Image analysis essentially encompasses a set of mathematical operations where, using the field of life sciences as an example, images of biological samples are processed to obtain information about size, shape, morphology, *etc*. Automated image-processing methods offer a variety of advantages, such as avoiding the human error inherent in manual analysis and reducing the time taken for data generation, which in turn allows for higher volumes of images to be collected and processed. Such an image-processing algorithm is directly applicable to the microscopy setup discussed above (Jaccard *et al.*, 2014b). The script developed by Jaccard *et al.*, involves the measurement of static stem cells and its growth over a period of few days from still images taken using a motorised microscope stage. The algorithm was based on a machine-learning approach, where stem cells in the images, converted to greyscale, were classified using seven basic imaging features (BIFs). Using this approach did not necessitate the identification and labelling of different cells as the histogram calculated from the BIFs yielded the identification of cell-wall boundaries based on symmetry. Using phase-contrast microscopy improved the recognition of a single stem cell based from its well-defined boundary. While being a simple yet accurate way to measure the size of stem cells, this approach couldn't be directly implemented to analyse irregular-shaped aggregates from a stream of high-speed image sequences. Local symmetry estimation would have been difficult to measure as it required phase-contrast imaging which significantly hinders the frame rate achievable in the high-speed camera, due to poor lighting.

A typical experiment with modern high-speed imaging technology might yield thousands of images, analysis of which would be a cumbersome process. There is thus a need for the development of a computational image-analysis routine to be developed alongside the imaging setup, in order to make the most of both the platform and the data generated.

4.2 Development of a high-speed imaging setup

Two high-speed cameras were selected for purpose of imaging particles flowing through the µ-flocculation device based on their capture framerate and availability: a Photron Fastcam MC-1 high-speed camera[♣] (Photron USA Inc., California, USA) and a Phantom Miro 4 high-speed camera[♣] (Vision Research Ltd., Bedford, UK).

The Photron Fastcam MC-1 captures images at a maximum of 2000 frames per second (fps) at its full resolution of 512 × 512 pixels, beyond which the resolution decreases (512 × 96 at 10,000 fps). The Phantom Miro 4 can record at up to 111,110 fps, but with a resolution of only 32 × 16 pixels, but like the Photron system is capable of a much higher resolution of 512 × 512 pixels at 2000 fps. Both cameras have storage capacities of around 2 Gigabytes (GB), which enables storage of up to 8000 monochromatic images, i.e. 4 seconds in real time at 2000 fps.

The Fastcam MC-1 was mounted on to a Nikon TE-2000 microscope (Nikon UK Ltd., UK), and the Phantom Miro 4 was mounted on a Nikon Ti-E system (Nikon UK Ltd., UK). The square image aspect ratio of 512 × 512 pixels was sufficient for the viewport to cover the full width of a 500 µm channel at a microscope magnification of around 20×. Because of the large channel depth, the imaging focal plane was manually adjusted to 250 µm (the centre of the channel) on the Nikon TE-2000 microscope, whereas the automated stage on the Nikon Ti-E microscope (MEC56110, Nikon UK Ltd., UK) could be used to adjust the focal plane more accurately. Using the manual stage in the TE-2000 microscope, the number of turns on the rotary Z-axis micrometer was recorded by focussing on the top of the channel followed by focussing at the channel-depth. The channel mid-plane was consequently estimated to be half the number of rotations on the micrometer.

[♣] The high-speed cameras were loaned for free, on a short-term basis, from the Engineering and Physical Sciences Research Council (EPSRC) Instrument Pool (www.eip.rl.ac.uk).

A powerful 30 W Halogen lamp was used as the illumination source for both microscopes. The minimum exposure times possible with the Fastcam MC-1 and Miro 4 cameras are 6 µs and 2 µs, respectively. A longer exposure of 16.7 µs was selected for both cameras based on visual observation of sample high-speed images taken; shutter speeds around 16 µs were found to give crisp images of particles in motion without visible streaking effects. Images recorded by the camera were saved as uncompressed TIF files and analysed offline. A simplified schematic of the system is shown in Figure 4.1.

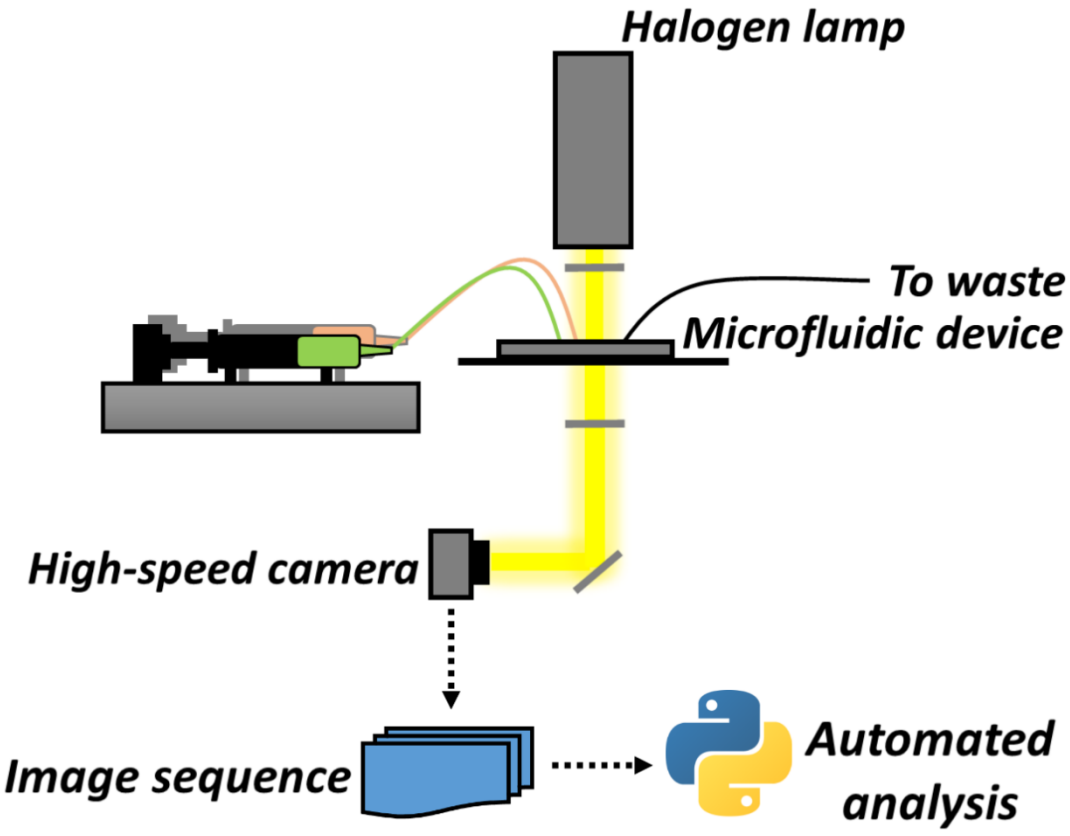

Figure 4.1: Schematic of the high-speed imaging setup developed for the in situ characterisation of floc particles within a µ-flocculation device. Image sequences from the high-speed camera are analysed offline by an analysis routine developed in the Python programming language.

4.3 Development of an automated modular image-processing script using Python

As outlined above, high-speed imaging of flocs travelling through a microfluidic device yields valuable information for characterisation. However, the advantages of

this approach can only be truly exploited with a software-assisted analysis of the images, as the large quantities of data generated prohibit manual analysis, particularly for high-throughput experiments. This section discusses the development of an image-analysis routine which is able to extract particle-size and morphology information from high-speed image sequences, including for non-circular particles and flocs which are larger than a single viewport frame.

Even though a lot of the processing steps (e.g. the morphology filters) are well-tested algorithms in MATLAB, so are the ones in Python. Since MATLAB is expensive, proprietary and, therefore, not completely portable, there is no obvious reason to use it. It also is troublesome when sharing a script, where other users must ensure they have the right version of the software – and with MathWorks releasing two versions per year – this can be confusing. Furthermore, because MATLAB is proprietary, the actual logical steps behind many syntax is not released by MathWorks, and hence, it can be difficult to deconstruct some functions implemented in MATLAB.

The bulk of the work in this part of the project was to combine these processing steps (Figure 4.1) into an analysis pipeline suitable for automating the workflow. The naive implementation of the analysis pipeline required optimisation, mainly because of the excessive memory requirements associated with having to hold a complete image sequence in memory while tracking flocs. The memory requirements were reduced by an order of magnitude, to levels more suitable for lightweight embedded devices (≤ 2 Gigabytes), by developing a more sophisticated implementation of the algorithm, without losing functionality. With substantial input from Dr Jonathan Skelton[♣], different arrays used to store image data were created using NumPy (numerical Python) structures, which arguably is more efficient than MATLAB. Furthermore, some of the computationally-intensive parts of the algorithm were also parallelised, and a near-linear speedup in the process was obtained. This would be beneficial for real-time applications; for example, if a high-speed camera with a high frame rate, one could pair it up with a high-performance computer, and run the processing across multiple cores. Implementing this section of the script was also done in collaboration with Dr Skelton. Thanks to several other features of Python, should one need to move on to embedded, real-time or integrated systems in the

[♣] Research Officer in Metastable Functional Materials, Department of Chemistry, University of Bath, UK. Previously, Department of Chemistry, University of Cambridge, UK.

future, there is scope for interfacing directly with the hardware, tighter optimisation of the code, and deployment with low-overhead versions of the Python interpreter. All three of these things would be difficult with MATLAB.

4.3.1 Algorithm overview

The image-analysis routine was developed in the Python programming language (version 3.2.5), an open-source high-level programming language similar to MATLAB and supported by thousands of third-party modules for applications ranging from web, software and game development to scientific computing. Although not as fast by design as lower-level languages such as C or C++, Python is very good for rapidly prototyping and testing ideas, and its use of constructs common to most widely-used imperative programming languages allow for easy subsequent porting of finalised code. For the image analysis, the functionality of various core Python modules and extensions was employed, as outlined in Table 4.1. The routine is encapsulated into a single Python source file, which has been structured so that all the user-configurable parameters can be found and modified at the beginning of the code. A flow-diagram outlining the routine is shown in Figure 4.2. The operation of the code is described in detail in the following subsections, and a complete list of parameters can be found in Appendix A4.1. The code can also be executed both in parallel mode (i.e. using multiple cores of a multicore CPU, if available) and in sequential mode (i.e. using only one core) for benchmarking purposes; for clarity, the following sections describe the operation of the code in the latter mode.

4.3.2 Image pre-processing sequence

4.3.2.1 Image thresholding

From a grayscale image (as captured by both high-speed cameras tested here), a binary image is obtained by thresholding to remove the colour information ("binarization"). By a careful selection of the threshold level, the image background is eliminated (Bovik, 2005), which facilitates the subsequent processing and analysis of the features in the image. If a greyscale image, $f(n)$, contains pixels with levels P_g (where P_g = 0 - 255, for 8-bit images), a thresholding value T_v is defined as an integer within this range (Equation 4.1). Selection of this value, T_v, is critical as it determines whether a particular pixel in the image is identified as being

part of the background (and thus discarded from the analysis), or as part of a feature.

Table 4.1: Python modules required by the image-analysis routine. Standard library modules are part of the core Python runtime, whereas other modules must be installed as extension packages.

Functionality	Module	Description
Generic operating-system services	`os` (Standard Library)	Operating system functionality and high-level file and directory handling.
	`time` (Standard Library)	To use time-related functions; especially helpful in benchmarking and calculating the time required for processing.
	`multiprocessing` (Standard Library)	Module containing constructs for performing parallel processing by creating sub-processes. This was used to exploit multiple processors to speed up CPU-intensive parts of the code.
Numerical and scientific processing	`math` (Standard Library)	Mathematical operations can be performed using this module.
	`random` (Standard Library)	To generate random sequences of integers (e.g. for generating sequences of colours for marking independent flocs in analysed images).
	`NumPy`	Package to seamlessly handle large N-dimensional arrays of data, with a variety of functions (van der Walt *et al.*, 2011). This module was used to handle pixel data extracted from high-speed images.

Functionality	Module	Description
	`SciPy`	Built on NumPy package, SciPy provides a collection of algorithms and functions for data-processing, to manipulate and visualize data (Oliphant, 2007).
Image file handling	`PyGame`	Essentially for developing games and multimedia programs, PyGame can be used for efficient handling of image files and extracting pixel data (Shinners, 2009).
File I/O handling	`csv` (Standard Library)	Module for reading and writing data from/to comma-separated values (CSV)-format files.

$$T_v \in \{0, 1, 2, ..., P_g - 1\} \tag{4.1}$$

$$g(n) = \begin{cases} 1, & f(n) \leq T_v \\ 0, & f(n) > T_v \end{cases} \tag{4.2}$$

Thresholding is then carried out by a simple comparison of each of the *n* pixels in the image $f(n)$ with T_v (Equation 4.2). This results in a binary image, $g(n)$, where each pixel is a Boolean value. To ensure an effective thresholding, a clear distinction between features in an image is critical. In the present case of particles flowing through the µ-flocculation device, pixels occupied by particles appear as dark (low P_g) values, whereas the channel bed in the background appears as light (whiter pixels/high P_g) values. The thresholding is performed so that pixels occupied by flocs are assigned the binary value 1, while background pixels are assigned the value 0. The selection of the thresholding value, T_v, was intentionally left as a manually-specified parameter, in spite of the availability of different automated algorithms for determining suitable values, because manual selection is known to provide the best binarization results (Bovik, 2005). This requires that sample images from each set of data are manually investigated, and the suitability of the chosen threshold visually confirmed. However, the thresholding step is not sufficient to cleanly separate the particles from the background, because features such as the channel walls or debris, which may in general be present in images, get included along with the particles.

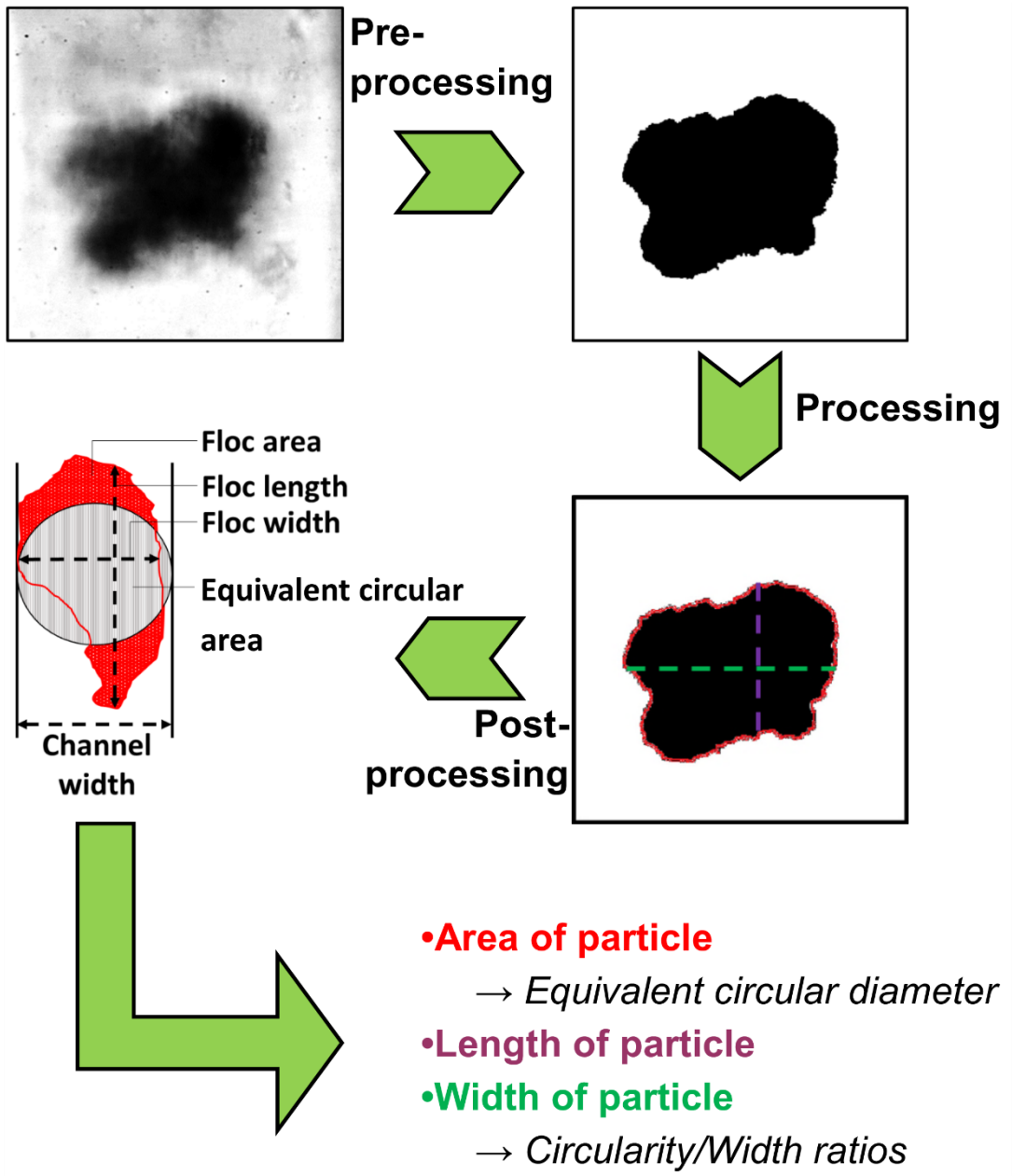

Figure 4.2: Schematic flow diagram of the image-analysis routine. The processing can be separated into three stages: pre-, main and post-processing. Upon successful completion, the script outputs two CSV files, one containing the "trace" of individual particles across the video stream as they pass through the camera viewport, and the second listing the length, width, area and equivalent circular diameter of flocs in pixels and µm.

4.3.2.2 Reference-image subtraction

Following the initial binarization of images, removal of channel features is assisted by comparison with sample images of the empty channel filled with water (to retain

a similar refractive index). The so-called reference image pre-processed as for sample images, but the inverse of Equation 4.2 is implemented, where pixel values above T_v are converted to ones, and pixels below T_v to zero. When the sample images are loaded, they are then compared with this thresholded reference array in order to remove artefacts such as channel walls and edges (Figure 4.3). The end result of the pre-processing is thus a sequence of binary arrays, one for each image frame, containing the features of particles in that particular frame.

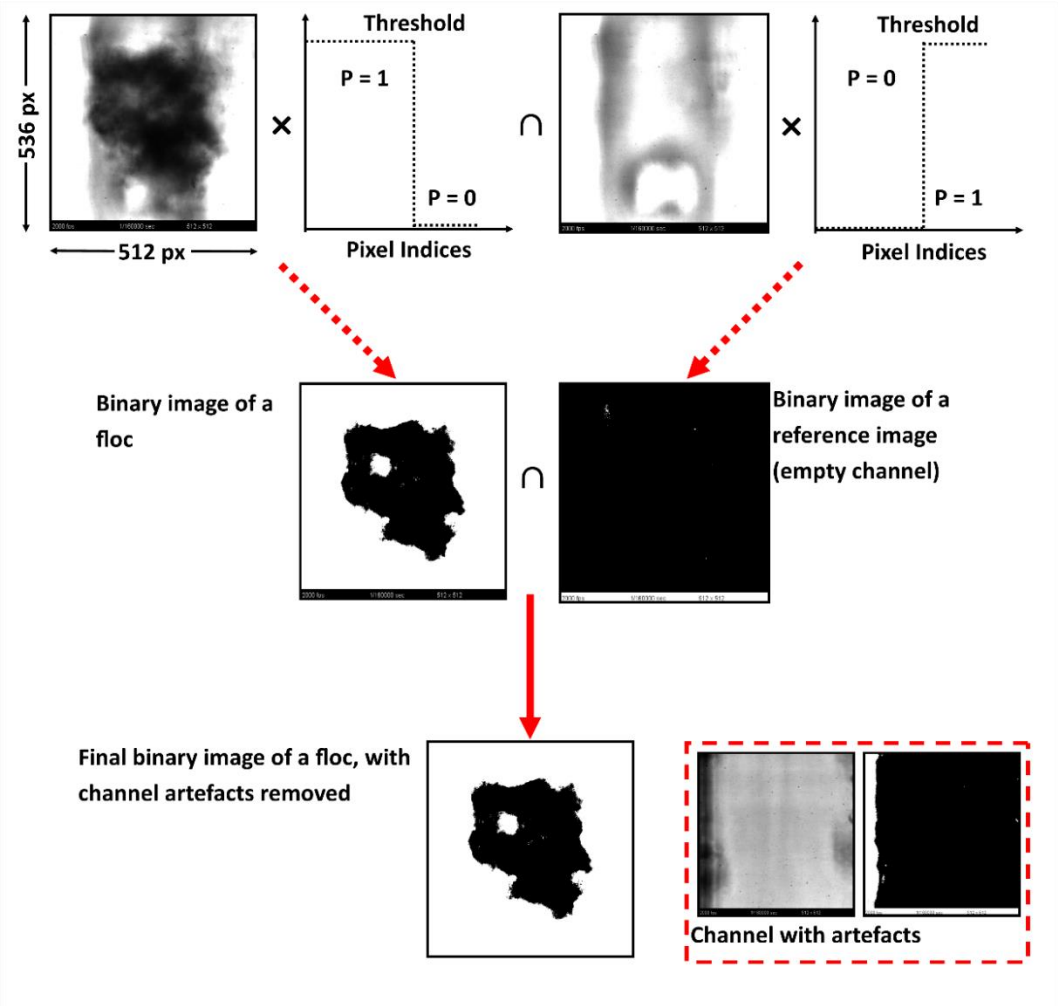

Figure 4.3: Image pre-processing. The grayscale sample and reference images are thresholded, and a logical AND filter is applied to remove channel walls and other artefacts marked in the latter from the former. 'P' refers to the Boolean pixel value after thresholding: 0 – background, 1 – feature.

4.3.2.3 Image batching

The script is supplied a pair of folders which are scanned for sample and reference images, with multiple reference images, if available, being averaged to obtain a

single reference array. The sample images are loaded into memory and pre-processed in batches, which keeps the memory requirements low by allowing the processed images in a set to be cleared before the next set is loaded.

4.3.3 Image processing

4.3.3.1 Morphological operations

The pre-processing steps provide a clear distinction between features and background of an image. However, this basic operation tends to leave jagged boundaries, which result in disconnected 'pixel-islands' or 'pixel chains' along the perimeter of each feature. Therefore, the main processing step utilises a more sophisticated class of binary-image processing operations to remove such gaps.

These morphological operations are all performed with the help of "structuring elements", masks which are moved over the image row- or column-wise to define the area over which the operation is carried out. The element can take different shapes, depending on the shape of the input images and the output required; in the present case, a simple two-dimensional square-shaped element was chosen for compatibility with the aspect ratio of the camera images.

As shown in Figure 4.4, different operators were tested for implementation in the processing step. The selection of an appropriate sequence of morphological operations had to be performed carefully, as they can lead to changes in feature sizes, thereby affecting the morphological characteristics measured in the analysis.

In general, the different operators function by applying simple logical operations (AND, OR, NOT, etc.) on an image with the structuring element. Fundamentally, the two basic morphological operators are dilation and erosion

Dilation can be represented mathematically as in Equation 4.3. This operation expands the size of the boundary objects, effectively smoothing them, and also fills in small holes (shrinking the background) if they are smaller than the structuring element, E.

$$g(n) \oplus E(x) = \cup\, g(n)_i \tag{4.3}$$

$$i \in (x) \tag{4.4}$$

In the SciPy implementation, the mesh element with centre *i* (Equation 4.4) moves row-wise across every pixel *n*. The increase in the size of small features can be

clearly seen in Figure 4.4; while this is useful for smoothing the boundaries, the exaggeration of the size of small features could lead to inaccuracies in the particle-size measurements, which is undesirable.

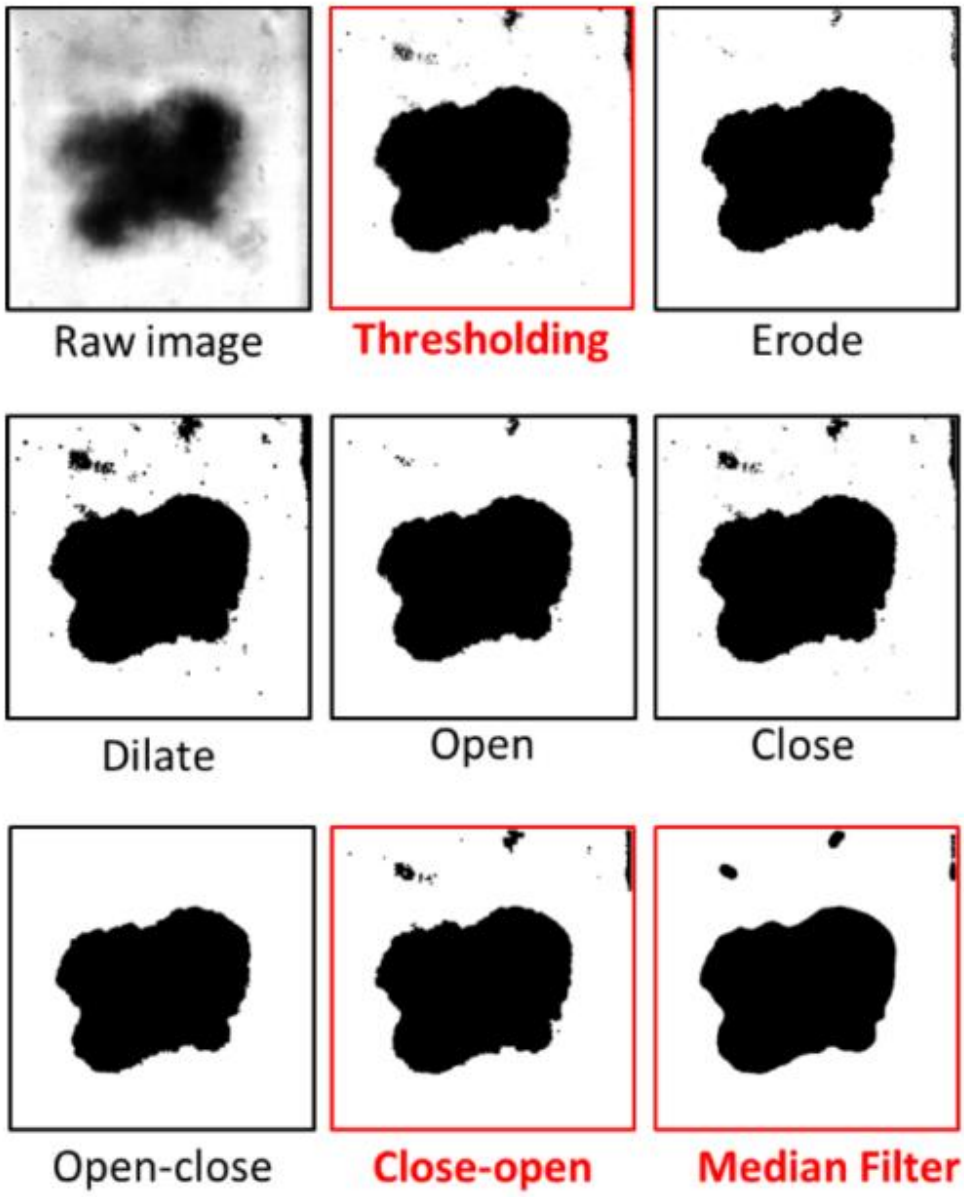

Figure 4.4: The effect of different morphological operations on a typical pre-processed image of a floc in the channel. Images with red border denote the chosen process-flow; i.e. the images were thresholded followed by a close-open and a median filter. Close-open filtering was the only effective way to remove pixel noise that passed through the threshold, which were not particles and were confirmed visually. At the same time, it seemed to preserve relatively small particles, unlike an open-close filter.

Erosion is often described as the inverse of dilation. While mathematically correct (Equation 4.5), this relationship rarely holds in practical applications, i.e. the erosion of a dilated image seldom returns the original image. Erosion leads to the removal of small isolated features, or tiny protrusions along the perimeter of a feature, if they are smaller than the mesh element E.

$$g(n) \ominus E(x) = \cap\, g(n)_i \tag{4.5}$$

The removal of small features as a result of erosion is illustrated in Figure 4.4. In practice, erosion is effective at removing noise from an image, but can also lead to the removal of small particles and reduction in the size of larger features.

Erosion and dilation, being effective operators for noise-removal and boundary-smoothing, respectively, can be used in conjunction in order to preserve the size of objects, even though they do not do so when used in isolation. This property of preserving feature size means combining operations is a potentially more effective technique than the isolated use of erosion or dilation.

Combining erosion and dilation yields two new operators, closing and opening. Closing (Equation 4.6) can be defined as a dilation followed by an erosion using the same structuring element, whereas opening (Equation 4.7) is the same operations employed in reverse order.

$$g(n) \bullet E(x) = [g(n) \oplus E(x)] \ominus E(x) \tag{4.6}$$

$$g(n) \circ E(x) = [g(n) \ominus E(x)] \oplus E(x) \tag{4.7}$$

While closing and opening are effective smoothing operators, they are unidirectional filters, i.e. biased filters that selectively modify one type of pixels (either foreground black pixels, or background white pixels). To make the morphological operation unbiased, the two operators can be applied sequentially. Mathematically, a close-open operation is the process of applying Equation 4.6 followed by Equation 4.7, while the reverse is performed in an open-close operation. Both filters preserve the size of larger features while effectively removing smaller ones. If the small features in an image are noise, then open-close is recommended (Bovik, 2005), as erosion is the first step, whereas, if they are to be preserved, close-open would be more effective. The effects of both these operations are illustrated alongside the others in Figure 4.4. Given that flocs of varying size (including small ones) would be

expected in a general case, the close-open filter is in principle the most appropriate, which is borne out by the comparison in Figure 4.4.

One of the consequences of applying the close-open filter is that noise features which are too small to be dilated from the erosion step. To correct for this, a median filter was applied following the close-open operation. The median filter works similarly to the close-open or an open-close filters, remove small features below a certain size, which depends on the area mask used, and hence smoothing detail. The median filter was found to be ineffective when used in isolation, but was appropriate as a 'clean-up' step after the close-open filter. This additional step was found to be instrumental in the further reduction of noise to filter out small "false" flocs. Because the behaviour of the morphological operations depend on the structuring element size, which have to be optimised for particular sorts of image data; this is discussed further in Section 4.5.2.

Finally, to widen the applicability of the algorithm, which was primarily developed around the imaging of solid flocs, an optional feature for measuring hollow particles was also implemented, making the routine suitable for particles such as whole cells or micro-particles, which typically have a hollow membrane with a thick perimeter. To do this, a "fill hole" step was added after the morphological operations, to fill the membrane (otherwise considered as background), thereby allowing the same characterisation as performed for solid flocs to be applied. The size of the structuring element for this step has to be chosen based on the size of the particles under investigation, e.g. by manual inspection of a subset of the camera frames. Since these particles, like flocs, have defined perimeters, the morphological operations implemented for the measurement of flocs are also applicable.

4.3.3.2 Feature labelling using connected-component labelling

Following the smoothing of features and noise removal, different features within a single frame are then identified and labelled. This is accomplished using a connected-component labelling (CCL) algorithm. CCL seeks to identify connected pixels in a group that have the same binary value (in this case 1). A square-shaped 3 × 3 structuring element is commonly used, with the central pixel placed on a reference pixel to establish the connectivity with its neighbours. Pixels in a feature are connected by comparing the "label" value of the reference pixel to those of its neighbours within the structuring element. This process is illustrated in Figure 4.5. For a 2-dimensional image $g(n)$, where $n \in (i,j)$ as shown in Equation 4.8, every

pixel *n* starting from (0,0) is checked for a pixel value of one. Simultaneously, an array *L(n)*, of the same shape as that of *g(n)* is created. The elements of *L(n)* are label values, *m*, for each unique isolated feature detected (Equation 4.9).

$$g(n) = \begin{matrix} (0,0) & \cdots & (0,j) \\ \vdots & \ddots & \vdots \\ (i,0) & \cdots & (i,j) \end{matrix} \tag{4.8}$$

$$L(n) = \begin{cases} 0, & g(n) = 0 \\ m, & g(n) = 1 \end{cases} \tag{4.9}$$

For every pixel *(i, j)* in the binary image, the algorithm checks whether the neighbouring pixels included in the structuring element and which have been scanned, i.e. *(i-1, j), (i-1, j-1), or (i, j-1)*, already have a label; if so, this is carried over to *(i, j)*, while if not the last-assigned label is incremented by 1 and assigned to the new feature (Equation 4.10).

$$\begin{gathered} If\ g(n)_{(i,j)} = 1\ \cap \left[g(n)_{(i-1,j)}\ or\ g(n)_{(i,j-1)}\ or\ g(n)_{(i-1,j-1)} = 1\right], \\ then\ L(n)_{(i,j)} = L(n)_{(i-1,j)} = m; \\ m = m + 1 \end{gathered} \tag{4.10}$$

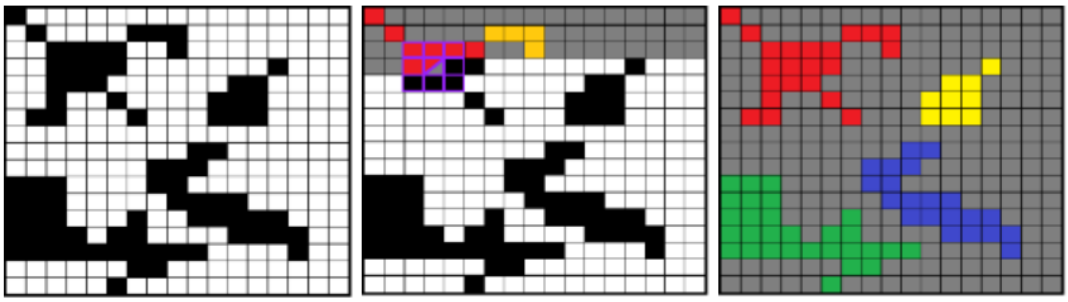

Figure 4.5: Schematic representation of connected-component labelling for identifying and labelling separate features within a binary image. The left-hand image shows an example binary image with black pixels denoting features and white pixels the background. The second image shows a square structuring element (purple mesh) scanning through each pixel from top-left to bottom-right, checking whether the neighbouring pixels within the element which have already been processed are part of already-labelled features. If so, this is then carried over; otherwise, a new label is created and assigned to it. In this image, the grey pixels denote the parts of the image already scanned by the algorithm. The third image shows the fully-labelled image obtained at the end of the labelling.

4.3.3.3 Three dimensional image relabelling

Connected-component labelling identifies the different features in a given image. In a sequence of high-speed images, the same floc will generally be present in multiple frames as it enters, travels across and exits the section of the channel captured in the viewport. “Connecting” flocs between frames is necessary for a number of reasons. It allows the size of the floc to be correctly determined, in particular where a particle is larger than the viewport. Secondly, it ensures that unique particles are only measured once, eliminating redundant measurements from the output dataset. The “relabelling” process is illustrated schematically in Figures 4.6. After CCL, each feature in a frame is compared against the features in the previous frame based on whether and to what extent their pixels overlap (Equation 4.11). For each feature, the number of overlapping pixels with every feature in the previous frame is counted, and the label is reassigned to that of the feature with maximum overlap, if any is found, or is otherwise changed to the value of an incremental counter for the complete image sequence stream (Figure 4.6b).

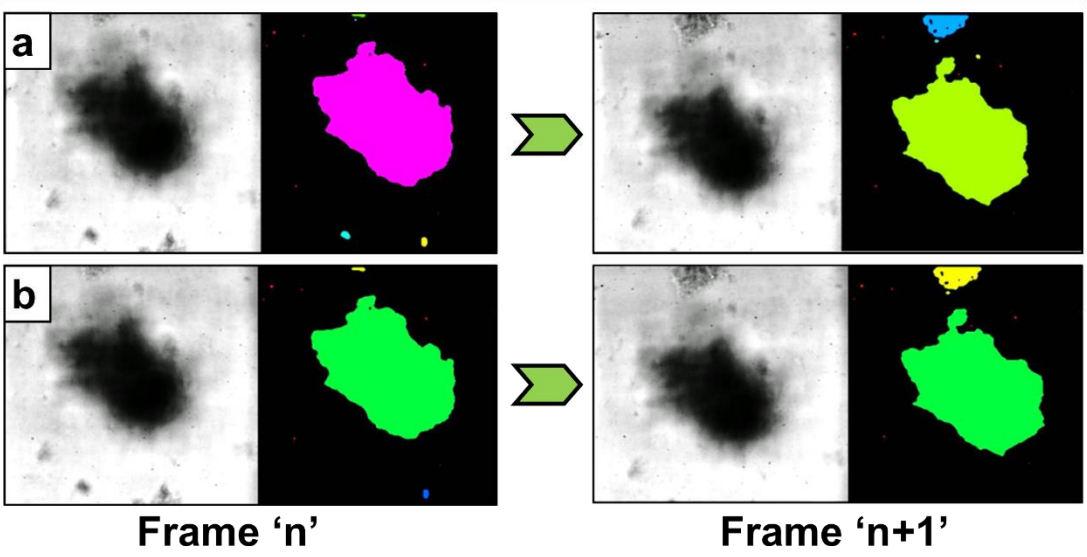

Figure 4.6: (a) Two consecutive video frames before labelling. At this stage the images are treated independently, and the particle receives a different label in each frame. (b) Video frames after relabelling. The analysis detects that the same floc is present in both frames, and assigns them a consistent label.

$$overlap = \sum (indices\ of\ labels\ in\ frame\ n \cap\ indices\ of\ labels\ in\ frame\ n+1) \quad (4.11)$$

This procedure allows individual flocs to be given a consistent label throughout the complete video stream, and also makes the analysis more robust against e.g. variations in image contrast, which could make a large floc appear to split in a particular frame, or flocs moving into and out of the focal plane. For smaller particles, which appear to move fast between frames and hence do not have any overlap, re-labelling was performed by calculating the centre of mass of the particle and extending it to a larger circle to detect overlap with particles in preceding frames.

4.3.4 Post-processing and data collection

4.3.4.1 Particle tracing

After labelling all particles in the video stream, the script then stores a trace of the area (in pixels; as shown in Figure 4.7 for micro-particles) of individual particles through the complete video stream. This provides an indication of the frames where each observed particle enters, is in the viewport, and exits. The traces are particularly helpful for diagnosing any unexpected occurrences.

As a particle enters the frame, the pixel area increases steadily, reaches a maximum when the entire particle is inside the viewport, and plateaus for those frames where it is completely within the viewport. The area then steadily decreases as the particle exits the field of view. The area of the flocs is then characterised as the maximum within the plateau region, and this value is stored for later processing. It is worth noting that in principle an analysis of the slope of the trace during the particle entrance and exit could provide an estimate of the velocity of the floc, but this is not pursued in the present version of the code.

From this area (in pixels^2), the corresponding area (in μm^2) is calculated using the magnification of the microscope, from which the equivalent circular diameter is computed by assuming particle to be circular. The script also finds the span of the floc along both axes (horizontally along pixel rows and vertically along pixel columns) and stores these as estimates of the length and breadth of the floc, providing a basic indicator of its morphology. It is worth noting that this analysis requires that the axes of the channel be aligned with the rectangle of the camera viewport. These four values, i.e. area, breadth, length, and circular diameter, are recorded for each particle measured.

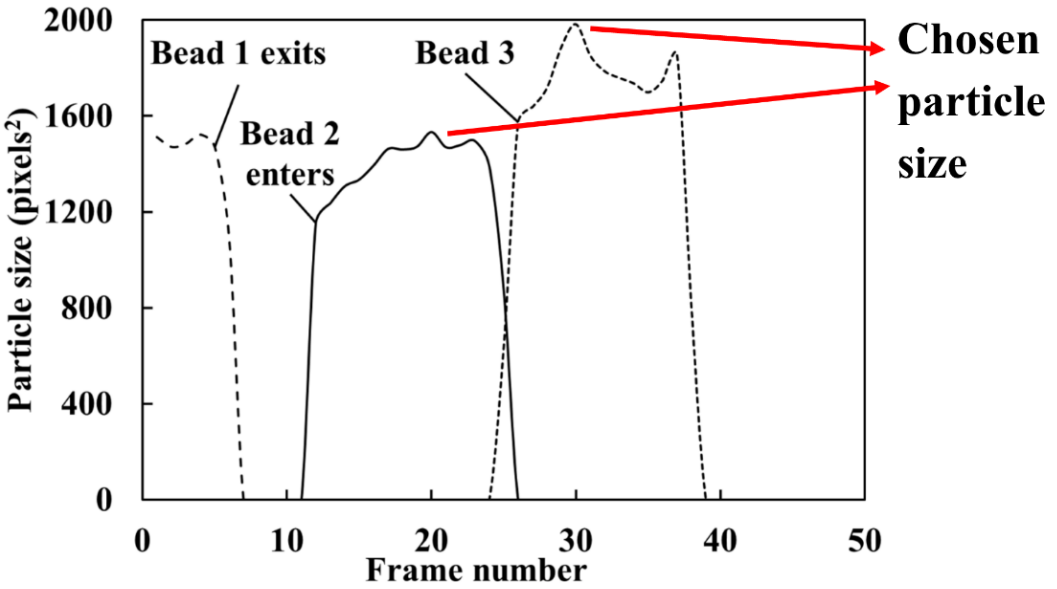

Figure 4.7: Representative trace profiles for micro-particles of around 30 µm diameter. The trace clearly shows the frames in which each particle enters, is fully within the viewport, and then exits the frame. The diameter is calculated from the maximum area occupied by the particle through the trace.

To tackle the issue of particles going out of focus, which can lead to inaccurate size distributions, a conditional filter was added to the script. Particles with unique labels are recorded in the characterisation only if they are found to pass through the trailing edge of the frame, which helps eliminate spurious particles from the measurements. Additionally, the array carrying the number of frames for which a certain particle is recorded is compared with an arbitrary number, below which the particle is expected to disappear or appear mid-way, and hence excluded from the characterisation. In short, a particle is included in the particle size distribution only if it flows past the exiting edge of the image frame, while being present and recorded for a minimum number of consecutive frames.

While this avoids the inaccurate representation of smaller floc particles out-of-focus, the elimination of such particles can lead to skewing of the PSD towards the larger particles. This stands as an experimental limitation because a large depth of microchannels was necessitated to allow growth of flocs in all three dimensions, thereby losing valuable information about smaller flocs outside the focal plane of measurement. Even though this conditional filtering affects the measurement of the largest 10 percent of the flocs recorded, its significance is reduced by assuming the presence of similar number of such filtered particles along the entire length of the µ-

flocculation device. The ratio between the number of filtered flocs and the total number of flocs recorded and was around 0.04 ± 0.006, across the imaging locations for a fixed flocculation condition. See Section 4.5.3 for the two different output files created by the script, from which the total number of flocs and the number of filtered flocs were taken.

The particle traces and morphology measurements are saved into comma-separated values (CSV)-format files for further analysis using e.g. Microsoft Excel. At the data-output stage, additional information is also computed/recorded, including whether each particle was identified as a "big floc" (requiring the image-stitching sequence; Section 4.3.4.2), its circularity value (ratio between the length and breadth of a particle), and also the ratio between its breadth and the width of the microchannel. An additional set of flags also allow the user to output a sequence of images illustrating the labelled/relabelled images against the original video frames, for demonstrating and checking the analysis routine (Figure 4.6).

4.3.4.2 Handling large particles

In some cases, flocs may be longer than the part of the microchannels captured within the camera frame, and hence the particle tracing method cannot estimate the size of such flocs. Therefore, these particles had to be handled separately, as follows. Since the flow of particles is either from the bottom to the top edge of the frame or vice versa, such "big particles" can be identified by the corresponding labelled region simultaneously touching both edges (within a specified pixel tolerance, to cope with image anomalies). When such particles are identified, the script considers the frames in which the leading edge of the floc has entered but is contained within the viewport, from which it estimates a velocity in terms of pixels per frame (Figure 4.8). Using this, the script calculates the size of the "image slice" (S) which is different for each frame, and hence builds up an image of the floc in segments, generating a composite image which can be analysed in the same manner as the smaller ones.

4.4 Testing the high-speed imaging setup

4.4.1 Validation of the analysis using micro particles

The μ-flocculation device was mounted onto an inverted bright-field microscope, with the fluids administered using two programmable syringe pumps (KDS200, KD Scientific Inc., Massachusetts, USA and Aladdin, WPI Ltd., Hertfordshire, UK). Polytetrafluoroethylene (PTFE, S1810- 10, Bola, Germany) tubing approximately 20

cm long (1/16 inch external diameter) was used to connect the syringes to the device through M6 interconnects and ferrules (P207X and P250X; Upchurch Scientific, Washington, USA). Volumetric flow rates of 75 µl min^{-1} and 85 µl min^{-1} were used to drive the fluids into the µ-flocculation device from the middle inlet and the side inlets, respectively (see Chapter 2 for details on the selection of the combined volumetric flow rates).

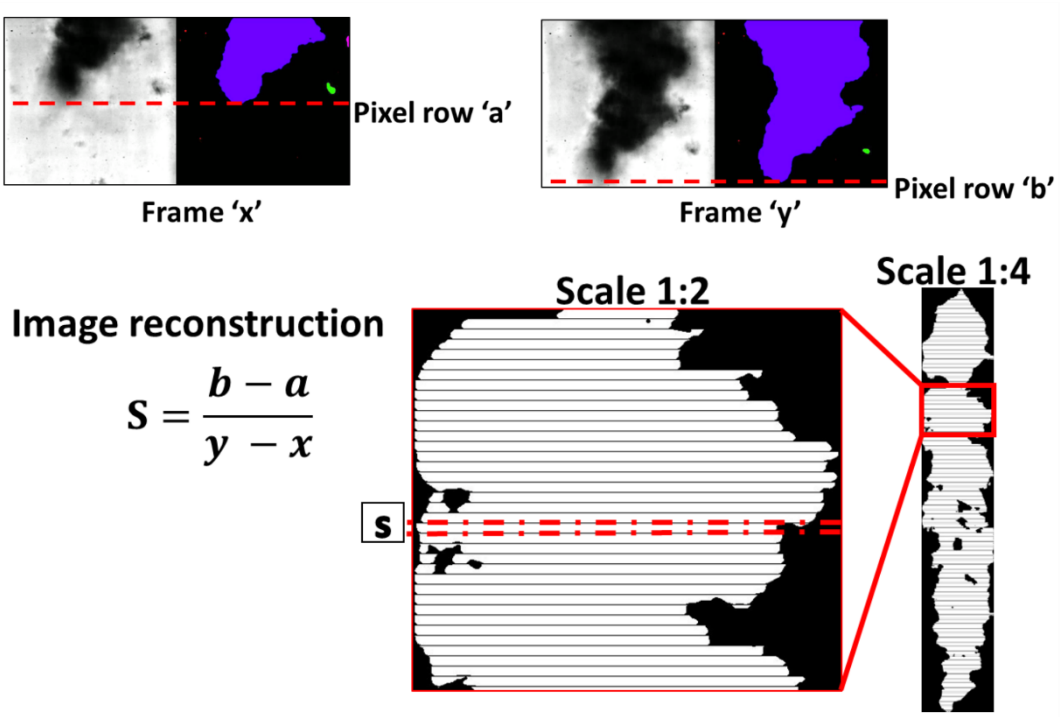

Figure 4.8: Illustration of how the code analyses flocs larger than the camera viewport. When a particle bigger than the field of view is encountered, the frame in which the leading edge of the particle appears is noted. The velocity of the particle in motion is then measured in pixel rows per frame by tracking the edge as it moves through the frame. The velocity allows the size of the previously-unseen slice in frames where the labelled particle touches both edges of the frame to be identified. A list of slices is built up until the trailing edge of the floc leaves the frame, under the assumption of constant velocity. Reconstruction of a composite image of a floc larger than the camera viewport, obtained by combining slices captured from the image sequence, is enabled. The size and diameter of the composite particle is then measured in the same manner as those which fit into the camera viewport.

The analysis routine was validated by comparing the measured sizes of the micro particles with data from a light-scattering instrument (Mastersizer 2000, Malvern Instruments, UK). 15 ± <0.2 µm polystyrene micro-particles (74964-5ML-F, Fluka

Analytics, Sigma Aldrich, UK) and 25 ± 2.5 µm Yellow Green Microspheres (Fluoresbrite® 18241-2, Polysciences Europe GmbH, Germany) were imaged using the Phantom Miro 4 camera mounted on the Nikon Ti-E microscope (30× magnification), and 30.1 ± 0.22 µm polystyrene micro-spheres (NIST traceable - Duke Scientific, USA) were imaged using the Photron MC-1 camera on the Nikon TE-2000 microscope (20× magnification). The movement of the beads was recorded near the ψ-shaped inlet of the µ-flocculation device.

To create particle size distributions (PSDs) in terms of % volume to be compared with the laser-scattering instrument results, a histogram of the number of flocs was generated using Python with similar bin widths to those used by the Mastersizer. A non-linear Gaussian curve fitting routine in the OriginPro 8.6 software (OriginLab Corporation, Massachusetts, USA) was used to fit the PSDs to a Gaussian distribution, again for comparison with the Mastersizer output.

4.4.2 Characterisation of flocs using the high-speed imaging setup

To compare the floc sizes measured by the image-analysis setup and a Mastersizer 2000 instrument, flocculation was performed both within the µ-flocculation device and in a bench-scale setup of 50 ml centrifuge tubes. The latter setup is explained in detail in Chapter 2; 25% Baker's yeast (*S. cerevisiae*) in phosphate buffer was homogenised at 5×10^7 Pa, with 5 passes at 4° C using a Lab 60 homogeniser. The homogenate was flocculated with equal volumes of 20 g poly(ethyleneimine) kg^{-1} yeast (0.5% w/v) at pH 7. Flocculation occurring at the ψ-shaped passive-injection mixer in the µ-flocculation device was recorded using the Photron MC-1 camera mounted on a Nikon TE-2000 microscope (30× magnification), at 2000 fps and with a 16.7 µs exposure time. Images were captured at different locations along the length of the microchannels, as shown in Figure 4.9. Data from the outlet of the device (x_7 = 59.9 cm) was selected for plotting particle-size distributions (PSDs) to give results most comparable with that of the Mastersizer. Images can be recorded practically at any point of length along the channel, as using the spiral number and the angle of rotation calculated from the images, the residence length and thereby, the average residence time can be estimated from the CAD file having the equation of the spiral. 10 ml sterile syringes (Plastipak with Luer-locks; Becton, Dickinson and Company, Oxford, UK) were used to inject the reactants with the help of two programmable syringe pumps (see Section 4.4.1).

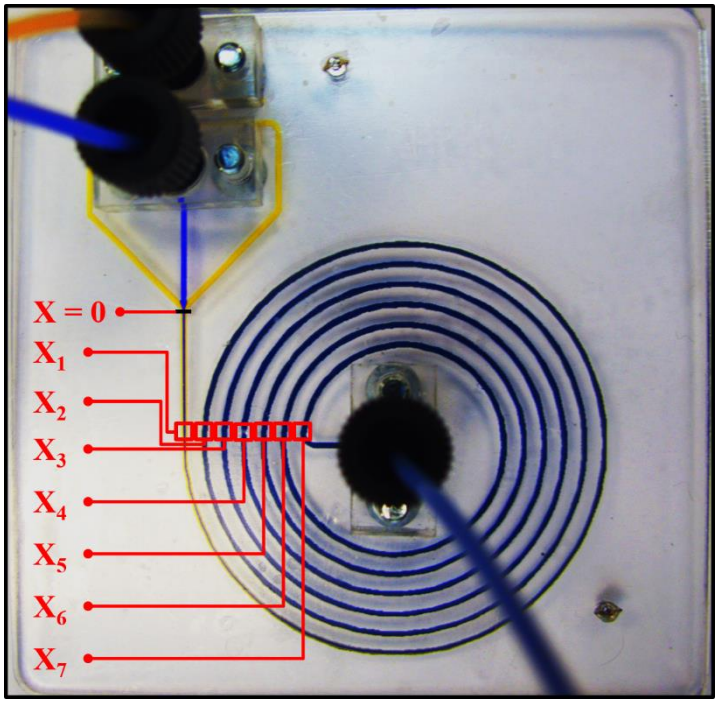

Figure 4.9: Image of the μ-flocculation device with the different imaging locations marked. 'x_i' refer to the distances (in cm) from the inlet where flocculation commences: x_1 = 1.44, x_2 = 14.32, x_3 = 25.94, x_4 = 36.31, x_5 = 45.42, x_6 = 53.28, and x_7 = 59.93 cm.

4.5 Results and discussion

In this section, we discuss several practical aspects of the setup, including the testing and validation of the image-processing algorithm, and the potential limitations of the analytical system as a whole.

4.5.1 Optimisation of the image-processing script

The high-speed imaging setup yields 8000 TIFF images, amounting to around 2 GB of memory, per dataset. The images were archived to an external hard-disk drive for offline analysis using the script. An initial serial implementation of the completed script was tested running sequentially on a standalone Windows PC with an Intel® Core™ i7 – 2630QM CPU with four 2 GHz physical cores (eight virtual cores with hyper-threading) and 8 GB RAM. The estimated time taken to process one set of 8000 images was initially around 12 hours. The algorithms were reworked, in particular to leverage NumPy array operations (which are performed in optimised C code rather than in the Python interpreter) and to reduce the memory footprint to avoid forcing the use of virtual memory by making the processing modular. With this approach, as outlined above the images are analysed in batches and then cleared

from memory before the next set are loaded, which allowed the memory usage to be kept to approx. 1 GB. This increases to around 2 GB when the script outputs images showing the analysis, but this is nonetheless manageable on a good modern desktop. The algorithm was also parallelised, which, along with the algorithm modifications, allowed the time taken to be reduced to around 20 minutes per dataset on four CPU cores. The time taken was found to depend heavily on the number of particles detected, and hence the number of features to be processed.

4.5.2 Optimisation of the morphology filters

Different structuring elements were tested for use with the close-open and median filters (Figure 4.10), and it was found that changes in particle shape as a result of the morphological operations affect the sizes of larger particles more significantly than smaller ones. In addition, as outlined previously, small particles (below 10 µm) were often found to move out of focus because of the large channel depth (500 µm), requiring a noise-removal step as part of the filtering, again keeping changes in particle size in mind.

As detailed in Section 4.3.3.1, a close-open morphological operator followed by a median filter was ultimately chosen for the image processing. The structuring element used with both the filters was varied, and the resulting variation in particle sizes observed. A structuring element too large can "dilate" large particles significantly (with dilation being the first step in the close-open filter), while effectively removing noise. On the other hand, smaller structuring elements preserve the size of large particles, but leave small pixelated features which later get identified as features.

These tests revealed that a 4 × 4 pixels^2 structuring element for the close-open filter led to an increase in particle size by ~3.7 µm for particles around 132.9 µm (2.8 %; Figure 4.11), while effectively removing noise. Elements of size 2 × 2, and 3 × 3 pixels^2 provided smaller increases in the size of these larger particles (0.8 % and 1.6 % respectively, but were poor at filtering out spurious small features, leading to an overall more detrimental effect on the recorded particle-size distribution.

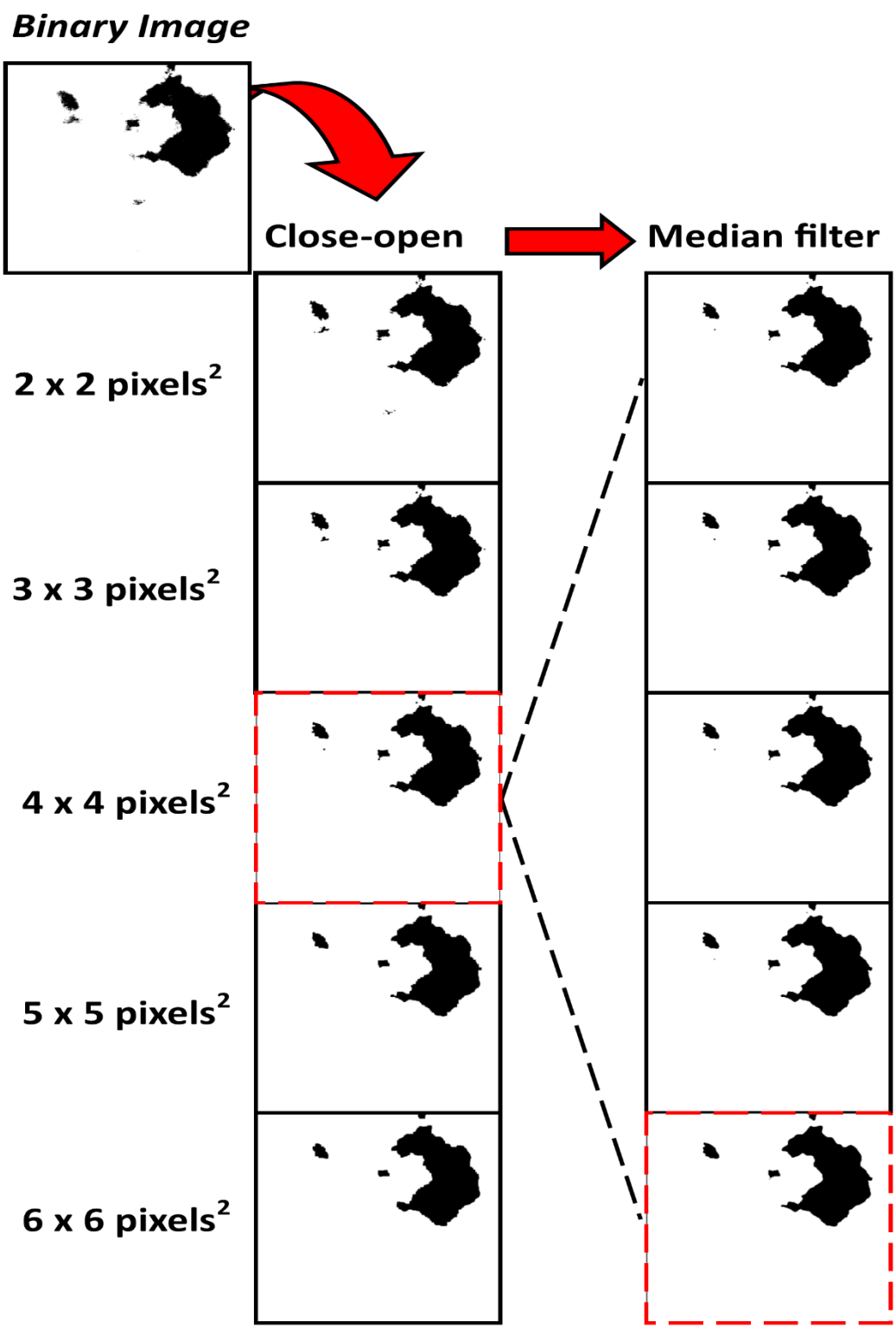

Figure 4.10: Characterisation of the variation in the floc morphology extracted from a sample image after close-open and median-filter operations using different structuring-element sizes. Different element sizes were tested for the close-open operation and a 4 × 4 pixels² element was chosen. This was followed by a median filter step with varying element sizes, where a 6 × 6 pixels² element seemed to be well-suited for removing small pixel features.

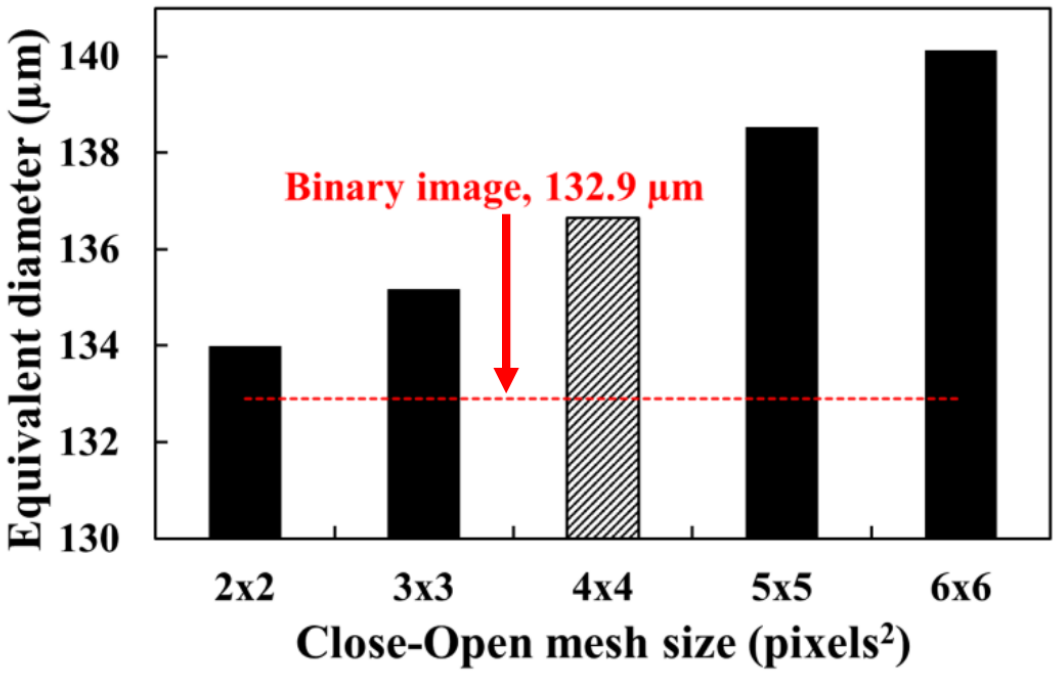

Figure 4.11: Variation of the equivalent circular particle diameter of a reference particle with different structuring-element sizes for the close-open morphological operation. The red dashed line denotes the size of the particle measured manually after binary image thresholding (132.9 µm). The dashed block (4 × 4 pixels^2) was chosen based on a balance of effective noise removal and preservation of the original particle size.

Applying a median filter after the close-open filtering step further reduces the noise and smooths the boundaries of particles. A 6 × 6 pixels^2 structuring element reduced the size of the reference particle from 136.6 µm (after the preceding close-open step) to ~133.8 µm; this opposes the increase in size resulting from the close-open, leading to an overall increase in size of 0.9 µm (0.67 %) from the 132.9 µm measured after thresholding (Figure 4.12). A 6 × 6 pixels^2 element translated to approx. 6 µm for the current experimental setup, and hence bigger element sizes weren't tested. It was noted that there is a trade-off between the lower limit of detection of the script and a robust noise removal. The chosen combination of a 4 × 4 pixels^2 close-open filter followed by a 6 × 6 pixels^2 median filter resulted in the removal of particles lower than *ca.* 6 µm at 20× magnification in the experimental setup being used here. This translates to ~4 µm particles at 30×. While these values can be used as a reference for the limit of detection of the image-analysis script, using higher-magnification lenses (e.g. 40× and above) on the microscope is expected to allow this to be reduced to below 4 µm. While this may suit some

applications, however, imaging a flocculating system, where larger particles are expected, necessitates the use of lower magnifications to accommodate the entire channel width of the µ-flocculation device within the viewport.

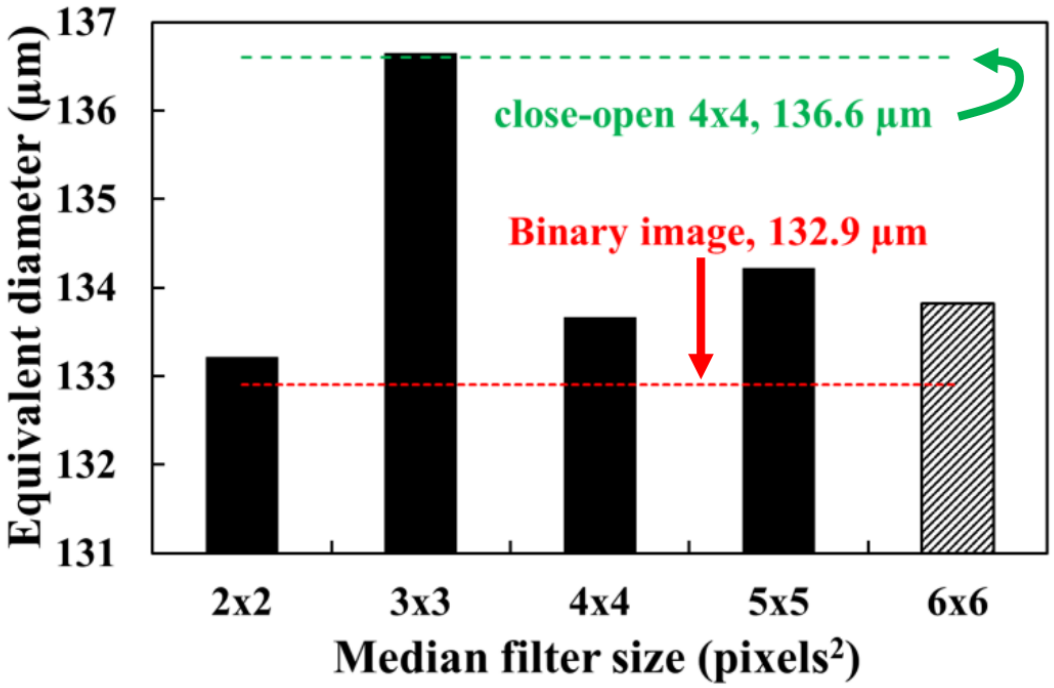

Figure 4.12: Variation of the equivalent circular particle diameter of a reference particle with the size of the structuring element used for the median filter applied after the close-open filtering. The red dashed line denotes the size of the particle measured manually after binary image thresholding (132.9 µm), whereas the green line denotes that after application of the preceding 4 × 4 pixels^2 close-open filter (136.6 µm). The dashed block (6 × 6 pixels^2) was chosen for effective removal of spurious small features which may skew the particle-size distribution. This filter size also reduces diameter of the particle from after the close-open step to 133.8 µm, leading to a final variation of around 0.9 µm with respect to the size measured immediately after thresholding.

On the other hand, the upper limit of detection is governed by the camera sensor resolution (i.e. pixels per unit area) and the magnification of the microscope. The natural breadth of the flocs (perpendicular to the fluid flow) is constrained due to the 500 µm channel widths. This can be addressed by building devices with larger channel dimensions, and correspondingly reducing the magnification. However, the combination of lower magnification and the camera-sensor quality can affect the reliability of measuring smaller particles. Arbitrary particle sizes along the flow

direction can be captured due to the image-stitching sequence implemented in the analysis routine. Therefore, for the current experimental setup with the μ-flocculation device, the upper limit of detection, of approximately spherical particles, can be considered to be the width of the microchannel (500 μm).

4.5.3 Validation with polystyrene beads

The analysis code was validated against micro particles of known diameter. Traces of each particle encountered in the image sequence were recorded, an example of which is shown in Table 4.2. As expected, particles which appear later in the video stream record zero pixel area for these frames. For each particle detected, the area increases as each particle enters the field of view, and reaches a plateau over the frames during which the entire particle is in view. The maximum pixel area in the plateau regions (Table 4.2; frames 5 to 7 for particle no. 1), are selected to be the area of the particles. These values are converted to μm^2 using a conversion factor based on the camera-sensor size and the magnification of the microscope, and are stored separately along with the length, breadth and equivalent circular diameter. A sample set of data from this characterisation is shown in Table 4.3.

While the measurements are evidently fairly accurate, the particles tend to be substantially longer than they are wide, indicating elongation in the direction of the fluid flow. It should be noted, however, that the data in the Table 4.3 lists only 10 of the 741 particles measured in 4 seconds. A detailed comparison of the widths and the lengths of flocs formed within the μ-flocculation device is presented in Chapter 5. Figure 4.13 shows the calculated particle-size distributions (PSDs) of micro particles of sizes 15, 25 and 30 μm, measured using both the image-analysis setup and a conventional light-scattering instrument (Mastersizer 2000). An accurate reading of the equivalent circular diameter (from the area of particles in $pixels^2$) was confirmed from the PSDs, in spite of the inherent approximations involved in the fitting of the data from the image-analysis routine to a Gaussian distribution. The lowest adjusted R^2 observed fitting the three sets of particle-size histogram was 0.75 for the 25 μm particles. This was possibly due to the presence of particle aggregates, which would have been labelled as single particles and hence have led to the distribution being skewed to larger sizes. It is also noteworthy that the % volume frequencies obtained from the two methods are significantly different, which can be attributed to the fact that the PSDs are directly proportional to the concentration of the particles, and these were not equated.

Table 4.2: Example trace recorded by the script. The maximum area corresponds to the 15 µm micro-particles used for testing. Images were recorded using a Phantom Miro 4 high-speed camera running at 2000 fps with a 16.7 µs exposure time, mounted on a Nikon Ti-E microscope. A graphical representation of the data in this table may be found in Figure 4.7. The units of area are px^2 (square pixels).

Frame No.	Total Occupied Area (px^2)	Particle No. 1 (px^2)	Particle No. 2 (px^2)	Particle No. 3 (px^2)
1	28	28	0	0
2	52	52	0	0
3	69	69	0	0
4	169	144	25	0
5	381	317	64	0
6	345	320	25	0
7	405	366	39	0
8	175	90	85	0
9	239	52	187	0
10	102	0	70	32
11	200	0	107	93
12	484	0	188	296
13	606	0	289	317
14	732	0	366	366
15	482	0	290	192
16	404	0	273	131
17	474	0	365	109
18	73	0	0	73
19	0	0	0	0

This is because the Mastersizer requires a suitable sample concentration to obscure the laser (see Chapter 2 for a detailed explanation), whereas controlling the number of particles flowing through viewport in four seconds of observation is not feasible. Based on these tests, it was confirmed that the script can accurately measure particles as small as 15 µm in a channel 500 µm deep, at 30× magnification, yielding results in good agreement with a more conventional light-scattering

instrument and without any unexpected anomalies. The wider applicability of the high-speed imaging setup was further supported through the successful analysis of images captured with both high-speed camera/microscope combinations.

Table 4.3: Sample characterisation of the particles observed in the test sequence. W, L and A denote the measured width, length and area of the particles, respectively. Particles 1-3, correspond to data extracted from the traces presented in Table 4.2. The (equivalent) circular diameter is calculated by assuming the area (μm^2) to be that of a circle (πr^2), and is useful for direct comparison to conventional particle-sizing instruments.

No.	W (px)	L (px)	A (px^2)	W (µm)	L (µm)	A (μm^2)	Circular Diameter (µm)
1	12	50	366	8.3	34.7	176.5	15.0
2	12	47	366	8.3	32.6	176.5	15.0
3	12	50	366	8.3	34.7	176.5	15.0
4	12	46	366	8.3	31.9	176.5	15.0
5	12	40	367	8.3	27.8	177.0	15.0
6	13	42	368	9.0	29.2	177.4	15.0
7	11	39	369	7.6	27.1	177.9	15.1
8	12	44	369	8.3	30.6	177.9	15.1
9	12	46	369	8.3	31.9	177.9	15.1
10	13	47	370	9.0	32.6	178.4	15.1

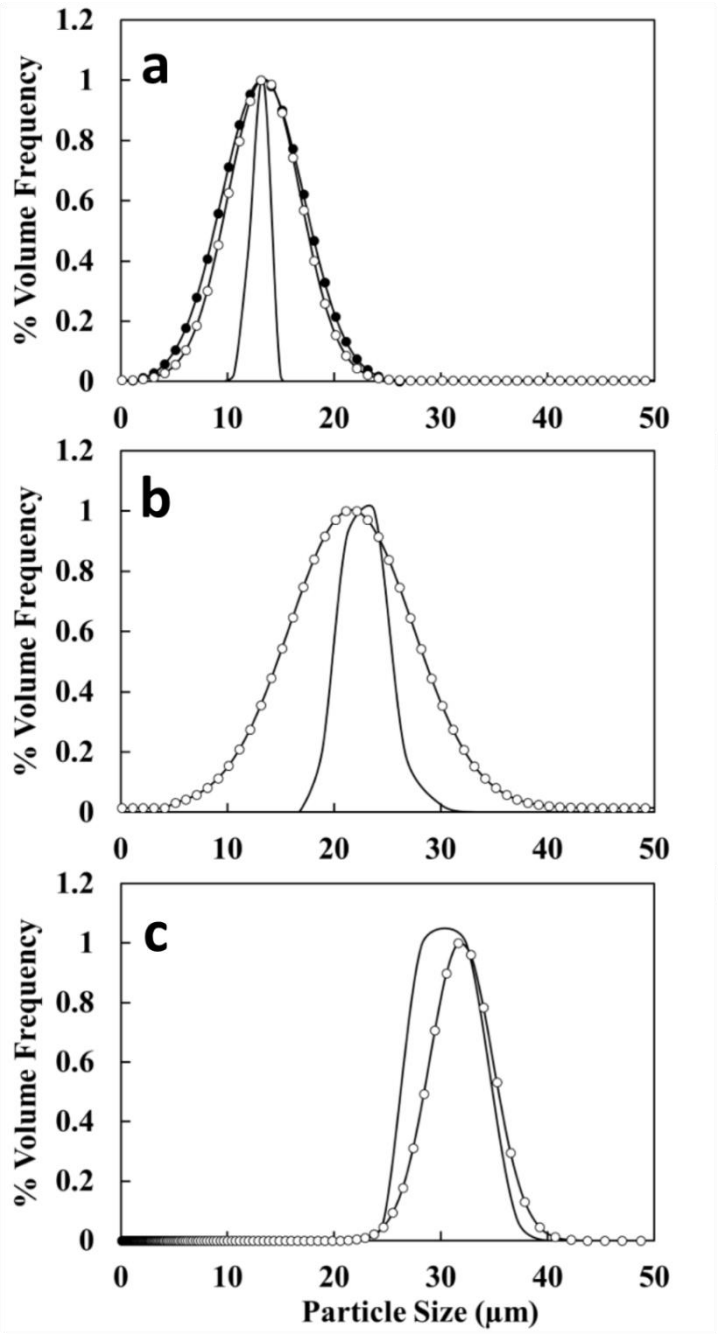

Figure 4.13: PSDs of different-sized micro particles, measured using both the image-analysis setup (lines with circular markers, ○) and the light-scattering equipment (line without markers). The three plots compare measurements of (a) 15 µm, (b) 25 µm, and (c) 30 µm micro particles. Histograms were generated from the data obtained from the image-analysis script using a second auxiliary Python program, and were fitted to Gaussian curves using the OriginPro software. The areas under the curve have been normalised. The 15 and 25 µm beads were recorded using the Miro 4 camera mounted on the Nikon Ti-E microscope, whereas the 30 µm beads were recorded using the Photron MC-1 camera on the Nikon TE 2000 microscope.

4.5.4 Preliminary measurements on irregular-shaped flocs

Figure 4.14 shows a sequence of high-speed images of a sample floc flowing through the microchannel, recorded by the high-speed camera. From visual observations, the particles were observed to flow through the centre of the channel, while showcasing a slight tumbling effect. It was also noted that the few smaller particles found flowing off-centre, seemed to attach with larger flocs flowing faster at the centre of the channel. This can be linked to the presence of an exaggerated floc-growth phase leading to bigger flocs in the µ-flocculation device than that of bench-scale system.

Apart from validation with polystyrene beads of fixed size and shape, the effectiveness of the script in measuring the size of flocs of undefined shapes was tested by comparison with manual floc-size measurement using ImageJ software. 50 random images from a single dataset was chosen and processed both through the script and manually in ImageJ. To make the manual measurements consistent, the images were converted to binary using the same threshold value used in the script. Following this step, the areas of different flocs were calculated by the in-built "Analyse Particles" function that labels different pixel islands from a binary image. 125 particles were measured from these 50 images, and Figure 4.15 shows a parity plot between the two methodologies. From the slope of the linear trend, it was observed that the script estimates sizes 1.5% higher than that of ImageJ. Alternatively, it is highly likely that ImageJ underestimated the sizes by not being able to accurately consider the boundary of flocs with just a binary-threshold. A size-preserving, bi-directional morphology filter seemed to function better in producing a clean floc-boundary while reducing noise and small pixel islands.

The standard error of the linear trendline was only 0.003 µm, with $R^2 = 0.999$. If any computational script involves machine-learning, the training step has to be performed rigorously and with a larger sample size (Jaccard *et al.*, 2014a, 2014b). The image analysis code developed for measuring floc sizes doesn't function based on a machine-learning algorithm, and has been validated already with NIST-traceable polystyrene beads. Therefore, comparison of sizes of 125 randomly chosen particles with ImageJ is considered to be an additional validation step to ensure an accurate measurement of floc sizes from pixel area.

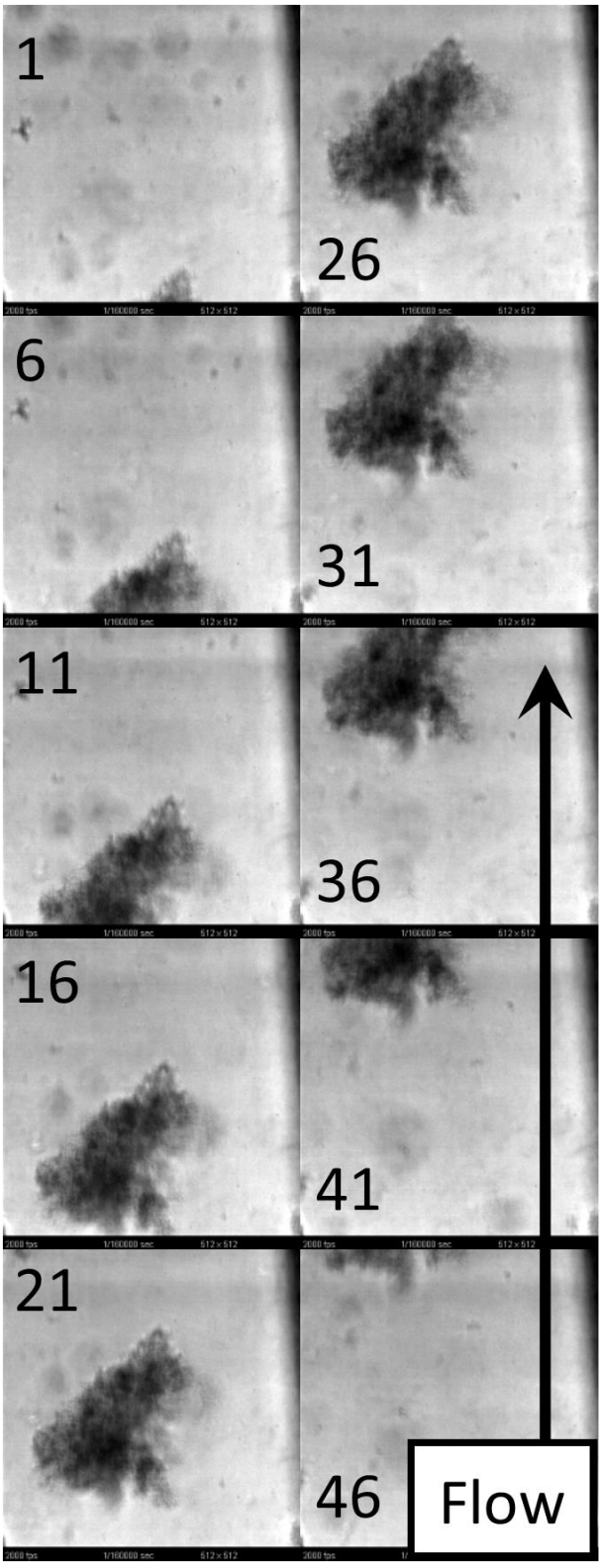

Figure 4.14: A sample image sequence of aggregates flowing through the microchannel. Images shown are every fifth frame from the high-speed image sequence, recorded at 2000 fps. The numbers represent the frame number of the high-speed images.

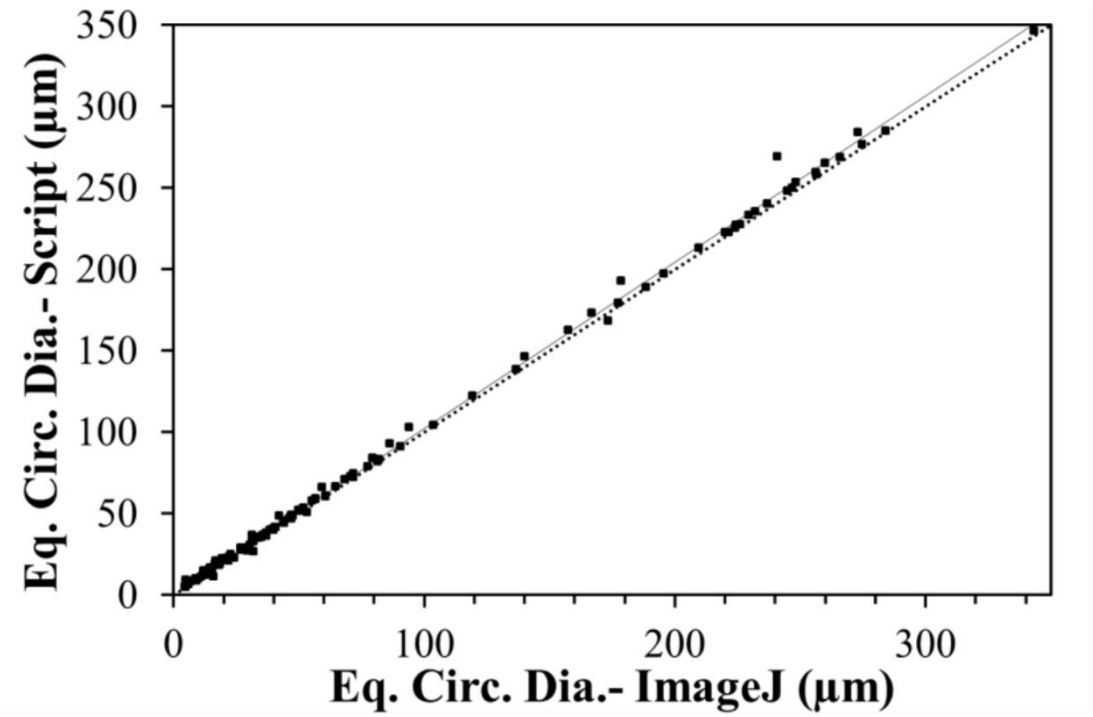

Figure 4.15: Graph represents the parity plot between diameters of flocs calculated using the image analysis script (Y axis) and manual measurement using ImageJ software (X axis). Data points represent 125 particles measured from 50 random images selected from a dataset of 8000 images. A linear correlation of y = 1.015x was observed with R^2 = 0.999.

Successful validation of the imaging setup, and analysis routine encouraged flocculation experiments for estimating the growth rates. Flocculation of a yeast homogenate - PEI (20 g kg^{-1} yeast, pH 7) system was observed with the standard parameters of a 2000 fps framerate and 16.7 µs shutter speed and a microscope magnification of 30×. A sample video sequence showing the flow of flocs, before and after re-labelling, can be found along a copy of this thesis (Appendix A4.2). For comparison, flocs prepared in a bench-scale setup (50 ml centrifuge tubes) were also administered directly into the microchannels for measurement. For characterising the flocculation performed in the µ-flocculation device, measurements were taken at several points along the channel as detailed in Section 4.4.2; measurements of the flocs prepared in the bench-scale setup were imaged near the ψ-shaped inlet. Complementary measurements of the flocs prepared at both scales were performed using the Mastersizer instrument. Figure 4.16 compares PSDs obtained from measurements on the µ-flocculation device and at bench scale measured using the two techniques.

The different floc sizes obtained at the two experimental scales, as measured using the Mastersizer, were discussed in Chapter 2; these plots highlight clearly the considerably larger floc sizes measured with the high-speed imaging setup, both within the µ-flocculation device and from the bench-scale preparation. The difference in size distribution between the two scales suggested by the imaging setup is higher than that recorded by the Mastersizer, and, moreover, the average size measured by the image-analysis script in both sets of experiments is much higher than that from light scattering. Since the accuracy of the script has been validated, this discrepancy can be attributed to the difference between an *in situ* sample measurement technique, which minimises sample handling, and the *ex situ* light-scattering instrument, which requires dispersing the sample. This further highlights the importance controlling shear rates in flocculation systems.

The high-speed imaging setup did record smaller floc particles (15-50 µm) in the bench-scale preparation (recorded near the inlet of the device), but very few flocs below 100 µm were observed, which was further reduced after the curve-fitting. This can possibly be attributed to the lower shear levels in the micro channels (as discussed in Chapter 3), leading to an exaggerated floc-growth condition where almost all polymeric flocculants flocculate with the cell debris following completion of passive micro-mixing. Comparing the average particle size and the size of the largest 10% of flocs (similar to the d50 and d90 particle sizes, typically quoted from light-scattering measurements), measured at different locations along the microchannel (as shown in Figure 4.9), showed significant floc-size variation (Figure 4.17), providing information about the growth rate of flocs for the particular flocculating condition employed in these experiments (i.e. 20 g PEI kg^{-1} yeast, pH 7).

The average diameter seems to remain constant at around 50 µm, while the d90 (equivalent) particle size increases from ~100 µm to 260 µm, after which the growth rate appears to plateau. The flocs seem to stop growing beyond around 250 µm (half of the channel width), which is possibly due to the exhaustion of the available flocculant strands preventing further nucleation, and also the increasing shear rates as the particle approaches the channel walls (see Chapter 3). The flocs seem to reach an average size of 50 µm at 1.44 cm from the inlet, suggesting a rapid agglomeration process near the inlet of the device, which is most likely further assisted by the passive mixing. This region, however, was experimentally difficult to analyse because of the presence of cell debris and the flocculant particles, which

were too small to be characterised, and led to significant noise which impeded the identification of larger particles by the image-processing algorithm.

Based on experimental evidence from Figure 4.17, these initial tests of the setup seem promising, and the imaging setup and analysis routine are well suited for the measurement of the growth kinetics of individual flocs formed within a microfluidic platform.

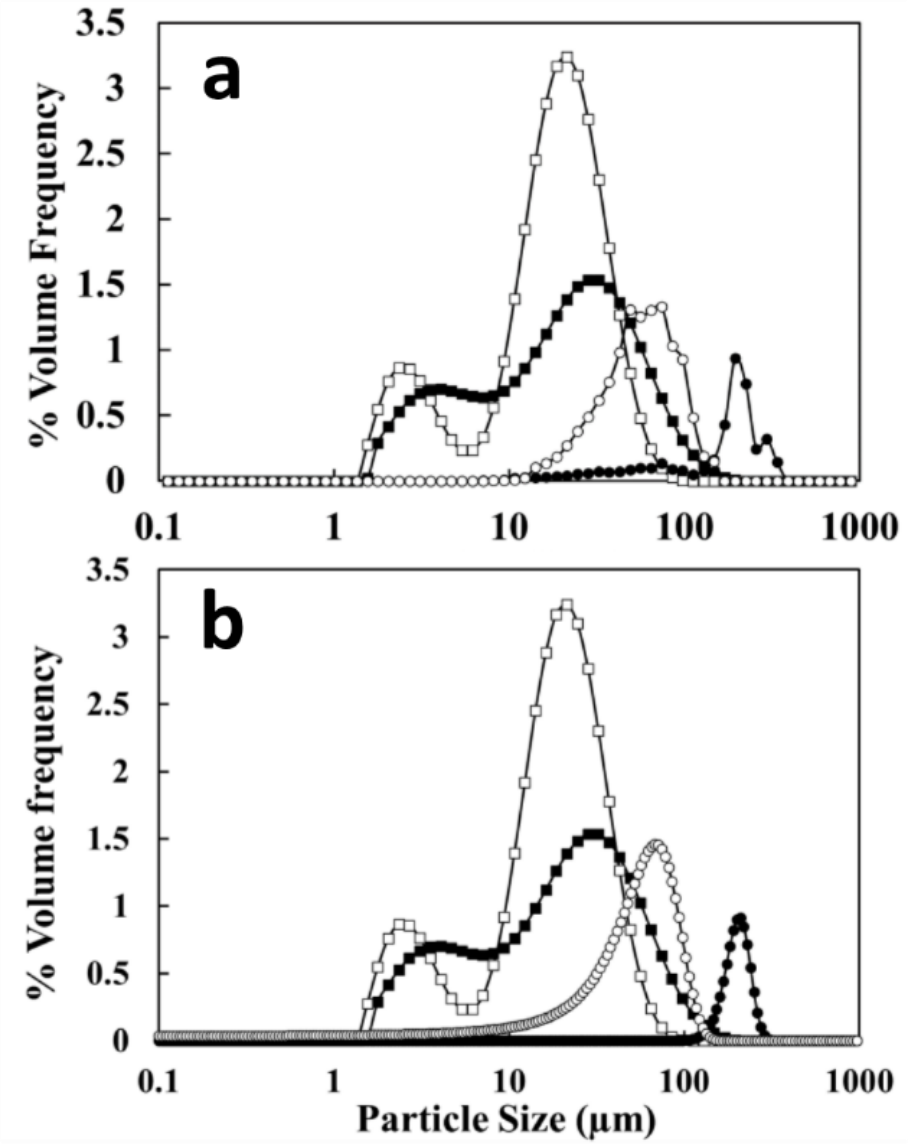

Figure 4.16: Particle-size distributions of flocs formed in the µ-flocculation device (closed markers) measured near the outlet (x_7 = 59.9 cm), and at bench scale (open markers). Square makers denote the PSDs obtained from the Mastersizer, while circular markers show the PSDs from the image-analysis technique. The PSDs from the image-analysis routine are shown both as histograms (a) and after fitting to a Gaussian curve (b; adjusted R^2 = 0.82).

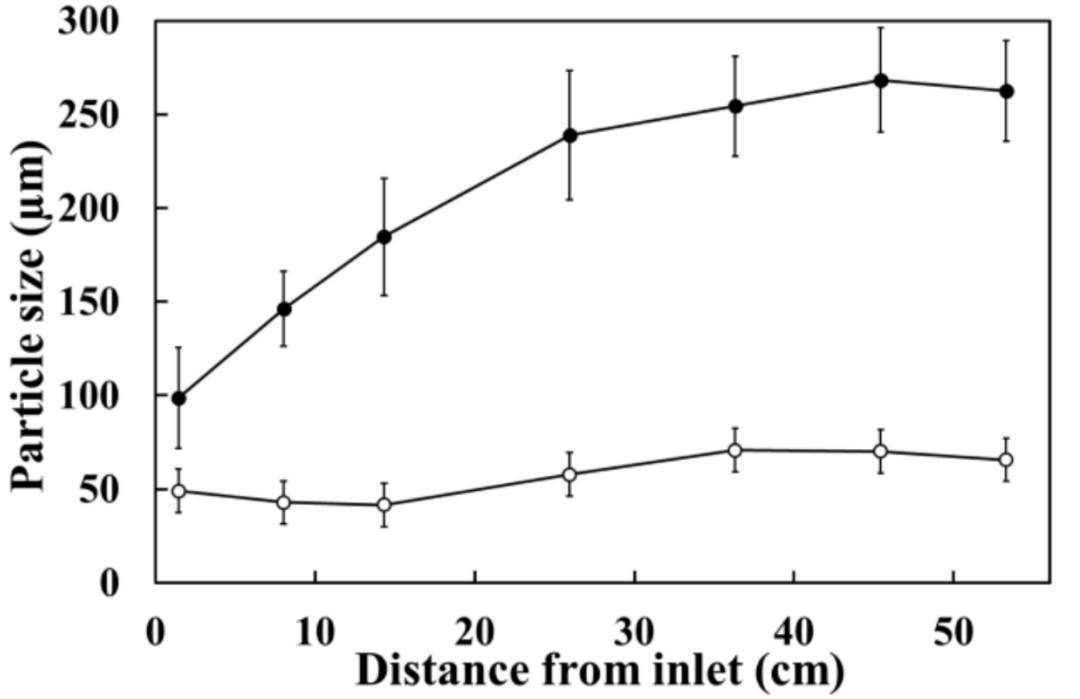

Figure 4.17: Floc sizes obtained by imaging at the different locations along the channel in the µ-flocculation device shown in Figure 4.9. 20 g PEI kg^{-1} yeast at pH 7 was used as the flocculant. The open markers indicate the average sizes of all the flocs observed in the image sequence (similar to the d50 particle size from the Mastersizer), and the closed markers show the largest 10% of flocs in the measurements made at each position. Error bars show ± 1 σ, calculated across the complete image sequence.

4.6 Conclusions

This chapter has presented the development of a high-speed imaging setup for real-time *in situ* measurements of particle morphologies in a µ-flocculation device. This system leverages the numerous advantages of optical-analytical technologies, in particular the ability of high-speed imaging to capture rapid events which otherwise cannot be probed with more conventional techniques. The imaging is performed with a conventional optical microscope and high-speed camera, and thus the platform can be built using easily-sourced laboratory equipment. The setup, in conjunction with a microfluidic device, facilitates spatial characterisation of flocculation events occurring within micro channels. Another key advantage is its bypassing the need for end-point analysis and sample handling, which can be tedious and potentially also error prone. The limits of detection depend on the experimental platform used; the setup described here allows measurement of particles between ~6 µm to around 500 µm, with the former being set by the

resolution of the images and the morphological filters, and the latter by the width of the channel walls.

To complement the hardware, an automated image-processing algorithm was developed and tested which rapidly and accurately extracts information on particle morphologies from large sequences of images. Images are binarized by thresholding, compared against a reference to remove artefacts/debris, processed using a set of carefully-selected and optimised image-filtering operations, and then features extracted and characterised. An “image-stitching” routine was developed to transparently handle flocs larger than the section of the channel captured in the camera viewport. The morphological information collected on each particle includes length, breadth, area and equivalent circular diameter, which can be used to simulate particle-size distributions comparable with e.g. light-scattering measurements. The script was also extensively optimised to minimise the memory and CPU requirements, and to parallelise the most compute-intensive parts of the algorithm, ultimately allowing datasets of 8,000 frames to be processed in 20 minutes on commodity computer hardware. The setup and analysis code were validated by analysing micro particles of three known sizes, with the measurements compared to those from light-scattering experiments, and excellent agreement was observed between the two techniques. The sizes measured by the script were then compared with floc-sizes manually measured using ImageJ software. The setup was then used to measure the size of flocs prepared both within the µ-flocculation device and in a bench-scale setup, and these results again highlighted the potential of this setup for recording the growth of flocs within the µ-flocculation device in real-time. Overall, the high-speed imaging setup with the automated image-processing algorithm seemed better suited than a commercially-available light-scattering instrument for characterising shear-sensitive particles such as flocs. Moreover, the imaging provides more information about particle morphology than the spherical volume obtained from light-scattering profiles, which could for example be important for studying anisotropic growth induced by the constraints of the channels in microfluidic devices. The setup is functionally versatile and could be applied to the measurement of other particles of arbitrary shape and size, such as the micro particles used for validation. Finally, as a language Python is easy to learn and has an active user and developer community which provides easy access to a large amount of functionality *via* add-on modules. This ecosystem will allow the present algorithm to be easily extended when it is released as open-source software in the future.

5. Estimation of flocculation growth kinetics in the μ-flocculation device

This chapter discusses the implementation of the microfluidic experimental platform (discussed in Chapter 2) along with the high-speed imaging setup (Chapter 4) devised to measure the growth of flocs *in situ*. A variety of flocculants were tested and the growth kinetics was compared, ultimately yielding a rapid growth kinetics measurement platform for screening of new flocculation systems.

5.1 Introduction

5.1.1 Importance of measuring growth kinetics of flocculation

The process of flocculation consists of different sub-processes taking place simultaneously. The initial adsorption process of the flocculants onto the surface of the colloidal particles is well-understood through different adsorption kinetics theories (Gregory and Barany, 2011). The flocculation of the micro-flocs to form larger aggregates have been broadly classified into four different types (Agerkvist, 1992; Bolto and Gregory, 2007; Duan and Gregory, 1996; Gregory and Barany, 2011; Treweek and Morgan, 1977). This has been discussed in detail in Chapter 1. Figure 5.1 is a representative image of the sequence of sub-processes taking place in a flocculating system.

While these mechanisms are well-understood, the detrimental factor in progressive research on flocculation has been the effect of different physicochemical parameters on flocculation, like pH (Mészáros *et al.*, 2004), flocculant dosage (Mondal *et al.*, 2013; Narong and James, 2006; Salt *et al.*, 1996) and shear (La Mer, 1960; Salt *et al.*, 1996; Wyatt *et al.*, 2013). In larger scales, these parameters have been screened for flocculation processes where there is equilibrium between floc-growth and breakage phases. The lack of appropriate analytical tools for these scales makes the study of growth kinetics experimentally unfeasible.

Modelling of flocculation taking into account different experimental factors involve various assumptions, such as having a high collision efficiency, a laminar flow profile, and perfectly spherical particles, to name a few (Thomas *et al.*, 1999). This deviates from reality, where modelling the relationship between floc growth, breakage and fluid properties of the system is complex (Šulc *et al.*, 2012). Moreover, the models developed so far consider only a two-body interaction within a

monodisperse sample population. This can be a significant limitation when applied to polydisperse biological cell suspensions (Wickramasinghe *et al.*, 2005).

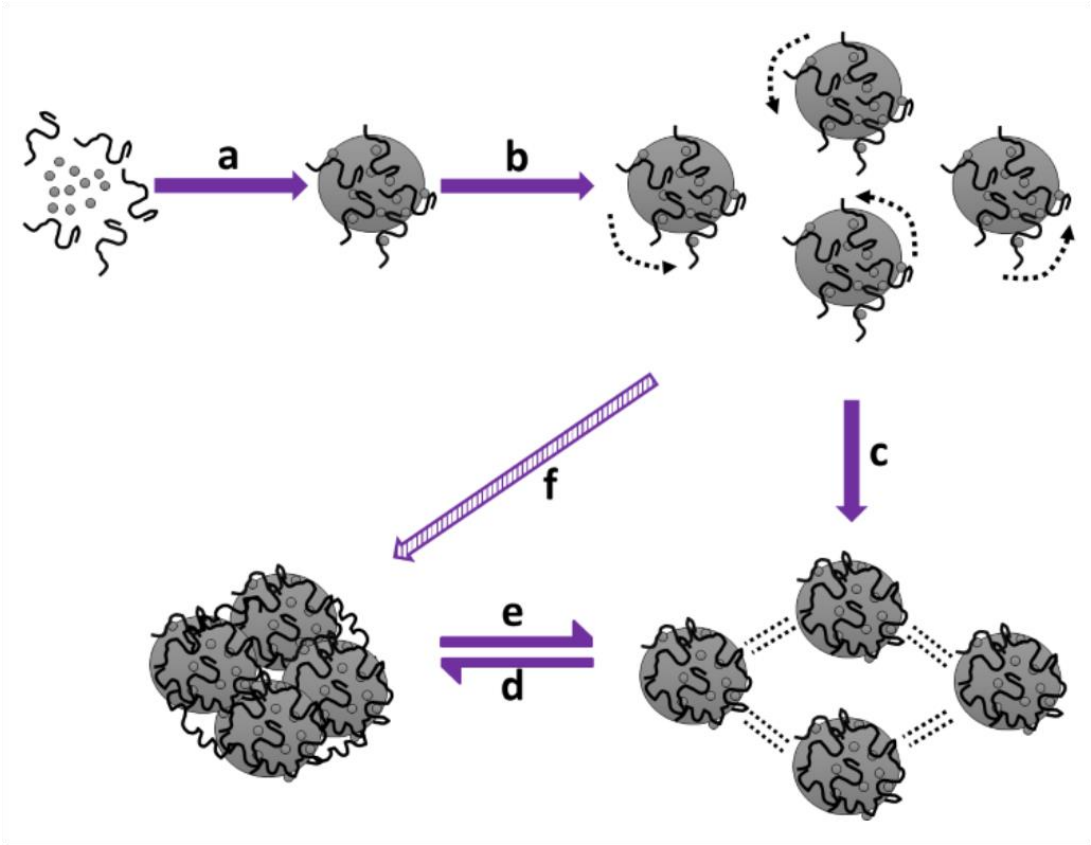

Figure 5.1: A schematic representation of the mechanism of flocculation using polymeric flocculants. (a) Adsorption of the flocculants onto the colloidal particles (~10 nm - 5 µm) to form unit flocs (i.e. micro-flocs, ~ 20-60 µm). (b) The adsorbed polymers undergo a 3D conformational change to attain a low-energy configuration. (c) The ageing process where the micro-flocs further changes its shape and size over a uniform shear level and improves its strength. (d) This is soon followed by the aggregation of the aged flocs to form large macro-flocs (~100-1000 µm). (e) This process is in a reversible equilibrium with breakage of flocs. (f) Depending on the uniformity and magnitude of shear exposed, the flocs may rapidly agglomerate to form large but weaker flocs, by-passing the ageing process. The image was adapted from Gregory 1988.

The necessity of measuring the rate of flocculation and its dependence on the concentration of the flocculant added was discussed by Gregory in 1973, where the importance of studying the rate of adsorption under non-equilibrium conditions, i.e. floc-growth in isolation from breakage, was mentioned. A non-equilibrium

flocculation state is also one of the other assumptions usually made while modelling a flocculation process.

The μ-flocculation device with the bespoke imaging platform has enabled the observation of the kinetics occurring during floc growth (between steps '*a'* to '*c'* in Figure 5.1) in isolation from the floc-ageing/breakage phases (steps *'d'* to *'f'* in Figure 5.1). This is of special interest for pharmaceutical and waste-water treatment industries, as the advancements in microfluidic technologies and optical imaging platforms have enabled a more fundamental understanding of flocculation growth kinetics experimentally. This system enables the rapid screening of newer synthetic flocculants, or different cell-lines expressing a variety of host-cell proteins, etc. and ultimately leads to a faster and more robust process development.

5.1.2 Choice of different flocculation systems

5.1.2.1 Cell suspension – Yeast homogenate

Baker's yeast (*Saccharomyces cerevisiae*) has been long known for its industrial importance, especially in the biopharmaceutical sector, and hence the product separation step involving its flocculation has been widely studied (Bauer *et al.*, 2010; Domingues *et al.*, 2000; Habib *et al.*, 2000; Milburn *et al.*, 1990; Salt *et al.*, 1996, 1995; Tsoka *et al.*, 2000; Wickramasinghe *et al.*, 2010). Yeast homogenate is anionic due to the presence of mostly lipids (45% of dry cell weight), DNA (0.4%), RNA (5%), etc. (Rose and Harrison, 1971) which act as contaminants and hence, requires selective removal to isolate soluble proteins. Therefore, as a well-studied cell suspension, the homogenate of Baker's yeast, was used for the flocculation growth kinetics study presented in this chapter.

5.1.2.2 Physical properties of polymeric flocculants

Polymeric flocculating agents have been procured from natural sources and more recently made from synthetic sources. Based on the charge carried by these polymers, they can be broadly classified as ionic (also known as polyelectrolytes), and non-ionic, flocculants. La Mer and Smellie Jr. in 1960 defined a polyelectrolyte as "a type of macromolecule in which the polymer possesses a number of electrical charges (or ionized states) along the molecular chain of carbon atoms". Electrical forces created by the charged species in a polyelectrolyte decide the shape of that particular molecule varying from a linear shape to a coiled one. A general characteristic of a flocculant is the presence of a long carbon chain with different side groups that carry charge, in the case of polyelectrolytes. Usually such

polyelectrolytic flocculants are used for separation purposes in different fields, ranging from waste water treatment to pharmaceutical drug manufacture. A detailed discussion of various flocculants, their physical characteristics, and the adsorption mechanisms have been covered by Bolto in 1995, and more recently by Gregory and Barany in 2011. The most important characteristic of choosing a flocculant depends on its molecular weight and charge density, which affect the rate of flocculation. The charge density is of prime importance as it decides the optimum dosage concentration, especially for a charge neutralisation mechanism. In the field of water treatment, typical doses are in the range of 1 to 10 mg per litre for polyelectrolytes used as primary coagulants, and only 0.1 to 0.2 mg per litre when used as a flocculation-aid (Bolto and Gregory, 2007). Because of the anionic property of the yeast homogenate, cationic flocculants were screened and two of the most commonly used cationic flocculants were selected, namely poly(ethyleneimine) (PEI), and poly(diallyldimethyl)-ammonium chloride (pDADMAC) (Letterman and Pero, 1990). Poly(ethylene) glycol (PEG) was also selected to test the growth of flocs in the µ-flocculation device with a non-ionic flocculant.

PEI is a widely used flocculating agent carrying a high cationic charge density due to the presence of primary, secondary and tertiary amines in the 1:2:1 ratio (Tang and Szoka, 1997), as shown in Figure 5.2a. This charge density is affected by the pH and ionic strength of the aqueous phase (Amin *et al.*, 2013; Mészáros *et al.*, 2004; Neu *et al.*, 2005), and hence the relation between the change in pH and the consequent alteration in the rate of flocculation becomes important. Implementation of co-polymers have also been studied, where PEI has been used along with non-ionic flocculants like PEG. A more recently applied flocculant- pDADMAC is known to be more cationic than PEI and has a 100 mol% charge density (Bolto and Gregory, 2007). It was first synthesized in 1957 by Butler G. in the University of Florida, and the polymer carries an N-substituted pyrrolidine structure (Figure 5.2b). They have seen an increasing interest as a flocculant, especially in the waste water treatment sector owing to their large molecular weights, and their properties have been discussed by Napper in 1983. Finally, PEG, a non-ionic polymer, is relatively linear in structure with long carbon chains (Figure 5.2c) and has been of interest as a surfactant and also a flocculant. These properties have been attributed to the capability of PEG to alter the interactions of cells and protein with water, and also between each other (Israelachvili, 1997).

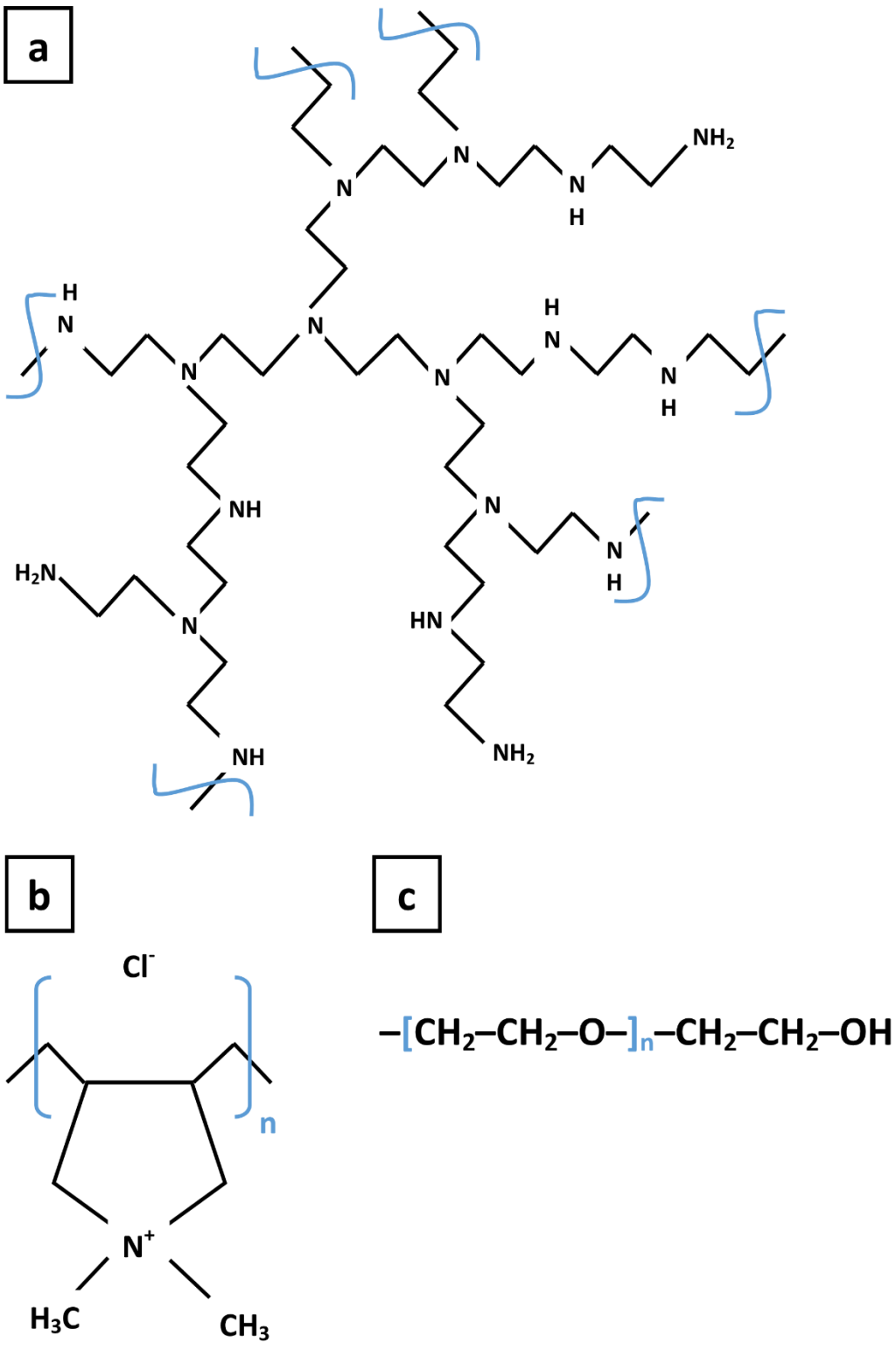

Figure 5.2: Structures of the different polymeric flocculants tested in this work. (a) Branched poly(ethyleneimine) – PEI (Tang and Szoka, 1997). *(b) Poly(diallyl dimethyl)-ammonium chloride (pDADMAC) adapted from* (Bolto and Gregory, 2007). *(c) Structure of poly(ethylene glycol) – PEG* (Israelachvili, 1997). *While PEI and pDADMAC are cationic flocculants, PEG is non-ionic.*

5.1.2.3 Safety considerations to be addressed during flocculant selection

It has been noted that non-ionic and anionic polymers are usually of low toxicities, but cationic polymers are known to be more toxic (Hamilton *et al.*, 1994), especially to aquatic species leading to a mechanical gill-blockage and suffocation. Consequently, the use of cationic polyelectrolytes have been stopped in countries like Japan and Switzerland for water treatment, and Germany and France have implemented stricter regulations (Bolto and Gregory, 2007). It has also been observed that monomers of these polyelectrolytes are more toxic, and a detailed review on the hazards and health significance of flocculants including pDADMAC and PEI can be found in Letterman and Pero 1990. As an example of the stringent regulations, the maximum allowed limit of the monomers of polyacrylamide (an anionic flocculant) and pDADMAC in drinking water are 0.025% and 0.5% respectively (Bolto and Gregory, 2007). In the bioprocessing sector, a cationic polymer dosage of above ~70 mg per litre has been known to significantly disrupt yeast cells. It is worthwhile to note that, anionic and non-ionic polymers do not have this effect on yeast, probably due to the absence of attractive forces (Narita *et al.*, 2001).

A brief note on the importance of considering the toxicity of cationic polymers has been discussed above. Therefore, while screening for flocculants to suit a selective product separation step of any biomolecular product, parameters like the charge density, molecular weight, and also safety properties must be taken into account. If the flocculant is of relatively high toxicity value, steps to ensure a low residual flocculant level downstream, must be taken to conform to country-specific regulations.

5.2 Materials and Methods

The experimental work presented in this chapter largely deals with the use of the µ-flocculation device placed on a microscope stage imaged using a high-speed camera to observe the rate of growth of flocs formed inside the microchannels, under varying concentrations and pH.

5.2.1 Flocculation setup

250 mg/ml of Baker's yeast (*S. cerevisiae*, DCL CraftBake Yeast, JW Pike, London, UK) was homogenised using a pilot-scale, Manton-Gaulin Lab 60 Homogeniser

(APV-SPX Ltd., Crawley, UK) at 5 × 10^7 Pa, 5 passes at 4 °C (Salt *et al.*, 1996). 1 kg yeast was dispersed in four litres of 100 mM phosphate buffer♠ at pH 6.5. Under total recycling conditions, five passes took 20 minutes (starting from the point when the pressure reaches 5 × 10^7 Pa). The resulting homogenate was used for the flocculation experiments after adjusting the pH using 2 M HCl and 2 M NaOH.

Two cationic flocculants – PEI and pDADMAC, and a non-ionic flocculant PEG were selected for this study and concentrations of 5, 10, 15, 20 and 25 g flocculant kg^{-1} initial yeast (0.125 to 0.625% w/v, respectively), were made for a set of experiments at pH 7. For the analysis at a range of pH (5 to 7.5), a constant flocculant concentration of 20 g kg^{-1} yeast (0.5% w/v) was used. The physical properties of the flocculants have been shown in Table 5.1.

Aliquots of varying concentrations of all the flocculants were prepared from their respective stock solutions and were stirred continuously overnight, to ensure a homogenous dispersion of the polymer in the aqueous medium and also to make certain that the flocculants reached a stable conformation.

Flow rates of 75 µl min^{-1} was applied for the yeast homogenate stream (focussed flow) and 85 µl min^{-1} for the flocculant in the sheath flow in two Hamilton 1010 TLL glass syringes (Hamilton Company, Nevada, USA), using two programmable syringe pumps- a KDS200 Infuse/Withdraw Programmable Syringe Pump (KD Scientific Inc., Massachusetts, USA) and an Aladdin Programmable Syringe Pump (WPI Ltd., Hertfordshire, UK). Approximately 20 cm long polytetrafluoroethylene (PTFE, S1810- 10, Bola, Germany) tubing (1/16 inch external, 0.8 mm internal diameters) was used to connect the syringes to the chip, through M6 interconnects and ferrules (P207X and P250X; Upchurch Scientific, Washington, USA).

5.2.2 Fluid transport into the µ-flocculation device

To ensure a reproducible, bubble-free priming of the flocculation components the transport of fluids was carried out as shown in Figure 5.3. The fluidic junction of M6 adapters contained connection between Male to Female Luer locks (P-657 Upchurch Scientific, Washington, USA) with Female to Male Luers (P-660 Upchurch Scientific) for quick alternation of tubing between the experimental reagents stream

♠ 100 mM disodium hydrogen orthophosphate + potassium dihydrogen orthophosphate, filtered using 0.2 µm Thermo Scientific Nalgene MF75 bottle top filter.

and the priming/cleaning line. 0.5 M NaOH was used to clean the channels between each experimental condition.

Table 5.1: List of flocculants used to study the growth kinetics with their molecular weights, size and cationic charge densities (CD).

Flocculant (stock conc.)	**Notation**	**Molecular weight (kDa)**	**Size♣ (nm)**	**CD (mol%)**	**CD (mEq g^{-1})**
PEI (99 % w/v)	PEI_L	10	6	20-45♥	20♦
PEI (30 % w/v)	PEI_M	70	15.9		
PEI (30 % w/v)	PEI_H	50-100	13.4-19		
PEG (100 %)	PEG_L	6	4.6	-	-
PEG (100 %)	PEG_H	100	19		
PDADMAC (35 % w/v)	$pDADMAC_L$	<100	<19	100♠	6.2♠
PDADMAC (20 % w/v)	$pDADMAC_M$	200-350	26.8-35.5		
PDADMAC (20 % w/v)	$pDADMAC_H$	400-500	37.9-42.4		

All three PEI and PEG_H were procured from Alfa Aesar, Massachusetts, USA; PEG_L from VWR Chemicals, Leicestershire, UK; and all three pDADMAC from Sigma-Aldrich Company Ltd., Dorset, UK.

Adsorption of the flocculant onto the channel walls, which can alter the flocculation process taking place in the microchannels, is an important factor that had to be considered. The importance of tracer adsorption and its effect on RTD has been discussed by Bodla *et al.*, 2013. Therefore, the removal of any clogs and any polymeric flocculent attached to the surface of the channels was verified manually, by visual observation along the channel length of the device. Once cleaning was performed, the tubing containing the homogenate and flocculant were re-connected and the fluids purged until a steady-state was achieved. Priming of the channels with the flocculation system was carried out for a period of at least twice the

♣ Sizes measured assuming zero charge density (Bolto and Gregory, 2007).
♥ From Suh *et al.* 1994.
♦ From Neu *et al.* 2005.
♠ From Bolto and Gregory 2007.

average residence time of the particles in the channel at the combined volumetric flow rate used (2τ = 114 s). This was *ca.* 1.7 times t_m and provided enough time for all the previous initial flocculating molecules diluted by water from the cleaning cycle to be purged out completely. High-speed imaging

Flocculation experiments of yeast homogenate with PEI and PEG were performed with a Photron MC-1 high-speed camera (Photron USA Inc., California, USA) attached to a Nikon Ti-E microscope (Nikon UK Ltd., UK) with an automated stage (MEC56110, Nikon UK Ltd., UK) to enable a spatial control over the imaging locations, reproducibly. Flocculation of yeast homogenate and pDADMAC was recorded using the Phantom Miro-4 high-speed camera (Vision Research Ltd., Bedford, UK). All images were recorded at 2000 fps, 16.7 µs exposure, and with a 30 W halogen light illumination at 30× magnification.

5.3 Results and Discussion

5.3.1 Reproducibility testing of the imaging setup

All the experiments presented in this chapter have been performed using the high-speed imaging platform (see Appendix A5.1), whose accuracy was tested and validated, explained in the previous chapter. In spite of the flocculation system being in a continuous process reaching steady-state, experiments with 20 g PEI_H kg^{-1} yeast at pH 7, were performed thrice in the µ-flocculation device to test the experimental variability. Figure 5.4 shows the d50 and d90 sizes obtained at two different locations in the device. The standard deviations at position X3 (25.9 cm from the inlet) was ± 5.9 µm for d50 and ± 7.1 µm for d90. This mildly increased only to ± 10.2 µm for d50 and ± 8.3 µm for d90, at the X6 position near the outlet of the device (53.2 cm from the inlet). Based on this evidence, a repeatable fluid-flow within the µ-flocculation device using the fluidic transport setup (Section 5.2.2) was confirmed.

The fluidic setup was initially tested with a 3-way valve connecting the flocculation reagents and the priming line, thereby having only a single tube for each inlet of the device. Flow was switched between experiments to purge the channels with NaOH and water. This led to problems in re-priming the system with the flocculation reagents, as it took considerably longer to overcome the dilution of the reagents with the residual de-ionised water in the tubing and also in achieving a steady-state. Moreover, the use of a 3-way valve added a dead-volume at the junction, where a diffusion of the reagents with water was visually observed. Therefore, the setup as

mentioned in Section 5.2.2 was implemented to overcome such issues, in spite of the requirement of additional M6 connectors.

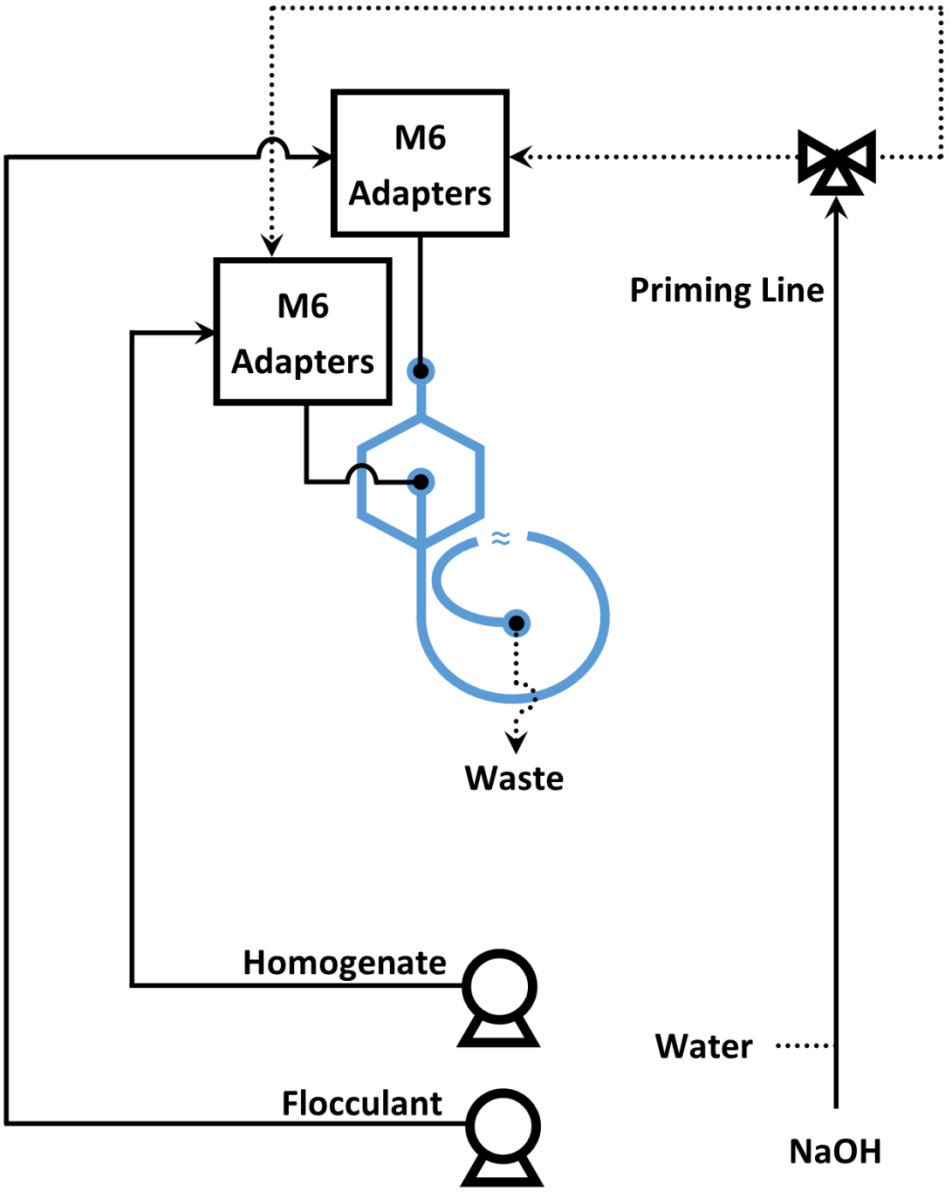

Figure 5.3: PID representation of the fluidics to transport the reagents for flocculation experiments. The µ-flocculation device has been presented in blue colour. The M6 adapters involved the use of Male to Female M6 Luer locks, with Female to Male M6 Luers, for easy switching between the flocculation tubing with the priming line to clean the microchannels in between experimental runs. 0.5 M NaOH was used to clean the channel followed by de-ionised water.

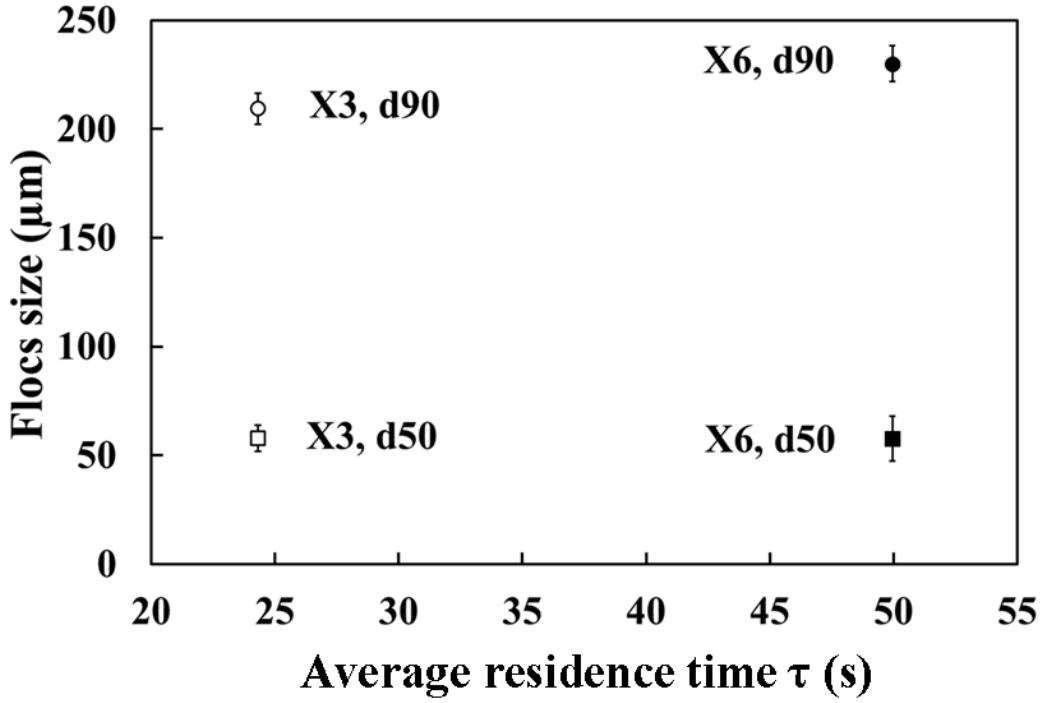

Figure 5.4: Repeats of flocculation trials at two different positions in the µ-flocculation device. Circular markers denote d90 floc size and square markers represent d50 floc sizes. Flocculation performed between yeast homogenate and 20 g PEI_H kg^{-1} yeast at pH 7. X3 is 25.9 cm from the ψ-shaped inlet, and X6 is the position at 53.2 cm. The error bars denote ± 1σ (n=3).

5.3.2 Investigation on the diameter of flocs

Images recorded for a duration of 4 seconds at each imaging location was analysed using the computational image analysis script discussed in Chapter 4. The illumination and the depth of field were adjusted so as to have a clear contrast between the flocs and the background (i.e. channel bed and walls). Sample high-speed images recorded between yeast homogenate and 25 g PEI_L kg^{-1} yeast at pH 7, have been shown in Figure 5.5, where the effect of secondary flow perpendicular to the fluid flow direction was not visually observed. As discussed in Chapter 3, the secondary-flow forces can be safely assumed to be lesser than the attractive forces between flocculating particles that partake in the nucleation of flocs, and hence negligible. However, particles of especially smaller sizes (below ~100 µm) seemed to undergo 'tumbling', where they appeared to rotate normal to the plane of view.

Flocculation of yeast homogenate with PEI_H (Mol. Wt. 50 – 100 kDa) was tested at varying concentrations and pH, and the floc sizes calculated as shown in Figure 5.6.

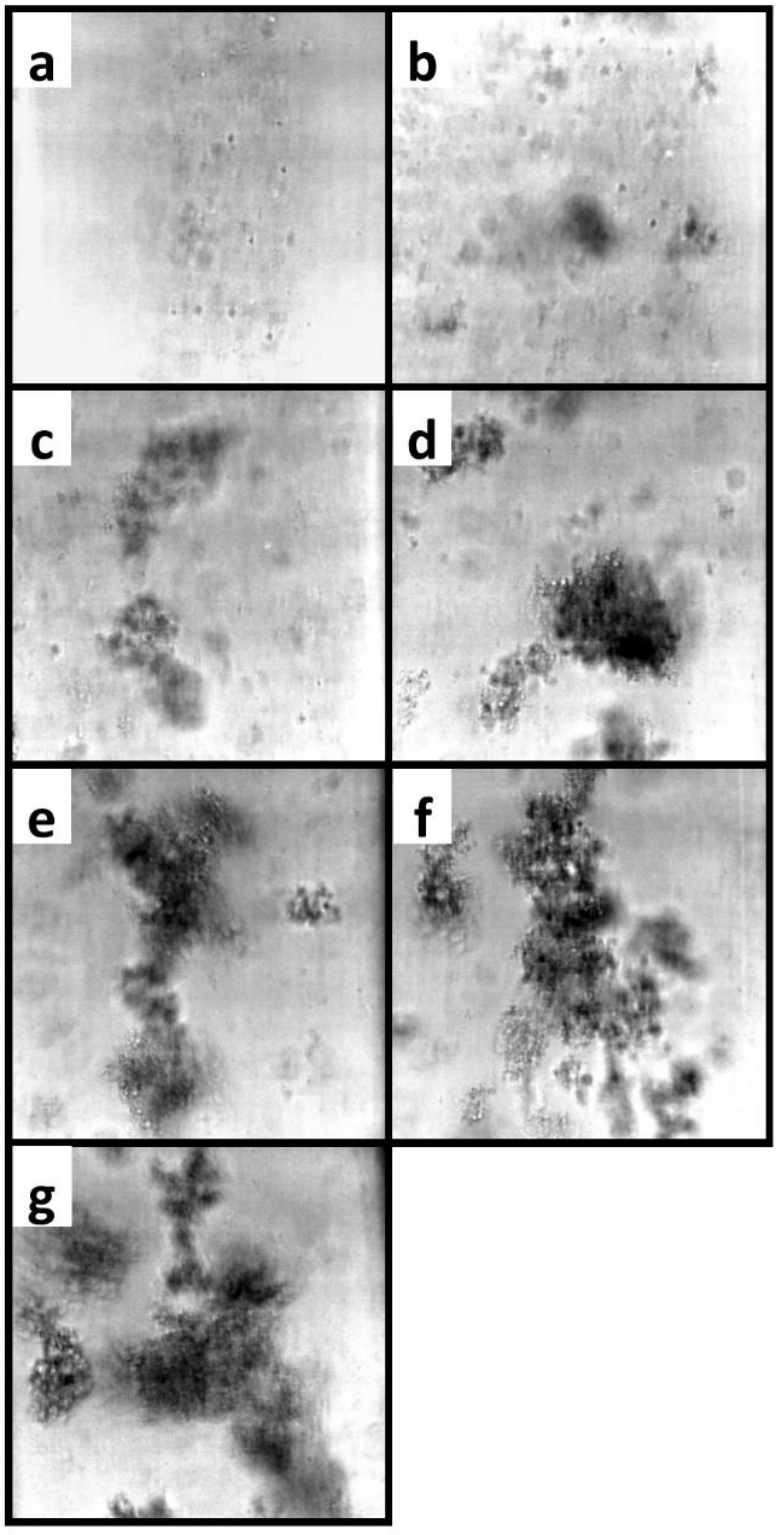

Figure 5.5: Sample high-speed images of flocs formed at different imaging locations. Distance from the ψ-shaped inlet: (a) 1.44 cm, (b) 8.03 cm, (c) 14.32 cm, (d) 25.94 cm, (e) 36.31 cm, (f) 45.42 cm, and (g) 53.28 cm. The imaged flocs were formed between yeast homogenate (focussed flow) and 25 g PEI_L kg^{-1} yeast (sheath flow), at pH 7. Volumetric flow rates of 75 µl min^{-1} (focussed flow) and 85 µl min^{-1} (sheath flow) were used for the experiments.

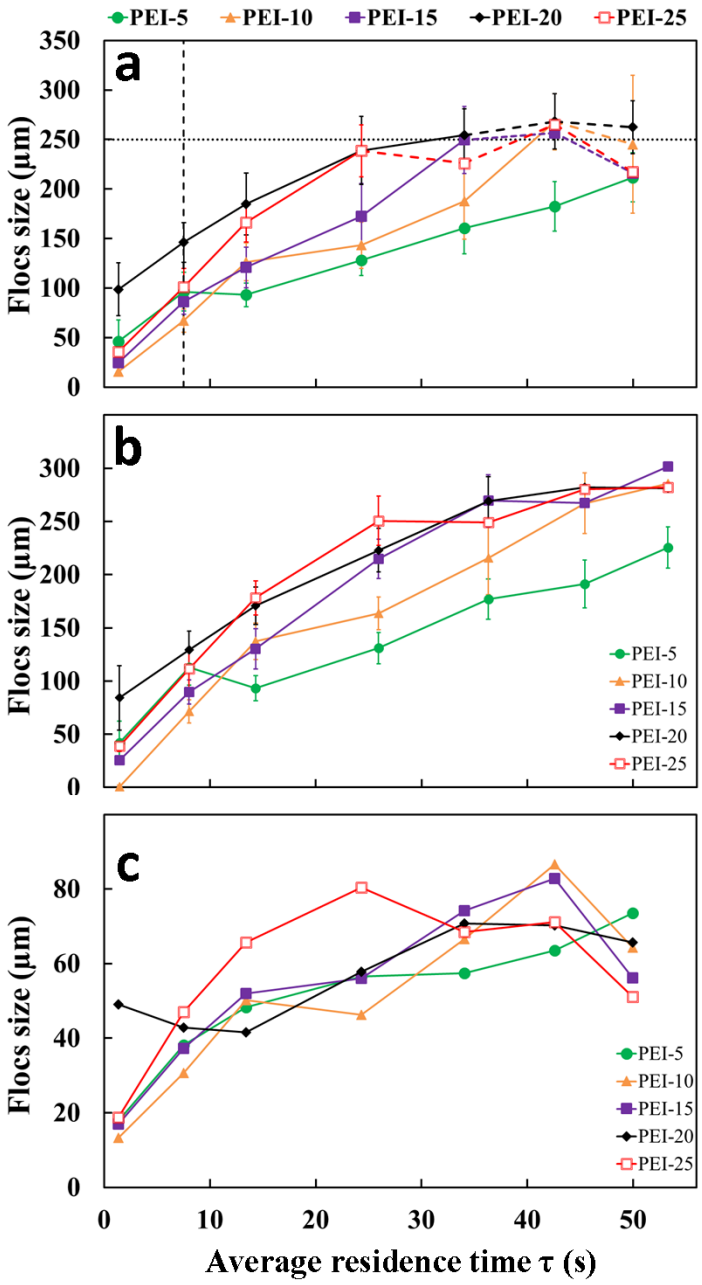

Figure 5.6: The growth of flocs formed between yeast homogenate and varying PEI_H concentrations: (●, PEI-5) - 5 g kg^{-1} yeast, (▲, PEI-10) - 10 g kg^{-1} yeast, (■, PEI-15) - 15 g kg^{-1} yeast, (♦, PEI-20) - 20 g kg^{-1} yeast and (□, PEI-25) - 25 g kg^{-1} yeast at pH 7. (a) Largest 10% of flocs recorded at each location, corresponding to the d90 (% number), whereas (b)Size of the largest 50 flocs recorded. The x-intercept at ca. 7.5 s (dashed line) is the point where complete fluid-homogeneity has been recorded, while the y-intercept at 250 µm (dotted line) is half of the width of the channel, where growth in floc-size appears to stop. Error bars denote ± 1σ of all flocs measured in 8000 image sequences at each location. (c) Average sizes of all flocs (d50, % number) recorded within one image sequence of 4 seconds at each imaging location.

Figure 5.6a, shows the d90 of the flocs observed, and a clear increase in the rate of floc-growth was observed with increasing concentrations. It was also noted that the growth of flocs declined above a d90 of 250 µm. This was possibly due to the depletion and exhaustion of the micro-flocs that are necessary to continue the nucleation process. Additionally, the increase in shear levels up to around 100 s^{-1} (Chapter 3) at around 125 µm from either walls of the channel may be detrimental to the floc-growth. Since the flocs stopped having a linear growth above 250 µm size, the growth kinetics was estimated for each flocculating condition for sizes only up to 250 µm.

The high-content of data generated by the computational code enabled the user to extract the floc size information in a variety of forms, for e.g. Figure 5.6b represents the increase in the sizes of the largest 50 flocs encountered in the system. This format helps in the analysis of the floc sizes independent of the distribution of the sample population. Figure 5.6c shows the average size of the flocs, where a distinct growth was not observed. This can be attributed to the reduction in the smaller particles that partake in the nucleation phase leading to the formation of bigger flocs. This is supported by the equation proposed by Gregory in 1988 (Equation 5.1), where the time taken (t_A) for the adsorption of a fraction of the flocculant '*f*', is inversely proportional to the growth constant (k_{12}) and the number of colloidal particles present (N_1). This was based on the assumption that the number of colloidal particles per unit volume (N_1) is equal to the number of polymeric flocculants per unit volume (N_2). A decrease in the growth constant was also predicted as the number of particles per unit volume decreased over time as flocculation continued.

$$t_A = -\frac{\ln(1-f)}{k_{12}.N_1} \tag{5.1}$$

The decrease in the average floc size after a time of ~35 s, for all concentrations above 10 g PEI_H kg^{-1} yeast, can therefore, be justified based on the above mentioned equation. A lower concentration (5 g PEI_H kg^{-1} yeast) may have sufficiently lower surface-site coverage of the polymers on the colloidal micro-flocs for the average size to grow continually. From each location, the particle size distribution (PSD) was plotted as shown in Figure 5.7. Near the ψ-shaped inlet, the PSD appeared to be wide indicating a wide range of floc sizes. As the d90 sizes increased in sample population along the channel, as observed in Figure 5.6a, the PSDs became narrower, and only a negligible number of flocs between 10-50 µm in

size was observed as the d90 approached 250 µm. This suggested that almost all micro-flocs aggregated to form large flocs irrespective of the flocculant concentration. The narrow PSD of flocs at 45 cm from the inlet also supported the reduction in the average particle size as seen in Figure 5.6c.

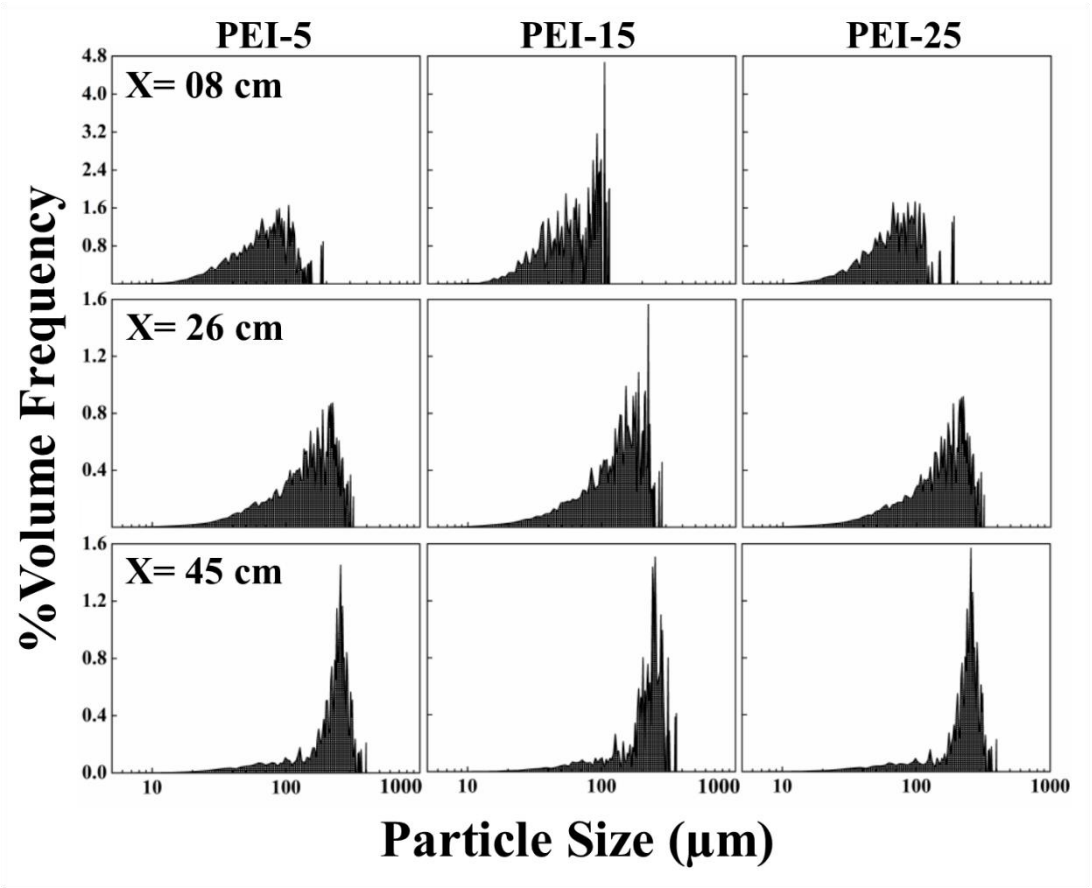

Figure 5.7: PSDs of flocs observed at each imaging location with varying PEI_H concentrations- 5 g PEI_H kg^{-1} yeast (PEI-5), 15 g PEI_H kg^{-1} yeast (PEI-15), 25 g PEI_H kg^{-1} yeast (PEI-25), in terms of % volume frequency. An increase in the size of the sample population can be observed. The raw data, in % number, from the image analysis script was converted to % volume frequency, by assuming a spherical shape for the particles, to be comparable with the light-scattering instrument. Graphs were plotted using the OriginPro 8.6 software (OriginLab Corporation, Massachusetts, USA).

The variation of d90 floc sizes with pH (Figure 5.8) had a less distinctive trend between each pH, than the varying concentration. An increase in the growth rate could be visually observed as the pH increases from 5 to 6 and gradually reduces thereafter. Adsorption kinetics of PEI on silica surfaces over changing pH was studied by Mészáros *et al.* in 2004, where a more favourable adsorption rate was

observed at around pH 6. The decrease in the growth rate can also be attributed to the decrease in the charge density of PEI from 20% (pH 5) to 15% at pH 7 (Suh *et al.*, 1994).

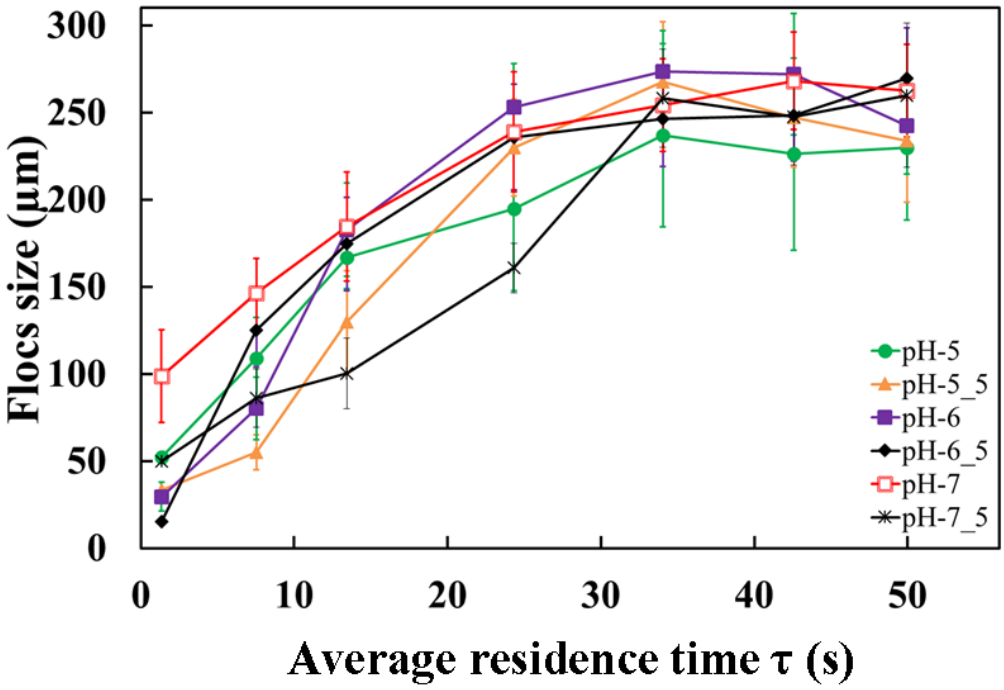

Figure 5.8: Growth of flocs formed between yeast homogenate and 20 g PEI_H kg^{-1} yeast with varying pH. The plots represent d90 diameter of floc. Error bars denote ± 1σ of all flocs measured in 8000 image sequences at each location.

The d90 floc sizes of other molecular weights of PEI at different concentrations have been shown in Appendix A5.2. Experiments performed with varying concentrations of $pDADMAC_H$ (Mol. Wt. 400-500 kDa) yielded similar growth patterns, with a faster growth rate observed with increasing concentrations (Figure 5.9). While flocs formed with 5 and 10 g $pDADMAC_H$ kg^{-1} yeast grew at a slower rate, the growth of flocs formed with 15 and 20 g $pDADMAC_H$ kg^{-1} yeast was considerably faster with the d90 reaching 250 µm within 30 s. Interestingly, at a higher concentration of 25 g $pDADMAC_H$ kg^{-1} yeast, the floc sizes attained a plateau at 200 µm. A similar growth trend previously reported, suggested the presence of the flocculant above the optimal level required for flocculation (Gregory, 1973), especially for large molecular weight polymers. A rapid increase in the floc size was observed due to the rapid adsorption, after which sections of polymers spanning out from the colloids may

have become too long with a strong positive charge, thereby, creating charge repulsion with other such polymers.

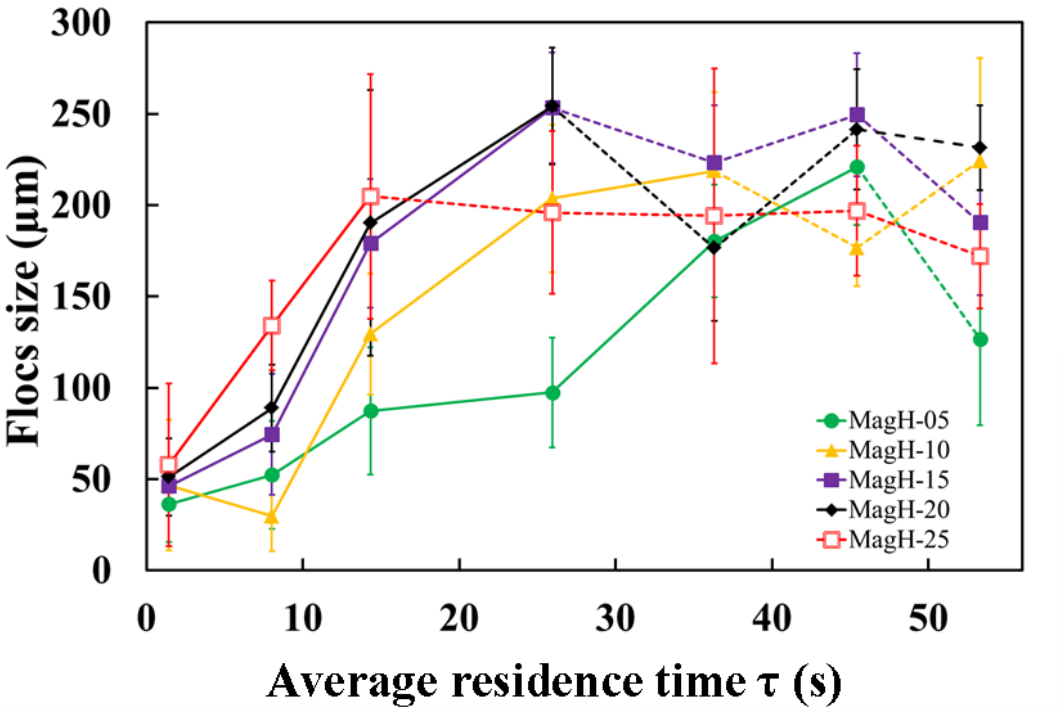

Figure 5.9: The largest 10% of flocs (d90) formed between yeast homogenate and varying pDADMAC$_H$ concentrations: (●, MagH-5) - 5 g kg^{-1} yeast, (▲, MagH-10) - 10 g kg^{-1} yeast, (■, MagH-15) - 15 g kg^{-1} yeast, (♦, MagH-20) - 20 g kg^{-1} yeast and (□, MagH-25) - 25 g kg^{-1} yeast at pH 7. Error bars denote ± 1σ of all flocs measured in 8000 image sequences at each location.

Furthermore, it has been predicted that as the size of the polymeric flocculant increases, the rate of adsorption purely due to diffusion decreases and the flocculation process depends on orthokinetic transport of the flocculants through external shear (Gregory, 1988). Additionally, the micro-flocs could have attained a complete surface-site coverage with the large molecular weight pDADMAC, thereby depending on orthokinetic shear for further continuation of flocculation through breakage and re-conformation. Floc sizes (d90) obtained from flocculation of yeast homogenate and lower molecular weights of pDADMAC have been shown in Appendix 5.3. Because the growth of flocs appeared stunted above 250 µm, consistently for all the flocculants tested, due to depletion of micro-flocs and increasing shear rates closer to the channel walls, the growth kinetics was measured through a linear regression for sizes only up to 250 µm. The growth of flocs is dependent on the charge density of the flocculant, and a comparison

between PEI_H and $pDADMAC_H$ has been shown in Figure 5.10. The cationic charge density of pDADMAC being 100% at pH 7, it was expected to have a faster growth rate due to higher attractive forces with the anionic cell suspension. It can be observed that the growth rate of flocs with 15 g $pDADMAC_H$ kg^{-1} yeast is almost equivalent to 25 g PEI_H kg^{-1} yeast. The growth of d90 floc size plateaued at ~200 µm for the 25 g $pDADMAC_H$ kg^{-1} yeast, the condition as shown in Figure 5.9, and hence the variation in floc size after this point was not considered.

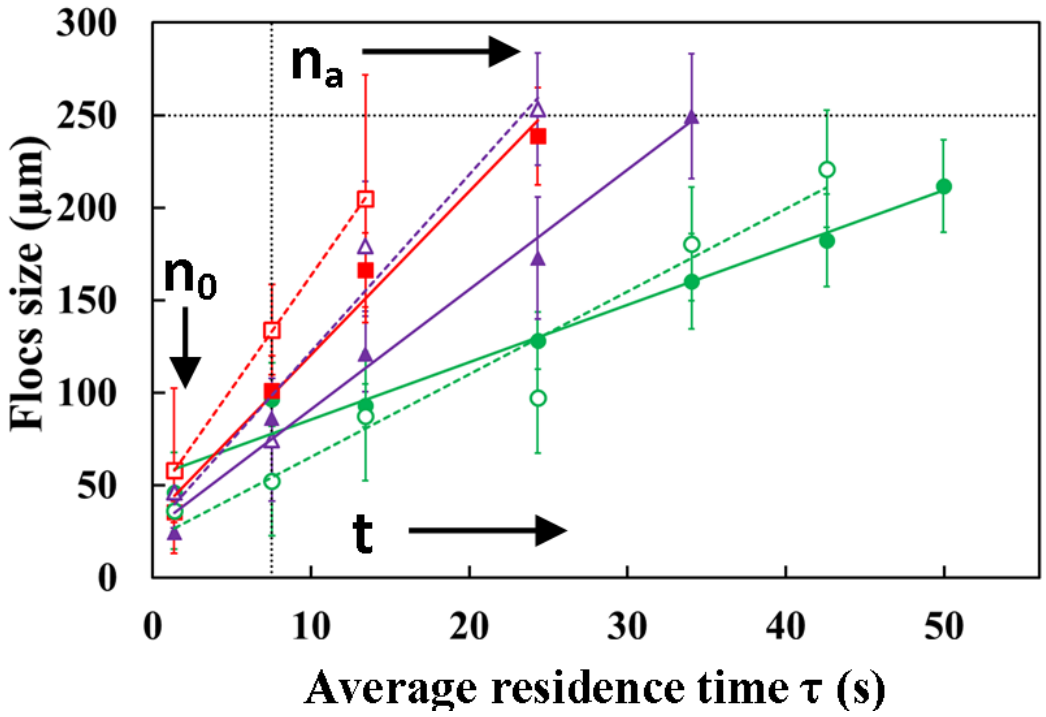

Figure 5.10: Comparison of linear growth of flocs, between PEI_H (closed markers with solid lines), and $pDADMAC_H$ (open markers with dashed lines). Circular markers represent 5 g flocculant kg^{-1} yeast, triangular markers 15 g flocculant kg^{-1} yeast, and square markers denote 25 g flocculant kg^{-1} yeast. A linear trend-line was applied to estimate the growth constant (d90 sizes up to 250 µm) for each condition. X-intercept at ~7.5 s depicts the mixing time within the µ-flocculation device, and the y-intercept at 250 µm denotes the half-width of the channels above which the floc growth was stunted. Error bars denote ± 1σ of all flocs measured in 8000 image sequences at each location. The term n_a refers to the number concentration of aggregates at time 't', where n_0 is the initial number of micro-flocs (see Section 5.3.5).

Flocculation using a non-ionic flocculant – PEG showed no growth of flocs with the measured diameters fluctuating between 50 and 80 µm for all concentrations tested (Figure 5.11). This was observed in the cases of both 6 and 100 kDa PEG tested.

This further supports the assumption of the dependence of flocculation with non-ionic flocculants on orthokinetic shear for the transport of the polymer onto the colloidal particles for either colloidal entrapment or sweeping.

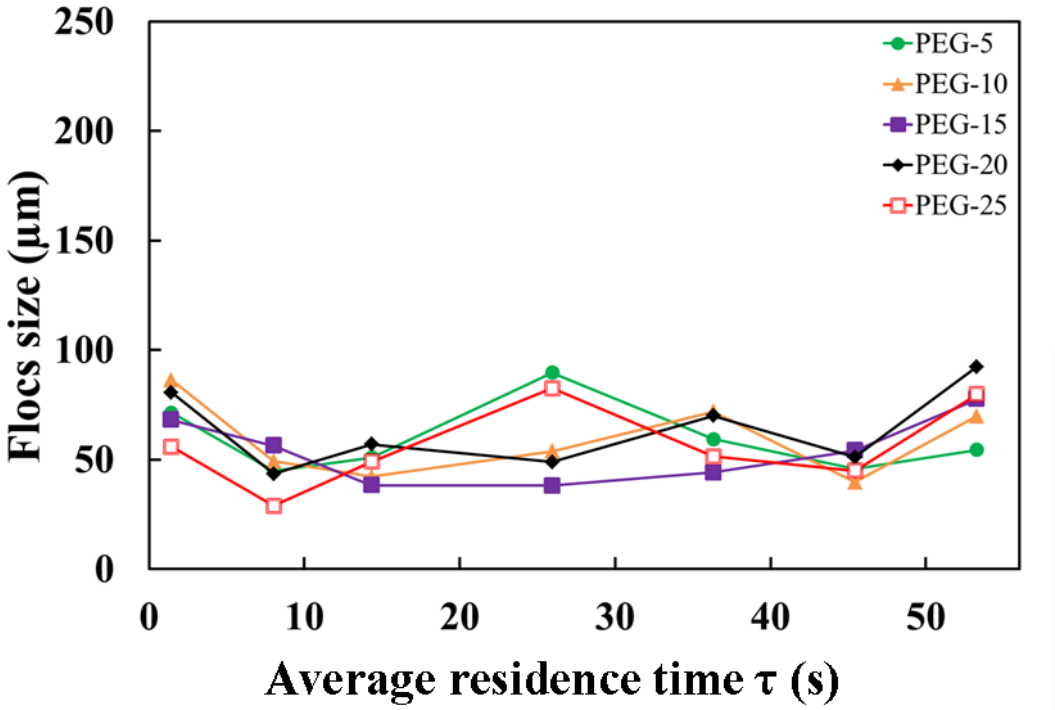

Figure 5.11: The largest 10% of flocs (d90) formed between yeast homogenate and varying PEG_H concentrations: (●, PEG-5) - 5 g kg^{-1} yeast, (▲, PEG-10) - 10 g kg^{-1} yeast, (■, PEG-15) - 15 g kg^{-1} yeast, (♦, PEG-20) - 20 g kg^{-1} yeast and (□, PEG-25) - 25 g kg^{-1} yeast at pH 7.

5.3.3 Variation of morphology of flocs with floc-growth

Another aspect made possible by the image analysis setup was the analysis of the morphology of the flocs formed during the growth phase. While the calculation of the diameter assumes a circular shape for the flocs, the measurement of the length and the width of flocs is a direct conversion of their longest lengths and widths in terms of number of pixels. Figure 5.12 shows that the lengths of flocs were consistently higher than the equivalent circular diameters. Although the length of a floc is not restricted by the dimensions of the channel, the reduction of growth in terms of the floc-length can be attributed to the depletion and exhaustion of polymers and thereby, the nucleation of the micro-flocs. Figure 5.13 shows that the width of the flocs were also observed to be consistently larger than the equivalent circular diameter, but due to the restriction of the natural growth by the width of the channel, the flocs seemed to stop increasing in size after 250 µm. On comparing

the widths of the flocs with their lengths (Figure 5.14), the flocs (near the inlet) seemed to be longer than their widths, indicating the process of flocculation being directly related to the convective forces along the direction of the flow. After the point of complete homogeneity, the widths of the flocs were observed to be higher than their lengths up to 250 µm. Above this size, the widths appear to be constricted by the width of the channel, while the lengths of the floc increased further until encountering the exhaustion of the polymeric flocculant.

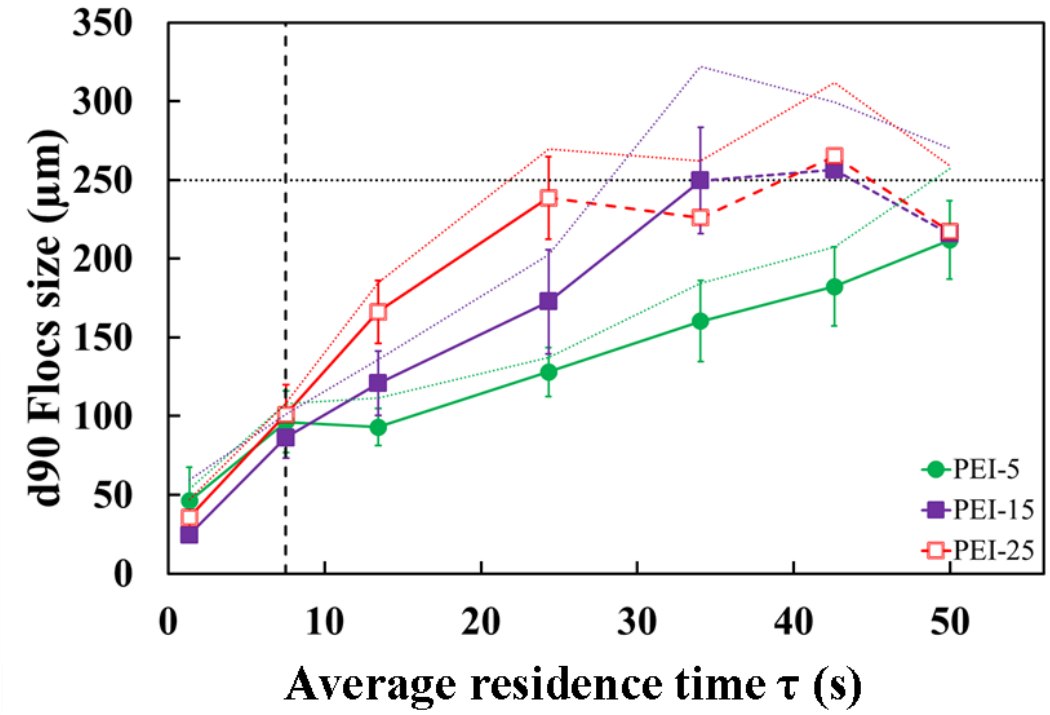

Figure 5.12: d90 floc sizes (largest 10 %; lines with markers) with the corresponding lengths of flocs (dotted lines) obtained from flocculation of yeast homogenate and PEI_H. PEI-5 denotes 5 g PEI_H kg^{-1} yeast, PEI-15 - 15 g PEI_H kg^{-1} yeast, and PEI-25 - 25 g PEI_H kg^{-1} yeast. The x intercept (dashed line at 7.5 s) represents the point of complete homogeneity, while the y-intercept (dotted line at 250 µm) shows the half-width of the channel above which a linear growth was not observed. Error bars denote ± 1σ of all flocs measured in 8000 image sequences at each location.

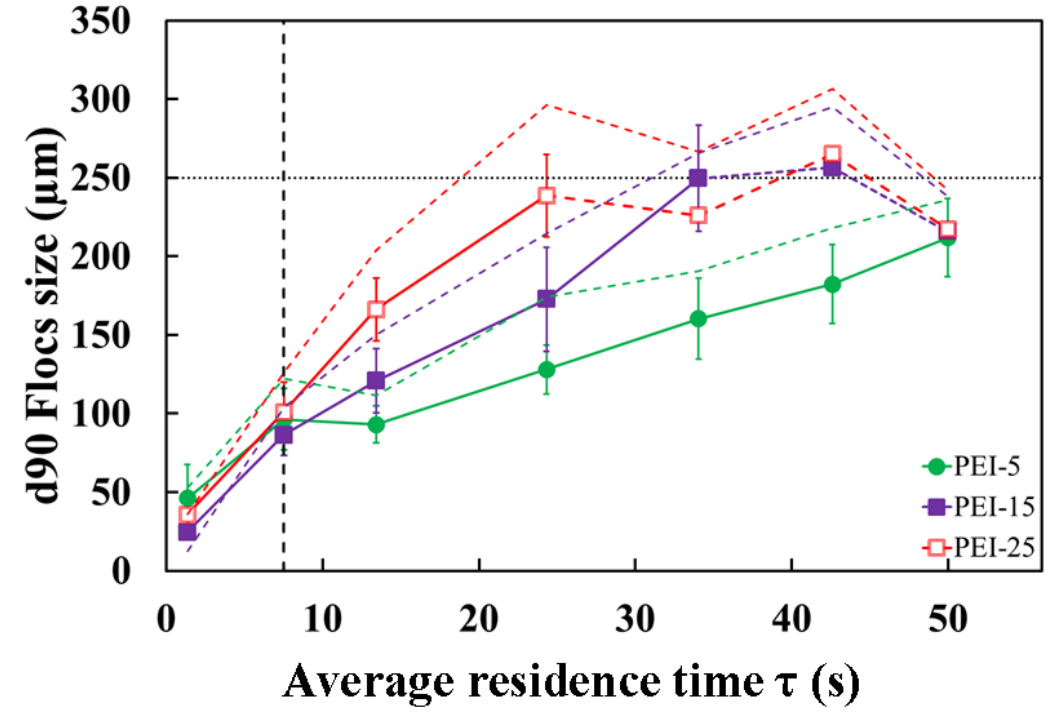

Figure 5.13: d90 floc sizes (largest 10 %; lines with markers) with the corresponding widths of flocs (dotted lines) obtained from flocculation of yeast homogenate and PEI_H. PEI-5 denotes 5 g PEI_H kg^{-1} yeast, PEI-15 - 15 g PEI_H kg^{-1} yeast, and PEI-25 - 25 g PEI_H kg^{-1} yeast. The x intercept (dashed line at 7.5 s) represents the point of complete homogeneity, while the y-intercept (dotted line at 250 µm) shows the half-width of the channel above which a linear growth was not observed. Error bars denote ± 1σ of all flocs measured in 8000 image sequences at each location.

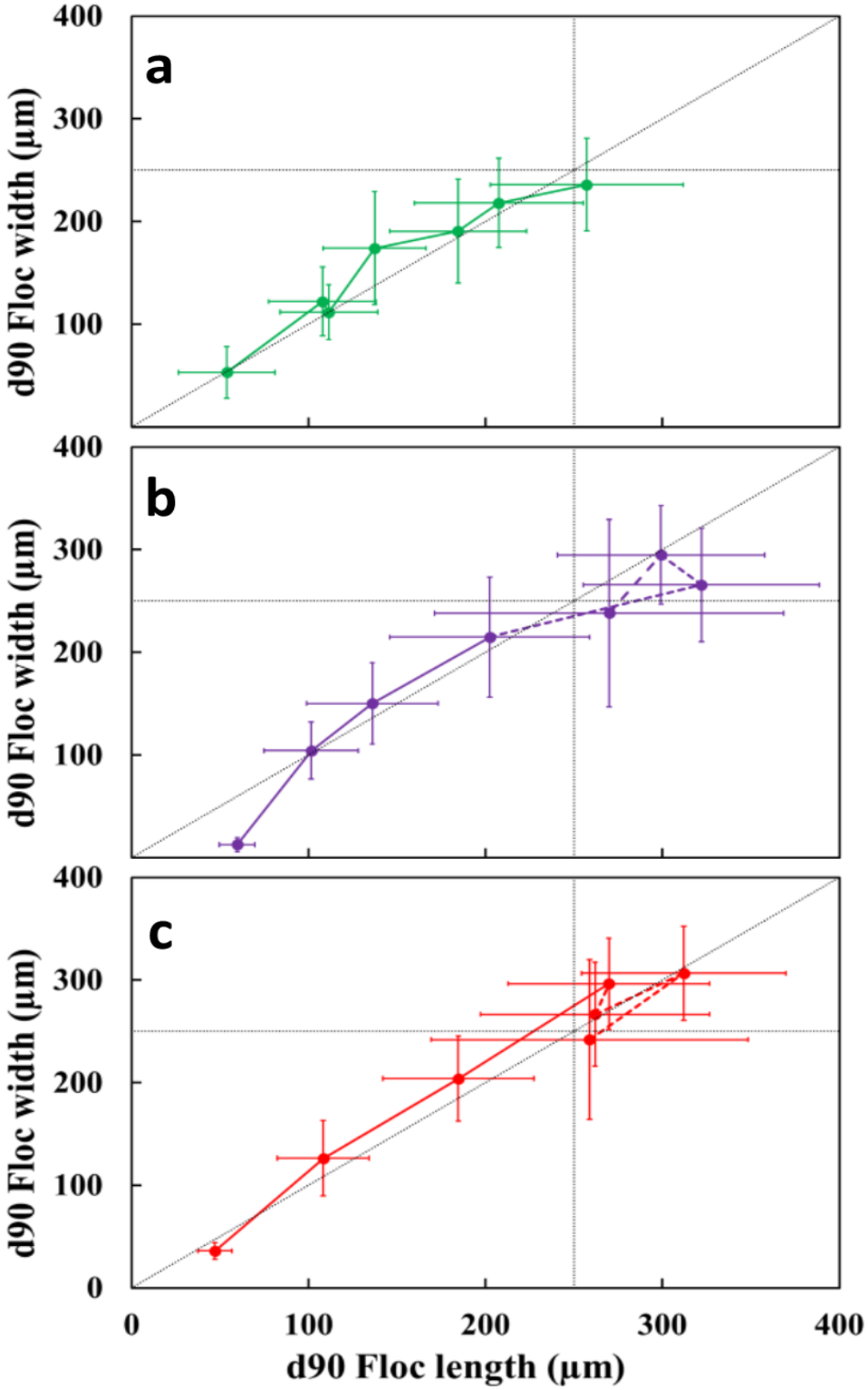

Figure 5.14: Parity plot between length and width of the largest 10% of flocs (by diameter; d90). (a) PEI_H concentration of 5 g kg^{-1} yeast. (b) 15 g PEI kg^{-1} yeast, and (c) 25 g PEI kg^{-1} yeast. Linear correlation is observed up to 250 µm for all three PEI_H concentrations. Each data point corresponds to increasing distance from the inlet (1.4 – 53 cm). Error bars represent ± 1σ within a single set of image sequence for each location.

5.3.4 Estimation of growth kinetics

As explained in the previous section, the growth kinetics of various flocculation systems were calculated through a linear regression for growth up to 250 µm, and these values were compared between flocculants.

5.3.4.1 Yeast homogenate - PEG system

Flocculation with PEG was expected to flocculate the cellular suspension through a polymer entrapment, or a sweeping method, as the non-ionic property of PEG doesn't enable a charge neutralisation approach. Therefore, flocculation with PEG heavily depends on external shear (orthokinetic) for the transport of the polymers to the surface of the colloids (Gregory and Barany, 2011; Gregory, 1988). Figure 5.15 shows the growth constant values of a yeast homogenate – PEG system where there was no growth observed. Similar cases were observed over varying pH for both molecular weights of PEG. This confirms the presence of lower shear levels in a laminar flow micro-system in the µ-flocculation device.

5.3.4.2 Yeast homogenate - PEI system

Flocculation between yeast homogenate and PEI is well studied. With a strong cationic charge density, PEI is one of the most commonly used flocculants. It was noted that flocculation with PEI_H had higher growth constants that ones with PEI_M and PEI_L, as seen in Figure 5.16. While the highest growth rate was observed at 25 g PEI kg^{-1} yeast for the large molecular weight PEIs (70 kDa and 50-100 kDa), thereby indicating a higher rate of polymer bridging, flocculation with 10 kDa PEI showed a maximum growth constant between 15 and 20 g kg^{-1} yeast. The smaller molecular weight PEI may adopt a charge neutralisation approach where the polymers weren't long enough to form bridges after achieving a fairly high surface-site coverage. It is also known that polymer bridging leads to a rapid increase in floc size, as seen from the overall higher growth constants for the larger molecular weight PEI polymers, than the 10 kDa PEI.

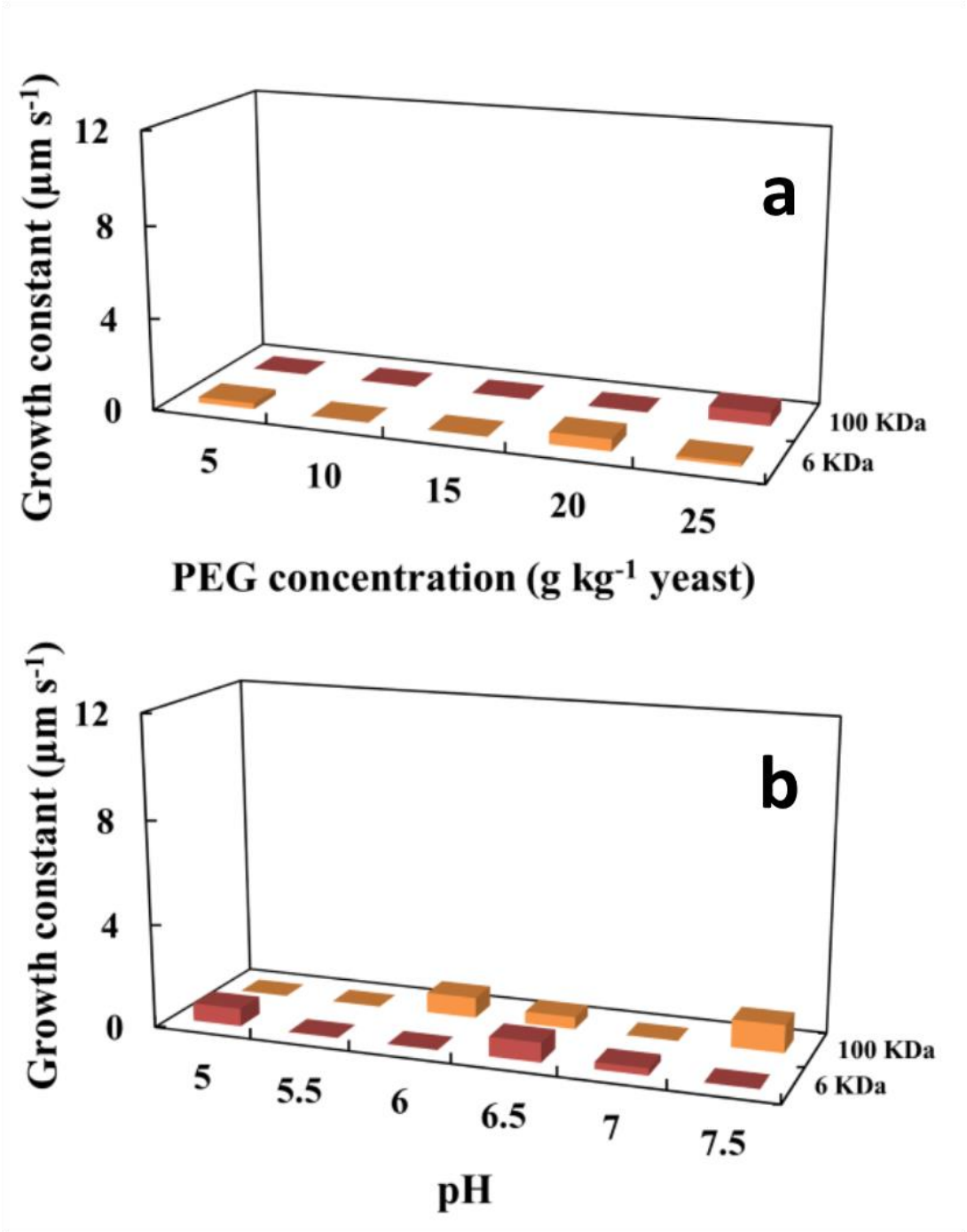

Figure 5.15: Growth constants measured from growth of flocs formed between yeast homogenate and PEG_L (6 kDa) and PEG_H (100 kDa). No growth was observed due to the low shear levels that is necessary for orthokinetic flocculation of non-ionic flocculants. (a) Flocculation with varying PEG concentrations were performed at pH 7, and (b) a constant concentration of 20 g PEG kg^{-1} yeast was used for the range of pH used.

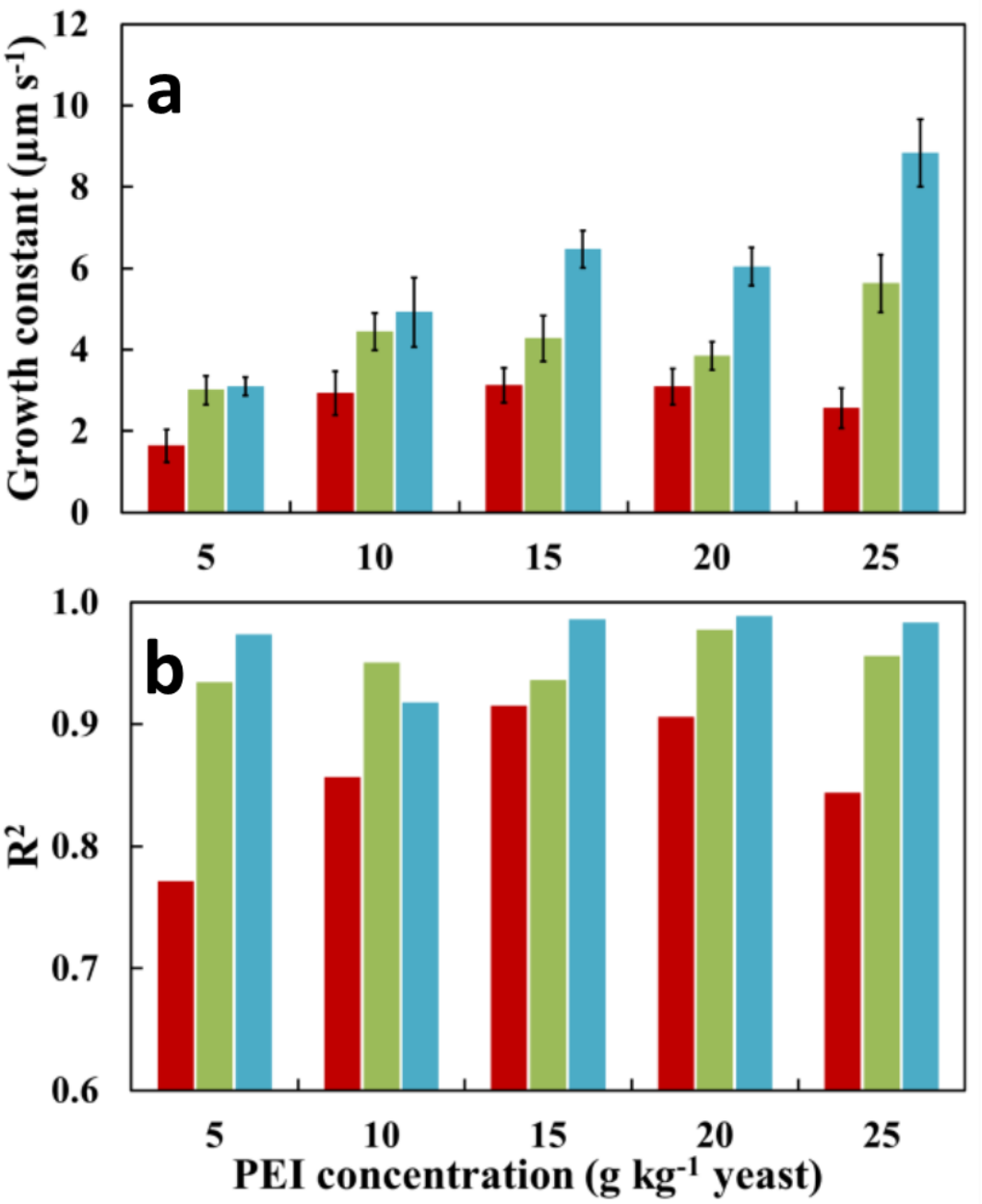

Figure 5.16: (a) Growth constants measured from the growth of flocs formed between yeast homogenate and varying concentrations of PEI (all three molecular weights) at pH 7. Error bars denote a standard error in the linear regression obtained from a LINEST function in MS Excel. (b) The coefficient of determination (R^2) obtained from the corresponding linear regression. Red bars represent PEI_L (10 kDa), Green – PEI_M (70 kDa) and Blue – PEI_H (50-100 kDa).

With varying pH (Figure 5.17), an increase in growth constant was observed towards pH 6. As discussed in Section 5.3.2, this may be due to the increase in the charge densities of PEI with increasing pH up to 6. At higher pH, the polymeric flocculant strands may not be in the most suitable conformation so as to achieve efficient surface-site coverage over the cell suspension (Gregory and Barany, 2011). The growth rate at pH 5 was same for all three molecular weights, which can be attributed to the acid precipitation of the colloidal suspension. The larger molecular weight flocculants of PEI (70 kDa and 50-100 kDa) recorded an even growth constant between pH 6.5 and 7.5, whereas the growth constants of the 10 kDa PEI at pH 5.5 and above, were consistently lower than that of pH 5, possibly due to the charge imbalance detrimental to the charge neutralisation mechanism expected for short molecular weight polymers.

5.3.4.3 Yeast homogenate - pDADMAC system

Dilute concentrations of flocculant lead to insufficient surface-site coverage, but enables an exaggerated adsorption of more polymers on to the colloidal particles, due to diffusion, irrespective of the size of the polymer. This was observed for all molecular weights of pDADMAC, as shown in Figure 5.18. At 10 g pDADMAC kg^{-1} yeast, the growth constant was low, possibly due to the slightly higher surface-site coverage but insufficient length of the polymers to form bridges (in the case of <100 kDa pDADMAC). In the cases of medium to large molecular weight pDADMACs, lower growth rates were recorded at this concentration probably due to the insufficient number of polymers available to continue the nucleation process through bridging. Increasing concentrations above 10 g $pDADMAC_L$ kg^{-1} yeast showed a steady increase in the growth rates, indicating a stronger neutralisation of charges around the micro-flocs.

The inverse dependence between the number of particles and the adsorption time, as observed from Equation 5.1, also suggested a slow polymer-adsorption for lower concentrations. This was experimentally observed where the growth rate constants seemed to be lower for more dilute systems (shown in Figure 5.16 and Figure 5.18). However, it has been reported elsewhere that this assumption may not be valid when the surface-site coverage is almost equal to one (Van De Ven, 1994) commonly encountered in large molecular weight polymers.

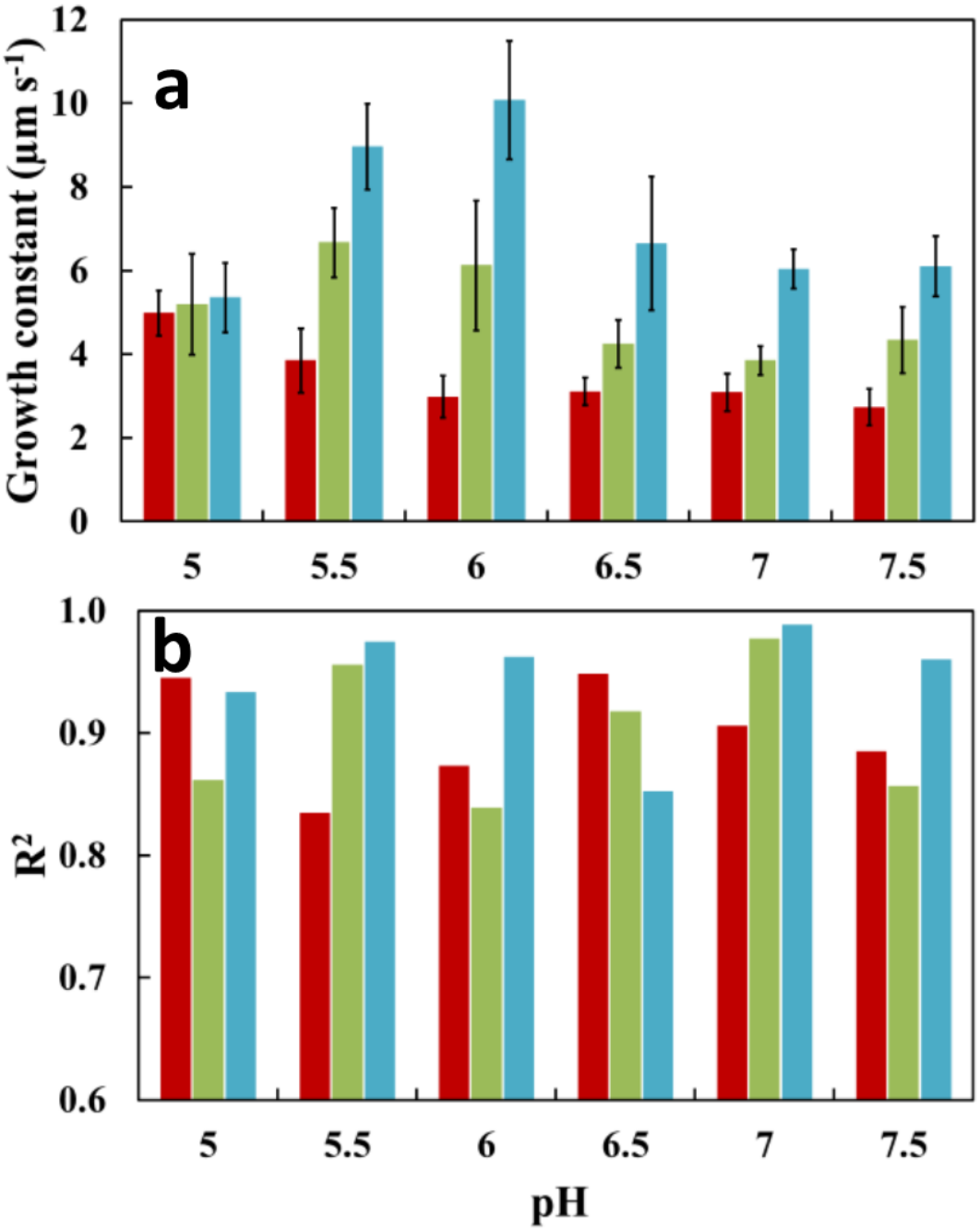

Figure 5.17: (a) Growth constants measured from the growth of flocs formed between yeast homogenate and 20 g PEI kg^{-1} yeast (all three molecular weights) with varying pH. Error bars denote a standard error in the linear regression obtained from a LINEST function in MS Excel. (b) The coefficient of determination (R^2) obtained from the corresponding linear regression. Red bars represent PEI_L (10 kDa), Green – PEI_M (70 kDa) and Blue – PEI_H (50-100 kDa).

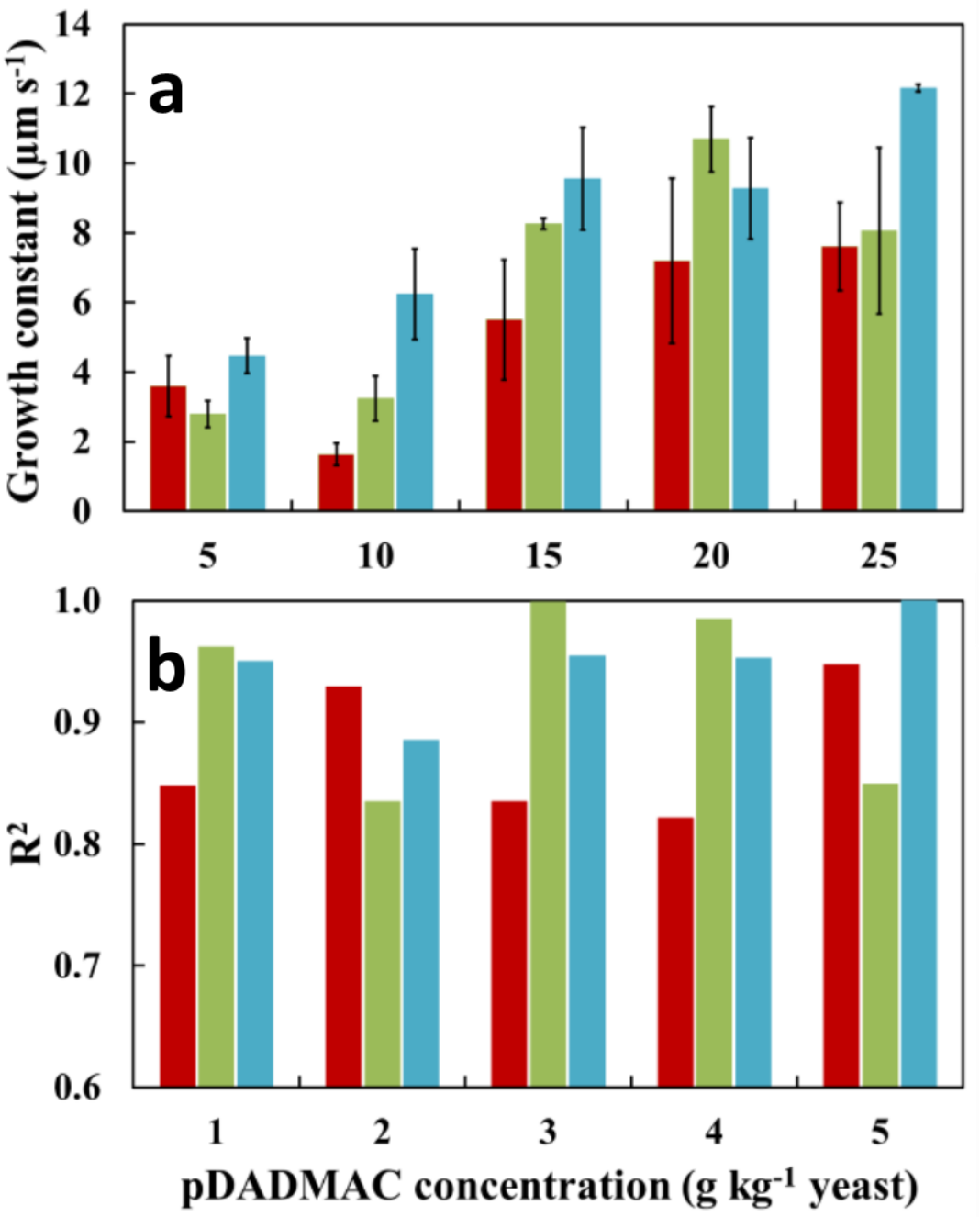

Figure 5.18: (a) Growth constants measured from the growth of flocs formed between yeast homogenate and varying concentrations of pDADMAC (all three molecular weights) at pH 7. Error bars denote a standard error in the linear regression obtained from a LINEST function in MS Excel. (b) The coefficient of determination (R^2) obtained from the corresponding linear regression. Red bars represent $pDADMAC_L$ (<100 kDa), Green – $pDADMAC_M$ (200-350 kDa) and Blue – $pDADMAC_H$ (400-500 kDa).

But this inverse dependence was found to be true for all the concentrations of the cationic flocculants used in this experimental study. Applying the growth constants and the mean residence times into Equation 5.1, confirmed a complete surface-site coverage due to diffusive effects in the presence of negligible orthokinetic shear levels. Figure 5.19 shows the variation of growth constants of different molecular weights of PEI with the standard error calculated from the slope of the linear trend.

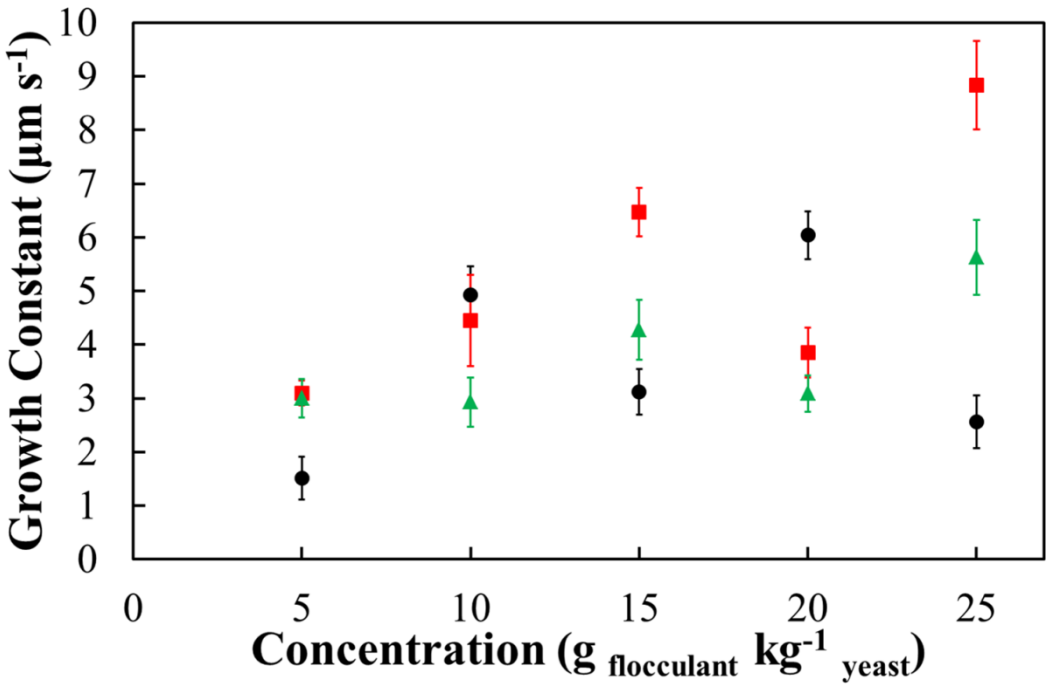

Figure 5.19: Rates of flocculation growth of different PEI molecular weights with varying concentrations at pH 7. Black circles denote growth constants of PEI_L, green triangles that of PEI_M, and red squares that of PEI_H. Error bars denote the standard error of the slope of linear floc-growth calculated via the LINEST function in MS Excel.

PEI_L showed a rather limited range of optimal flocculation without the presence of any electrolytes, because the low molecular weight polymers initiate flocculation just by charge neutralisation and are incapable of forming bridges. Therefore, as the concentration increased to above 20 g PEI_L kg^{-1} yeast, a charge imbalance was possibly created affecting the nucleation process. In the cases of PEI_M and PEI_H flocculants, a clear indication of polymer bridging was witnessed at high concentrations, where a mix of charge neutralisation and bridging can be expected even at lower concentration (5-15 g $PEI_{M/H}$ kg^{-1} yeast). Flocculation growth with pDADMAC had similar profiles for both low and high molecular weights (Figure

5.20), where $pDADMAC_M$ showed a profile as that of a low molecular weight flocculant (e.g. PEI_L) and the growth constant at 25 g $pDADMAC_M$ may be a potential outlier. Because $pDADMAC_L$ has a molecular weight of above 50 kDa, it can be considered as a high molecular weight polymer (Gregory, 1973), and this supports the reason behind a similar profile as that of $PEI_{H/M,}$ and $pDADMAC_H$. It was observed that the point of zero zeta potential for PEI_H was between 15 and 20 g kg^{-1} yeast (see Chapter 2, and Salt *et al.* 1996). This can possibly hold true for PEI_M due to its similar polymer size range, and this may extend to pDADMAC as well.

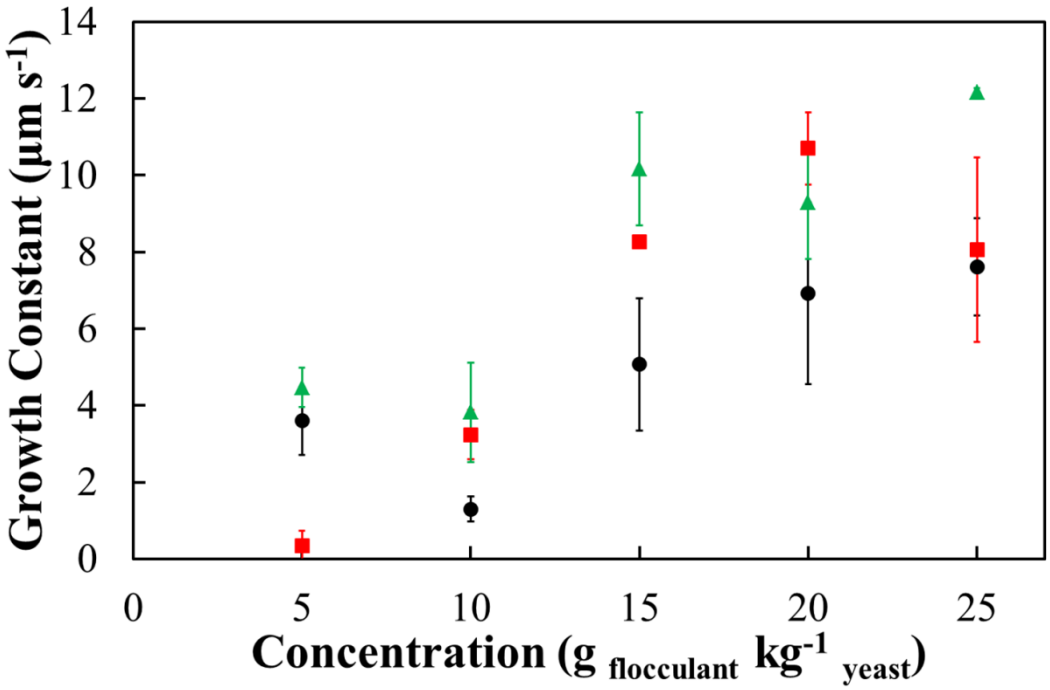

Figure 5.20: Rates of flocculation growth of different pDADMAC molecular weights with varying concentrations at pH 7. Black circles denote growth constants of $pDADMAC_L$, red squares that of $pDADMAC_M$, and green triangles that of $pDADMAC_H$. Error bars denote the standard error of the slope of linear floc-growth calculated via the LINEST function in MS Excel.

To study the significance of the varying growth rates, an attempt may be made to characterise the growth rates at incrementally increasing concentrations and thereby, analysing the trend.

5.3.5 Improved parameter fitting of Smoluchowski's equation

Most flocculation models have been based on the theory proposed by Smoluchowski and this theory has since become the core of almost all subsequent

research on flocculation. The classical expression of Smoluchowski's model can be represented as in Equation 5.2 (Rahn-Chique *et al.*, 2012; Thomas *et al.*, 1999; Wang and Friedlander, 1967). The number concentration of primary flocs '*k*' at a given time '*t*' is n_k, where '*k*' is formed by the aggregation of particles '*i*' and '*j*' of number concentrations $n_i \; and \; n_j$ respectively. The rate of aggregation of '*i*' and '*j*' to produce '*k*' is denoted by k_{ij}, whereas the rate of breakage of '*k*' to particles of size '*i*' is k_{ik}.

$$\frac{dn_k}{dt} = \frac{1}{2}\sum_{i=1,j=k-i}^{i=k-1} k_{ij} n_i n_j - n_k \sum_{i=1}^{\infty} k_{ik} n_i \tag{5.2}$$

This equation is governed by two aspects namely – perikinetic (due to Brownian motion and diffusive adsorption, leading to attachment) and orthokinetic flocculation (transport of flocculants in a sheared system). In the practical sense, steps a – c in Figure 5.1 is governed by perikinetic flocculation, and steps d – f by orthokinetic flocculation. Alternatively, the rate of flocculation can be expressed as in Equation 5.3, where α is the collision efficiency, between 0 and 1, indicating the success rate of attachment when two colloids collide. $\beta_{i,j}$ is a more important expression which represents the collision frequency between particles '*i*' and '*j*'; and n_i and n_j are the number concentrations of particles of sizes '*i*' and '*j*' respectively (Gregory and Barany, 2011; Thomas *et al.*, 1999). There has been a wide interest in modelling different equations to represent $\beta_{i,j}$ accurately to predict the behaviour of different flocculating systems, mostly monodisperse (Thomas *et al.*, 1999). Equations 5.4 and 5.5 are the analytical deductions that represent perikinetic and orthokinetic modes of flocculation (i.e. the first and second terms of the right side of Equation 5.2), respectively.

$$Rate\ of\ flocculation = \alpha\beta_{i,j}\left(n_i \times n_j\right) \tag{5.3}$$

$$\beta_{perikinetic} = 2k_f \frac{\left(d_i + d_j\right)^2}{d_i \times d_j} \tag{5.4}$$

$$\beta_{orthokinetic} = \left(\frac{1}{6}\right)\left(\frac{du}{dy}\right)\left(d_i + d_j\right)^3 \tag{5.5}$$

Here d_i and d_j represent the diameters of particles '*i*' and '*j*' that are colliding, and du/dy is the velocity gradient of the liquid. k_f is the collision coefficient which is

generally defined by Equation 5.6, portraying adsorption purely under a diffusional condition.

$$k_f = \frac{2K_B T}{3\eta} \tag{5.6}$$

Here K_B is the Boltzmann constant, and T and η are the temperature and the viscosity of the liquid respectively. An analytical form of perikinetic flocculation, deduced by Smoluchowski, has been shown in Equation 5.7 (Lee, 1983; Rahn-Chique *et al.*, 2012; Urbina-Villalba and García-Sucre, 2005), where n_a is the number concentration of aggregates as a function of time, and n_0 is the initial number concentration of micro-flocs. The deduction of Equation 5.2 into 5.7 assumes that the rate of flocculation of all particles irrespective of their sizes are equal (i.e. k_{ij}=k_f). This equation provides an insight into the reduction in the number of aggregates as flocculation progresses over time '*t*'.

$$n_a = \frac{n_0}{(1 + k_f n_0 t)} \tag{5.7}$$

A similar solution for orthokinetic flocculation is shown in Equation 5.8 (Thomas *et al.*, 1999), where φ is the volume fraction of the flocs.

$$n_a = n_0 e^{4/\pi} \left(\frac{du}{dy}\right) \varphi t \tag{5.8}$$

At the outset, while solving the classical form of the Smoluchowski's equation, a few assumptions are usually made, such as that – a) the collision efficiency α, is equal to unity (i.e. any collision between two particles will lead to an aggregate formation), b) the liquid has a laminar shear, c) there is absence of floc-breakage, d) all particles are monodisperse, e) all particles are spherical, and f) collision occurs only between two particles (Thomas *et al.*, 1999). Through the implementation of the µ-flocculation device to facilitate a continuous steady-state flocculation, assumptions a) to c) have been experimentally realized, where the collision frequency is expected to be close to unity due to the absence of orthokinetic shear, and convective mixing occurring at high P_e numbers. Apart from the assumptions stated above, another drawback is that almost all flocculation models only consider a two-body interaction, which makes their application on flocculation of biological cells unfeasible (Wickramasinghe *et al.*, 2005).

Since the growth kinetics was experimentally calculated in a system with perikinetic flocculation, an investigation on Equation 5.4 has been discussed in the following section. This can be seen as a parametric calculation of the collision frequency through experimental data of flocs formed by perikinetic flocculation. As an alternative approach to implement the purely-perikinetic condition, k_f (Equation 5.6) was calculated from experimental results through a simple re-arrangement of Equation 5.7, yielding Equation 5.9.

$$k_f = \left[\left(\frac{1}{n_a} - \frac{1}{n_0}\right)\left(\frac{1}{t}\right)\right] \tag{5.9}$$

The output from the image-processing code provided the number of flocs detected and measured at each imaging location for every flocculation condition. This was converted to number concentration by dividing the number of flocs by the volume (channel width × channel depth × length covered by the camera's field-of-view). In this case, all the dimensions were 500 µm. The term n_0 was calculated to be the number concentration of flocs near the inlet of the channel (i.e. the first imaging location – at 8.03 cm from the ψ-shaped inlet). Owing to the continuous, steady-state nature of the flocculation system, this consideration is valid, as n_0 reduces to n_a after time '*t*', which is equal to τ. The terms n_a and '*t*' were obtained from the point along the channel where the linear growth of flocs ceased (i.e. when the d90 reached ~250 µm). The high-speed imaging setup measured the flocculation events in a two-dimensional plane (channel width and length), where the aggregation events occurring along the depth of the channel couldn't be captured, and hence not quantified. Therefore, k_f from Equation 5.9 was calculated on a 'per unit area (A)' basis (Equation 5.10), thereby also normalising the different numbers of particles recorded over a four-second video stream.

$$k_f = \left[\left(\frac{1}{n_a} - \frac{1}{n_0}\right)\left(\frac{1}{At}\right)\right] \tag{5.10}$$

The term $\beta_{perikinetic}$ (Equation 5.4) was thus, calculated by applying the k_f values for varying concentrations of each flocculant. While the classical Smoluchowski's equation is known to be a simplified form, various groups have since modified it to add correction factors to take into consideration the polydispersity of a sample population (Lee, 1983; Rahn-Chique *et al.*, 2012; Wang and Friedlander, 1967). It has to be noted that these equations assume a monodisperse PSD of flocs, and therefore, to account for the significant polydispersity of the experimental

flocculation system the d10 and d90 were considered. Equation 5.4, was applied in the form of Equations 5.11 and 5.12.

$$\beta^{L}_{perikinetic} = 2k_f \frac{(d^{L}_{10} + d^{L}_{90})^2}{d^{L}_{10} d^{L}_{90}} \tag{5.11}$$

$$\beta^{H}_{perikinetic} = 2k_f \frac{(d^{H}_{10} + d^{H}_{90})^2}{d^{H}_{10} d^{H}_{90}} \tag{5.12}$$

Superscripts '*L*' and '*H*' denote the predicted collision frequencies at two positions along the channel – near the channel inlet where flocculation has just commenced and the point where the linear growth appeared to cease, respectively. The latter point is similar to the point from where terms n_a and '*t*' were calculated. The d10 and d90 diameters were chosen as the sizes of the two colliding particles to predict the collision frequency model, also due to the prolonged nucleation phase in the micro-environment in the µ-flocculation device, where the d90 particles grew linearly up to 250 µm possibly due to the aggregation with the smaller d10 particles.

While $\beta^{L}_{perikinetic}$ was expected to provide a good estimate, comparable to the experimental growth constants, $\beta^{H}_{perikinetic}$ was calculated to only anticipate how the existing experimental floc growth would continue if it wasn't restricted by the dimensions of the microchannels, or if there was no exhaustion of the flocculants and micro-flocs to continue floc-growth.

Figure 5.21 shows the results obtained from the modified Smoluchowski's perikinetic model. The collision frequencies seemed to be of the same order as that of the experimental growth constants, however, a few outliers were identified. The $\beta^{L}_{perikinetic}$ values appeared similar to the experimental growth constant for almost all molecular weights, except pDADMAC$_M$. The $\beta^{H}_{perikinetic}$, on the other hand, deviated from the experimental data, as anticipated, because it was used to predict the continuation of floc-growth of particles already ~250 µm in size (d90). Values suggested that the larger particles may have a higher flocculation rate, probably due to the large surface-area covered by the indiviual big flocs, and also due to the high cationic charge density of medium to high molecular weight PEI and pDADMAC. Table 5.2 shows the root mean square error between $\beta^{L}_{perikinetic}$ and the experimental growth constants to observe the deviation of the model. Due to the fact that the rather simplistic perikinetic model was observed to have large

deviations (highest being 93% for $pDADMAC_L$), a model fitting step at this stage may be considered as a first approach in the experimental estimation of collision frequencies.

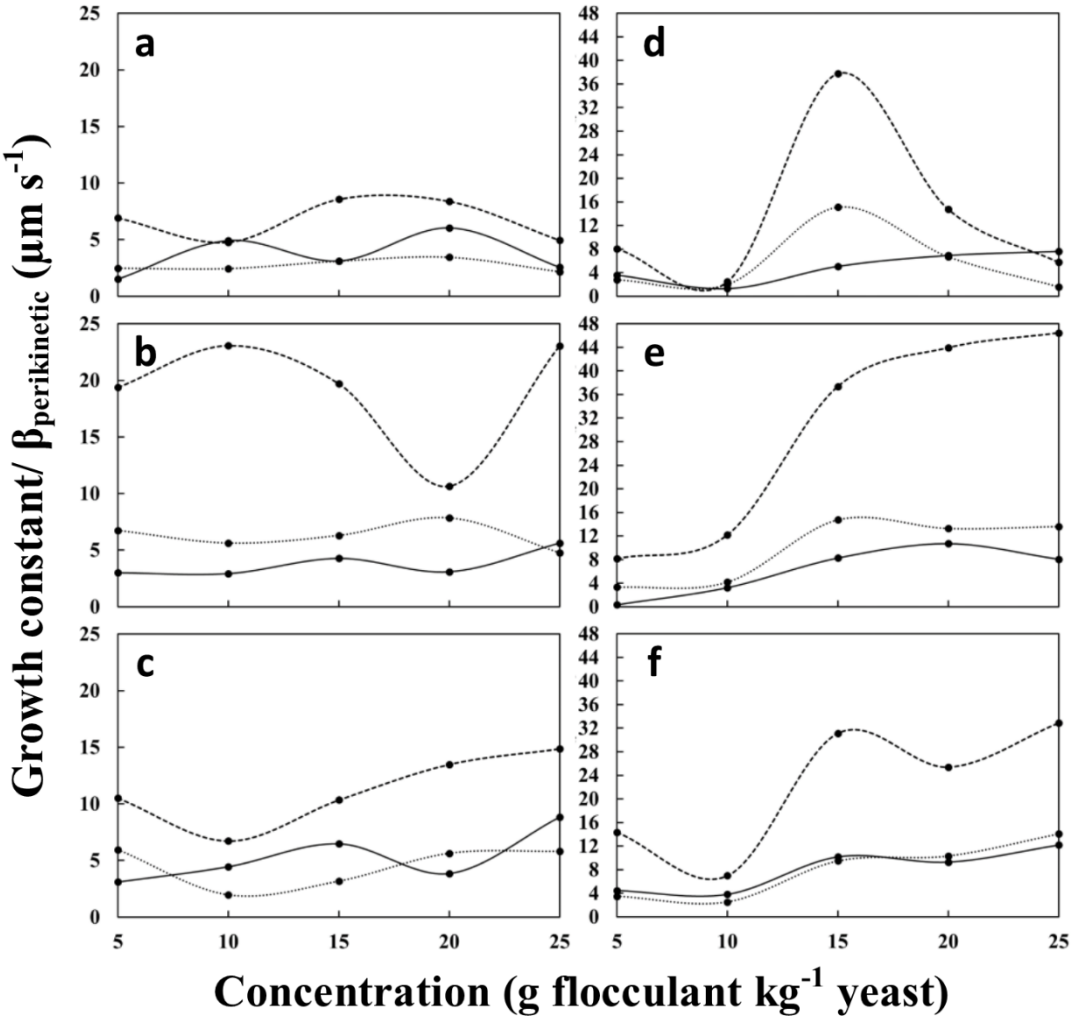

Figure 5.21: Comparison between experimental growth constant (solid lines) with a numerical solution of the Smoluchowski's equation for perikinetic flocculation. Dashed lines represent $\beta^{H}_{perikinetic}$ *at the point where linear growth ceases. Dotted lines denote* $\beta^{L}_{perikinetic}$ *considering the d10 and d90 at the position 8.03 cm from the inlet. (a)* PEI_L *(10 kDa), (b)* PEI_M *(70 kDa), (c)* PEI_H *(50-100 kDa), (d)* $pDADMAC_L$ *(<100 kDa), (e)* $pDADMAC_M$ *(200-350 kDa), (f)* $pDADMAC_H$ *(400-500 kDa). All experiments were performed in the μ-flocculation device with the high-speed imaging setup at pH 7.*

Furthermore, to calculate the goodness of fit between the measured growth rates and the modified Smoluchowski's perikinetic model, a simple statistical analysis involving a Chi-Squared test was performed between the experimental growth

constant and the predicted collision frequency at the channel inlet ($\beta^{L}_{perikinetic}$). The Chi-Squared function χ^2_{sample} can be defined as:

$$\chi^2_{sample} = \sum_i \left(\frac{growth\ constant - \beta^{L}_{perikinetic}}{\sigma_{experiment}} \right)^2 \quad (5.13)$$

Table 5.2: Root Mean Square Error (RMSE) between the theoretical collision frequencies and experimental growth constants. NRMSE represents the %normalised RMSE over the average deviation. χ^2_{sample} is the Chi-Squared function values to estimate the goodness of fit between theoretical collision frequencies and experimental growth constants.

Flocculant	RMSE	NRMSE	χ^2_{sample}
PEI_L	1.67	61.41	61.5
PEI_M	2.73	60.70	353.3
PEI_H	3.12	49.89	241.2
$pDADMAC_L$	5.25	93.23	61.9
$pDADMAC_M$	4.22	42.96	1778.8
$pDADMAC_H$	1.25	15.72	357.5

Where, i = number of samples – which is the range of concentrations used, and $\sigma_{experimental}$ is the error in measurement. Because the measured growth rate was considered to be the slope of a linear trend (up to 250 μm), the standard error of this slope was considered to be the $\sigma_{experiment}$, which is an estimated value and not directly measured. χ^2_{sample}values were then compared with the Chi-Squared reference ($\chi^2_{0.95}$), obtained from a Chi-Squared distribution with degrees of freedom = range of flocculant concentrations (5), and a 95% probability. $\chi^2_{0.95}$ was equal to 11.1. χ^2_{sample} values for all the flocculants used were 1-2 orders of magnitude higher than $\chi^2_{0.95}$ (Table 5.2), leading to the failure of the Chi-Squared test. This indicated that the simplified perikinetic model used does not predict the process of flocculation growth accurately. This is further confirmation for the necessity to develop more accurate models, which has the potential to advance research in flocculation of biological systems.

This has to be performed with the inclusion of the effect of pH, ionic strength of the polymers, etc. (Duan and Gregory, 1996; Gregory, 1973), which have only been

considered in other simple models for non-biological flocculation involving monodisperse particulates. Additionally, the experimental parameter fitting of Smoluchowski's model was an initial fundamental approach to address flocculation growth kinetics of biological cellular suspensions, like yeast homogenate using polymeric flocculants. Modelling flocculation using polyelectrolytes becomes even more complex, when the effect of electrostatic attraction is taken into account. Models like the DLVO theory discusses this effect (Chang and Ku, 2001; Narong and James, 2006), but there has been no research undertaken to correlate it with the hydrodynamic and physico-chemical effects on flocculation, as yet.

5.4 Conclusions

The experimental platform in conjunction with the analytical toolbox was implemented to test two cationic polymers and a non-ionic flocculant, and their floc sizes were measured. The robustness of the device was confirmed through a fine-tuned hydrodynamic control, thereby achieving a continuous and steady-state condition in a repeatable manner.

As anticipated, the non-ionic polymer did not record any increase in the d90 floc sizes, indicating its dependence on orthokinetic flocculation. On the other hand, all molecular weights of PEI and pDADMAC showed considerable growth, recording higher rates of aggregation with increasing concentrations in most cases. The PSDs at increasing distances from the inlet, showed an overall increase in the floc size of the sample population. Furthermore, the distribution of flocs appeared to become more monodisperse (as the flocs reached around 45 cm from the inlet). The high-content of data generated by the image-processing script was further confirmed through the floc-morphology data made available. The widths of the flocs were consistently higher than their lengths for $PEI_{H,}$ after the point of complete homogeneity in the microchannels, but only up to 250 µm, where the floc-widths started getting constricted by the channel-width and also due to the exhaustion of micro-flocs to continue to the nucleation process. Based on this evidence, growth constants were calculated for floc sizes growing up to 250 µm, through a linear regression. Due to a higher charge density, pDADMAC recorded a much faster growth rate than PEI of comparable molecular weights. These results were then compared with theoretical perikinetic growth rates from classical Smoluchowski's equation for flocculation. While this was a first approach to fit experimental growth kinetics data, the modified analytical form of the equation provided collision frequencies in the same magnitude as that of the experimental growth rate.

However, this model has failed to accurately predict the variation of growth rates, thereby necessitating a more in-depth mathematical modelling step taking into consideration the effects of ionic strength, pH, etc.

This setup has successfully advanced an experimental approach in the estimation of flocculation growth, but the second aspect of Smoluchowski's equation dealing with orthokinetic flocculation needs to be addressed as well. With a miniaturised piezo-electric microfluidic device to expose the flocs to shear (see Chapter 7), experimental data can be gathered to correlate shear rate with individual floc sizes, hence enabling the estimation of desorption (breakage) constants (k_{ik}). A complete image can then be obtained leading to practically relevant variants of the Smoluchowski's model. This can eventually be extended to a macroscopic approach (Thomas *et al.*, 1999; Yeung and Pelton, 1996), which requires knowledge on the fractal dimensions of the flocs – which has also been made available through the work presented in this thesis (see Section 5.3.3 for measurements of floc widths and lengths).

Finally, this platform has enabled a rapid testing of new flocculation systems and screening of flocculants from a wide variety of synthetic polyelectrolytes. A thorough screening is of prime importance to both pharmaceutical and water-treatment industries, as apart from their experimental suitability, physical characteristics and cost, their storage properties, environmental impact and toxicity also need to be taken into consideration. Valuable knowledge on growth kinetics shall hence, potentially help to reduce the time-taken to carry out the above said procedure drastically, which are usually tedious and costly.

6. Concluding remarks

The implementation of flocculation as a downstream product separation unit operation has been seeing a growing interest in the field of pharmaceutical manufacture, where its applicability had originally pertained only to waste water treatment and sludge conditioning. The research project discussed in this thesis is aimed at achieving a more in-depth fundamental understanding of the process of flocculation through the implementation of a microfluidic device with an optical imaging analytical platform. The rationale behind this approach was underpinned by the limitations of the existential flocculation setups in the larger scales, and also the sensitive nature of the flocculation process to various parameters. These factors made it experimentally difficult to de-couple the sub-processes of flocculation in order to achieve a clearer knowledge. The final outcome of this research has led to the development of a small-scale test system that can be implemented for a rapid-screening of different control parameters affecting flocculation growth. These variables can range from the choice of flocculating agents and/or cell suspension, their concentration, ionic strength, pH, etc. to quickly evaluate their effect on the growth rate through *in situ* measurements.

Initially, the basic idea of pursuing a microfluidic experimental platform seemed counterintuitive, due to the anticipated problems like channel-clogging and scalability. Initially, two designs were rapidly fabricated using a laser ablation technique and later the design with a spiral microfluidic channel was micro-milled on PMMA substrates that offered various operational advantages. The devised microfluidic setup was observed to be suitable for flocculation, with the problem of clogging of the microchannels overcome by adopting appropriate cleaning strategies between experiments. The µ-flocculation device also enabled a rapid experimentation capability without the dependence on conventional analytical equipment that may have otherwise led to loss of valuable growth kinetics information. Flocculation of yeast homogenate and PEI, in this device saw the formation of larger flocs in comparison with that of a bench-scale setup, and upon further investigation, a prolonged flocculation growth phase was observed within the microchannels. The particle size distributions of flocs formed in the µ-flocculation device appeared to have a higher polydispersity than the bench-scale counterpart, suggesting the presence of lower shear rates in the microchannels with a laminar flow profile. A further understanding of the hydrodynamics within the microchannels was hence necessitated. The zeta potentials of the flocs formed under varying

conditions were measured and compared with that of the bench-scale setup, and the results confirmed the presence of a non-biased microenvironment for flocculation within confined spaces. With one of the aims being to by-pass the use of conventional analytical equipment for particle size measurements, the µ-flocculation device facilitated a dynamic *in situ* measurement of flocs through a simple microscopy setup.

In order to achieve a better understanding of the hydrodynamics within the microchannels, mixing time analysis was performed with a simple coloured dye-Allura Red and the point of complete homogeneity was quantified using an image-processing methodology. Under the given volumetric flow rates used, the device was observed to have a high convective mixing (P_e = ~2500) under a laminar flow profile (R_e = 5). A mixing time of 7.5 s was calculated and theoretical values using mixing equations from literature supported this result. A residence time distribution study was also carried out, and the microchannels had a mean residence time of ~ 70 s. An asymmetry in the exit-age distribution curve, and a mean residence time greater than theoretical residence time revealed the presence of cross-migration of particles in the spiral channels. Theoretical data suggested that for a flocculating system, particles above 35 µm may encounter similar forces (at the highest D_e = 0.011), while the effect of inertial lift forcing the flocs to move to equilibrium positions cannot be ruled out. A prolonged growth of the flocs in the µ-flocculation device may be due to the low levels of shear, and results from finite element modelling showed that the shear rates ranged from 12 to 80 s^{-1} (from the centre of the channel to 125 µm on either side), with a maximum of around 220 s^{-1} observed at the channel walls.

As described above, an optical imaging platform was developed to enable a dynamic *in situ* imaging of flocs that avoids the need for sample-handling and the subsequent sample-dispersion in commonly used particle-sizing instruments. Two high-speed imaging cameras were used for this purpose to capture the flocculation events at different points along the channel, at 2000 fps. To complement this high-speed imaging setup, and also to have a robust analysis of floc sizes through thousands of images, a computational image-processing script was developed using the Python programming language. This script had a sequence of operations dealing with the identification of individual flocs, removal of background noise, and subsequently generating a high volume of data regarding the length, width, area, and corresponding equivalent circular diameter of each floc detected. Python is as

easy to use as MATLAB and has comparable functionality/performance, while being free, open-source and actively developed. It is easier to learn and faster to prototype in Python than a low-level language like C, but has the facility to interface fairly easily with such languages when required. It has the capability to scale from a proof-of-concept implementation of a processing pipeline, like the one presented in Chapter 4, to powering an integrated system on an embedded device, which MATLAB does not.

The advantages of the µ-flocculation device used in conjunction with the high-speed imaging platform was exploited and different flocculants were tested to measure floc growth rates in isolation from floc breakage, something that hasn't been achieved using other conventional flocculation rigs. Two cationic flocculants (PEI and pDADMAC), and a non-ionic flocculant (PEG) were selected and the growth kinetics were observed. PEI and pDADMAC recorded a significant growth of flocs with yeast homogenate, with the rates becoming faster with increasing concentrations for almost all molecular weights. It was observed that the particle size distributions became increasingly monodisperse as flocculation progressed down the microchannels. With varying pH, growth rates seemed to be dependent on PEI's pH-dependence. Because the growth of flocs plateaued after 250 µm (d90 size), growth rates were calculated for flocs growing up to 250 µm, for varying concentrations of PEI and pDADMAC. From the high-content of data generated by the image-processing code, the collision frequency in the Smoluchowski's equation was experimentally estimated under a perikinetic condition, and these values were tested with the experimental growth rates. It was observed that the experimental estimation of the collision frequency parameter was in the same order of magnitude as that of the experimental growth rates, although the prediction did not provide an accurate fit. This was due to the simplicity of the model that was proposed solely for monodisperse particles. However, the use of the µ-flocculation device with an *in situ* imaging of flocs, has facilitated an improved experimental parameter fitting of a well-known equation that may now be advanced further to include the effect of pH, ionic strength etc. to achieve an in-depth understanding of flocculation growth. Furthermore, an advancement of the current microfluidic setup to accommodate a piezoelectric device (Section 7.2) can lead to the estimation of the orthokinetic collision frequency, which is an indication of floc-breakage/ageing. This would ultimately yield a complete knowledge on the rates of flocculation for biological samples with polydisperse particles, thereby leading to the modification of simple flocculation models to more accurate ones based on experimental parameter fitting.

7. Future Directions

7.1 Improvements on the current experimental setup

Recommendations for continuation of this body of work can be broadly categorised into: (i) a larger characterisation of process variables in the existing system, (ii) improvements in the current microfluidic device, (iii) a more detailed study on the hydrodynamics within the microchannels, and (iv) the online adaptation of the computational image analysis script.

The work reported in this thesis was a multi-disciplinary approach leading to the development of a microfluidic experimental platform, a suitable analytical tool and a high-throughput data-processing algorithm. With the high-content of data provided by this set up, it will be of much more importance if a wider range of process variables affecting flocculation was tested. In the μ-flocculation device reported in this thesis, the flow rates can be varied to see the effect of varying shear stresses on floc growth. Additionally, similar designs can be micro-milled with varying channel depths and widths (at an aspect ratio of 1). This will provide insight on whether the growth rate is affected by different shear stresses, and convective effects. Following these hydrodynamics-based experiments, flocculation parameters like ionic strength can be characterised by incrementally increasing the concentration of NaCl in the flocculating media. With a Design of Experiments based approach, study of growth kinetics may be extended to non-polymeric flocculants as well.

The designs of the spiral microchannels were fabricated on PMMA for the work presented in this thesis. While PMMA offers a range of advantages, one of the limitations arises from the loss of optical transparency due to thermo-compression bonding. Even though alternative solutions like bonding with adhesives may be tested, it doesn't provide a uniform seal across the surface-area of the device. To enable a completely transparent optical platform silicon channels with a complete through-hole can be fabricated through Deep Reactive Ion Etching (DRIE) – to provide an almost perpendicular cut for large dimensions (~500 μm). This layer can then be sandwiched between two glass substrates using an anodic plasma bonding step to achieve high bond-strengths. The hydrophobicity of the glass layers may also be altered (Wong and Yu, 2013) to address the problem of clogging, thereby enabling a 'self-cleaning' status for continuous flocculation experiments. Furthermore, another advantage of using these substrates for device-fabrication is

that it can lead to a successful integration of the piezoelectric embedded device to study floc-breakage (Section 7.2), as PMMA generally has low acoustic impedance leading to a loss in acoustic energy dissipated. The equipment necessary for fabrication of a glass-silicon-glass device can be found at the London Centre for Nanotechnology.

With regards to the hydrodynamics, the study of flocculation growth can also be tested using a segmented flow system, i.e. studying the growth of flocs within individual droplets surrounded by an immiscible layer. Using controlled hydrodynamics, the number concentrations of the polymers and density of colloidal particles within each droplet can be characterised for more accurate growth kinetics estimation. Additionally, as the droplets have a thin film of the immiscible carrier liquid around it, the interaction between the charged flocculant with the silicon layers can be prevented. Achieving this requires a more precise fluidic transport and also a control over the pressure difference between the droplet layer and the carrier liquid. A control over the size and frequency of droplets can be achieved through the use of back-pressure regulators commonly sold by companies like Upchurch Scientific, USA or Swagelok Inc., UK. This type of glass-silicon-glass microfluidic device can be used with a simple microscopy setup. High-speed cameras like the ones used for the reported work may be used, or a complete optical high-speed imaging setup like the VW-9000 from Keyence, UK, or the high-speed camera and microscope system (Part number- 3200050, Dolomite Microfluidics, UK) with a PixeLINK camera (PixeLINK, USA) can be sought. It has to be noted that the latter setup with a Dolomite microfluidic device comes with a glass-etched microchannel that has a circular surface-profile as opposed to a rectangular one, and hence may affect the image analysis step.

One of the prime limitations of flocculation modelling has been the assumption of a two-body interaction for monodisperse particles. Moreover, there are only a limited number of research groups across the world that work on computational physics involving ionic interactions between particles, as commonly seen in a flocculating system. With a droplet-based microfluidic device, the footprint of the flocculation microenvironment is further reduced drastically, and a computational model of a

similar footprint may be more feasible. Collaboration may be sought with such a computational physics group in the University of Edinburgh[♠].

Finally, the high-speed imaging setup used enables a real-time, dynamic imaging of flocs *in situ*. However, the analysis of these images is currently performed offline. The script, being developed on the Python programming language, provides room for online adaptation of the code, by making the analysis of the flocs sizes in real-time. The setup can be modified in such a way that the camera is set to record a burst of images at set intervals (e.g. by an external trigger), and its on-board memory is made permanently accessible to a connected computer running the computational script. The script can be programmed to loop over to periodically check for new batches of images and go to "sleep" mode for a set interval after completion. The delay time for the sleep mode can be set to be larger than the current processing time for a batch of images. To complement this analysis technique, cameras with high-speed data transfer ports can be selected (e.g. USB 3.0 or Firewire). While this may not be necessary in achieving a more in-depth understanding of the growth kinetics of flocculation, it would certainly support a rapid screening of new flocculants, thereby reducing the time for process-development drastically.

7.2 Design concept of a piezoelectric embedded microfluidic device to study flocculation breakage

Ultrasonic transducers have been widely used in the field of microfluidics primarily for particle manipulation. In general, there are three different types of acoustic coupling: bulk acoustic waves, surface acoustic waves, and plate waves. The readers are directed to Barnkob *et al.*, 2012, 2010; and Iranmanesh *et al.*, 2013 for a more detailed explanation of the acoustophoretic theory and its applications in microfluidics. To expose the flocs to shear, bulk acoustic waves are preferred, where standing waves are generated either across the channel or from top to bottom.

7.2.1 Design requirements

As a rule of thumb the thickness of the top layer (above the fluid channel) must be much smaller than the wavelength of sound waves (λ) used- around < 0.1(λ). The

[♠] Dr. Timm Krüger, University of Edinburgh, School of Engineering, Institute for Materials and Processes, King's Buildings, Mayfield Road, Scotland, UK.

transducer must then be chosen with an appropriate resonance frequency, usually in a few MHz range, and subsequently, the wavelength of the transducer must be matched with either the channel length (L) or width (W) such that

$$L \text{ or } W = \frac{\lambda}{2} \tag{7.1}$$

Distance of the transducer from the channel is not critical, but choosing a carrier layer with a low acoustic impedance is important. PMMA has a moderate-to-high acoustic impedance value, and yet has been successfully tested for ultrasonication studies[♠]. Therefore, PMMA may be used only for rapid prototyping of devices to check for the application suitability, and later glass-silicon-glass devices can be implemented, with silicon acting as the carrier layer. Silicon is generally the most widely preferred material that has a relatively low acoustic impedance value.

A sample design of a prototype device has been shown in Figure 7.1, where the green slot with a circular through-hole can be used to attach a 50 µm thick poly(dimethyl siloxane) (PDMS) membrane for transduction. This may pose a considerable challenge, as the PDMS depends on compression seal from PMMA inset around it, and the device is also prone to leaks.

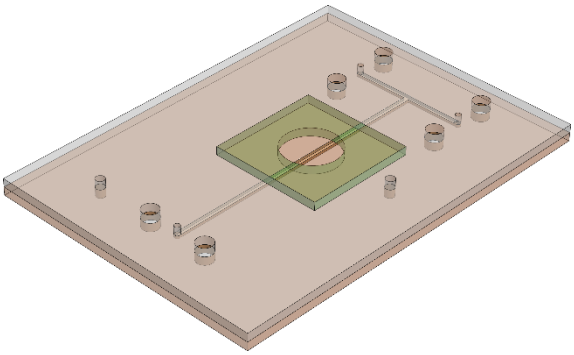

Figure 7.1: 3D CAD design of a PMMA device for rapid testing of a miniaturised piezoelectric transducer. The green slot acts as a compression seal for a PDMS membrane that can alternatively be used for transduction from the piezoceramic material placed directly above it. The width and the depth of the channel is around 500 µm.

[♠] (Harris *et al.*, n.d.)

7.2.2 Required materials and equipment

To develop a miniaturised piezoelectric embedded device, the following components are fundamental for achieving a successful acoustic transduction.

1. A piezo-ceramic transducer (PZ26 Ferroperm, Denmark) of around 2.7 MHz resonance frequency based on PMMA properties and width of channel (Figure 7.2).
2. Conductive silver-epoxy glue (CircuitWorks® Conductive Epoxy CW2400, Chemtronics, USA) for damping of the exposed part of the transducer, and to prevent the loss of acoustic energy.
3. Quick drying adhesive gel (Tensive, Parker Labs, USA) to glue transducer on to the device.
4. Reworking flux gels (MULTIFIX™, Henkel Loctile, UK) for achieving a clean solder of copper wires to the transducer.
5. A function generator (DS345, Stanford, USA) coupled to an RF amplifier (75A250, Amplifier research, USA) to transduce the piezoelectric element using either a sinusoidal or a square wave.
6. An oscilloscope (TDS220, Tektronix, USA), to measure the peak-to-peak voltage of the output of the function generator.

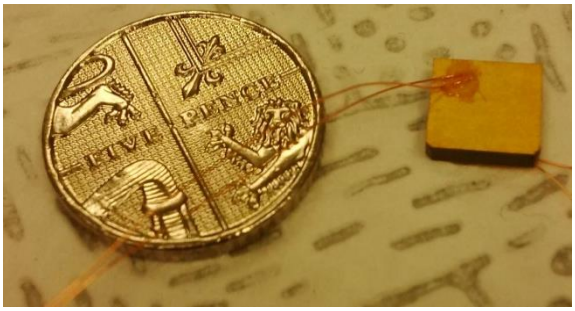

Figure 7.2: Image of a miniature ceramic piezoelectric transducer to be embedded on a microfluidic device. Copper wire was connected to the transducer with the conductive adhesive gel.

An image of an assembled prototype PMMA device (without PDMS membrane) with the piezoelectric transducer has been shown in Figure 7.3. Once the device has been assembled, and tested to be leak-proof, it is critical to evaluate the acoustic energy density (E_{ac}, J m^{-3}) within the channels. The operating variables are usually the frequency of transduction (MHz) and the pressure amplitude (Pa), which are

varied to measure the E_{ac}, by either quantitative optical tracking of beads, or impedance spectroscopy.

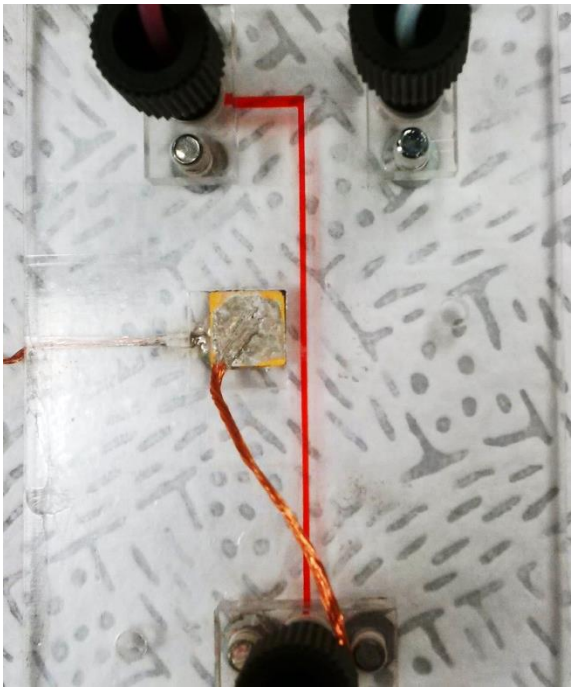

Figure 7.3: An assembled prototype PMMA microfluidic device with a miniature piezoelectric transducer. Copper wires were connected to the transducer with a conductive adhesive gel, and the transducer was attached to the bottom layer of the device with a silver epoxy glue.

Once the suitability of the corresponding dimensions of the channel is tested, the device can be fabricated on silicon, anodically bonded to the top and bottom layers in glass. A design concept to study the floc breakage *in situ* has been shown in Figure 7.4. The device shown can be integrated with the current optical imaging platform to investigate the growth and breakage kinetics of flocs in real-time. The computational image analysis script can be employed to measure the size of the ruptured flocs as well. This shall ultimately lead to the experimental estimation of both the perikinetic and orthokinetic collision frequencies of the Smoluchowski's model for flocculation as explained in Chapter 5, Section 5.3.5.

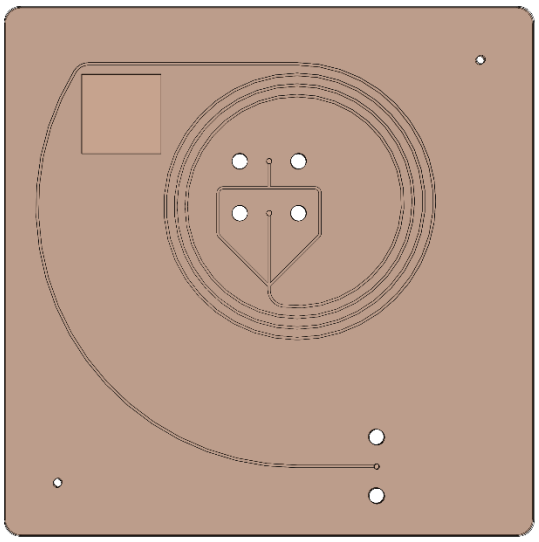

Figure 7.4: A design concept for studying flocculation breakage kinetics in a microfluidic device. The long residence time in the spiral microchannels can be used to study the growth kinetics, and floc-breakage observed in the long curvilinear channel near the outer edge. The slot in the left top, indicates the location where the piezoelectric transducer may be embedded. The width and the depth of the channels are 500 µm, and the length ~60 cm.

8. References

Abonnenc, M., Josserand, J., Girault, H.H., 2009. Sandwich mixer–reactor: influence of the diffusion coefficient and flow rate ratios. Lab Chip 9, 440–448.

Agerkvist, I., 1992. Mechanisms of flocculation with chitosan in Escherichia coli disintegrates: effects of urea and chitosan characteristics. Colloids and Surfaces 69, 173–187.

Amin, Z.R., Rahimizadeh, M., Eshghi, H., Dehshahri, A., Ramezani, M., 2013. The effect of cationic charge density change on transfection efficiency of Polyethylenimine. Iran. J. Basic Med. Sci. 16, 150–156.

Andersson, H., Berg, A. van den, 2004. Microfabrication and microfluidics for tissue engineering: state of the art and future opportunities. Lab Chip 4, 98.

Asmolov, E.S., 1999. The inertial lift on a spherical particle in a plane Poiseuille flow at large channel Reynolds number. J. Fluid Mech. 381, S0022112098003474.

Atencia, J., Beebe, D.J., 2005. Controlled microfluidic interfaces. Nature 437, 648–655.

Ayazi Shamlou, P., Siddiqi, S.F., Titchener-Hooker, N.J., 1995. A physical model of high-pressure disruption of bakers' yeast cells. Chem. Eng. Sci. 50, 1383–1391.

Barany, S., Szepesszentgyörgyi, A., 2004. Flocculation of cellular suspensions by polyelectrolytes. Adv. Colloid Interface Sci. 111, 117–129.

Barnkob, R., Augustsson, P., Laurell, T., Bruus, H., 2010. Measuring the local pressure amplitude in microchannel acoustophoresis. Lab Chip 10, 563–570.

Barnkob, R., Iranmanesh, I., Wiklund, M., Bruus, H., 2012. Measuring acoustic energy density in microchannel acoustophoresis using a simple and rapid light-intensity method. Lab Chip 12, 2337.

Bauer, F.F., Govender, P., Bester, M.C., 2010. Yeast flocculation and its biotechnological relevance. Appl. Microbiol. Biotechnol. 88, 31–39.

Bell, D.J., Dunnill, P., 1982. Shear disruption of soya protein precipitate particles and the effect of aging in a stirred tank. Biotechnol. Bioeng. 24, 1271–1285.

Berrill, A., Ho, S. V., Bracewell, D.G., 2008. Ultra scale-down to define and improve the relationship between flocculation and disc-stack centrifugation. Biotechnol. Prog. 24, 426–431.

Bhagat, A.A.S., Kuntaegowdanahalli, S.S., Papautsky, I., 2008a. Enhanced particle filtration in straight microchannels using shear-modulated inertial migration. Phys. Fluids 20, 101702.

Bhagat, A.A.S., Kuntaegowdanahalli, S.S., Papautsky, I., 2008b. Continuous particle separation in spiral microchannels using dean flows and differential migration. Lab Chip 8, 1906.

Blankenstein, G., Larsen, U.D., 1998. Modular concept of a laboratory on a chip for chemical and biochemical analysis. Biosens. Bioelectron. 13, 427–438.

Boccazzi, P., Zanzotto, A., Szita, N., Bhattacharya, S., Jensen, K.F., Sinskey, A.J., 2005. Gene expression analysis of Escherichia coli grown in miniaturized bioreactor platforms for high-throughput analysis of growth and genomic data. Appl. Microbiol. Biotechnol. 68, 518–532.

Bodla, V.K., Seerup, R., Krühne, U., Woodley, J.M., Gernaey, K. V., 2013. Microreactors and CFD as Tools for Biocatalysis Reactor Design: A case study. Chem. Eng. Technol. 36, 1017–1026.

Bolto, B., 1995. Soluble polymers in water purification. Prog. Polym. Sci. 20, 987–1041.

Bolto, B., Gregory, J., 2007. Organic polyelectrolytes in water treatment. Water Res. 41, 2301–2324.

Bovik, A.C., 2005. Basic Binary Image Processing, in: Handbook of Image and Video Processing, Communications, Networking and Multimedia. Elsevier, Burlington, pp. 39–55.

Broadwell, I., Fletcher, P.D., Haswell, S.J., McCreedy, T., Zhang, X., 2001. Quantitative 3-dimensional profiling of channel networks within transparent lab-on-a-chip microreactors using a digital imaging method. Lab Chip 1, 66–71.

Bruus, H., 2008. Theoretical Microfluidics. Oxford University Press, New York.

Butkus, M.A., Bays, J.T., Labare, M.P., 2003. Influence of Surface Characteristics on the Stability of Cryptosporidium parvum Oocysts. Appl. Environ. Microbiol. 69, 3819–3825.

Chang, Y.-I., Ku, M.-H., 2001. Gravity-induced flocculation of non-Brownian particles. Colloids Surfaces A Physicochem. Eng. Asp. 178, 231–247.

Chatel, A., Kumpalume, P., Hoare, M., 2014. Ultra scale-down characterization of the impact of conditioning methods for harvested cell broths on clarification by continuous centrifugation-Recovery of domain antibodies from rec E. coli. Biotechnol. Bioeng. 111, 913–924.

Cheng, J.-Y., Wei, C.-W., Hsu, K.-H., Young, T.-H., 2004. Direct-write laser micromachining and universal surface modification of PMMA for device development. Sensors Actuators B Chem. 99, 186–196.

Clarkson, A.I., Lefevre, P., Titchener-Hooker, N.J., 1993. A study of process interactions between cell disruption and debris clarification stages in the recovery of yeast intracellular products. Biotechnol. Prog. 9, 462–467.

Clicq, D., Vervoort, N., Baron, G. V, Desmet, G., 2004. Shear-Driven Flow LC: Dispensing with Pumps and Voltage Supplies for Increased Speed and Resolution. LCGC Eur. 17, 278–290.

Cordes, R.M., Sims, W.B., Glatz, C.E., 1990. Precipitation of nucleic acids with poly(ethyleneimine). Biotechnol. Prog. 6, 283–285.

Crosland-Taylor, P.J., 1953. A device for counting small particles suspended in a fluid through a tube. Nature 171, 37–38.

Davies, M.J., Marques, M.P.C., Radhakrishnan, A.N.P., 2014. Chapter 2. Microfluidics Theory in Practice, in: Labeed, F.H., Fatoyinbo, H.O. (Eds.), Microfluidics in Detection Science : Lab-on-a-Chip Technologies. Royal Society of Chemistry, London, pp. 29–60.

De Mello, A., 2002. On-chip chromatography: the last twenty years. Lab Chip 2, 48N–54N.

Di Carlo, D., 2009. Inertial microfluidics. Lab Chip 9, 3038–3046.

Di Carlo, D., Edd, J.F., Humphry, K.J., Stone, H. a., Toner, M., 2009. Particle segregation and dynamics in confined flows. Phys. Rev. Lett. 102, 1–4.

Di Carlo, D., Edd, J.F., Irimia, D., Tompkins, R.G., Toner, M., 2008. Equilibrium Separation and Filtration of Particles Using Differential Inertial Focusing. Anal. Chem. 80, 2204–2211.

Di Carlo, D., Irimia, D., Tompkins, R.G., Toner, M., 2007. Continuous inertial focusing, ordering, and separation of particles in microchannels. Proc. Natl. Acad. Sci. U. S. A. 104, 18892–18897.

Dittrich, P.S., Manz, A., 2006. Lab-on-a-chip: microfluidics in drug discovery. Nat. Rev. Drug Discov. 5, 210–218.

Dittrich, P.S., Tachikawa, K., Manz, A., 2006. Micro Total Analysis Systems. Latest Advancements and Trends. Anal. Chem. 78, 3887–3908.

Domingues, L., Vicente, A.A., Lima, N., Teixeira, J.A., 2000. Applications of yeast flocculation in biotechnological processes. Biotechnol. Bioprocess Eng. 5, 288–305.

Droppo, I.G., Ongley, E.D., 1992. The state of suspended sediment in the freshwater fluvial environment: A method of analysis. Water Res. 26, 65–72.

Duan, J., Gregory, J., 1996. Influence of soluble silica on coagulation by aluminium sulphate. Colloids Surfaces A Physicochem. Eng. Asp. 107, 309–319.

Eisenlauer, J., Horn, D., 1987. Fibre-optic on-line flocculant dose control in water treatment operations. Colloids and Surfaces 25, 111–129.

Eisenlauer, J., Horn, D., 1985. Fibre-optic sensor technique for flocculant dose control in flowing suspensions. Colloids and Surfaces 14, 121–134.

Eisma, D., Kalf, J., 1996. *In situ* particle (floc) size measurements with the Nioz in situ camera system. J. Sea Res. 36, 49–53.

Espuny Garcia del Real, G., Davies, J., Bracewell, D.G., 2014. Scale-down characterization of post-centrifuge flocculation processes for high-throughput process development. Biotechnol. Bioeng. 111, 2486–2498.

Fogler, H.S., 1999. Elements of Chemical Reaction Engineering, Third. ed. Prentice-Hall Inc., New Delhi.

Fredrickson, C.K., Fan, Z.H., 2004. Macro-to-micro interfaces for microfluidic devices. Lab Chip 4, 526–533.

Fu, L.-M., Yang, R.-J., Lin, C.-H., Pan, Y.-J., Lee, G.-B., 2004. Electrokinetically driven micro flow cytometers with integrated fiber optics for on-line cell/particle detection. Anal. Chim. Acta 507, 163–169.

Garstecki, P., Gitlin, I., DiLuzio, W., Whitesides, G.M., Kumacheva, E., Stone, H.A., 2004. Formation of monodisperse bubbles in a microfluidic flow-focusing device. Appl. Phys. Lett. 85, 2649.

Gregory, J., 1988. Polymer adsorption and flocculation in sheared suspensions. Colloids and Surfaces 31, 231–253.

Gregory, J., 1985. Turbidity fluctuations in flowing suspensions. J. Colloid Interface Sci. 105, 357–371.

Gregory, J., 1973. Rates of flocculation of latex particles by cationic polymers. J. Colloid Interface Sci. 42, 448–456.

Gregory, J., Barany, S., 2011. Adsorption and flocculation by polymers and polymer mixtures. Adv. Colloid Interface Sci. 169, 1–12.

Groβ, G.A., Koöhler, J.M., 2010. Residence Time Distribution and Nanoparticle Formation in Microreactors, in: Microfluidic Devices in Nanotechnology. John Wiley & Sons, Inc., Hoboken, NJ, USA, pp. 317–340.

Gupta, R., Baldock, S.J., Carreras, P., Fielden, P.R., Goddard, N.J., Mohr, S., Razavi, B.S., Treves Brown, B.J., 2011. A microfluidic device for self-synchronised production of droplets. Lab Chip 11, 4052.

Habib, G., Zhou, Y., Hoare, M., 2000. Rapid monitoring for the enhanced definition and control of a selective cell homogenate purification by a batch-flocculation process. Biotechnol. Bioeng. 70, 131–142.

Habib, G.B., Holwill, I., Hoare, M., 1997. Rapid piloting of a selective flocculation process for product purification. J. Biotechnol. 59, 91–101.

Hamilton, J.D., Reinert, K.H., Freeman, M.B., 1994. Aquatic Risk Assessment of Polymers. Environ. Sci. Technol. 28, 186A–192A.

Harris, N.R., Keating, A., Hill, M., n.d. A Lateral Mode Flow-through PMMA Ultrasonic Separator.

He, P., Greenway, G., Haswell, S.J., 2010. Development of a monolith based immobilized lipase micro-reactor for biocatalytic reactions in a biphasic mobile system. Process Biochem. 45, 593–597.

Healy, T.W., La Mer, V.K., 1964. The energetics of flocculation and redispersion by polymers. J. Colloid Sci. 19, 323–332.

Heng, X., Erickson, D., Baugh, L.R., Yaqoob, Z., Sternberg, P.W., Psaltis, D., Yang, C., 2006. Optofluidic microscopy--a method for implementing a high resolution optical microscope on a chip. Lab Chip 6, 1274–1276.

Hertzog, D.E., Michalet, X., Jager, M., Kong, X., Santiago, J.G., Weiss, S., Bakajin, O., 2004. Femtomole mixer for microsecond kinetic studies of protein folding. Anal. Chem. 76, 7169–7178.

Hessel, V., Löwe, H., Schönfeld, F., 2005. Micromixers—a review on passive and active mixing principles. Chem. Eng. Sci. 60, 2479–2501.

Holwill, I.J., Chard, S.J., Flanagan, M.T., Hoare, M., 1997. A kalman filter algorithm and monitoring apparatus for at-line control of fractional protein precipitation. Biotechnol. Bioeng. 53, 58–70.

Hou, H.W., Bhattacharyya, R.P., Hung, D.T., Han, J., 2015. Direct detection and drug-resistance profiling of bacteremias using inertial microfluidics. Lab Chip 15, 2297–2307.

Hubbuch, J., Kula, M.R., 2008. Confocal laser scanning microscopy as an analytical tool in chromatographic research. Bioprocess Biosyst. Eng. 31, 241–259.

Huh, D., Gu, W., Kamotani, Y., Grotberg, J.B., Takayama, S., 2005. Microfluidics for flow cytometric analysis of cells and particles. Physiol. Meas. 26, R73–R98.

Huh, D., Tung, Y.C., Wei, H.H., Grotberg, J.B., Skerlos, S.J., Kurabayashi, K., Takayama, S., 2002. Use of air-liquid two-phase flow in hydrophobic microfluidic channels for disposable flow cytometers. Biomed. Microdevices 4, 141–149.

Hung, P.J., Lee, P.J., Sabounchi, P., Lin, R., Lee, L.P., 2005. Continuous perfusion microfluidic cell culture array for high-throughput cell-based assays. Biotechnol. Bioeng. 89, 1–8.

Hunter, J.D., 2007. Matplotlib: A 2D Graphics Environment. Comput. Sci. Eng. 9, 90–95.

Iranmanesh, I., Barnkob, R., Bruus, H., Wiklund, M., 2013. Tunable-angle wedge transducer for improved acoustophoretic control in a microfluidic chip. J. Micromechanics Microengineering 23, 105002.

Israelachvili, J., 1997. The different faces of poly(ethylene glycol). Proc. Natl. Acad. Sci. U. S. A. 94, 8378–8379.

Jaccard, N., Griffin, L.D., Keser, A., Macown, R.J., Super, A., Veraitch, F.S., Szita, N., 2014a. Automated method for the rapid and precise estimation of adherent cell

culture characteristics from phase contrast microscopy images. Biotechnol. Bioeng. 111, 504–517.

Jaccard, N., Macown, R.J., Super, A., Griffin, L.D., Veraitch, F.S., Szita, N., 2014b. Automated and Online Characterization of Adherent Cell Culture Growth in a Microfabricated Bioreactor. J. Lab. Autom. 19, 437–443.

Jamali, S., Yamanoi, M., Maia, J., 2013. Bridging the gap between microstructure and macroscopic behavior of monodisperse and bimodal colloidal suspensions. Soft Matter 9, 1506.

Jarvis, P., Jefferson, B., Gregory, J., Parsons, S.A., 2005. A review of floc strength and breakage. Water Res. 39, 3121–3137.

Jensen, K.F., 1998. Smaller, faster chemistry. Nature 393, 735–736.

Kang, Q.-S., Shen, X.-F., Hu, N.-N., Hu, M.-J., Liao, H., Wang, H.-Z., He, Z.-K., Huang, W.-H., 2013. A 3D porous polymer monolith-based platform integrated in poly(dimethylsiloxane) microchips for immunoassay. Analyst 138, 2613–9.

Kayode, T.O., Gregory, J., 1988. A new technique for monitoring alum sludge conditioning. Water Res. 22, 85–90.

Kennedy, M.J., Stelick, S.J., Sayam, L.G., Yen, A., Erickson, D., Batt, C. A., 2011. Hydrodynamic optical alignment for microflow cytometry. Lab Chip 11, 1138–1143.

Kim, J., Akeprathumchai, S., Wickramasinghe, S.R., 2001. Flocculation to enhance microfiltration. J. Memb. Sci. 182, 161–172.

Kim, L., Vahey, M.D., Lee, H.-Y., Voldman, J., 2006. Microfluidic arrays for logarithmically perfused embryonic stem cell culture. Lab Chip 6, 394–406.

Kirk, T. V, Marques, M.P., Radhakrishnan, A.N.P., Szita, N., 2016. Quantification of the oxygen uptake rate in a dissolved oxygen controlled oscillating jet-driven microbioreactor. J. Chem. Technol. Biotechnol. 91, 823–831.

Knight, J., Vishwanath, A., Brody, J., Austin, R., 1998. Hydrodynamic Focusing on a Silicon Chip: Mixing Nanoliters in Microseconds. Phys. Rev. Lett. 80, 3863–3866.

Kricka, L.J., 1998. Miniaturization of analytical systems, in: Clinical Chemistry. pp. 2008–2014.

Kunstmann-Olsen, C., Hoyland, J.D., Rubahn, H.-G., 2012. Influence of geometry on hydrodynamic focusing and long-range fluid behavior in PDMS microfluidic chips. Microfluid. Nanofluidics 12, 795–803.

La Mer, V.K., 1966. Filtration of colloidal dispersions flocculated by anionic and cationic polyelectrolytes. Discuss. Faraday Soc. 42, 248.

La Mer, V.K., 1964. Coagulation symposium introduction. J. Colloid Sci. 19, 291–293.

La Mer, V.K., 1960. Theory of Flocculation, Subsidence and Refiltration Rates of Colloidal Dispersions Flocculated by Polyelectrolytes. Clays Clay Miner. 9, 295–314.

LaMer, V.K., Smellie, R.H., Lee, P.-K., 1957. Flocculation, subsidence, and filtration of phosphate slimes. J. Colloid Sci. 12, 566–574.

Lee, G., Hung, C., Ke, B., Huang, G., Hwei, B.-H., 2001. Micromachined pre-focused 1× N flow switches for continuous sample injection. J. Micromechanics Microengineering 11, 567–573.

Lee, G.-B., Chang, C.-C., Huang, S.-B., Yang, R.-J., 2006. The hydrodynamic focusing effect inside rectangular microchannels. J. Micromechanics Microengineering 16, 1024–1032.

Lee, K., 1983. Change of particle size distribution during Brownian coagulation. J. Colloid Interface Sci. 92, 315–325.

Letterman, R.D., Pero, R.W., 1990. Contaminants in polyelectrolytes used in water treatment. J. Am. Water Work. Assoc. 82, 87–97.

Levenspiel, O., 1999. Chemical Reaction Engineering, Third. ed. John Wiley & Sons, Inc., New York.

Leyden, M.R., Messinger, R.J., Schuman, C., Sharf, T., Remcho, V.T., Squires, T.M., Minot, E.D., 2012. Increasing the detection speed of an all-electronic real-time biosensor. Lab Chip 12, 954.

Lion, N., Reymond, F., Girault, H.H., Rossier, J.S., 2004. Why the move to microfluidics for protein analysis? Curr. Opin. Biotechnol. 15, 31–37.

Lips, A., Smart, C., Willis, E., 1971. Light scattering studies on a coagulating polystyrene latex. Trans. Faraday Soc. 67, 2979.

Locher, G., Sonnleitner, B., Fiechter, A., 1992. On-line measurement in biotechnology: exploitation, objectives and benefits. J. Biotechnol. 25, 55–73.

Manz, A., Graber, N., Widmer, H.M., 1990. Miniaturized total chemical analysis systems: A novel concept for chemical sensing. Sensors Actuators B Chem. 1, 244–248.

Manz, A., Verpoorte, E., Effenhauser, C.S., Burggraf, N., Raymond, D.E., Harrison, D.J., Widmer, H.M., 1993. Miniaturization of separation techniques using planar chip technology. J. High Resolut. Chromatogr. 16, 433–436.

Marques, M.P.C., Fernandes, P., 2011. Microfluidic Devices: Useful Tools for Bioprocess Intensification. Molecules 16, 8368–8401.

Martín-Banderas, L., Flores-Mosquera, M., Riesco-Chueca, P., Rodríguez-Gil, A., Cebolla, Á., Chávez, S., Gañán-Calvo, A.M., 2005. Flow Focusing: A Versatile Technology to Produce Size-Controlled and Specific-Morphology Microparticles. Small 1, 688–692.

Mashmoushy, H., Zhang, Z., Thomas, C.R., 1998. Micromanipulation measurement of the mechanical properties of baker's yeast cells. Biotechnol. Tech. 12, 925–929.

Matas, J.-P., Glezer, V., Guazzelli, E., Morris, J.F., 2004a. Trains of particles in finite-Reynolds-number pipe flow. Phys. Fluids 16, 4192.

Matas, J.-P., Morris, J.F., Guazzelli, É., 2004b. Inertial migration of rigid spherical particles in Poiseuille flow. J. Fluid Mech. 515, 171–195.

Matthews, B., Rhodes, C., 1970. Studies of the coagulation kinetics of mixed suspensions. J. Colloid Interface Sci. 32, 332–338.

Meinders, J., Noordmans, J., Busscher, H., 1992. Simultaneous monitoring of the adsorption and desorption of colloidal particles during deposition in a parallel plate flow chamber. J. Colloid Interface Sci. 152, 265–280.

Melton, L.A., Lipp, C.W., Spradling, R.W., Paulson, K. A., 2002. Dismt - Determination of mixing time through color changes. Chem. Eng. Commun. 189, 322–338.

Mészáros, R., Varga, I., Gilányi, T., 2004. Adsorption of poly(ethyleneimine) on silica surfaces: Effect of pH on the reversibility of adsorption. Langmuir 20, 5026–5029.

Middelberg, A.P.J., 1995. Process-scale disruption of microorganisms. Biotechnol. Adv. 13, 491–551.

Milburn, P., Bonnerjea, J., Hoare, M., Dunnill, P., 1990. Selective flocculation of nucleic acids, lipids, and colloidal particles from a yeast cell homogenate by polyethyleneimine, and its scale-up. Enzyme Microb. Technol. 12, 527–532.

Millis, J.R., 1996. Handbook of Downstream Processing, First. ed, Handbook of Downstream Processing. Springer Netherlands, Dordrecht.

Mondal, S., Leong, Y.K., Liow, J.L., Wickramasinghe, S.R., 2013. Flocculation of yeast suspensions by a cationic flocculant. Powder Technol. 235, 426–430.

Mora, M.F., Greer, F., Stockton, A.M., Bryant, S., Willis, P.A., 2011. Toward Total Automation of Microfluidics for Extraterrestial In situ Analysis. Anal. Chem. 83, 8636–8641.

Morgan, J.J., Stumm, W., 1964. Colloid-chemical properties of manganese dioxide. J. Colloid Sci. 19, 347–359.

Muehle, K., Domasch, K., 1991. Stability of particle aggregates in flocculation with polymers. Chem. Eng. Process. 29, 1–8.

Napper, D.H., 1983. Polymeric Stabilization of Colloidal Dispersions. Academic Press, London.

Narita, T., Ohtakeyama, R., Matsukata, M., Gong, J.P., Osada, Y., 2001. Kinetic study of cell disruption by ionic polymers with varied charge density. Colloid Polym. Sci. 279, 178–183.

Narong, P., James, A.E., 2006. Effect of pH on the ζ-potential and turbidity of yeast suspensions. Colloids Surfaces A Physicochem. Eng. Asp. 274, 130–137.

Nasir, M., Price, D.T., Shriver-Lake, L.C., Ligler, F., 2010. Effect of diffusion on impedance measurements in a hydrodynamic flow focusing sensor. Lab Chip 10, 2787–2795.

Neu, M., Fischer, D., Kissel, T., 2005. Recent advances in rational gene transfer vector design based on poly(ethylene imine) and its derivatives. J. Gene Med. 7, 992–1009.

Nguyen, N.-T., Wereley, S.T., 2006. Fundamental and Applications of Microfluidics, Second. ed. Artech House Inc., Norwood.

Nguyen, N.-T., Wu, Z., 2004. Micromixers—a review. J. Micromechanics Microengineering 15, R1–R16.

O'Sullivan, B., Al-Bahrani, H., Lawrence, J., Campos, M., Cázares, A., Baganz, F., Wohlgemuth, R., Hailes, H.C., Szita, N., 2012. Modular microfluidic reactor and inline filtration system for the biocatalytic synthesis of chiral metabolites. J. Mol. Catal. B Enzym. 77, 1–8.

Oliphant, T.E., 2007. Python for Scientific Computing. Comput. Sci. Eng. 9, 10–20.

Pena-Pereira, F., Costas-Mora, I., Romero, V., Lavilla, I., Bendicho, C., 2011. Advances in miniaturized UV-Vis spectrometric systems. TrAC - Trends Anal. Chem. 30, 1637–1648.

Pfleging, W., Kohler, R., Schierjott, P., Hoffmann, W., 2009. Laser patterning and packaging of CCD-CE-Chips made of PMMA. Sensors Actuators, B Chem. 138, 336–343.

Pollack, L., Tate, M.W., Darnton, N.C., Knight, J.B., Gruner, S.M., Eaton, W.A., Austin, R.H., 1999. Compactness of the denatured state of a fast-folding protein measured by submillisecond small-angle x-ray scattering. Proc. Natl. Acad. Sci. 96, 10115–10117.

Psaltis, D., Quake, S.R., Yang, C., 2006. Developing optofluidic technology through the fusion of microfluidics and optics. Nature 442, 381–386.

Raasch, J., Umhauer, H., 1989. Computation of the Frequency Distributions of Distances Between Particles Randomly Dispersed in a Fluid Flow. Part. Part. Syst. Charact. 6, 13–16.

Raasch, J., Umhauer, H., 1984. Errors in the Determination of Particle Size Distributions Caused by coincidences in optical particle counters. Part. Part. Syst. Charact. 1, 53–58.

Rahn-Chique, K., Puertas, A.M., Romero-Cano, M.S., Rojas, C., Urbina-Villalba, G., 2012. Nanoemulsion stability: Experimental evaluation of the flocculation rate from turbidity measurements. Adv. Colloid Interface Sci. 178, 1–20.

Regenberg, B., Krühne, U., Beyer, M., Pedersen, L.H., Simon, M., Thomas, O.R.T., Nielsen, J., Ahl, T., 2004. Use of laminar flow patterning for miniaturised biochemical assays. Lab Chip 4, 654–657.

Reichen, M., Super, A., Davies, M.J., Macown, R.J., O'Sullivan, B., Kirk, T.V., Marques, M.P.C., Dimov, N., Szita, N., 2014. Characterisation of an Adhesive-free Packaging System for Polymeric Microfluidic Biochemical Devices and Reactors. Chem. Biochem. Eng. Q. J. 28, 189–202.

Richardson, P., Hoare, M., Dunnill, P., 1990. A new biochemical engineering approach to the fractional precipitation of proteins. Biotechnol. Bioeng. 36, 354–366.

Rodriguez, G., Weheliye, W., Anderlei, T., Micheletti, M., Yianneskis, M., Ducci, A., 2013. Mixing time and kinetic energy measurements in a shaken cylindrical bioreactor. Chem. Eng. Res. Des. 91, 2084–2097.

Rose, A.H., Harrison, J.S., 1971. The Yeasts: Physiology and biochemistry of yeasts. Academic Press, London.

Sabourin, D., Dufva, M., Jensen, T., Kutter, J., Snakenborg, D., 2010. One-step fabrication of microfluidic chips with in-plane, adhesive-free interconnections. J. Micromechanics Microengineering 20, 037001.

Sabourin, D., Snakenborg, D., Dufva, M., 2009. Interconnection blocks: a method for providing reusable, rapid, multiple, aligned and planar microfluidic interconnections. J. Micromechanics Microengineering 19, 035021.

Salt, D.E., Bentham, A.C., Hay, S., Idris, A., Gregory, J., Hoare, M., Dunnill, P., 1996. The mechanism of flocculation of a Saccharomyces cerevisiae cell homogenate using polyethyleneimine. Bioprocess Eng. 15, 71.

Salt, D.E., Hay, S., Thomas, O.R.T., Hoare, M., Dunnill, P., 1995. Selective flocculation of cellular contaminants from soluble proteins using polyethyleneimine: A study of several organisms and polymer molecular weights. Enzyme Microb. Technol. 17, 107–113.

Schneider, C.A., Rasband, W.S., Eliceiri, K.W., 2012. NIH Image to ImageJ: 25 years of image analysis. Nat. Methods 9, 671–675.

Schonberg, J. A., Hinch, E.J., 1989. Inertial migration of a sphere in Poiseuille flow. J. Fluid Mech. 203, 517.

Schrum, D.P., Culbertson, C.T., Jacobson, S.C., Ramsey, J.M., 1999. Microchip Flow Cytometry Using Electrokinetic Focusing. Anal. Chem. 71, 4173–4177.

Segré, G., Silberberg, A., 1961. Radial Particle Displacements in Poiseuille Flow of Suspensions. Nature 189, 209–210.

Shan, J., Xia, J., Guo, Y., Zhang, X., 1996. Flocculation of cell, cell debris and soluble protein with methacryloyloxyethyl trimethylammonium chloride—acrylonitrile copolymer. J. Biotechnol. 49, 173–178.

Shapiro, M.S., 2009. Design and characterization of microliter scale chromatography for the comparison with preparative scale chromatography. University College London.

Shapiro, M.S., Haswell, S.J., Lye, G.J., Bracewell, D.G., 2009. Design and characterization of a microfluidic packed bed system for protein breakthrough and dynamic binding capacity determination. Biotechnol. Prog. 25, 277–285.

Shinners, P., 2009. PyGame - Python Game Development.

Shiu, C., Zhang, Z., Thomas, C.R., 1999. A novel technique for the study of bacterial cell mechanical properties. Biotechnol. Tech. 13, 707–713.

Siddiqi, S.F., Titchener-Hooker, N.J., Shamlou, P.A., 1997. High pressure disruption of yeast cells: The use of scale down operations for the prediction of protein release and cell debris size distribution. Biotechnol. Bioeng. 55, 642–649.

Silberberg, A., 1968. Adsorption of Flexible Macromolecules. IV. Effect of Solvent–Solute Interactions, Solute Concentration, and Molecular Weight. J. Chem. Phys. 48, 2835–2851.

Siu, S.C., Boushaba, R., Liau, J., Hjorth, R., Titchener-Hooker, N.J., 2007. Confocal imaging of chromatographic fouling under flow conditions. J. Chem. Technol. Biotechnol. 82, 871–881.

Siu, S.C., Boushaba, R., Topoyassakul, V., Graham, A., Choudhury, S., Moss, G., Titchener-Hooker, N.J., 2006. Visualising fouling of a chromatographic matrix using confocal scanning laser microscopy. Biotechnol. Bioeng. 95, 714–723.

Somasundaran, P., Yu, X., 1994. Flocculation/dispersion of suspensions by controlling adsorption and conformation of polymers and surfactants. Adv. Colloid Interface Sci. 53, 33–49.

Squires, T.M., Quake, S.R., 2005. Microfluidics: Fluid physics at the nanoliter scale. Rev. Mod. Phys. 77, 977–1026.

Srinivasan, A., Bach, H., Sherman, D.H., Dordick, J.S., 2004. Bacterial P450-catalyzed polyketide hydroxylation on a microfluidic platform. Biotechnol. Bioeng. 88, 528–535.

Suh, J., Paik, H.J., Hwang, B.K., 1994. Ionization of Poly(ethylenimine) and Poly(allylamine) at Various pH′s. Bioorg. Chem. 22, 318–327.

Šulc, R., Lemanowicz, M., Gierczycki, A.T., 2012. Effect of flocculant sonication on floc growth kinetics occurring in an agitated vessel. Chem. Eng. Process. Process Intensif. 60, 49–54.

Sun, Y., Kwok, Y.C., Nguyen, N.-T., 2006. Low-pressure, high-temperature thermal bonding of polymeric microfluidic devices and their applications for electrophoretic separation. J. Micromechanics Microengineering 16, 1681–1688.

Sun, Y., Satyanarayan, M.V.D., Nguyen, N.T., Kwok, Y.C., 2008. Continuous flow polymerase chain reaction using a hybrid PMMA-PC microchip with improved heat tolerance. Sensors Actuators B Chem. 130, 836–841.

Szita, N., Boccazzi, P., Zhang, Z., Boyle, P., Sinskey, A.J., Jensen, K.F., 2005. Development of a multiplexed microbioreactor system for high-throughput bioprocessing. Lab Chip 5, 819–826.

Tabeling, P., 2009. A brief introduction to slippage, droplets and mixing in microfluidic systems. Lab Chip 9, 2428–2436.

Tabeling, P., 2005. Introduction to Microfluidics by Patrick Tabeling. Oxford University Press, New York.

Takayama, S., McDonald, J.C., Ostuni, E., Liang, M.N., Kenis, P.J., Ismagilov, R.F., Whitesides, G.M., 1999. Patterning cells and their environments using multiple laminar fluid flows in capillary networks. Proc. Natl. Acad. Sci. U. S. A. 96, 5545–5548.

Takeuchi, S., Garstecki, P., Weibel, D.B., Whitesides, G.M., 2005. An Axisymmetric Flow-Focusing Microfluidic Device. Adv. Mater. 17, 1067–1072.

Tan, R.-K., Eberhard, W., Büchs, J., 2011. Measurement and characterization of mixing time in shake flasks. Chem. Eng. Sci. 66, 440–447.

Tang, M.X., Szoka, F.C., 1997. The influence of polymer structure on the interactions of cationic polymers with DNA and morphology of the resulting complexes. Gene Ther. 4, 823–832.

Terry, S.C., Jerman, J.H., Angell, J.B., 1979. A gas chromatographic air analyzer fabricated on a silicon wafer. IEEE Trans. Electron Devices 26, 1880–1886.

Thomas, D.N., Judd, S.J., Fawcett, N., 1999. Flocculation modelling: A review. Water Res. 33, 1579–1592.

Tomer, R., Khairy, K., Amat, F., Keller, P.J., 2012. Quantitative high-speed imaging of entire developing embryos with simultaneous multiview light-sheet microscopy. Nat. Methods 9, 755–763.

Treweek, G.P., Morgan, J.J., 1977. The mechanism of E. coli aggregation by polyethyleneimine. J. Colloid Interface Sci. 60, 258–273.

Tsao, C.-W., DeVoe, D.L., 2009. Bonding of thermoplastic polymer microfluidics. Microfluid. Nanofluidics 6, 1–16.

Tsoka, S., Ciniawskyj, O.C., Thomas, O.R.T., Titchener-Hooker, N.J., Hoare, M., 2000. Selective flocculation and precipitation for the improvement of virus-like particle recovery from yeast homogenate. Biotechnol. Prog. 16, 661–667.

Tustian, A.D., Salte, H., Willoughby, N.A., Hassan, I., Rose, M.H., Baganz, F., Hoare, M., Titchener-Hooker, N.J., 2007. Adapted Ultra Scale-Down Approach for Predicting the Centrifugal Separation Behavior of High Cell Density Cultures. Biotechnol. Prog. 23, 1404–1410.

Urbina-Villalba, G., García-Sucre, M., 2005. Role of the secondary minimum on the flocculation rate of nondeformable droplets. Langmuir 21, 6675–6687.

Van De Ven, T.G.M., 1994. Kinetic aspects of polymer and polyelectrolyte adsorption on surfaces. Adv. Colloid Interface Sci. 48, 121–140.

Van der Walt, S., Colbert, S.C., Varoquaux, G., 2011. The NumPy Array: A Structure for Efficient Numerical Computation. Comput. Sci. Eng. 13, 22–30.

Van Rossum, G., 1995. Python Tutorial, Technical Report CS-R9526. Amsterdam.

Vincent, P.E., Plata, A. M., Hunt, A. A. E., Weinberg, P.D., Sherwin, S.J., 2011. Blood flow in the rabbit aortic arch and descending thoracic aorta. J. R. Soc. Interface 8, 1708–1719.

Vinuselvi, P., Park, S., Kim, M., Park, J.M., Kim, T., Lee, S.K., 2011. Microfluidic technologies for synthetic biology. Int. J. Mol. Sci. 12, 3576–3593.

Voldman, J., Gray, M.L., Schmidt, M.A., 2000. An integrated liquid mixer/valve. J. Microelectromechanical Syst. 9, 295–302.

Walker, G.M., Ozers, M.S., Beebe, D.J., 2004. Cell infection within a microfluidic device using virus gradients. Sensors Actuators, B Chem. 98, 347–355.

Wang, C., Friedlander, S., 1967. The self-preserving particle size distribution for coagulation by Brownian motion. J. Colloid Interface Sci. 24, 170–179.

Wang, J., 2004. Microchip devices for detecting terrorist weapons. Anal. Chim. Acta 507, 3–10.

Weng, Y., Delgado, F.F., Son, S., Burg, T.P., Wasserman, S.C., Manalis, S.R., 2011. Mass sensors with mechanical traps for weighing single cells in different fluids. Lab Chip 11, 4174.

Werts, M.H.V., Raimbault, V., Texier-Picard, R., Poizat, R., Français, O., Griscom, L., Navarro, J.R.G., 2012. Quantitative full-colour transmitted light microscopy and dyes for concentration mapping and measurement of diffusion coefficients in microfluidic architectures. Lab Chip 12, 808–820.

West, J., Becker, M., Tombrink, S., Manz, A., 2008. Micro total analysis systems: Latest achievements. Anal. Chem. 80, 4403–4419.

Whitesides, G.M., 2006. The origins and the future of microfluidics. Nature 442, 368–373.

Wickramasinghe, S.R., Han, B., Akeprathumchai, S., Jaganjac, A., Qian, X., 2005. Modeling flocculation of biological cells. Powder Technol. 156, 146–153.

Wickramasinghe, S.R., Leong, Y.K., Mondal, S., Liow, J.L., 2010. Influence of cationic flocculant properties on the flocculation of yeast suspensions. Adv. Powder Technol. 21, 374–379.

Wit, P.J., Noordmans, J., Busscher, H.J., 1997. Tracking of colloidal particles using microscopic image sequence analysis Application to particulate microelectrophoresis and particle deposition. Colloids Surfaces A Physicochem. Eng. Asp. 125, 85–92.

Wong, J.X.H., Yu, H.-Z., 2013. Preparation of Transparent Superhydrophobic Glass Slides: Demonstration of Surface Chemistry Characteristics. J. Chem. Educ. 90, 1203–1206.

Wong, P.K., Lee, Y.-K., Ho, C.-M., 2003. Deformation of DNA molecules by hydrodynamic focusing. J. Fluid Mech. 497, 55–65.

Wu, Z., Nguyen, N.-T., 2005. Hydrodynamic focusing in microchannels under consideration of diffusive dispersion: theories and experiments. Sensors Actuators B Chem. 107, 965–974.

Wyatt, N.B., Gloe, L.M., Brady, P. V., Hewson, J.C., Grillet, A.M., Hankins, M.G., Pohl, P.I., 2012. Critical conditions for ferric chloride-induced flocculation of freshwater algae. Biotechnol. Bioeng. 109, 493–501.

Wyatt, N.B., O'Hern, T.J., Shelden, B., Hughes, L.G., Mondy, L.A., 2013. Size and structure of Chlorella zofingiensis /FeCl3 flocs in a shear flow. Biotechnol. Bioeng. 110, 3156–3163.

Xu, Z.-R., Yang, C.-G., Liu, C.-H., Zhou, Z., Fang, J., Wang, J.-H., 2010. An osmotic micro-pump integrated on a microfluidic chip for perfusion cell culture. Talanta 80, 1088–1093.

Xuan, X., Zhu, J., Church, C., 2010. Particle focusing in microfluidic devices. Microfluid. Nanofluidics 9, 1–16.

Yamada, M., Kasim, V., Nakashima, M., Edahiro, J., Seki, M., 2004. Continuous cell partitioning using an aqueous two-phase flow system in microfluidic devices. Biotechnol. Bioeng. 88, 489–494.

Yang, B.H., Wang, J., Joseph, D.D., Hu, H.H., Pan, T.-W., Glowinski, R., 2005. Migration of a sphere in tube flow. J. Fluid Mech. 540, 109.

Yeung, A.K.C., Pelton, R., 1996. Micromechanics: A New Approach to Studying the Strength and Breakup of Flocs. J. Colloid Interface Sci. 184, 579–585.

Yu, J., Liu, H., Chen, J., 1999. "Modified flocculation" of protein with a combination of anionic copolymer and polyacrylamide. Chem. Eng. Sci. 54, 5839–5843.

Yu, J., Liu, H.Z., Chen, J.Y., 2002. Selective precipitation of water-soluble proteins using designed polyelectrolyte. Sep. Sci. Technol. 37, 217–228.

Zanzotto, A., Szita, N., Boccazzi, P., Lessard, P., Sinskey, A.J., Jensen, K.F., 2004. Membrane-aerated microbioreactor for high-throughput bioprocessing. Biotechnol. Bioeng. 87, 243–254.

Zanzotto, A., Szita, N., Schmidt, M. A., Jensen, K.F., 2002. Microfermentors for the rapid screening and analysis of biochemical processes. 2nd Annu. Int. IEEE-EMBS Spec. Top. Conf. Microtechnologies Med. Biol. Proc. (Cat. No.02EX578) 164–168.

Zbik, M.S., Smart, R.S.C., Morris, G.E., 2008. Kaolinite flocculation structure. J. Colloid Interface Sci. 328, 73–80.

Zeleznik, M.J., Segatta, J.M., Ju, L.K., 2002. Polyethyleneimine-induced flocculation and flotation of cyanobacterium Anabaena flos-aquae for gas vesicle production. Enzyme Microb. Technol. 31, 949–953.

Zhang, Y., Lei, H., Li, Y., Li, B., 2012. Microbe removal using a micrometre-sized optical fiber. Lab Chip 12, 1302.

Zhang, Z., Ferenczi, M.A., Lush, A.C., Thomas, C.R., 1991. A novel micromanipulation technique for measuring the bursting strength of single mammalian cells. Appl. Microbiol. Biotechnol. 36, 208–210.

Zhang, Z., Sisk, M.L., Mashmoushy, H., Thomas, C.R., 1999. Characterization of the breaking force of latex particle aggregates by micromanipulation. Part. Part. Syst. Charact. 16, 278–283.

Zhang, Z., Szita, N., Boccazzi, P., Sinskey, A.J., Jensen, K.F., 2006. A well-mixed, polymer-based microbioreactor with integrated optical measurements. Biotechnol. Bioeng. 93, 286–296.

Zhou, X., Liu, D., Zhong, R., Dai, Z., Wu, D., Wang, H., Du, Y., Xia, Z., Zhang, L., Mei, X., Lin, B., 2004. Determination of SARS-coronavirus by a microfluidic chip system. Electrophoresis 25, 3032–3039.

Zhou, Y., Franks, G. V., 2006. Flocculation mechanism induced by cationic polymers investigated by light scattering. Langmuir 22, 6775–6786.

Zhu, X., Liu, G., Guo, Y., Tian, Y., 2007. Study of PMMA thermal bonding. Microsyst. Technol. 13, 403–407.

9. Appendix A: Supplementary Figures

Figure A2.1: CAD drawings of the top and bottom layers of the spiral microfluidic device and the interconnect bar, designed using SolidWorks® 2011 software. All dimensions are in mm.

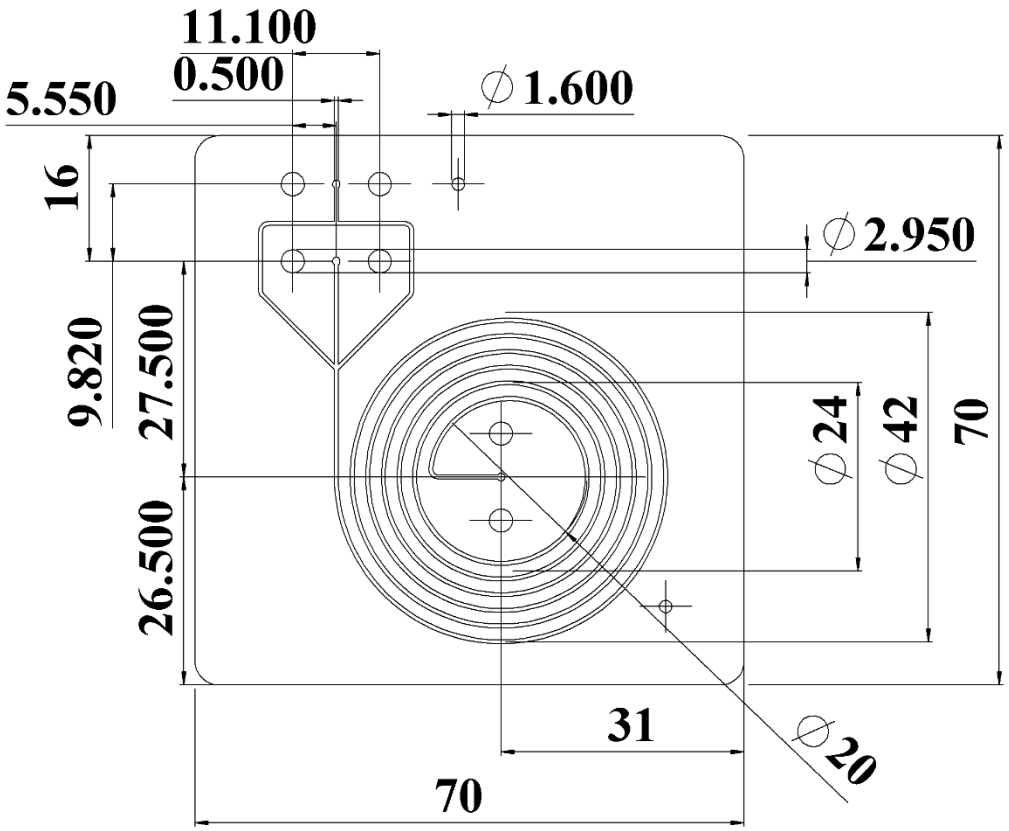

Bottom Layer

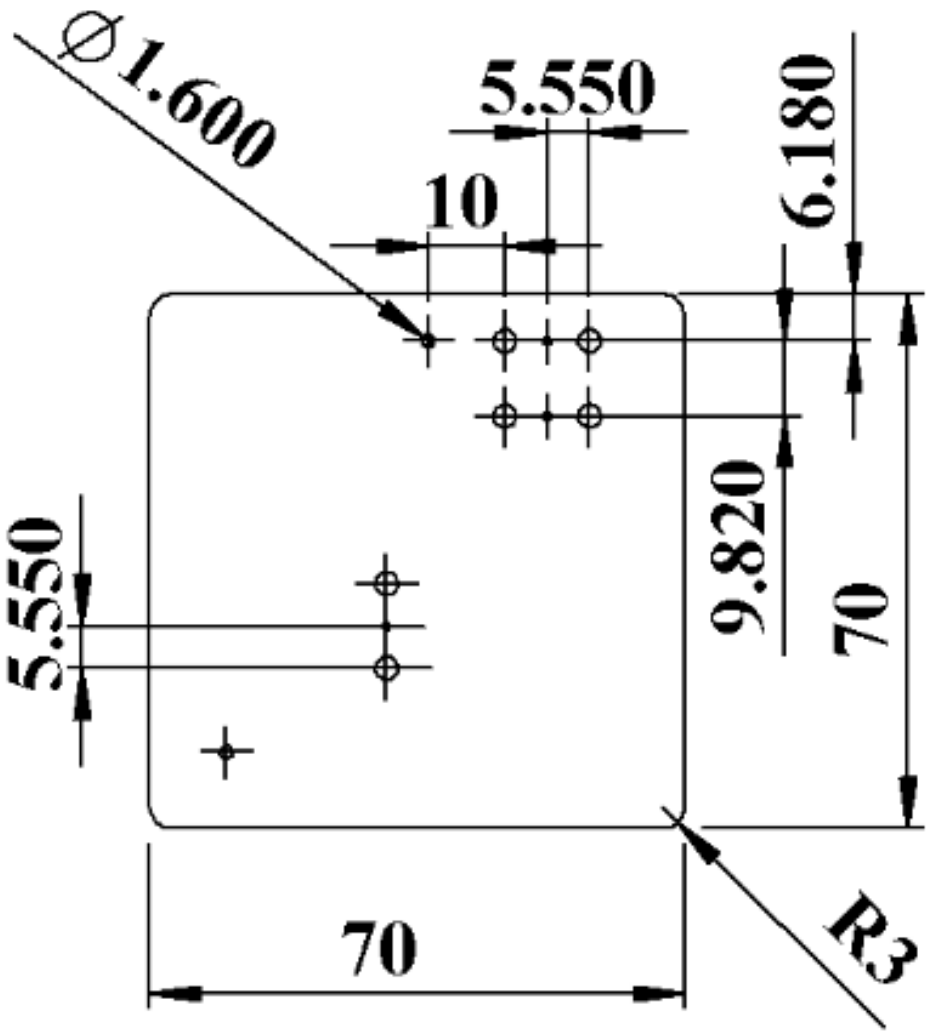

Top Layer

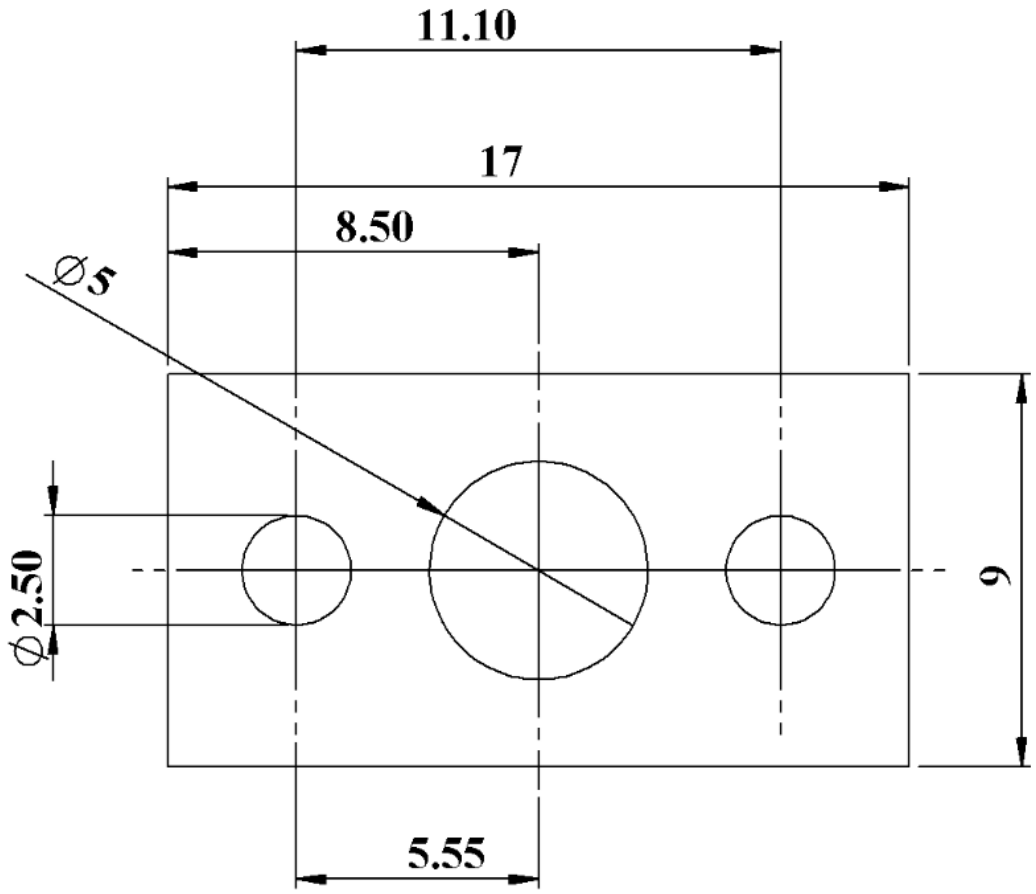

Inter-connect bar

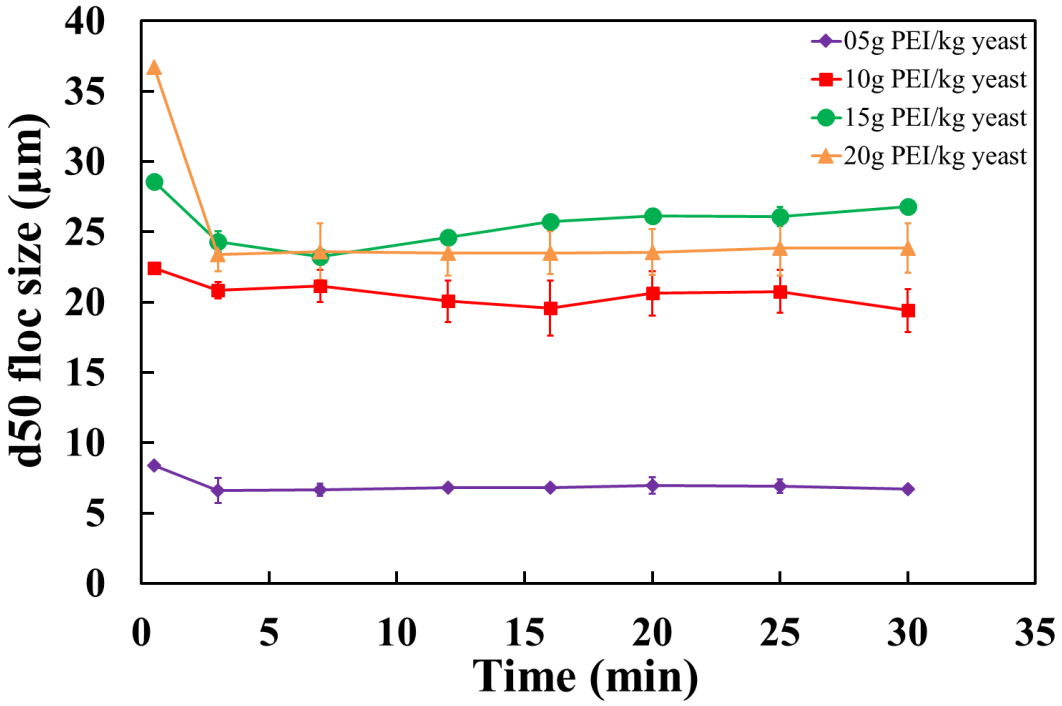

Figure A2.2: Variation of floc sizes over time, in a non-agitated bench scale system (50 ml centrifuge tubes). Flocculation between yeast homogenate and 50-100 kDa PEI, at pH 7.4. The error bars represent ±1σ, n = 3.

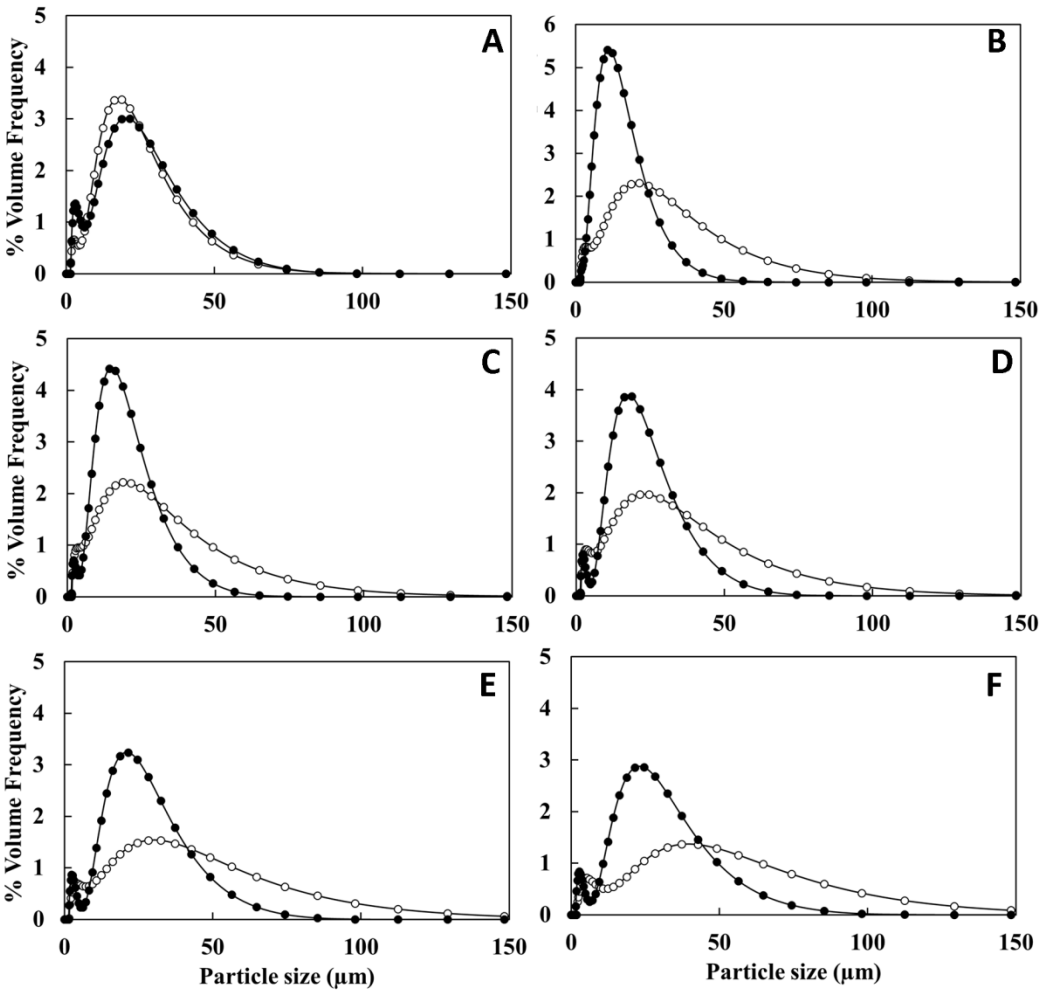

Figure A2.3: Comparison of the PSDs between floc sizes obtained in the ○ - microfluidic chip and ● - bench-scale; at 20 g kg^{-1} PEI (mol. wt. = 50-100 kDa), with varying pH. (a) 5, (b) 5.5, (c) 6, (d) 6.5, (e) 7 and (f) 7.5; at 25% solids yeast homogenate. Volumetric flow rate in the microfluidic chip: yeast homogenate = 75 µl min-1, PEI = 85 µl min-1. Average PSDs have been shown, n=5.

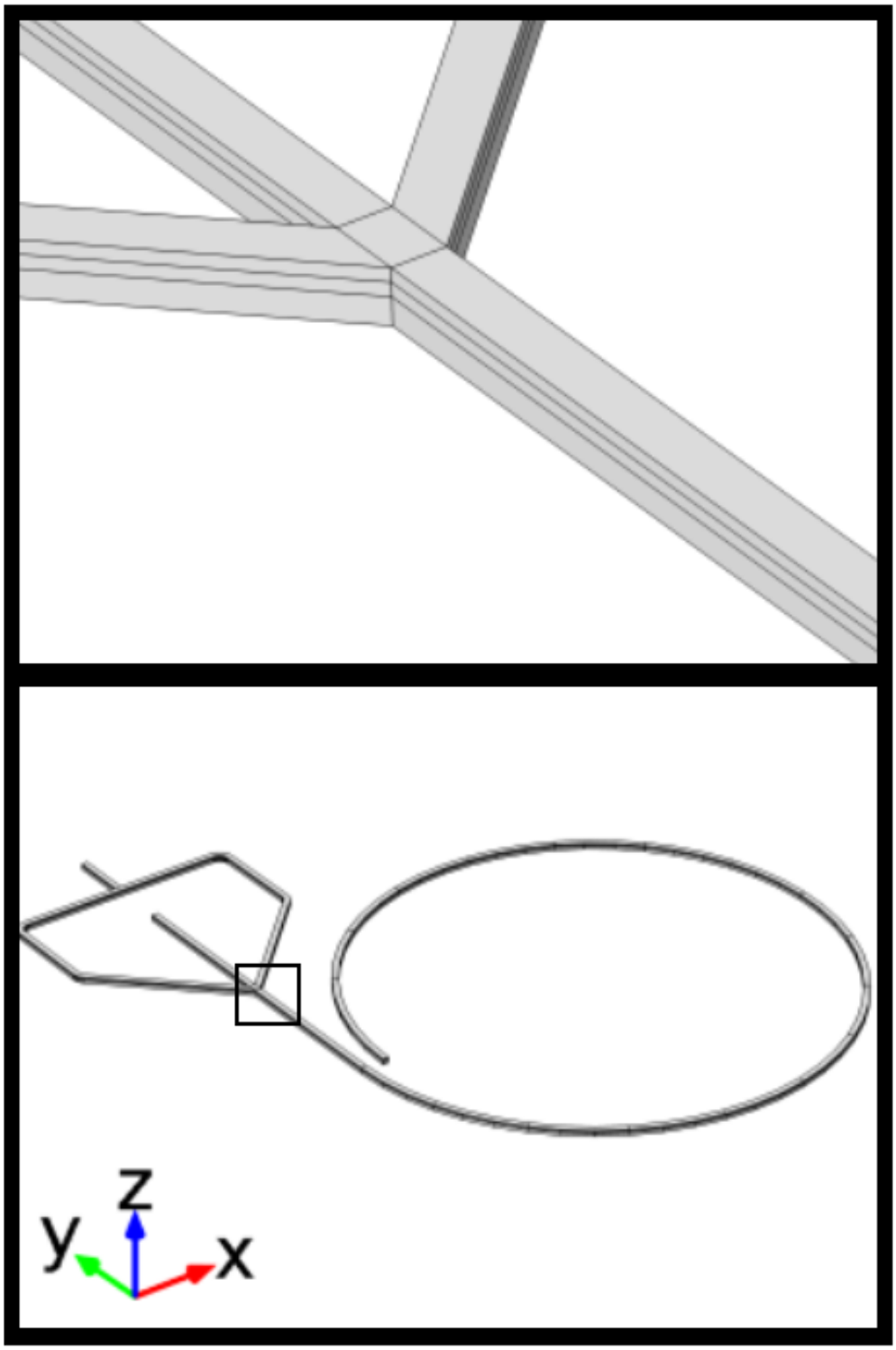

Figure A3.1: Images of the geometry of the µ-flocculation device imported into COMSOL for FEM. Additional planes were inserted to extract data at specific cross-sections and extrudes added at specific lengths of the channel.

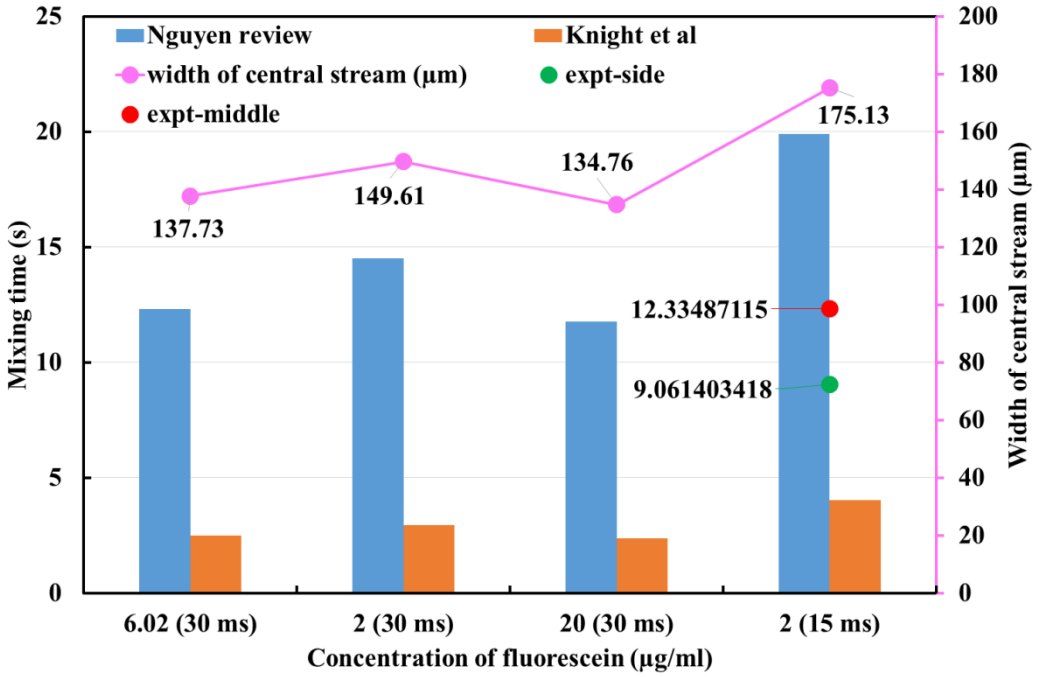

Figure A3.2: Graph showing the variation of the theoretical mixing times based on the width of the focussed flow measured from fluorescent images, at varying Fluorescein concentrations. The red and green markers denote the experimentally estimated mixing times at 2 µg ml^{-1}, 15 ms camera exposure. Blue bars – data calculated from Nguyen and Wu, 2004, and orange bars that from Knight et al., 1998.

Figure A4.1: A schematic flow-chart explaining the functioning of the computational image analysis script to automatically detect and measure the size and morphology of individual flocs. It has to be noted that this flow-chart is a simplified version and may syntactically vary from the actual script.

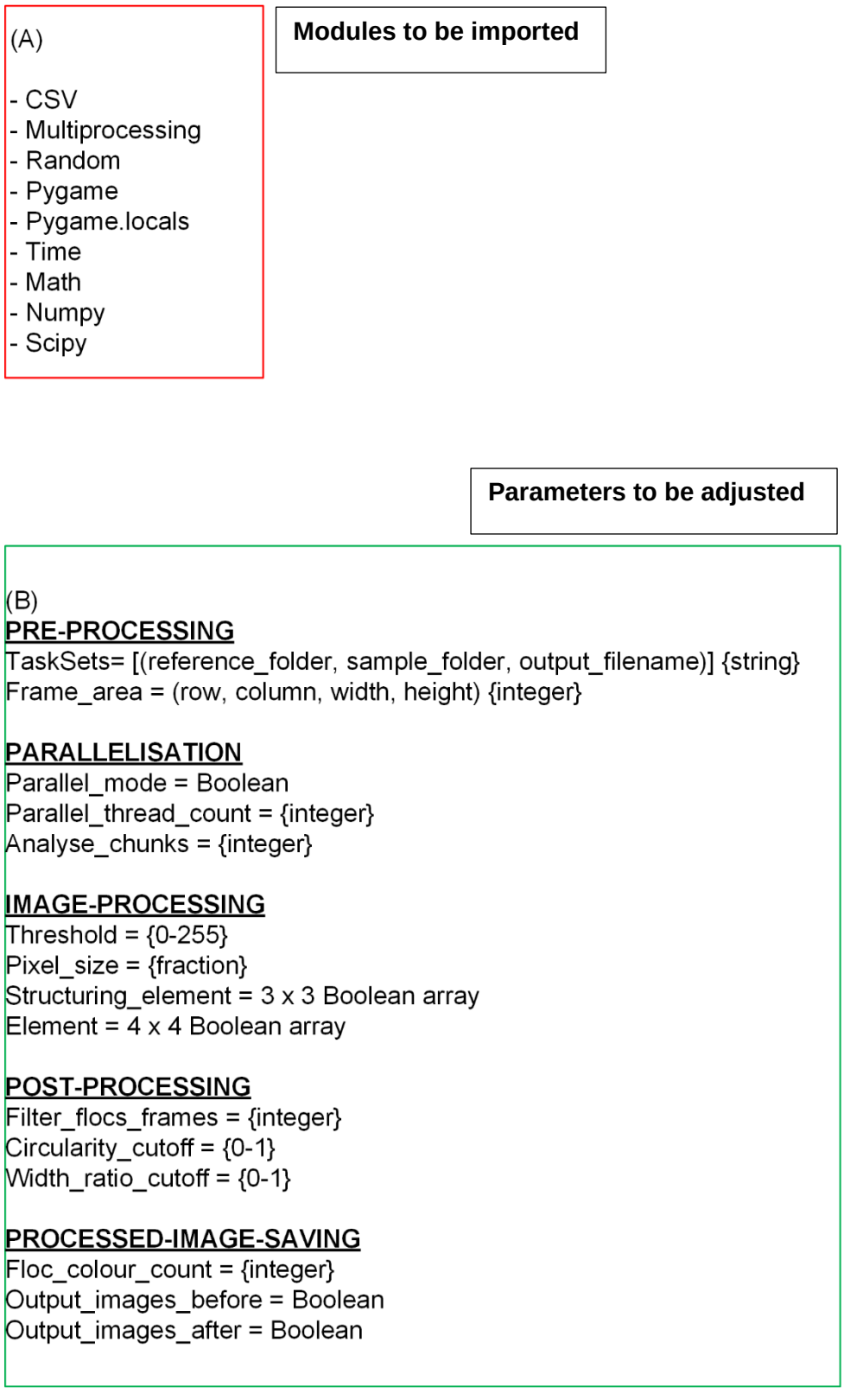

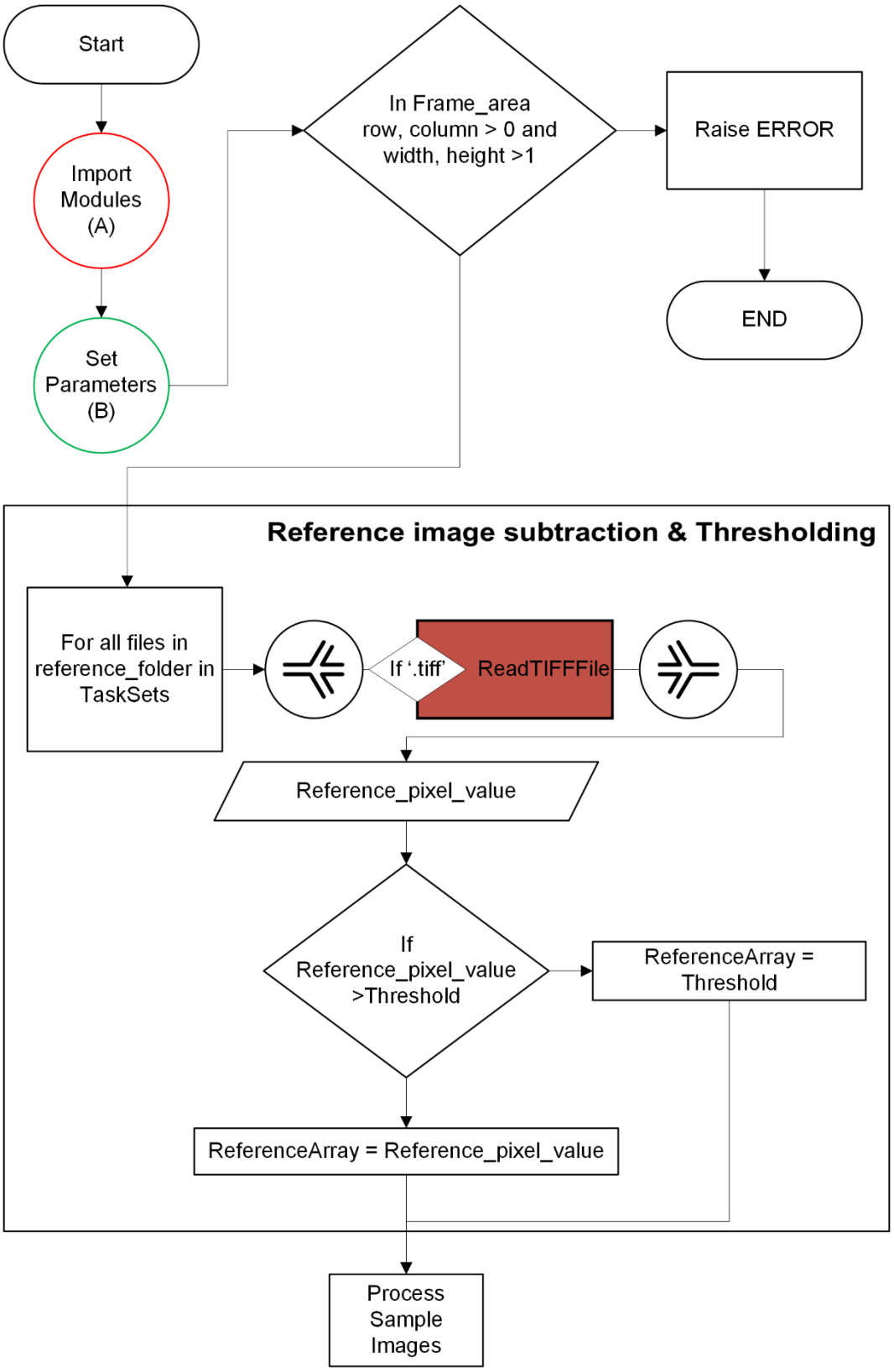
Start
Import Modules (A)
Set Parameters (B)
In Frame_area row, column > 0 and width, height >1
Raise ERROR
END
Reference image subtraction & Thresholding
For all files in reference_folder in TaskSets
If '.tiff'
ReadTIFFFile
Reference_pixel_value
If Reference_pixel_value >Threshold
ReferenceArray = Threshold
ReferenceArray = Reference_pixel_value
Process Sample Images

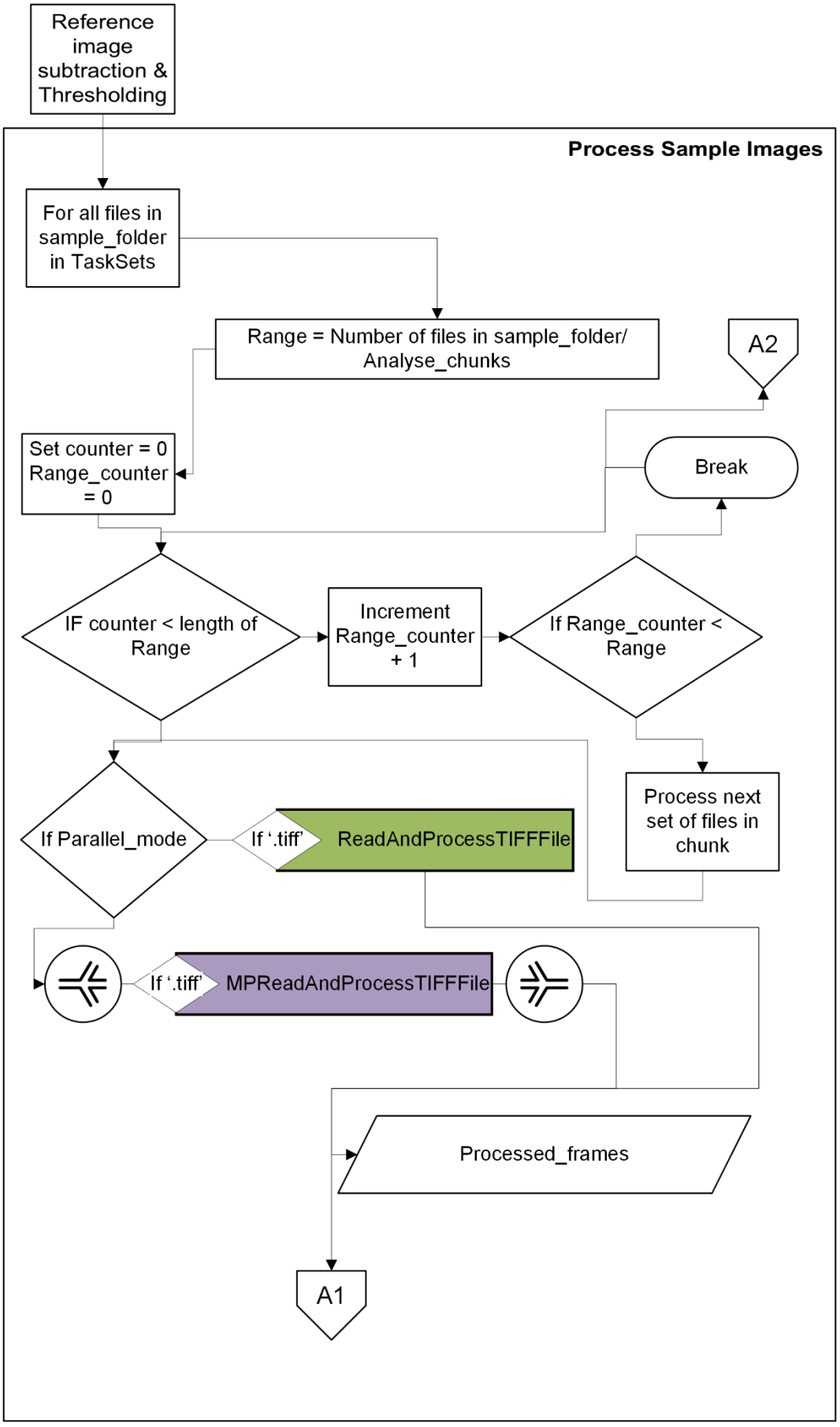
Reference image subtraction & Thresholding
Process Sample Images
For all files in sample_folder in TaskSets
Range = Number of files in sample_folder/ Analyse_chunks
A2
Set counter = 0 Range_counter = 0
Break
IF counter < length of Range
Increment Range_counter + 1
If Range_counter < Range
If Parallel_mode
If '.tiff'
ReadAndProcessTIFFFile
Process next set of files in chunk
If '.tiff'
MPReadAndProcessTIFFFile
Processed_frames
A1


A1
A2
Append counter = number of files processed
Output_images_before = True
If Parallel_mode
If '.tiff'
SaveSideBySideImage
If '.tiff'
MPSaveSideBySideImage
Images of flocs before relabelling

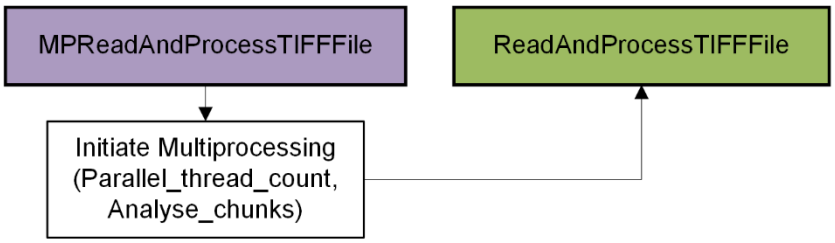
MPReadAndProcessTIFFFile
ReadAndProcessTIFFFile
Initiate Multiprocessing (Parallel_thread_count, Analyse_chunks)

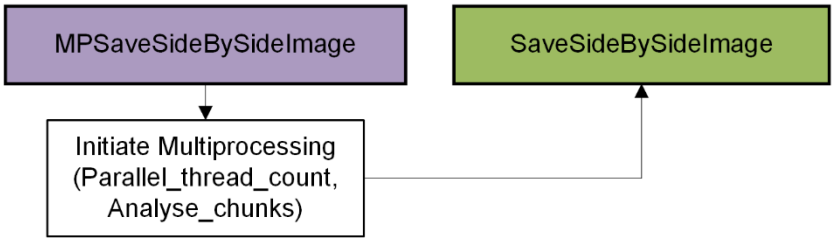
MPSaveSideBySideImage
SaveSideBySideImage
Initiate Multiprocessing (Parallel_thread_count, Analyse_chunks)

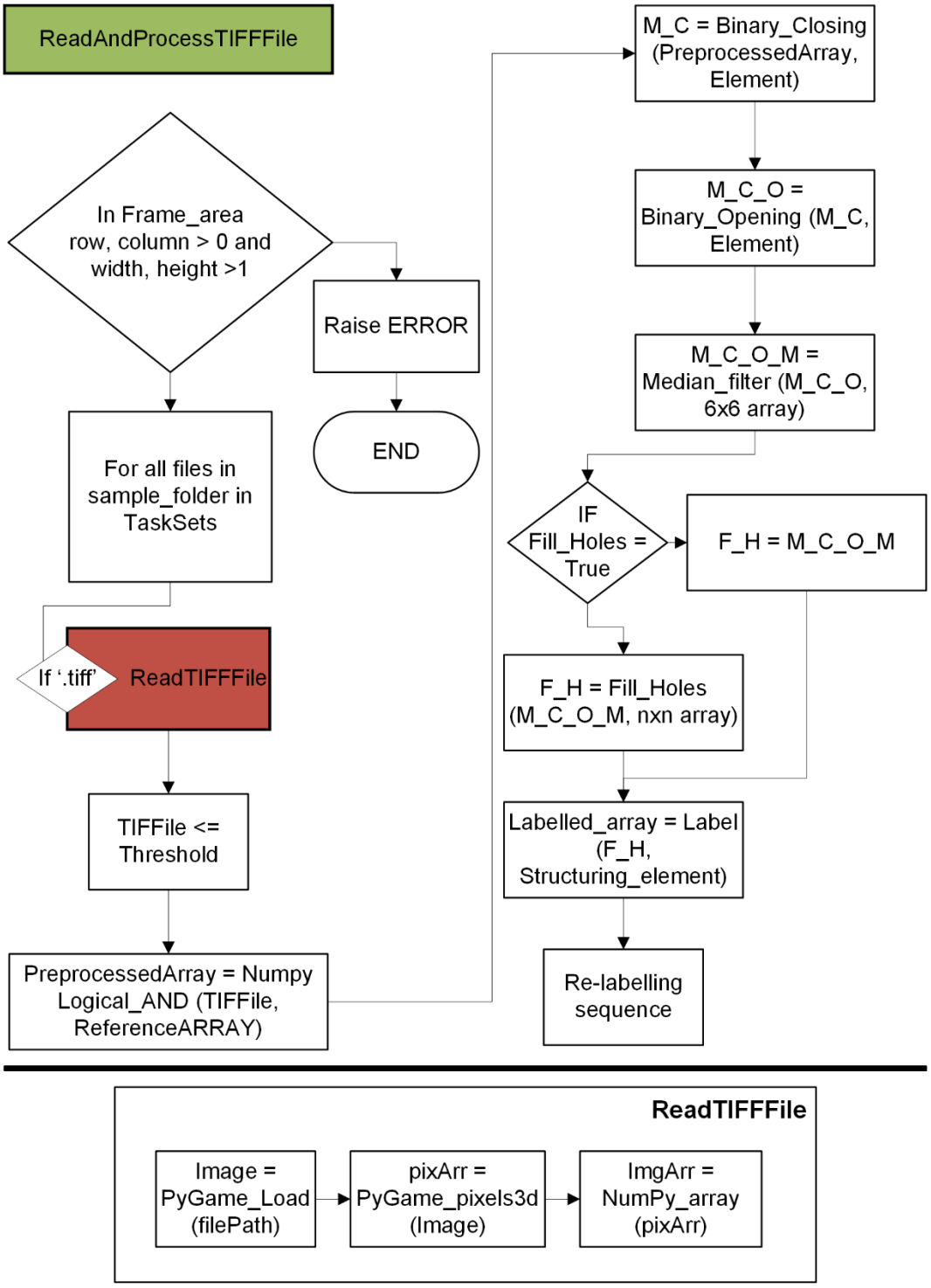
ReadAndProcessTIFFFile
In Frame_area row, column > 0 and width, height >1
Raise ERROR
END
For all files in sample_folder in TaskSets
If '.tiff'
ReadTIFFFile
TIFFile <= Threshold
PreprocessedArray = Numpy Logical_AND (TIFFile, ReferenceARRAY)
M_C = Binary_Closing (PreprocessedArray, Element)
M_C_O = Binary_Opening (M_C, Element)
M_C_O_M = Median_filter (M_C_O, 6x6 array)
IF Fill_Holes = True
F_H = M_C_O_M
F_H = Fill_Holes (M_C_O_M, nxn array)
Labelled_array = Label (F_H, Structuring_element)
Re-labelling sequence
ReadTIFFFile
Image = PyGame_Load (filePath)
pixArr = PyGame_pixels3d (Image)
ImgArr = NumPy_array (pixArr)

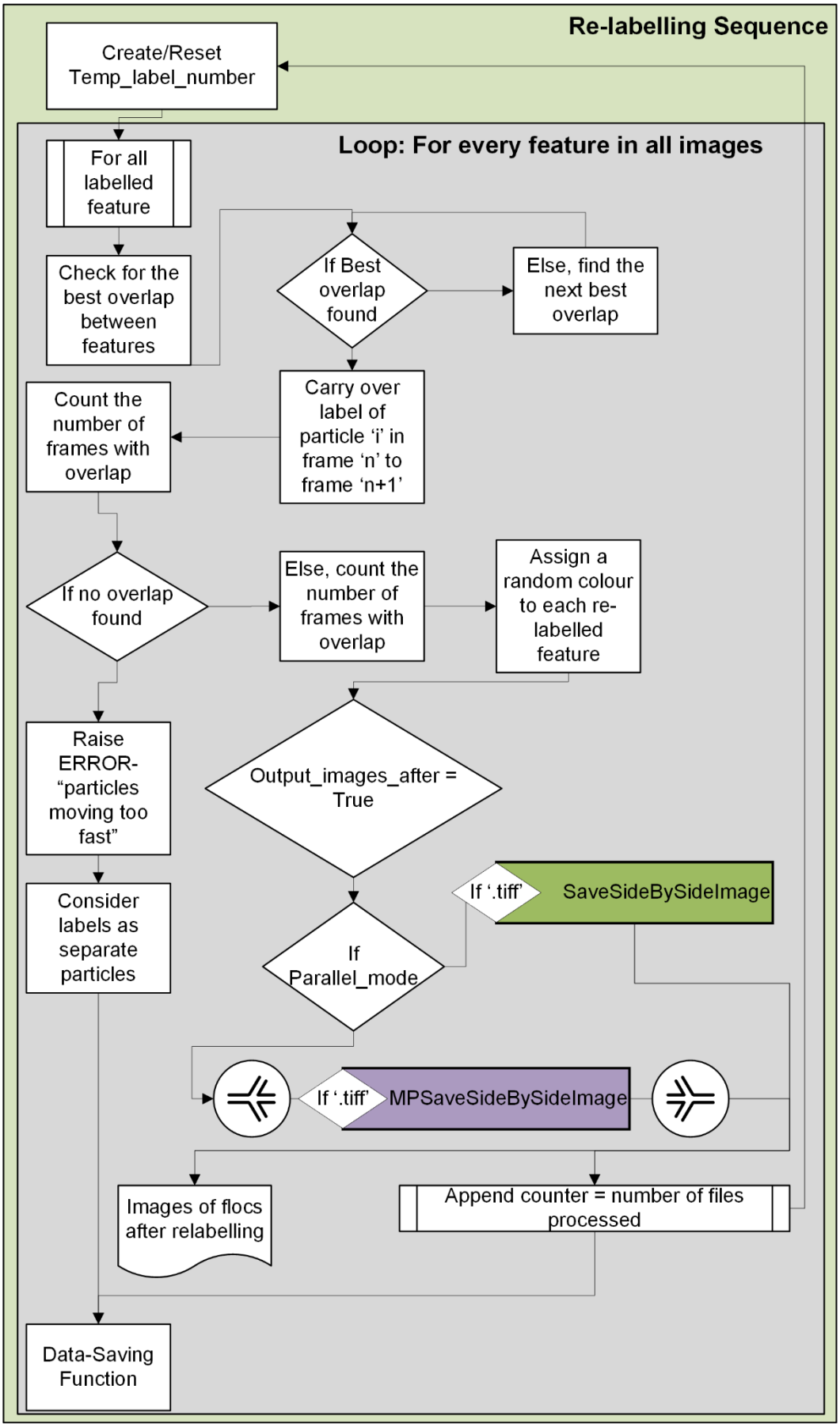
Re-labelling Sequence
Create/Reset Temp_label_number
Loop: For every feature in all images
For all labelled feature
Check for the best overlap between features
If Best overlap found
Else, find the next best overlap
Carry over label of particle 'i' in frame 'n' to frame 'n+1'
Count the number of frames with overlap
If no overlap found
Else, count the number of frames with overlap
Assign a random colour to each re-labelled feature
Raise ERROR- "particles moving too fast"
Output_images_after = True
Consider labels as separate particles
If '.tiff'
SaveSideBySideImage
If Parallel_mode
If '.tiff'
MPSaveSideBySideImage
Images of flocs after relabelling
Append counter = number of files processed
Data-Saving Function

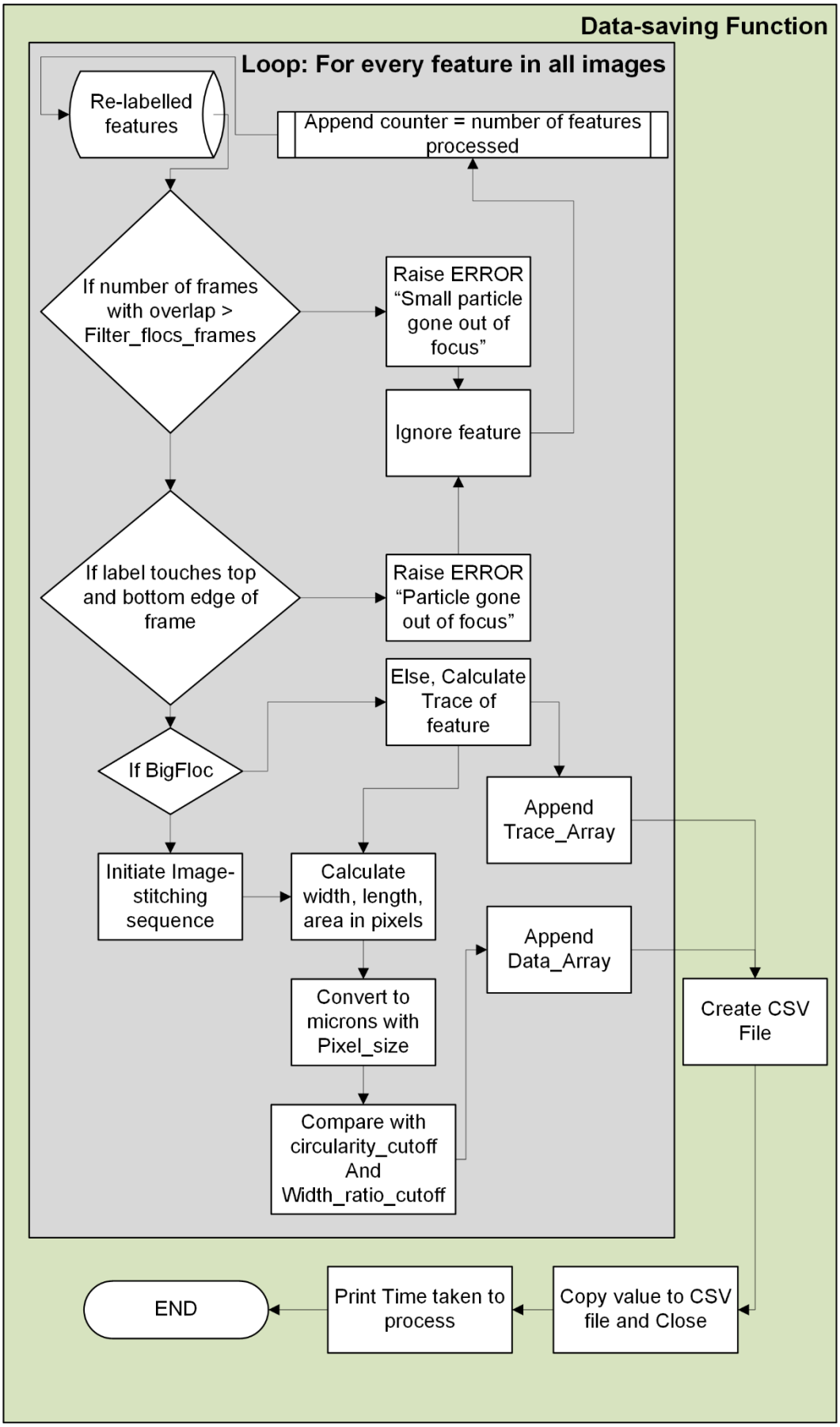
Data-saving Function
Loop: For every feature in all images
Re-labelled features
Append counter = number of features processed
If number of frames with overlap > Filter_flocs_frames
Raise ERROR "Small particle gone out of focus"
Ignore feature
If label touches top and bottom edge of frame
Raise ERROR "Particle gone out of focus"
Else, Calculate Trace of feature
If BigFloc
Append Trace_Array
Initiate Image-stitching sequence
Calculate width, length, area in pixels
Append Data_Array
Convert to microns with Pixel_size
Create CSV File
Compare with circularity_cutoff And Width_ratio_cutoff
END
Print Time taken to process
Copy value to CSV file and Close

Figure A4.2: A sample video, before and after re-labelling, of flocs formed between yeast homogenate and 20 g PEI kg^{-1} yeast, can be found with the DVD-ROM attached with the hard-copy of the thesis.

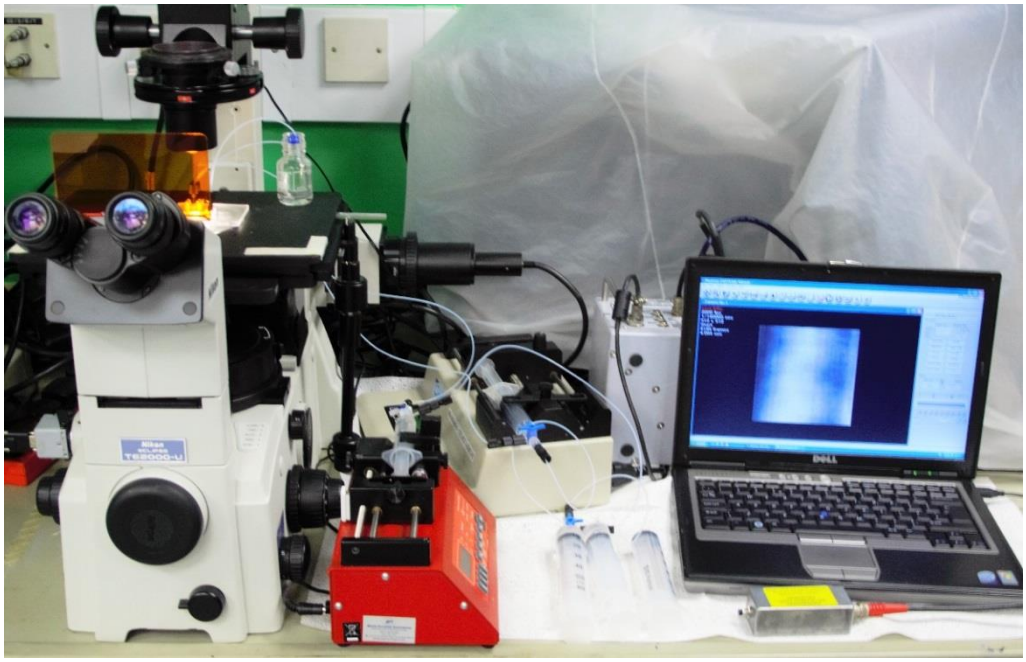

Figure A5.1: An image of the μ-flocculation device used with a high-speed camera (Photron MC-1) attached to a Nikon TE-2000 microscope. Also shown is the fluidic transport system with two programmable syringe pumps.

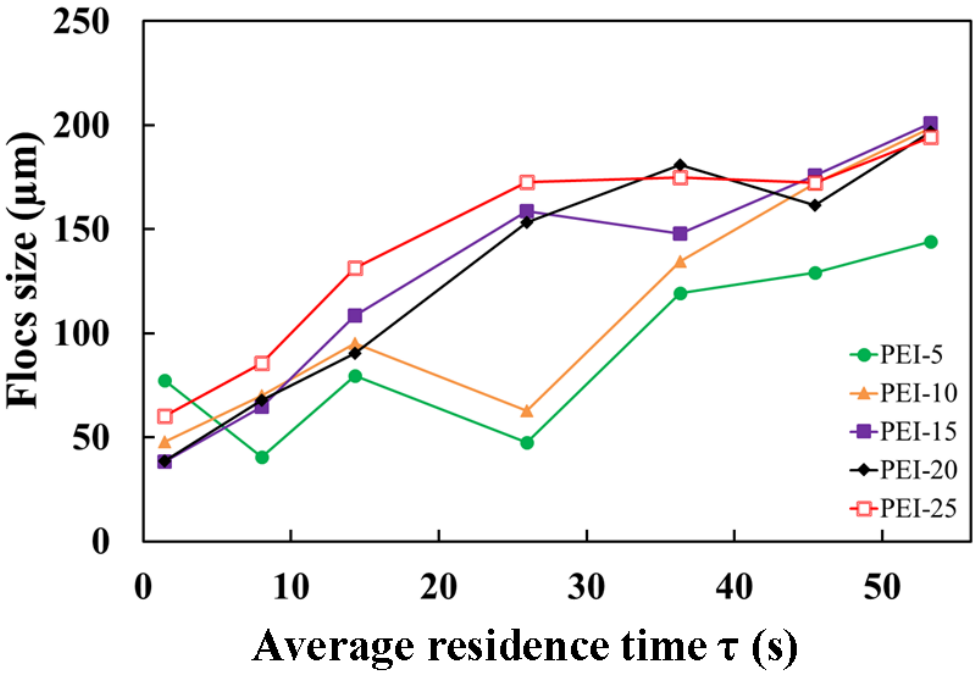

Figure A5.2: The growth of flocs formed between yeast homogenate and varying PEI_L concentrations: (●, PEI-5) - 5 g kg^{-1} yeast, (▲, PEI-10) - 10 g kg^{-1} yeast, (■, PEI-15) - 15 g kg^{-1} yeast, (♦, PEI-20) - 20 g kg^{-1} yeast and (□, PEI-25) - 25 g kg^{-1} yeast at pH 7.

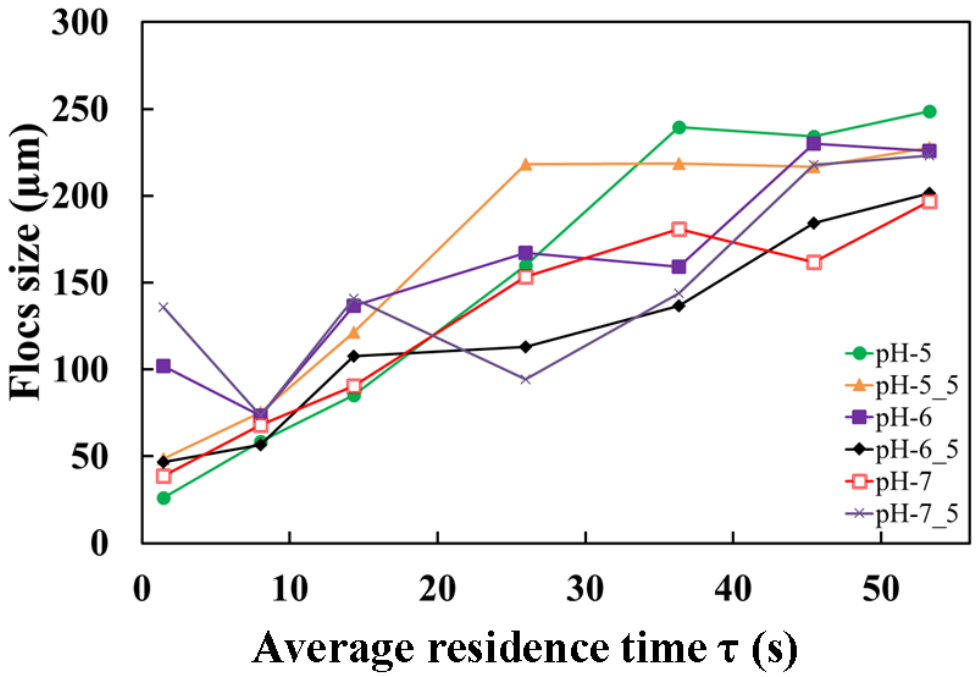

Growth of flocs formed between yeast homogenate and 20 g PEI_L kg^{-1} yeast with varying pH. The plots represent d90 diameter of floc. Error bars denote ± 1σ of all flocs measured in 8000 image sequences at each location.

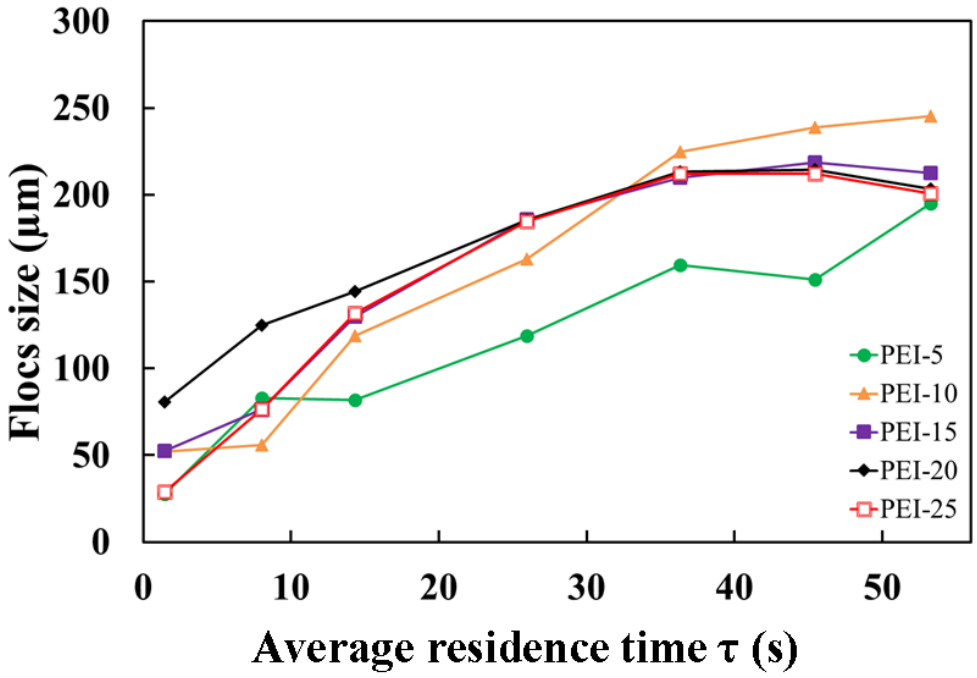

The growth of flocs formed between yeast homogenate and varying PEI_M concentrations: (●, PEI-5) - 5 g kg^{-1} yeast, (▲, PEI-10) - 10 g kg^{-1} yeast, (■, PEI-15) - 15 g kg^{-1} yeast, (♦, PEI-20) - 20 g kg^{-1} yeast and (□, PEI-25) - 25 g kg^{-1} yeast at pH 7.

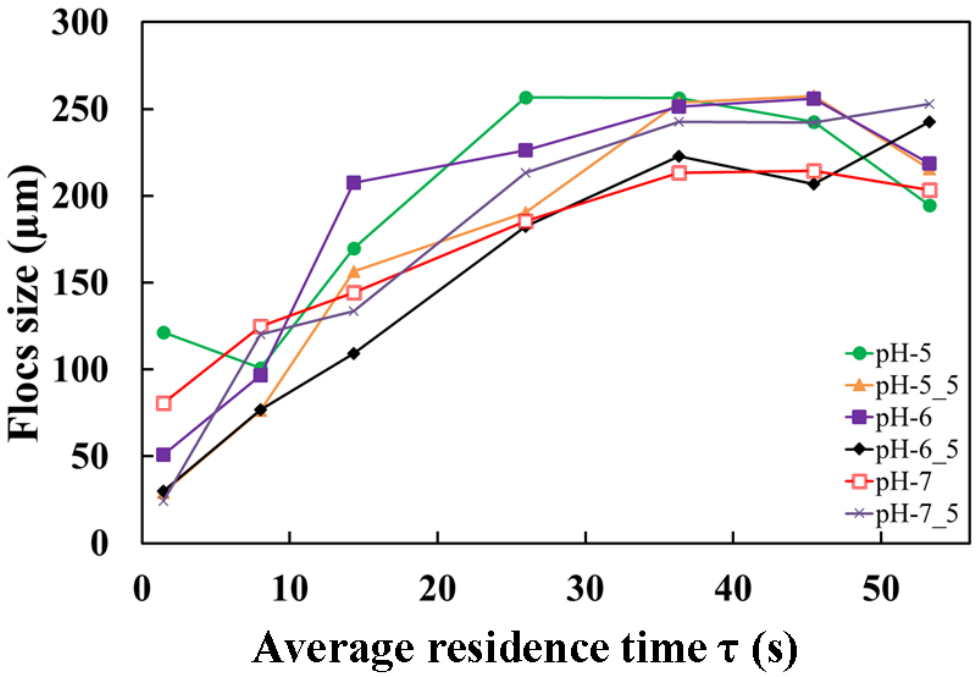

Growth of flocs formed between yeast homogenate and 20 g PEIM kg-1 yeast with varying pH. The plots represent d90 diameter of floc. Error bars denote ± 1σ of all flocs measured in 8000 image sequences at each location.

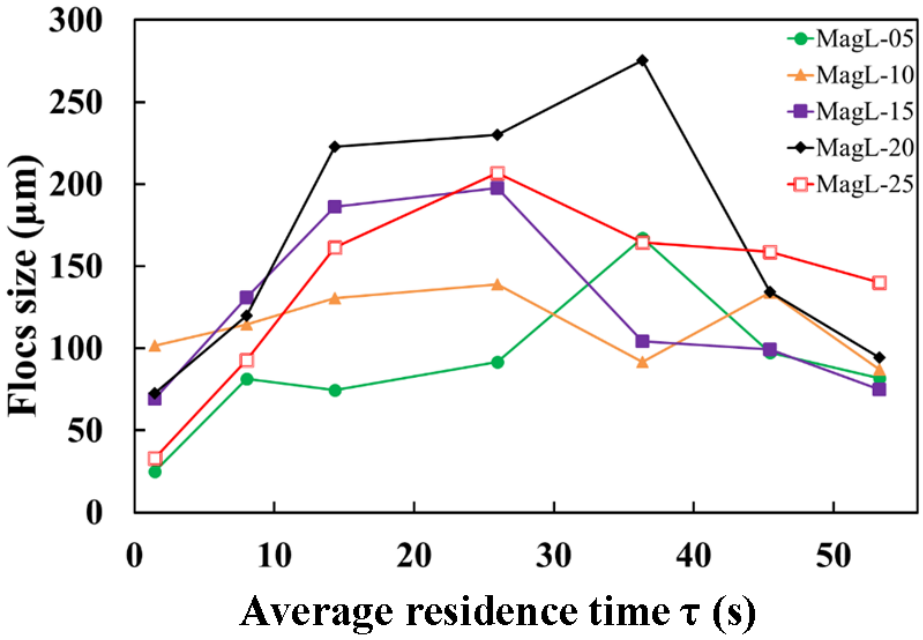

Figure A5.3: The largest 10% of flocs (d90) formed between yeast homogenate and varying pDADMAC$_L$ concentrations: (●, MagL-5) - 5 g kg^{-1} yeast, (▲, MagL-10) - 10 g kg^{-1} yeast, (■, MagL-15) - 15 g kg^{-1} yeast, (♦, MagL-20) - 20 g kg^{-1} yeast and (□, MagL-25) - 25 g kg^{-1} yeast at pH 7. Error bars denote ± 1σ of all flocs measured in 8000 image sequences at each location.

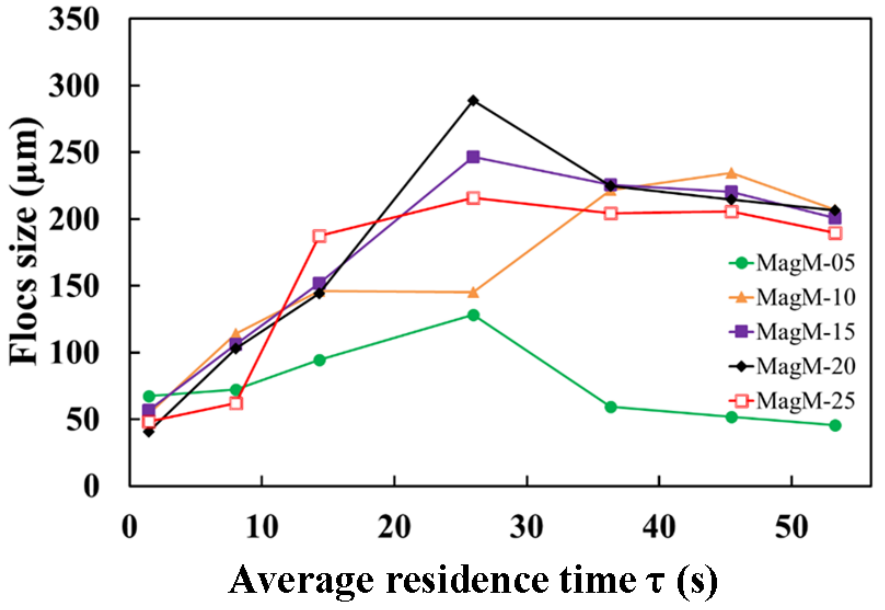

The largest 10% of flocs (d90) formed between yeast homogenate and varying pDADMAC$_M$ concentrations: (●, MagM-5) - 5 g kg^{-1} yeast, (▲, MagM-10) - 10 g kg^{-1} yeast, (■, MagM-15) - 15 g kg^{-1} yeast, (♦, MagM-20) - 20 g kg^{-1} yeast and (□, MagM-25) - 25 g kg^{-1} yeast at pH 7. Error bars denote ± 1σ of all flocs measured in 8000 image sequences at each location.

10. Appendix B: Publications and Conferences

Articles

1. **A.N.P. Radhakrishnan**, M.P.C. Marques, M.J. Davies, B. O'Sullivan, D.G. Bracewell & N. Szita; Rapid determination of floc growth conditions through single floc analysis. A microfluidic approach for the analysis of primary floc-formation, and its comparison with bench scale; Lab on a Chip (submitted for peer-review).
2. T.V. Kirk, M.P.C. Marques, **A.N.P. Radhakrishnan** & N. Szita (2016); Quantification of the oxygen uptake rate in a dissolved oxygen controlled oscillating jet-driven microbioreactor. Journal of Chemical Technology and Biotechnology (Manuscript accepted for publication).

Book Chapter

1. M.J. Davies, M.P.C. Marques, and **A.N.P. Radhakrishnan** (2014); Microfluidics Theory in Practice in "Microfluidics in Detection Science: Lab-on-a-chip Technologies"; London: RSC Publishing.

Articles in preparation

1. **A.N.P. Radhakrishnan**, M.P.C. Marques, N. Szita and D.G. Bracewell; Physico-chemical characterisation of flocculation to elucidate the growth kinetics of flocs in a microfluidic flocculation device.
2. **A.N.P. Radhakrishnan**, N. Szita and D.G. Bracewell; High-content computational image processing for real-time particle size and morphology measurements of flocs in continuous flow within a microfluidic device.

Conferences

1. 10th European Symposium on Biochemical Engineering Sciences and 6th IFIBiop, Lille, France, 2014 (Poster).
2. 17th International Conference on Miniaturized Systems for Chemistry and Life Sciences, Freiburg, Germany, 2013 (Poster).